

1N-20-CR

182490

153 P

# Electric Propulsion System Technology

Report — 1991

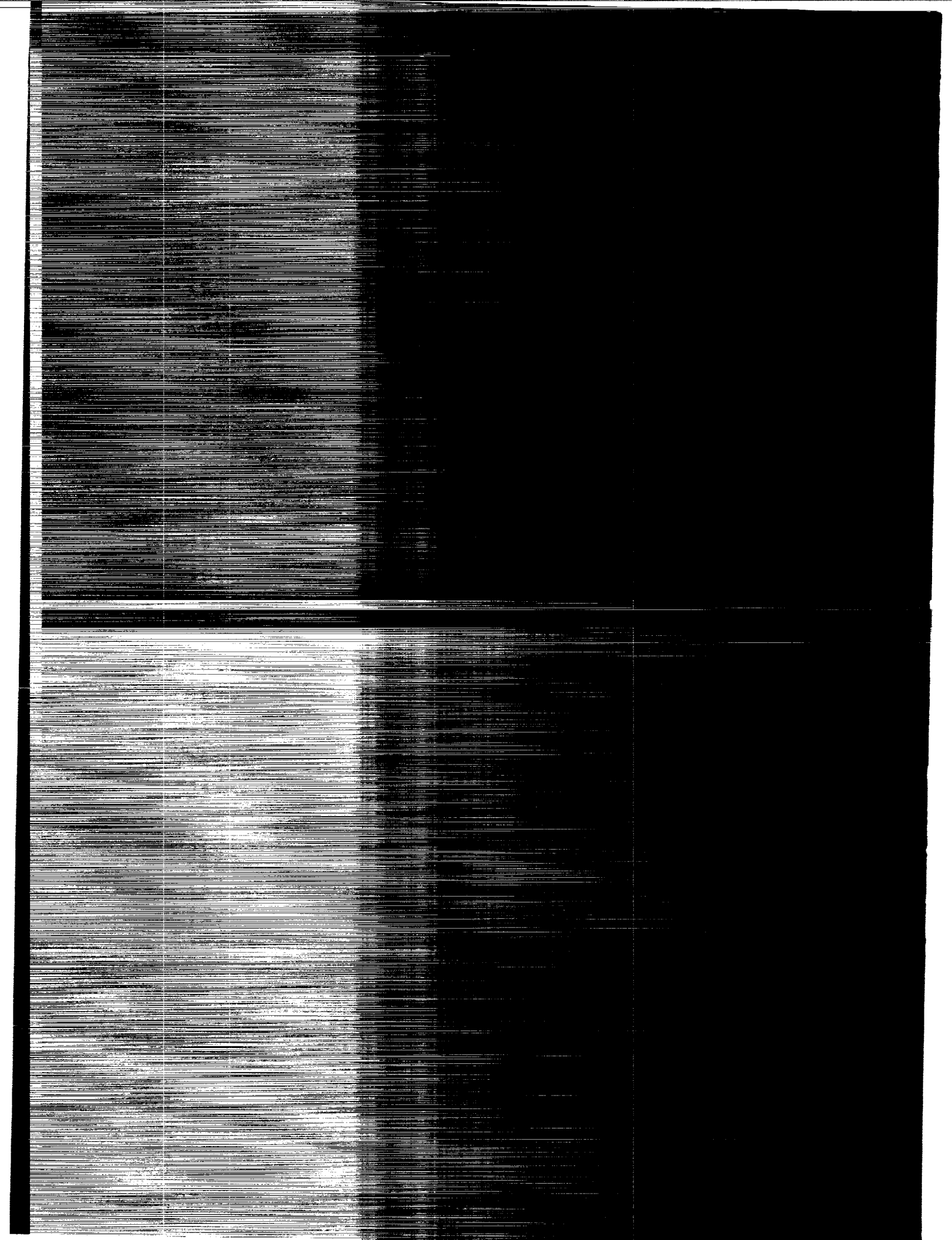
Donny  
Earner  
Bedfellow  
Pivrotto  
olk

(NASA-CR-194099) ELECTRIC  
PROPULSION SYSTEM TECHNOLOGY Annual  
Report, 1991 (JPL) 153 p

N94-13068

Unclass

G3/20 0182490



# Electric Propulsion System Technology

Annual Report — 1991

John R. Brophy  
Charles E. Garner  
Keith D. Goodfellow  
Thomas J. Pivrotto  
James E. Polk

November 1992



National Aeronautics and  
Space Administration

Jet Propulsion Laboratory  
California Institute of Technology  
Pasadena, California

The research described in this publication was carried out by the Jet Propulsion Laboratory, California Institute of Technology, under a contract with the National Aeronautics and Space Administration.

Reference herein to any specific commercial product, process, or service by trade name, trademark, manufacturer, or otherwise, does not constitute or imply its endorsement by the United States Government or the Jet Propulsion Laboratory, California Institute of Technology.



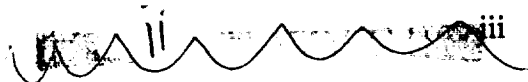
## Abstract

This publication describes the work performed in fiscal year (FY) 1991 under the Propulsion Technology Program RTOP (Research and Technology Objectives and Plans) No. (55) 506-42-31 for Low-Thrust Primary and Auxiliary Propulsion technology development. The objectives of this work fall under two broad categories. The first of these deals with the development of ion engines for primary propulsion in support of solar system exploration. The second with the advancement of steady-state magnetoplasmadynamic (MPD) thruster technology at 100 kW to multimewatt input power levels.

The major technology issues for ion propulsion are demonstration of adequate engine life at the 5 to 10 kW power level and scaling ion engines to power levels of tens to hundreds of kilowatts. Tests of a new technique in which the decelerator grid of a three-grid ion accelerator system is biased negative of neutralizer common potential in order to collect facility induced charge-exchange ions are described. These tests indicate that this SAND (Screen, Accelerator, Negative Decelerator) configuration may enable long duration ion engine endurance tests to be performed at vacuum chamber pressures an order of magnitude higher than previously possible. The corresponding reduction in pumping speed requirements enables endurance tests of 10 kW class ion engines to be performed within the resources of existing technology programs. The results of a successful 5,000-hr endurance of a xenon hollow cathode operating at an emission current of 25 A are described, as well as the initial tests of hollow cathodes operating on a mixture of argon and 3% nitrogen. Work performed on the development of carbon/carbon grids, a multi-orifice hollow cathode, and discharge chamber erosion reduction through the addition of nitrogen are also described.

Critical applied-field MPD thruster technical issues remain to be resolved, including demonstration of reliable steady-state operation at input powers of hundreds to thousands of kilowatts, achievement of thruster efficiency and specific impulse levels required for missions of interest, and demonstration of adequate engine life at these input power, efficiency and specific impulse levels. To address these issues we have designed, built, and tested a 100 kW class, radiation-cooled applied-field MPD thruster and a unique dual-beam thrust stand that enables separate measurements of the applied- and self-field thrust components. We have also initiated the development of cathode thermal and plasma sheath models that will eventually be used to guide the experimental program. In conjunction with the cathode modeling, a new cathode test facility is being constructed. This facility will support the study of cathode thermal behavior and erosion mechanisms, the diagnosis of the near-cathode plasma and the development and endurance testing of new, high-current cathode designs. To facilitate understanding of electrode surface phenomenon, we have implemented a telephoto technique to obtain photographs of the electrodes during engine operation. In order to reduce the background vacuum tank pressure during steady-state engine operation in order to obtain high fidelity anode thermal data, we have developed and are evaluating a gas-dynamic diffuser.

A review of experience with alkali metal propellants for MPD thrusters led to the conclusion that alkali metals, particularly lithium, offer the potential for significant engine



performance and lifetime improvements. These propellants are also condensible at room temperature, substantially reducing test facility pumping requirements. The most significant systems-level issue is the potential for spacecraft contamination. Subsequent experimental and theoretical efforts should be directed toward verifying the performance and lifetime gains and characterizing the thruster flow field to assess its impact on spacecraft surfaces. Consequently, we have begun the design and development of a new facility to study engine operation with alkali metal propellants.

## **Acknowledgments**

The authors would like to thank Lewis C. Pless, Alison G. Owens, William R. Thogmartin, and Robert L. Toomath for their expert assistance in performing the experimental work described in this publication.



# Table of Contents

1. Introduction .....	1
2. Ion Engine Technology .....	2
2.1 Ion Engine Endurance Testing .....	2
2.1.1 Preliminary Three-Grid Tests .....	4
2.1.2 Modeling of SAND Accelerator Systems .....	8
2.1.3 More SAND Optics Tests .....	11
2.1.4 SAND Optics Endurance Test .....	17
2.2 Cathode Endurance Testing .....	19
2.2.1 Facility Modifications .....	20
2.2.2 Cathode Description and Assembly .....	21
2.2.3 Cathode No. 1 Operation .....	25
2.2.4 Cathode No. 2 Assembly .....	29
2.3 Discharge Chamber Erosion Studies .....	30
2.4 Carbon/Carbon Grid Development .....	30
2.5 Divergent-Field Thruster Performance .....	33
2.6 Multi-Orifice Hollow Cathode .....	33
2.7 High-Power Ion Engines .....	35
3. Magnetoplasmadynamic (MPD) Thruster Technology .....	38
3.1 Operation of an Applied-Field MPD Thruster .....	38
3.2 Diffuser Evaluation .....	46
3.3 Electrode Thermal Modeling .....	51
3.3.1 Thermal Model Selection .....	51
3.3.2 Cathode Tip Thermal Model .....	52
3.3.3 Preliminary Electrode Thermal Models .....	52
3.4 Cathode Sheath Model .....	55
3.5 Cathode Surface Studies .....	56
3.6 Cathode Test Facility .....	58
3.7 Investigation of Alkali Metal Propellants .....	59
4. References .....	63
5. Appendices	
A. A 5,000 Hour Xenon Hollow Cathode Life Test .....	A-1
B. Metal and Metal Nitride Erosion Rates in a Divergent Field Ion Engine .....	B-1
C. Near-Term, 100-kW Class Ion Engines .....	C-1
D. An Experimental and Numerical Investigation of an Applied-Field Magnetoplasmadynamic Space Propulsion Engine .....	D-1
E. Alkali Metal Propellants for MPD Thrusters .....	E-1

## List of Figures

2.1.1	Accelerator grid current is a strong function of vacuum chamber pressure due to the formation of charge exchange ions which are attracted by the negative grid potential . . . . .	3
2.1.2	The use of a three-grid accelerator system with the third grid at neutralizer common potential reduces the ion current to the accelerator grid . . . . .	5
2.1.3	Three-grid power supply schematic . . . . .	6
2.1.4	The screen, accelerator, negative decelerator (SAND) three-grid accelerator system configuration results in substantially reduced accelerator grid currents. . . . .	7
2.1.5	The sputter yield of xenon on molybdenum is a nonlinear function of the ion energy and decreases rapidly with decreasing energies . . . . .	8
2.1.6	Computer calculation of ion trajectories and equal potential contours through the accelerator system geometry used in the 890-hour endurance test of Ref. 9 . . . . .	9
2.1.7	Ion trajectories and equal potential contours for a conventional three-grid accelerator system with the decelerator grid at zero volts . . . . .	10
2.1.8	Accelerator system operation with insufficient negative voltage on the accelerator grid resulting in electron back-streaming . . . . .	11
2.1.9	A negative decelerator grid enables the magnitude of the negative voltage applied to the accelerator grid to be reduced while still preventing electron back-streaming . . . . .	12
2.1.10a	"Screen-accel.-accel." SAND optics configuration . . . . .	13
2.1.10b	"Screen-screen-accel." SAND optics configuration . . . . .	13
2.1.11a	Accelerator grid current data for two-grid accelerator systems including data from NASA LeRC (ring-cusp thruster) and JPL (divergent-field thruster) . . . . .	15
2.1.11b	The "screen-screen-accel." SAND optics configuration results in almost no variation in accelerator grid current with vacuum chamber pressure . . . . .	15

## List of Figures (cont'd)

2.1.12	"Screen-screen-accel." SAND configuration data showing essentially no variation in accelerator grid current with tank pressure at a beam current of 2.0 A . . . . .	16
2.1.13	For the "screen-screen-accel." SAND optics, decreasing the accelerator grid voltage changes the distribution of charge exchange ion current to the grids . . . . .	16
2.1.14	A negative voltage applied to the decelerator grid enables operation at higher net-to-total voltage ratios before the onset of electron back-streaming . . . . .	18
2.2.1	Propellant distribution schematic for the hollow cathode endurance test . . . . .	21
2.2.2	Schematic design of the endurance test cathode . . . . .	22
2.2.3	Photograph of the life-test cathode components . . . . .	23
2.2.4	Photograph of an end view of the cathode, keeper electrode, polepiece, and discharge chamber . . . . .	24
2.2.5	Photograph of the molybdenum anode face plate . . . . .	25
2.2.6	Photograph of new keeper electrode geometry . . . . .	26
2.2.7	Scanning electron micrograph (SEM) photograph of the cathode orifice plate . . . . .	27
2.2.8	SEM photograph of deposits surrounding the cathode orifice . . . . .	27
2.2.9a	SEM photograph of tungsten deposits surrounding the cathode orifice. . . .	28
2.2.9b	SEM photograph of tungsten and tantalum deposits surrounding the cathode orifice. . . . .	28
2.2.10	Plot of increase in propellant line pressure with time during extended leak check . . . . .	29

## List of Figures (cont'd)

2.4.1	Plot of coefficient of linear expansion as a function of temperature for carbon/carbon and molybdenum . . . . .	32
2.4.2	Plot of sputter yield as a function of xenon ion energy for carbon/carbon and molybdenum . . . . .	32
2.6.1a	Schematic of multi-orifice cathode . . . . .	36
2.6.1b	Multi-orifice cathode endcap . . . . .	36
2.6.1c	Multi-orifice cathode end view . . . . .	36
2.6.2a	Schematic of downstream multi-orifice cathode position . . . . .	37
2.6.2b	Schematic of upstream multi-orifice cathode position . . . . .	37
2.6.3	Thruster performance with the multi-orifice cathode and no baffle falls between that for operation with and without the baffle using a conventional hollow cathode . . . . .	38
3.1.1	Schematic of MPD thruster . . . . .	39
3.1.2	Plot of calculated and measured magnetic-field strength . . . . .	39
3.1.3	Schematic of MPD thruster dual-beam thrust stand . . . . .	40
3.1.4	Photograph of side view and front view of thrust stand . . . . .	41
3.1.5	Plot of MPD thrust data . . . . .	43
3.1.6	Photograph of experimental cathode tips after testing . . . . .	44
3.1.7	Illustration of pre-test and post-test cathode tip geometries . . . . .	44
3.1.8	Photograph of MPD thruster cathode tip and eroded throat . . . . .	45
3.1.9	Photograph of sectioned graphite nozzle . . . . .	45
3.2.1	Plot of arcjet diffuser data . . . . .	47
3.2.2	Plot of MPD thruster diffuser data . . . . .	48



## **List of Figures (cont'd)**

3.2.3	Schematic of arcjet test facility and diffuser installation . . . . .	48
3.2.4	Schematic of arcjet engine . . . . .	49
3.2.5	Schematic of MPD thruster diffuser installation . . . . .	50
3.3.1	Example of cathode temperature distribution . . . . .	53
3.3.2	Example of anode temperature distribution . . . . .	54
3.5.1	Photograph of hot cathode tip showing axisymmetric patterns . . . . .	57
3.5.2	Photograph of hot cathode tip showing formation of crystals in a ring pattern . . . . .	57
3.6.1	Photograph of vacuum chamber for cathode test facility . . . . .	59
3.6.2	Schematic of laboratory layout. . . . .	60
3.6.3	Plot of vacuum system performance . . . . .	61

## List of Tables

2.1.1	Nominal 150-hour Endurance Test Operating Parameters . . . . .	19
2.5.1	Ion Engine Performance Comparison . . . . .	34

# 1. Introduction

Challenging space missions of the next decades will require propulsion systems that perform well beyond the limits of advanced chemical systems. Electric propulsion offers substantial benefits relative to conventional chemical systems including increased payloads, reduced initial spacecraft masses, and reduced trip times (but, generally not all at the same time). In particular, the use of nuclear electric propulsion (NEP) with high power ion engines has been shown to be mission enabling for the detailed exploration of the outer planets.<sup>1</sup> Solar electric propulsion with ion engines can also provide substantial benefits over chemical propulsion.<sup>2</sup> The major technology issues for ion propulsion are demonstration of adequate engine life at the 5- to 10-kW power level and engine scaling to power levels of hundreds of kilowatts. Demonstration of a 10,000-hour engine life at the 5- to 10-kW level requires the use of a test facility with a very high pumping speed to adequately simulate the space environment. Endurance tests performed in inadequately pumped facilities result in artificially short engine lifetimes due to charge exchange erosion of the accelerator grid caused by operation at high vacuum chamber pressures. The requirement for very high pumping speeds has heretofore made endurance testing of 10-kW class ion engines prohibitively expensive. A new technique which promises to make these endurance tests affordable within existing technology programs is described in this publication. The other ion engine technology development activities described in this publication are divided along the two major technology issues mentioned above namely, lifetime at 5- to 10-kW, and scaling to higher powers. The cathode endurance testing and discharge chamber erosion tests deal with the engine lifetime issue. The carbon/carbon grid development activity, segmented ion engine design, and multi-orifice cathode tests deal primarily with issues associated with scaling ion engines to higher power levels.

The applied-field MPD thruster, operated at SP-100 class power levels, is a potential alternative to a multi-engine ion thruster system, and multimewatt MPD thrusters are being seriously considered for application to the Space Exploration Initiative (SEI).<sup>3</sup> The major applied-field MPD thruster technical issues are the achievement of performance levels (efficiency and specific impulse) that are of interest to planetary and SEI applications, the demonstration of adequate engine life at these performance levels, and the scaling of steady-state engine input powers to megawatt levels. To address these issues a 100-kW-class, radiation-cooled, applied-field, MPD thruster and a unique dual-beam thrust stand that allows us to measure the applied-field and self-field thrust components separately were designed, built, and tested. We have also initiated the development of electrode thermal and plasma sheath models that will be used to guide the thruster development program. To understand electrode surface phenomenon, we have implemented a telephoto technique to obtain close-up photographs of the MPD thruster electrodes during engine operation. In order to reduce the background vacuum tank pressure during steady-state engine operation, we have developed and are evaluating a gas-dynamic diffuser. Finally, we have begun the design and development of new facilities to study MPD engine cathodes and to operate and study engines operating with alkali metal propellants.

## 2. Ion Engine Technology

*John R. Brophy and Charles E. Garner*

### 2.1 Ion Engine Endurance Testing

Ion engines have been under development for 30 years and have long since achieved performance levels (thrust, specific impulse, and efficiency) that are attractive for planetary missions. The power-limited, low-thrust nature of ion propulsion, however, results in the requirement for very long engine burn times to produce the desired spacecraft velocity change. Engine burn times of 10,000 to 15,000 hours are required for typical deep space missions of interest (see, for example, Ref. 2). Demonstrating useful lifetimes of this magnitude, for engines to be used for primary propulsion, has historically proven to be an intractable problem, and yet such a demonstration is believed to be essential before this technology will be used on a planetary spacecraft.

A substantial effort, as represented by numerous life tests of the 30-cm-diameter mercury ion engine in the 1970s and early 1980s, was expended to demonstrate adequate engine life.<sup>3-8</sup> Not one of these tests, however, successfully demonstrated a 10,000- to 15,000-hour useful life at full thrust. By far the most successful test was the 4,200 hour, full power test of the J-Series engine designated J1.<sup>7</sup> Other significant tests included a 5,000-hour test of the J5 thruster at 1/4 power,<sup>8</sup> and a 10,000-hour test of a 700-series thruster.<sup>4</sup> This 10,000-hour test is considered significant in that a 30-cm-diameter thruster was operated for 10,000 hours. However, the thruster itself suffered considerable internal erosion damage due to ion sputtering and could only be operated at a small fraction of its full thrust level by the end of the test. In addition, frequent intervention on the part of the operators was required in order to keep the thruster operating. The results of this test prompted the design changes that resulted in the 900-series engine.<sup>3</sup>

These and most other ion engine endurance tests were performed using mercury as the propellant. Very low vacuum chamber pressures (typically less than  $3 \times 10^{-6}$  torr) were maintained during engine testing by cryopumping the mercury exhaust on liquid nitrogen temperature surfaces. Cryopumping results in very high effective pumping speeds if large surface areas are used, resulting in low background pressures. The major cost of mercury ion engine life testing turned out to be the cost of the liquid nitrogen.

The switch from mercury to xenon propellant for ion engines aggravated the already difficult life-testing problem. Xenon gas cannot be effectively cryopumped at liquid nitrogen temperatures. Furthermore, the heavy atomic mass of xenon greatly reduces the effective pumping speed of large oil diffusion pumps relative to air and the 5-kW xenon thruster under development at the NASA Lewis Research Center (LeRC)<sup>9</sup> operates at a propellant flow rate that is 60% higher than that of the 2.7 kW J-series mercury engine. The combination of these factors makes endurance testing of 5-kW class xenon ion engines prohibitively expensive.

Very low background pressures are required for ion engine life-testing in order to minimize charge exchange ion erosion of the accelerator grid. The accelerator grid is the downstream electrode of a conventional two-grid ion accelerator system and is typically biased several hundred volts negative of neutralizer common. Charge exchange ions created downstream of the engine are accelerated into the negative accelerator grid causing sputter erosion. The production rate of charge exchange ions is a strong function of the background pressure as indicated in Fig. 2.1.1. In this figure, the increase in accelerator grid current results from the increase in charge exchange ion production with tank pressure. The datum point labeled "LeRC 890 HR LIFE TEST" represents the accelerator grid current at which an 890-hour endurance test of a 5-kW xenon ion engine was performed.<sup>9</sup> The solid line in this figure is a curve fit to data taken at NASA LeRC<sup>10</sup> for a xenon engine operating at a beam current of 3.2 A, and indicates that the accelerator grid current asymptotically approaches a minimum value of 11.2 mA (0.35% of the beam current) at zero background pressure.

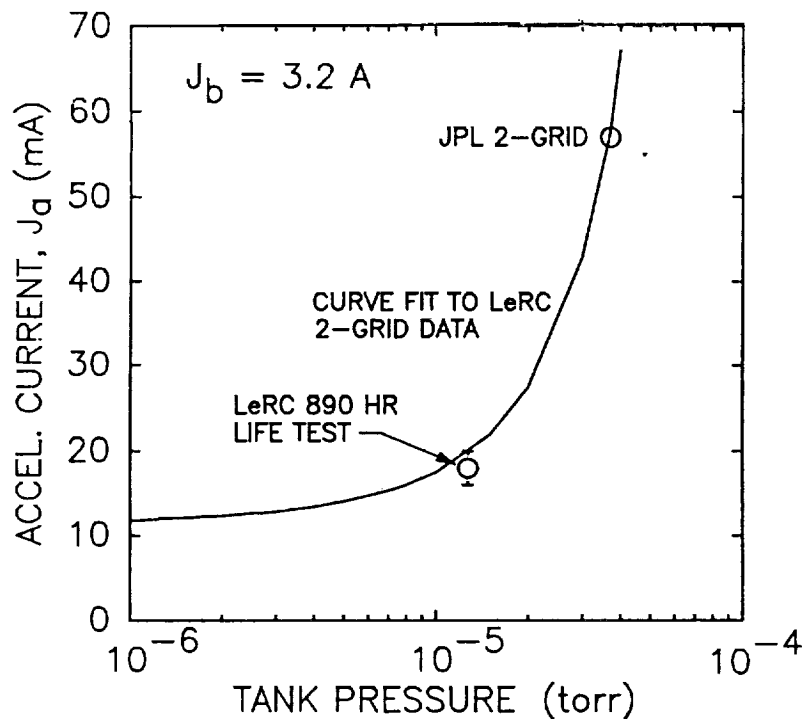


**Fig. 2.1.1 Accelerator grid current is a strong function of vacuum chamber pressure due to the formation of charge exchange ions which are attracted by the negative grid potential.**

The 5-kW endurance test of Ref. 9 was performed with an accelerator current of  $17.5 \pm 1.5$  mA, which is approximately 60% higher than the zero pressure current. At this current level, and an accelerator grid voltage of between -300 and -375 V, holes were eroded completely through the accelerator grid webbing in less than 890 hours. The solid line in Fig. 2.1.1 indicates that the accelerator current can be reduced to approximately 12 mA with a background pressure

of  $10^{-6}$  torr. To achieve this background pressure during full power operation, however, requires a pumping speed of approximately 700,000 liters/s. The large Tank 5 at NASA LeRC with two helium cryopanel is projected to have a pumping speed of 250,000 liters/s on xenon.<sup>10</sup> Even so, reducing the accelerator grid current from 17.5 mA to 12 mA by increasing the pumping speed from 55,000 liter/s<sup>9</sup> to 700,000 liters/s may be expected to increase the time to erode completely through the accelerator grid from less than 890 hours to only about 1300 hours. This is still far less than the required engine life of 10,000 to 15,000 hours. It should be noted that the accelerator grid is still functional even with holes eroded completely through the webbing between the holes. A consensus definition for the end of life for the accelerator grid has not been established; however, the time to erode completely through the grid webbing would seem to be an upper limit.

The datum point labeled "JPL 2-GRID" in Fig. 2.1.1 indicates the accelerator grid current measured in the JPL 2.4-m-diameter x 4.6-m-long electric propulsion test facility at the minimum achievable tank pressure during engine operation at a 3.2 A beam current (corresponding to an input power of approximately 5.5 kW). This accelerator grid current point agrees well with the curve-fit data from NASA LeRC. The current is a factor of three higher than that from the 890-hour endurance test of Ref. 9 due to the higher tank pressure and suggests that holes would be eroded through the grid webbing in less than 300 hours if an endurance test was attempted at this thrust level in the JPL facility.

### 2.1.1 Preliminary Three-Grid Tests

To address this problem an investigation into the use of three-grid optics was initiated. It is well known that the addition of a third grid downstream of the accelerator grid, with this third grid maintained at neutralizer common potential, will reduce the ion current to the accelerator grid as indicated in Fig. 2.1.2 from Ref. 11. In this figure, the circular data points indicate the accelerator grid current as a fraction of the total beam current for a two-grid system operating with mercury propellant. The square data points represent the accelerator grid current for a three-grid system under similar operating conditions, and the triangular points represent the decelerator grid of this three-grid system. Clearly the addition of the third grid reduces the ion current to the accelerator grid even for operation at the low background pressures under which these data were taken.

A three-grid accelerator system was assembled to investigate the feasibility of decreasing the accelerator grid ion current further by biasing the decelerator grid either positive or negative of neutralizer common potential. This three-grid system was assembled from two sets of 600 series, 30-cm-diameter, two-grid ion optics (in this older electrode series, the screen-grid and accelerator-grid apertures are the same diameter). The two sets of two-grid optics were disassembled and the stiffening ring from one of the accelerator grids was cut off using a laser-machining processes. This electrode served as the accelerator grid for the new three-grid system, and the other accelerator grid, with the stiffening ring still attached, served as the decelerator grid. The three-grid accelerator system was assembled by separating the electrodes with mica washers and pressing the three-grid/two-mica-washer sandwich arrangement with the new

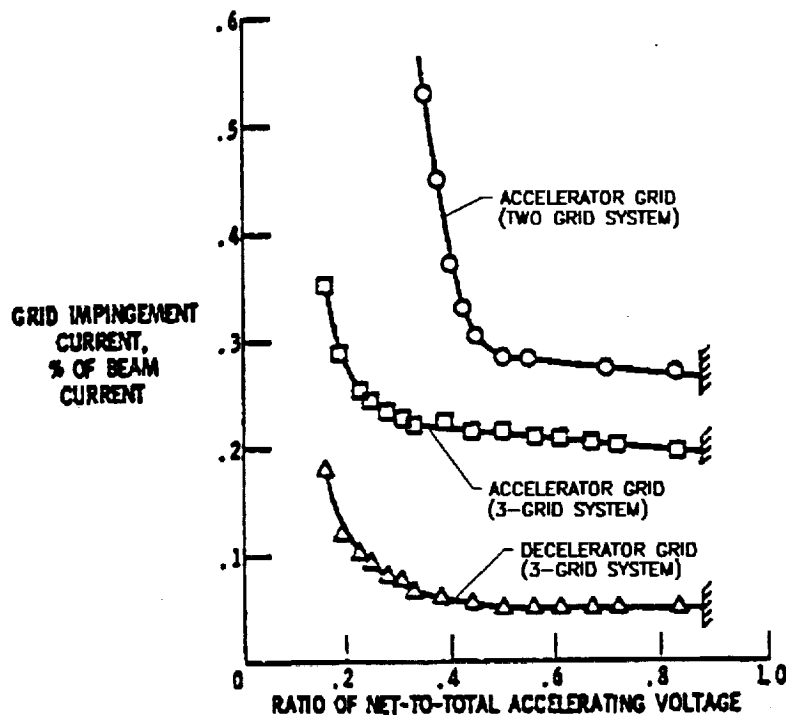


**Fig. 2.1.2** The use of a three-grid accelerator system with the third grid at neutralizer common potential reduces the ion current to the accelerator grid.

decelerator grid attached to the accelerator system mounting ring. The power supply schematic, shown in Fig. 2.1.3, was used to apply the desired voltages to the grid electrodes. The polarity of the decelerator grid supply could be reversed in order to bias this grid either positive or negative of neutralizer common potential.

Tests with the decelerator grid biased positive of neutralizer common potential were performed based on the hypothesis that a positive potential on this grid would direct positive charge exchange ions away from the accelerator system. It was recognized that a positive decelerator grid would also function as a secondary anode for the neutralizer cathode, and the effect of this was unknown. The tests indicated that applying a positive potential to the decelerator grid did not reduce the ion current to the accelerator grid. In fact, biasing the decelerator grid more than approximately 15 V above neutralizer common potential actually increases the ion current to the accelerator grid. The explanation for this is relatively simple, and in hindsight, rather obvious. The negative voltage on the accelerator grid is used to prevent electron backstreaming. To prevent electron backstreaming, the electrons must "see" this negative voltage. Biasing the decelerator grid positive of the beam plasma does not prevent the electrons from "seeing" the negative accelerator grid potential. If it did, then the negative accelerator grid voltage would not be required; but tests with this configuration showed that it

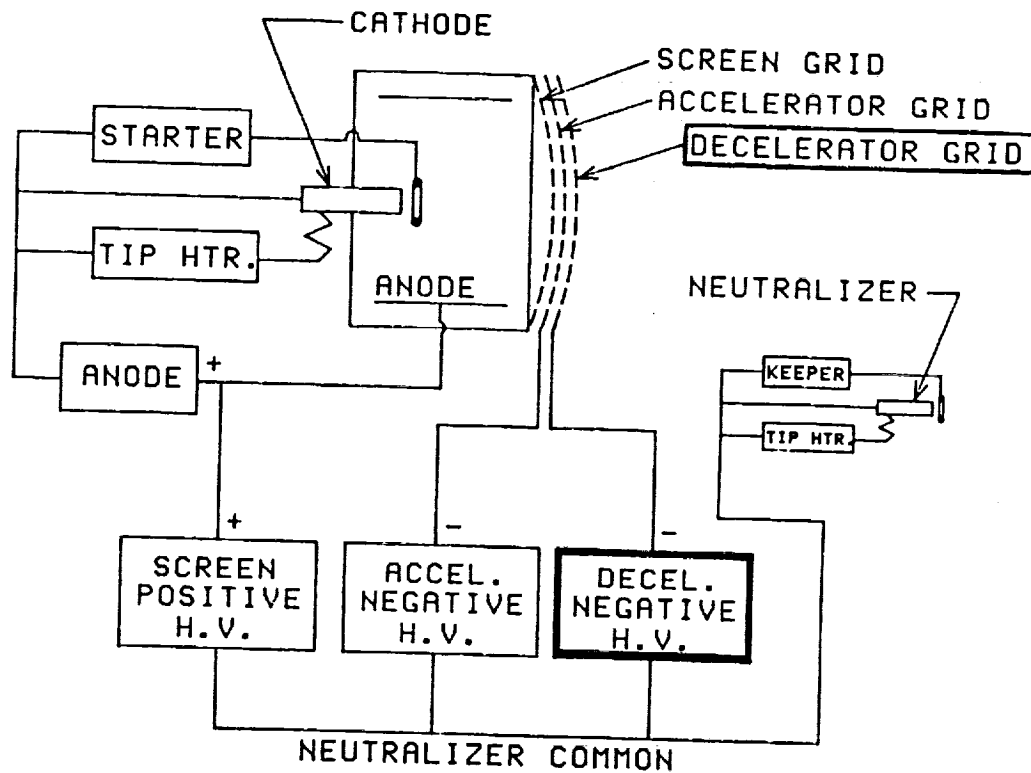


**Fig. 2.1.3 Three-grid power supply schematic.**

definitely is required. Therefore, if the electrons in the beam plasma "see" the accelerator grid negative potential, then the charge exchange ions in this plasma will also "see" it and be attracted to the grid. Thus, the positive potential on the decelerator grid is not effective in shielding the accelerator grid from the charge exchange ions. It is believed that the increase in ion current to the accelerator grid for decelerator grid voltages of more than 15 V above neutralizer common potential results from the acceleration of electrons toward the positive decelerator grid. In this acceleration process, some electrons acquire sufficient energy to ionize the ambient propellant gas resulting in the production of additional low energy ions near the accelerator system. The production of low energy ions just downstream of the accelerator system by electron bombardment has been proposed as a mechanism to explain the high accelerator grid currents observed at high vacuum chamber pressures.<sup>12</sup>

Tests in which the decelerator grid is biased negative of neutralizer common potential revealed two beneficial effects: (1) with the decelerator grid biased sufficiently negative, it appears to collect the vast majority of the charge exchange ions produced downstream of the accelerator system, substantially reducing the flux of ions to the accelerator grid even at high vacuum chamber pressures; and (2) with a negative voltage on the decelerator grid, the magnitude of the negative voltage required on the accelerator grid to prevent electron back-streaming can



be significantly reduced. Thus, by using a three-grid accelerator system and by biasing the decelerator grid negative of neutralizer common potential, the erosion rate of the accelerator grid is substantially reduced through two mechanisms: the reduction of ion current to the grid, and the reduction of the energy of these ions (which is determined by the magnitude of the negative voltage applied to the accelerator grid).

A 30-cm-diameter, divergent field discharge chamber was used with the three-grid set assembled from the two sets of 600-series electrodes. Operation of this discharge chamber/ion optics combination on xenon at a beam current of 3.2 A resulted in an accelerator grid current of 14 mA at a corrected tank pressure of  $3.7 \times 10^{-5}$  torr with the following voltages applied to the grids: (1) a screen grid voltage of 1110 V, (2) an accelerator grid voltage of -300 V, and (3) a decelerator grid voltage of -100 V. This datum point is compared to that for the two-grid case in Fig. 2.1.4. This accelerator grid current is actually less than that measured in the course of the 890-hour endurance test in Ref. 9 even though the endurance test was performed in a facility with a much higher pumping speed resulting in a vacuum chamber pressure approximately a factor of three less than in the JPL facility during these tests. According to the curve fit to the NASA LeRC data, an accelerator grid current of 14 mA is comparable to that which would be expected at a tank pressure of approximately  $5 \times 10^{-6}$  torr on a conventional two-grid accelerator system and corresponds to an effective pumping speed, in terms of accelerator grid erosion, of 350,000 liters/s. The actual pumping speed of the JPL vacuum system on xenon at this pressure

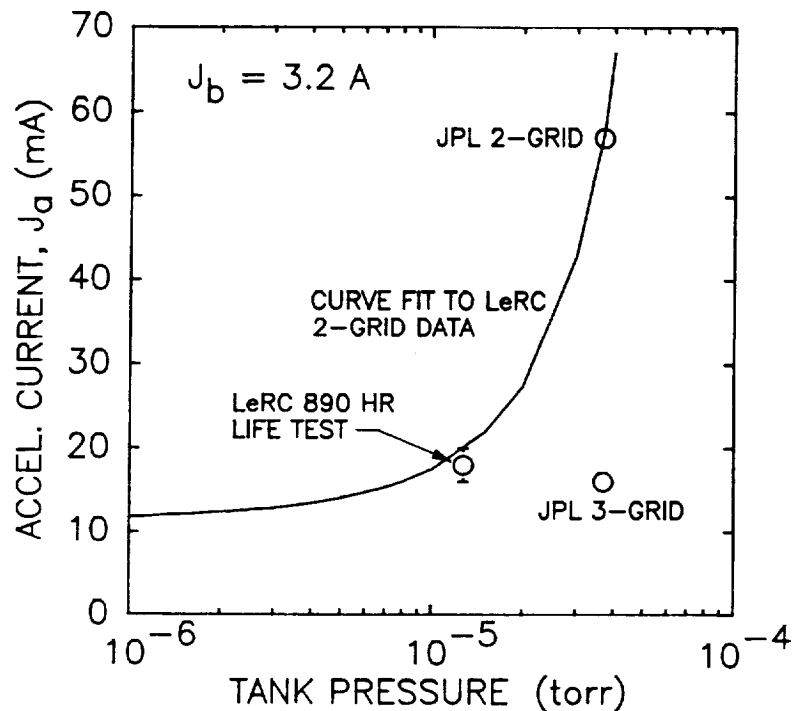
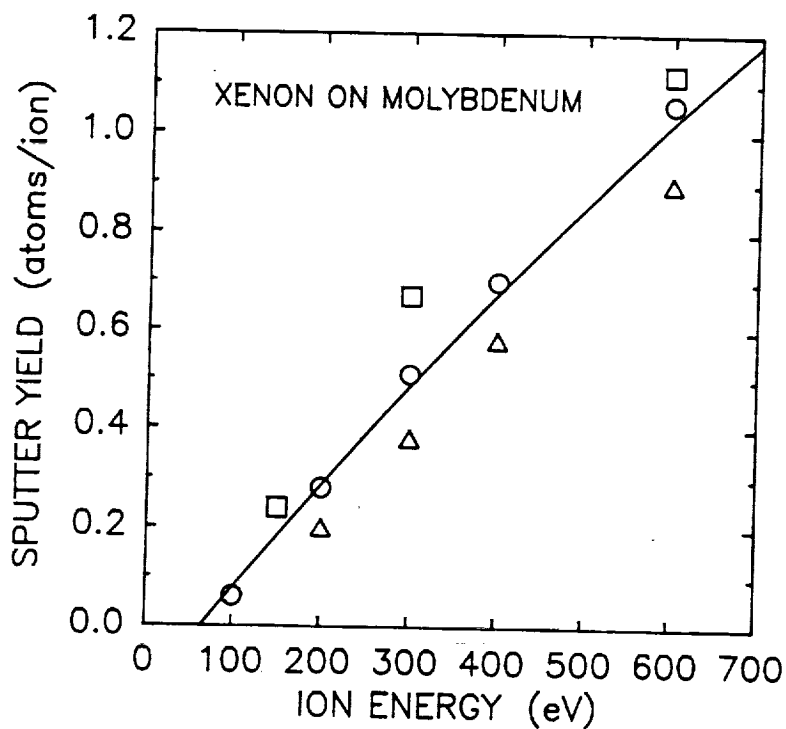


Fig. 2.1.4 The screen, accelerator, negative decelerator (SAND) three-grid accelerator system configuration results in substantially reduced accelerator grid currents.

is approximately only 14,000 liters/s. This corresponds to over an order of magnitude increase in effective pumping speed.

With this screen, accelerator, negative decelerator (SAND) three-grid technique, the charge exchange ion current that previously struck the accelerator grid is now collected by the negatively biased decelerator grid. It might then be expected that we have simply traded a severe accelerator grid erosion problem for an equally severe decelerator grid erosion problem. However, this is not the case because the magnitude of the decelerator grid voltage is significantly less than that applied to the accelerator grid, and the sputter yield of xenon ions on molybdenum decreases rapidly with ion energy as indicated in Fig. 2.1.5. The data in this figure are from Ref. 13 and indicate that the sputter yield at 100 eV is roughly a factor of ten less than at 300 eV. Furthermore, the yield at 200 eV is approximately half that at 300 eV.



**Fig. 2.1.5** The sputter yield of xenon on molybdenum is a nonlinear function of the ion energy and decreases rapidly with decreasing energies.

### 2.1.2 Modeling of SAND Accelerator Systems

Numerical calculations of two- and three-grid accelerator system behavior were performed in order to understand the effects of a negative decelerator grid on the accelerator system operation and to select candidate SAND electrode geometries for further experimental evaluation. The numerical calculations were performed using a computer code, written by K. Ishihara and

Y. Arakawa of the University of Tokyo, that assumes an axisymmetric geometry. The program was modified slightly to enable the voltage on the decelerator grid to be a user input rather than fixed at zero volts as in the original code. The results of applying this code to the accelerator system geometry and potentials used in Ref. 9 for the 890-hour endurance test are shown in Fig. 2.1.6. The top half of this figure indicates the trajectories of selected ions, while the bottom half indicates equal potential contours through the accelerator system. When the equal potential contours are positive, the increment between contours is 100 V. For negative contours the increment is 10 V. Two zero-volt contours are seen to cross the centerline of the grid aperture; however, the -10 V contour does not. This suggests that the accelerator system under these conditions is probably operating close to the electron back-streaming limit (i.e., at as high a net-to-total voltage ratio as possible). These calculations were made for an normalized perveance per hole (NP/H) of  $2.0 \times 10^{-9} \text{ A/V}^{3/2}$ , which corresponds roughly to the centerline value for the operating conditions of the 890-hour test. The equal potential contours downstream of the accelerator grid suggest that ions formed in this region will be directed toward the webbing of the accelerator grid.

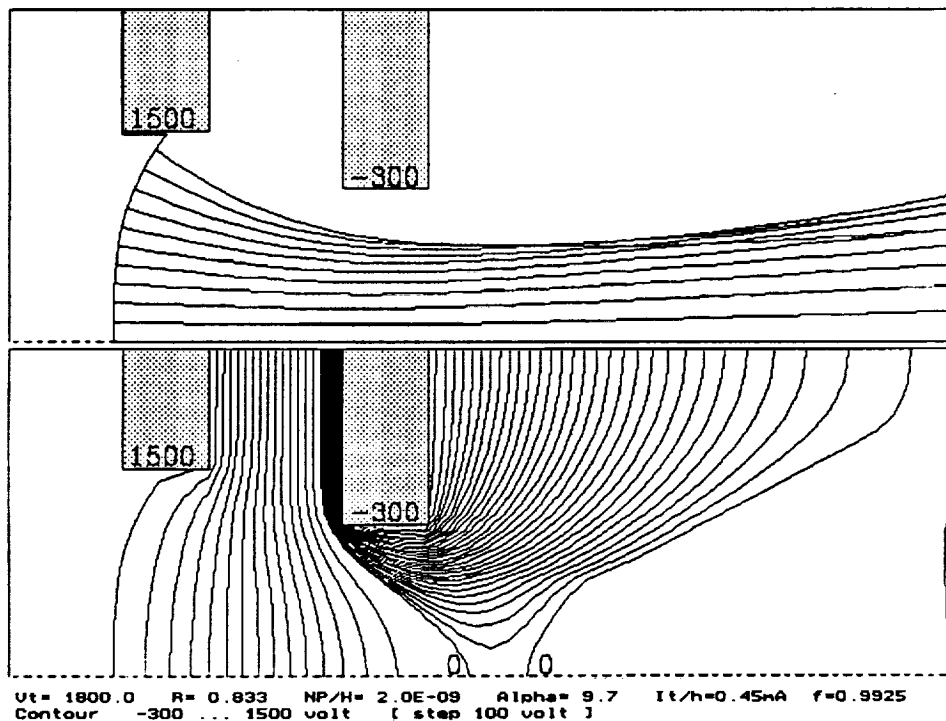


**Fig. 2.1.6** Computer calculation of ion trajectories and equal potential contours through the accelerator system geometry used in the 890-hour endurance test of Ref. 9.

Calculations for a conventional three-grid system with the decelerator grid potential maintained at zero volts (roughly neutralizer common potential) are given in Fig. 2.1.7 for the same grid geometry (hole sizes, grid thicknesses, and separations) as for Fig. 2.1.6 with the

addition that the decelerator grid aperture diameter is the same as that for the screen grid apertures (1.91 mm). The decelerator grid thickness is the same as the screen and accelerator grids (0.381 mm), and the accelerator/decelerator grid separation is the same as the screen/accelerator gap (0.61 mm). The accelerator grid apertures are 1.14 mm in diameter. The calculations in Fig. 2.1.7 are for a NP/H of  $1.0 \times 10^{-9} \text{ A/V}^{3/2}$ , which correspond roughly to the average NP/H across a 30-cm-diameter accelerator system for operation at a beam current of 3.2 A and a beam flatness parameter of 0.5. The equal potential contours in this figure again indicate operation close to the electron back-streaming limit. Furthermore, the negative contours suggest that charge exchange ions formed downstream of the accelerator grid will be directed toward the edge of the accelerator grid hole. The grid erosion patterns suggested by Figs. 2.1.6 and 2.1.7 are in rough\* qualitative agreement with observed erosion patterns for two- and three-grid accelerator systems.

If the geometry of Fig. 2.1.7 is maintained, but the accelerator grid voltage is changed from -300 V to -200 V, the results shown in Fig. 2.1.8 are obtained. In this case, there is insufficient negative voltage on the accelerator grid to prevent electron back-streaming as indicated by the fact that there are no negative equal potentials which cross the centerline of the grid apertures. Electrons from the beam plasma will easily "see" the +100 V equal potential

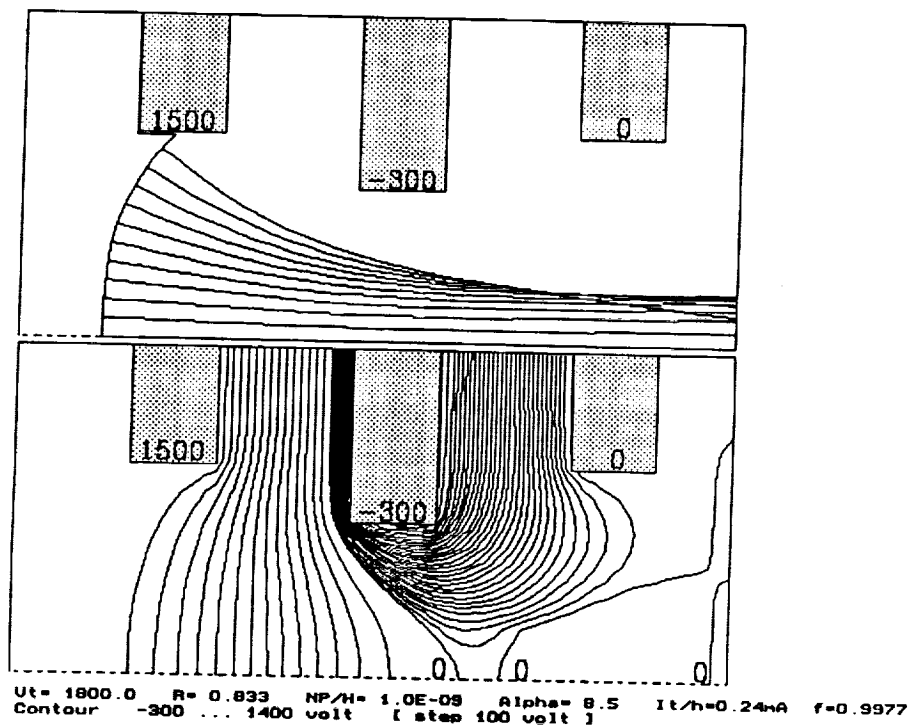


**Fig. 2.1.7** Ion trajectories and equal potential contours for a conventional three-grid accelerator system with the decelerator grid at zero volts.

\*The qualitative agreement can only be rough due to the axial symmetry assumed in the computer model.

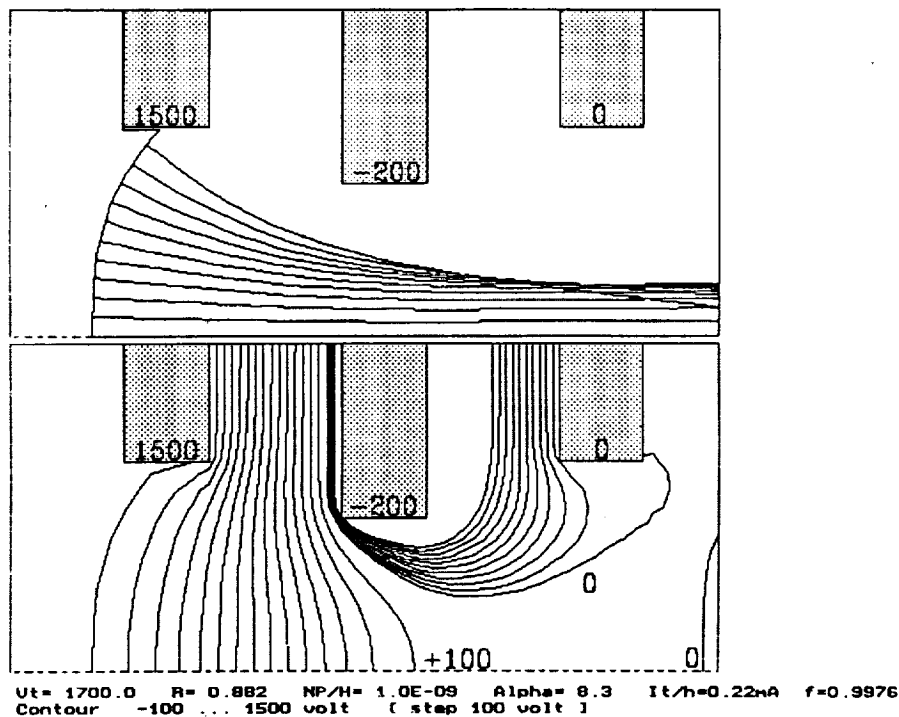


**Fig. 2.1.8 Accelerator system operation with insufficient negative voltage on the accelerator grid resulting in electron back-streaming.**

contour and be accelerated upstream into the positive high voltage discharge chamber. In Fig. 2.1.9 the same conditions as in Fig. 2.1.8 are maintained with the exception that the decelerator grid is now biased at a potential of  $-100$  V. In this case we see that the  $-10$  V contour now crosses the centerline of the grid apertures and electron back-streaming is eliminated. Thus, the application of negative voltage to the decelerator grid enables accelerator system operation with less negative voltage applied to the accelerator grid or, in other words, enables operation at higher net-to-total voltage ratios.

### 2.1.3 More SAND Optics Tests

Based on the positive results of the three-grid tests performed with the accelerator system assembled from 600 series electrodes, a new three-grid system was assembled, this time using J-series electrodes.<sup>14</sup> The J-series screen grid has 1.91-mm-diameter holes with an open area fraction of 0.67 and is 0.38 mm thick. The accelerator grid has 1.14-mm-diameter holes with a center-to-center hole spacing that is 0.3% larger than that of the screen grid, and is also 0.38 mm thick. As with the 600 series electrodes, the stiffening rings were removed from one of the J-series grids, when required, by drilling out the rivets which attach the electrode to the stiffening ring. There are two possible three-grid configurations of interest that can be assembled from the inventory of J-series electrodes (i.e., two screen grids and two accelerator grids). The first arranges the electrodes in a "screen-accel.-accel." configuration (for the screen-accelerator-decelerator of the three-grid system) in which one of the J-series accelerator grids is used as the

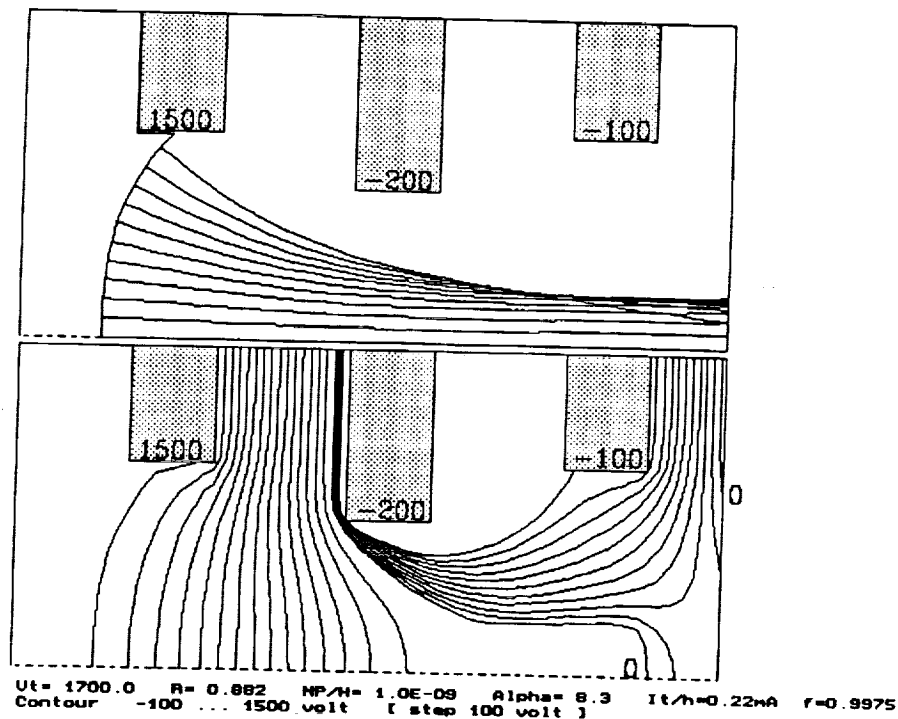


**Fig. 2.1.9** A negative decelerator grid enables the magnitude of the negative voltage applied to the accelerator grid to be reduced while still preventing electron back-streaming.

decelerator grid. The other combination is "screen-screen-accel." In this case one of the J-series screen grids is used as the new accelerator grid and one of the J-series accelerator grids is used as the decelerator grid for the three-grid system.

Computer simulations of these two configurations are given in Fig. 2.1.10. The equal potential contours for both configurations suggest that most charge exchange ions will be collected by the decelerator grid instead of the accelerator grid. Furthermore, despite the use of small holes for the decelerator grid the simulation indicates no direct ion impingement on this grid even at the high perveance level selected. It is believed that this is due in part to operation at high net-to-total voltage ratios and in part to the negative voltage on the decelerator grid. Both of these effects serve to limit deceleration of the ions and minimize expansion of the beamlets at the location of the decelerator grid.

The "screen-screen-accel." three-grid configuration (Fig. 2.1.10a) was assembled and tested. The initial tests with this configuration indicated an accelerator system perveance which is substantially poorer than would be expected based on the computer simulation of Fig. 2.1.10b. The real accelerator system differs from the ideal simulation in two important aspects. The first is that there are slight differences in the dish depths of the two sets of J-series optics used. Thus, when the screen grid from the second set was used as the accelerator grid for the three-grid system the difference in dish depth resulted in a grid-to-grid separation that was substantially larger than the 0.61 mm assumed in the simulation. The second aspect is that the

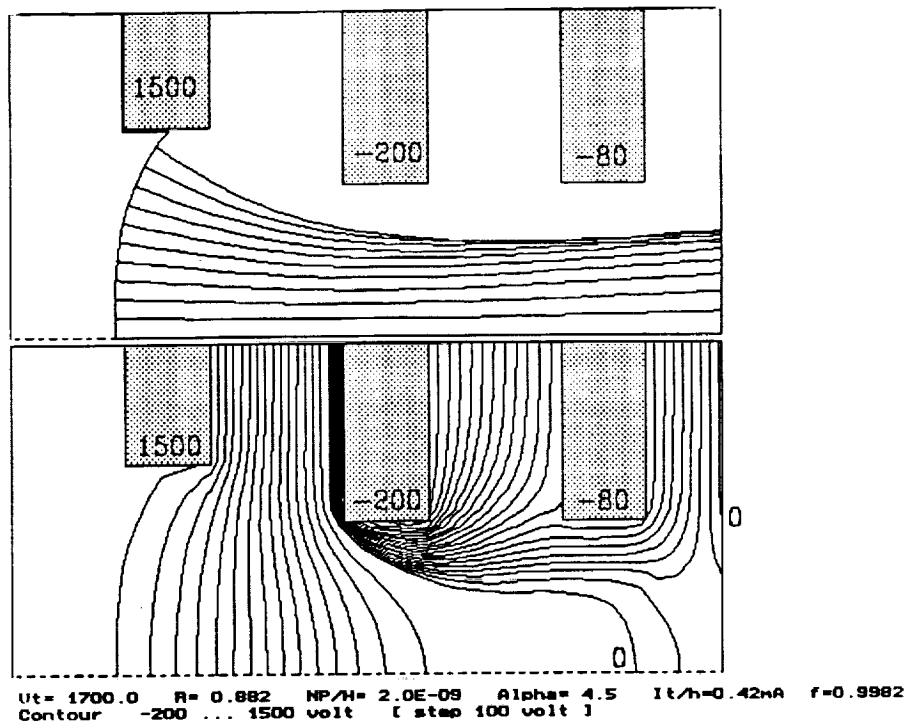


**Fig. 2.1.10a "Screen-accel.-accel." SAND optics configuration.**

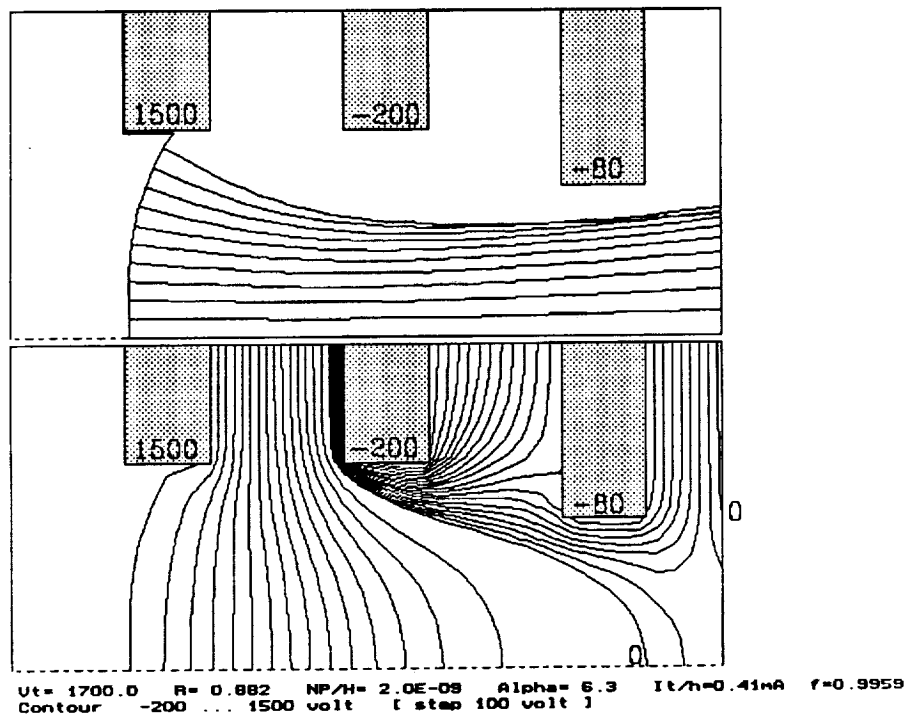


**Fig. 2.1.10b "Screen-screen-accel." SAND optics configuration.**

best grid aperture alignment is not possible. Again the use of the second J-series screen grid as the accelerator grid is the problem. Both J-series screen grids have the same center-to-center hole spacing. When two of these grids are used as a screen/accelerator grid pair, the grid-to-grid separation causes the holes to be incorrectly aligned due to the grid curvature. In fact the hole alignment is such that the individual beamlets are deflected away from the axis of the thruster. Although the center-to-center hole spacing for the accelerator grid is larger than for the screen grid in the J-series optics, the outward bending of the individual beamlets in the "screen-screen-accel." three-grid assembly still results in direct ion impingement on the third grid. Consequently, in order to use this three-grid configuration it was necessary to enlarge the decelerator grid apertures by ion machining. Even after this machining process it was not possible to operate at beam currents above 3.0 A on xenon with a screen voltage of 1500 V due to the large separation between the screen and accelerator grids in this three-grid assembly. Tests were, therefore, performed at beam currents of 1.45 and 2.0 A.

For a beam current of 1.45 A and operation on xenon propellant, the variation of accelerator grid current with tank pressure for a conventional two-grid accelerator system (J-series electrodes) is given in Fig. 2.1.11a. The solid line in this figure is a curve fit to data taken at NASA LeRC in Tank 5 (using only the diffusion pumps) for operation of a 30-cm-diameter ring cusp thruster at the same beam current. Similar data for the "screen-screen-accel." three-grid accelerator system is given in Fig. 2.1.11b for a beam current of 1.45 A. In this case both the accelerator and decelerator grid currents are plotted as functions of the vacuum chamber pressure. The voltages of the three grids are given in the legend for this figure where  $V_b$  is the beam voltage (screen grid voltage),  $V_A$  is the accelerator grid voltage, and  $V_{DG}$  is the decelerator grid voltage. The remarkable aspect of this data is that the accelerator grid current exhibits almost no variation with tank pressure and has a value of approximately 0.35% of the beam current. This is roughly the level of accelerator grid currents obtained with two-grid systems operating on mercury propellant at very low background pressures. It is clear from these data that the negative decelerator grid is collecting almost all of the charge exchange ion current. It is likely that the only charge exchange ions which now reach the accelerator grid are only those formed in the intragrid region.

For operation at a beam current of 2.0 A, similar results were obtained as indicated in Fig. 2.1.12. Again the accelerator grid current is essentially independent of the tank pressure. Finally, the effect of accelerator grid voltage on the accelerator grid current for the "screen-screen-accel." SAND configuration is given in Fig. 2.1.13 for operation at a 2.0 A xenon beam current, with a beam voltage of 1400 V and a decelerator grid voltage of -80 V. These data indicate that as the accelerator grid (i.e., the middle grid) voltage is reduced the distribution of charge exchange ion current between the accelerator and decelerator grid changes with fewer charge exchange ions going to the accelerator grid when it is less negative.



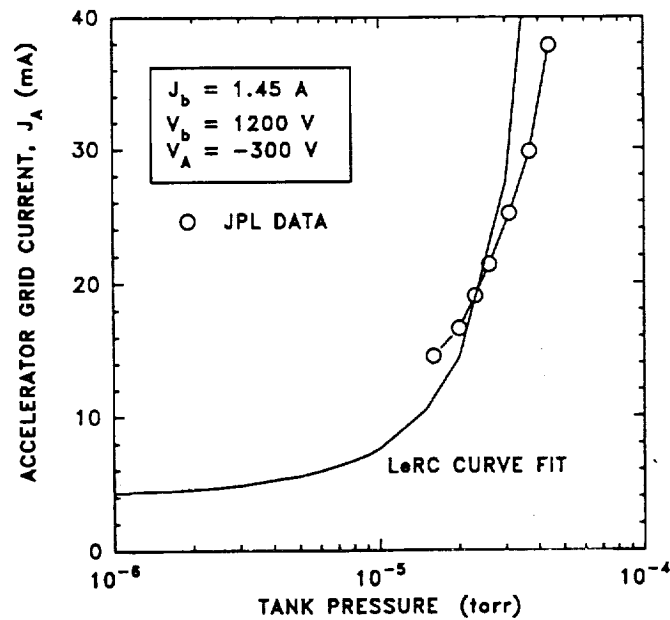


**Fig. 2.1.11a** Accelerator grid current data for two-grid accelerator systems including data from NASA LeRC (ring-cusp thruster) and JPL (divergent-field thruster).

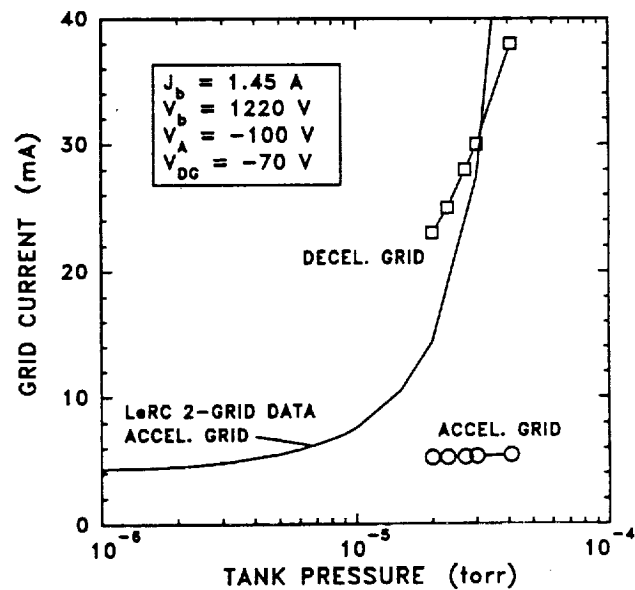


**Fig. 2.1.11b** The "screen-screen-accel." SAND optics configuration results in almost no variation in accelerator grid current with vacuum chamber pressure.

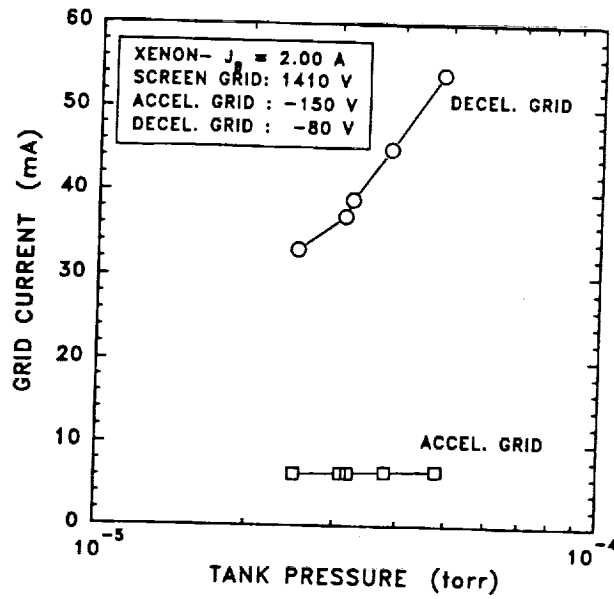


**Fig. 2.1.12 "Screen-screen-accel." SAND configuration data showing essentially no variation in accelerator grid current with tank pressure at a beam current of 2.0 A.**

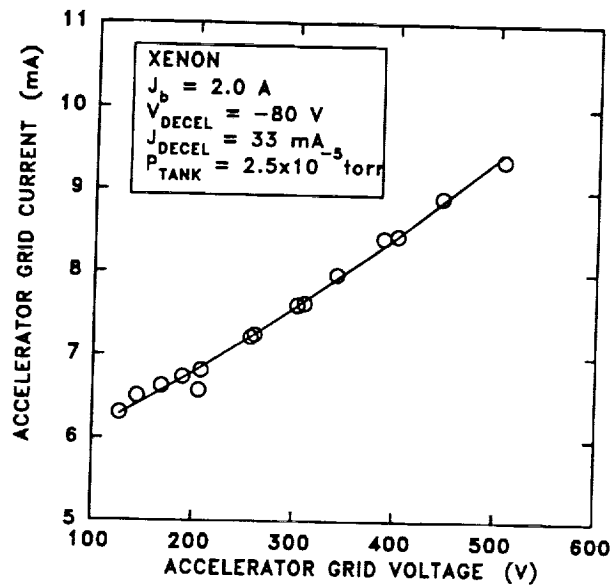


**Fig. 2.1.13 For the "screen-screen-accel." SAND optics, decreasing the accelerator grid voltage changes the distribution of charge exchange ion current to the grids.**

### 2.1.4 SAND Optics Endurance Test

To test the utility of the SAND optics approach, a 1000-hour test of a 30-cm-diameter, three-grid accelerator system was planned. For this test an unused three-grid accelerator system was supplied by NASA LeRC. This accelerator system had been fabricated by the Hughes Research Laboratory (HRL) under contract to LeRC several years ago, and consists of three 0.38-mm-thick molybdenum electrodes with molybdenum stiffening rings mounted on radially flexible supports attached to a titanium mounting ring. The screen and accelerator grid apertures are identical to the J-series, two-grid electrodes. The decelerator grid apertures are 1.52 mm in diameter. From the point of view of the SAND optics technique, this accelerator system configuration is probably not optimum, however, it was clearly superior for a long duration test than either of the three-grid systems assembled with mica washers separating the grids. The ideal SAND optics configuration will have to be determined through a combination of computer modeling and testing, and will most likely have screen, accelerator, and decelerator grids with different thicknesses, hole diameters, and grid-to-grid separations.

The LeRC/HRL three-grid accelerator system (which we will refer to as the endurance tests optics) was installed on a 30-cm divergent-field thruster and the decelerator grid connected to a power supply to provide the desired negative voltage as in the other SAND optics tests. Preliminary tests of this accelerator system were performed at a xenon beam current of 2.0 A. Measurements to determine the maximum net-to-total ratio,  $R$ , were performed at this beam current, a beam voltage of 1200 V and either 0 V or -100 V applied to the decelerator grid. The results of these tests are given in Fig. 2.1.14. These data indicate that the application of a negative voltage to the decelerator grid enables operation at higher net-to-total voltage ratios. The increase in indicated beam current at high  $R$  ratios denotes the onset of electron back-streaming (electrons back-streaming into the discharge chamber "look" like ions leaving and so the measured beam current increases). The ability to operate at higher  $R$  ratios means that the magnitude of the negative voltage applied to the accelerator grid is smaller, and since this voltage determines the energy of the ions striking the grid the erosion rate of the accelerator grid is reduced.

The cost to perform a 1000-hour accelerator system endurance test using xenon is prohibitively expensive without a xenon recovery system, and since such a recovery system does not yet exist at JPL it was decided to perform the test using argon. Operation of the 30-cm divergent-field discharge chamber on argon, however, is well known to require high discharge voltages (typically 40 to 50 V).<sup>15</sup> To have the highest probability that discharge chamber erosion will not adversely affect the grid endurance test, it was decided to operate on a mixture of argon and 3% nitrogen by mass. The 3% nitrogen level was selected for the reasons discussed in Section 2.2 of this publication. In preparation for the 1000-hour test, the engine with the endurance test optics was operated for a total of 150 hours at the operating conditions given in Table 2.1.1. Note that the accelerator grid current is approximately 0.34% of the beam current and that the decelerator grid is collecting most of the charge exchange current. The grid voltages were selected for the following reasons. The screen grid voltage was selected to be similar to that used in the 890-hour test in Ref. 9. The decelerator grid voltage was a compromise between

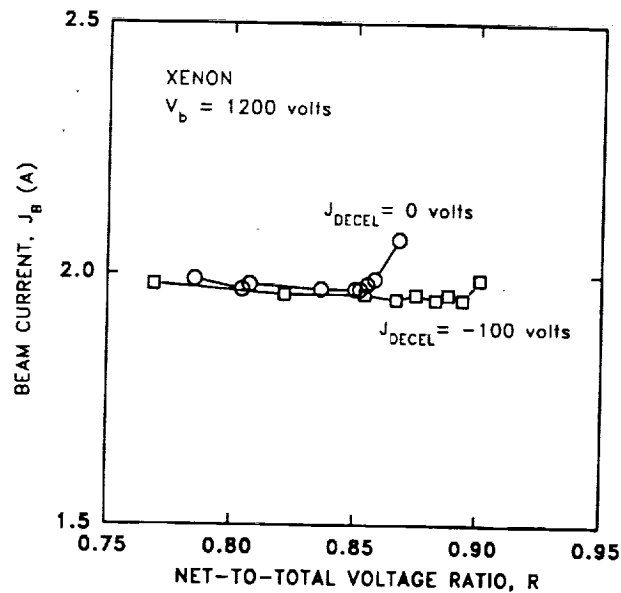


**Fig. 2.1.14** A negative voltage applied to the decelerator grid enables operation at higher net-to-total voltage ratios before the onset of electron back-streaming.

decelerator grid erosion (which is reduced with less negative voltage levels) and operation at high net-to-total voltage ratios (which is possible with larger negative decelerator grid voltages). The accelerator grid voltage was selected experimentally to be approximately 20% greater than the electron back-streaming limit. The beam current was selected to have a conservative margin less than the maximum current capability of the screen grid supply to avoid any problems which might arise from long term operation near the maximum capability of the commercial power supply.

At the end of the 150-hour test, the engine was disassembled and inspected. Significant numbers of material flakes were found in the discharge chamber. Analyses of these flakes revealed them to be molybdenum. In the current discharge chamber configuration, the only source of molybdenum is the accelerator system. Apparently, even with 3% nitrogen, long term operation at a discharge voltage of 45 V still results in significant screen grid erosion. The flakes of material seem to have spalled-off from the downstream face of the anode pole piece, since several other similar looking "flakes" of material were still attached at this location.

**Table 2.1.1 Nominal 150-hour Endurance Test Operating Parameters**

Item	Value
Beam current	3.55 A
Beam voltage	1400 V
Discharge current	14.5 A
Discharge voltage	46.0 V
Accelerator grid current	12.0 mA
Accelerator grid voltage	-200 V
Decelerator grid current	25 mA
Decelerator grid voltage	-80 V

For the grid currents and voltages given in Table 2.1.1 and using sputter yield data from Ref. 13 for argon on molybdenum, it is possible to estimate the expected mass losses for the accelerator and decelerator grids. Assuming a sputter yield of 0.08 atoms/ion at 80 eV, the mass loss for the decelerator grid after 150 hours is calculated to be about 0.4 grams. For the accelerator grid, assuming a sputter yield of 0.4 atoms/ion at 200 eV results in a calculated mass loss of about 1 gram. For 1000 hours of operation, the decelerator grid is expected to lose approximately 3 grams and the accelerator grid 8 grams.

The accelerator system was disassembled and the individual grids weighed to compare with their pretest weights. These data indicate that the screen grid lost 0.4 grams, the accelerator grid *gained* approximately 0.8 grams, and the decelerator grid lost approximately 1 gram. The reasons for the discrepancies between measured and calculated weight losses are not known, but neither the effect of back-sputtered material onto the accelerator system electrodes nor the effect of nitrogen in the vacuum chamber have been taken into account in the calculated grid mass losses. Witness slides were installed prior to the 150-hour test in order to provide information on the deposit rate of back-sputtered material, but these slides have not yet been analyzed. In addition, the neutralizer cathode failed approximately half-way through the test and the second half of the test was performed with neutralizer common grounded to the vacuum chamber. Finally, there is considerable uncertainty in the sputter yields of molybdenum at low incident ion energies. There is little doubt, however, that longer duration tests of the accelerator system are required to better determine the grid erosion rates.

## 2.2 Cathode Endurance Testing

Recent long duration testing of hollow cathodes at JPL has included operation of a 6.35-mm-diameter cathode on xenon for 5000 hours at 25 A<sup>16</sup> (see Appendix A), and a 12.7-mm-diameter cathode on argon for 1000 hours at 100 A<sup>17</sup>. Argon is of interest because of potential

applications of argon ion engines to the Space Exploration Initiative<sup>18-20</sup>. However, erosion rates in the ion engine discharge chamber are expected to be greater with argon propellant (compared to krypton or xenon) because higher discharge currents are required, and in some cases the argon sputter-yield may be greater.

Testing performed in 1990 showed conclusively that when small quantities of nitrogen are added to the xenon propellant, erosion rates of components in the discharge chamber can be reduced by a factor of 10 or more<sup>21</sup>. It is expected that similar reductions in erosion rates will be obtained with nitrogen added to argon, although the magnitude of the reduction is unknown. Two erosion reduction mechanisms have been identified: removal of a chemisorbed nitrogen surface layer, and formation of sputter-resistant surface nitrides. In both cases, the nitrogen in the discharge chamber must be continuously replenished.

From a systems point of view, the simplest method of introducing nitrogen into the discharge chamber is to pre-mix the nitrogen with the propellant in the propellant tanks. In this way, separate storage and flow control systems for the nitrogen are not required. Of particular concern, however, are the unknown effects of nitrogen on the chemical reactions which take place in the hollow cathode.

To test the long-term effects of nitrogen on the physical chemistry in the insert, a cathode endurance test program was initiated to study the cathode operation on a mixture of argon and nitrogen (3% by mass). This ratio of nitrogen to argon provides approximately the same number density of nitrogen atoms as was used in erosion reduction testing with xenon and nitrogen<sup>21-24</sup>.

### **2.2.1 Facility Modifications**

The life test was performed in the same vacuum facility and discharge apparatus that was used for the 5000-hour xenon life test<sup>16</sup>. Minor modifications to the facility and test apparatus included conversion of the water cooling system for the diffusion pumps to a closed-loop system, substitution of a tantalum keeper electrode in place of a molybdenum one, and removal of the solenoid valve flow controller. The new keeper was designed to provide the maximum amount of viewing area of the cathode orifice and orifice plate during the test. Tantalum was selected because it is the material which has in the past shown the greatest reduction in erosion rates when nitrogen is added to the propellant, and should, therefore, minimize the erosion of this component.

The flow controller was removed because experience has shown that, over long duration testing, the flow controller drifts out of calibration by 5% or more due to the zero shift with time. The flow controller was replaced by a micrometer valve and a precision pressure regulator. The pressure regulator maintains a fixed pressure at the micrometer valve; once the flow rate has been adjusted to the desired level by adjusting the micrometer valve, the flow rate should remain unchanged as long as the gas temperature is unchanged.

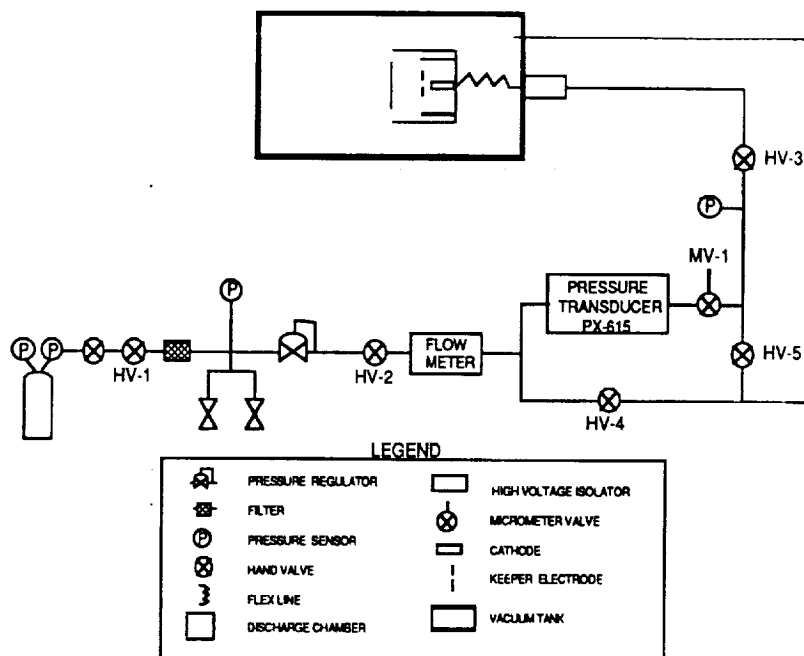


**Fig. 2.2.1 Propellant distribution schematic for the hollow cathode endurance test.**

A schematic diagram of the propellant system is shown in Fig. 2.2.1. Most, but not all, of the new propellant lines that were installed were cleaned in acetone and rinsed in alcohol. The parts not cleaned in acetone and alcohol include the tip heater, the flexible line connecting the gas bottle to the pressure regulator, and the propellant assembly containing the pressure regulator (the area between hand valves HV-1 to HV-2). It was not possible to clean this welded assembly.

The propellant system was leak-checked in a manner similar to that described in Ref. 16. First, the propellant lines were pressurized to approximately 26.5 PSIA, and the pressure indicated by pressure transducer PX615 was noted (see Fig. 2.2.1). Next, hand valves HV-2, HV-3, HV-4, and HV-5 were closed. By measuring the decrease in propellant line pressure and estimating the propellant line volume, a total leak rate out of the propellant system can be calculated. The data from approximately 50 hours of this testing indicated that the leak rate was at most  $4 \times 10^{-4}$  sccm. At this point the flow meter was zeroed (at the working pressure). Subsequently, the flow meter was calibrated on the argon/nitrogen blend.

## 2.2.2 Cathode Description and Assembly

The cathodes in these tests are identical to the cathode used in the successful 5000-hour cathode life test, with the exception of the tip heater length. The cathode insert, a hollow porous tungsten cylinder impregnated with a low work function oxide (a 4:1:1 mix of barium, calcium,

and aluminum oxides) was identical to that used in the 5000-hour xenon test, and is described in detail in Ref. 16.

A schematic diagram of the hollow cathode design is shown in Fig. 2.2.2. A molybdenum tube 6.4 mm in diameter, approximately 57 mm long, and with a wall thickness of approximately 0.38 mm, houses the hollow cathode insert. This tube is electron-beam welded to a molybdenum flange at the downstream end, and to a 2% thoriated tungsten orifice plate at the upstream end. The orifice plate is approximately 1.5 mm in thickness, with an orifice diameter of approximately 1.8 mm. A 56-deg half-angle chamfer is machined into the downstream face of the orifice plate. The tip heater is similar in construction to that described in the 5000-hour xenon test, except that it is 12.5 mm longer. Grafoil<sup>25</sup> was sandwiched between the molybdenum flange and a stainless-steel flange to make a the gas-tight seal between the cathode and the rest of the flow system. A swagelok fitting welded to the stainless flange connected the cathode to the propellant distribution system. A photograph of the unassembled cathode, minus the insert, is shown in Fig. 2.2.3.

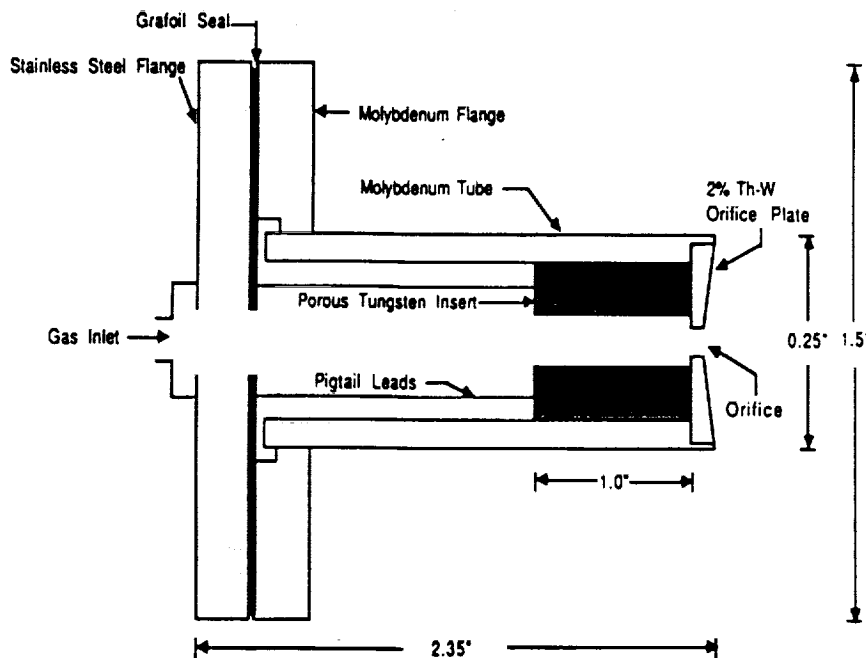


Fig. 2.2.2 Schematic design of the endurance test cathode (not to scale).



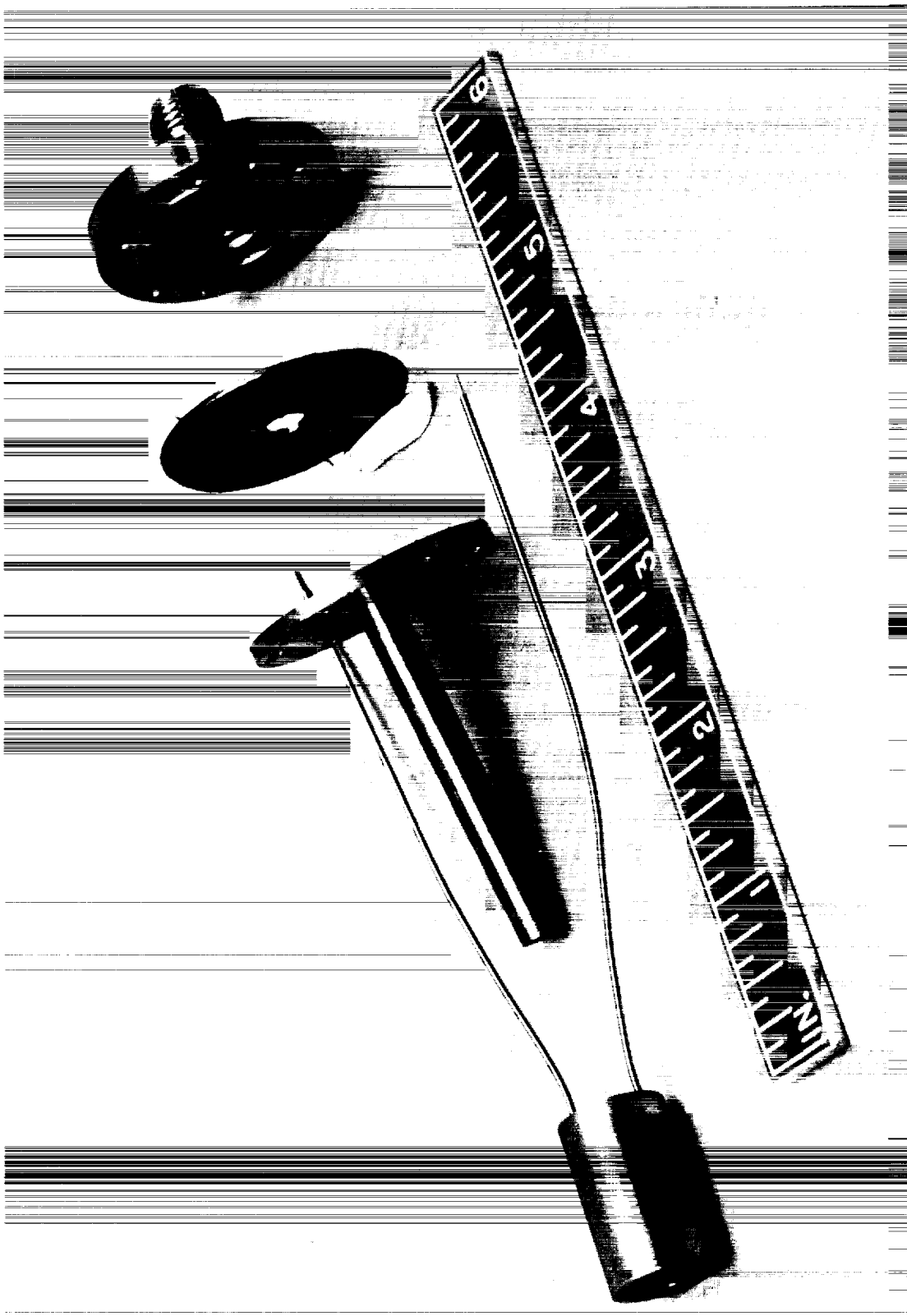
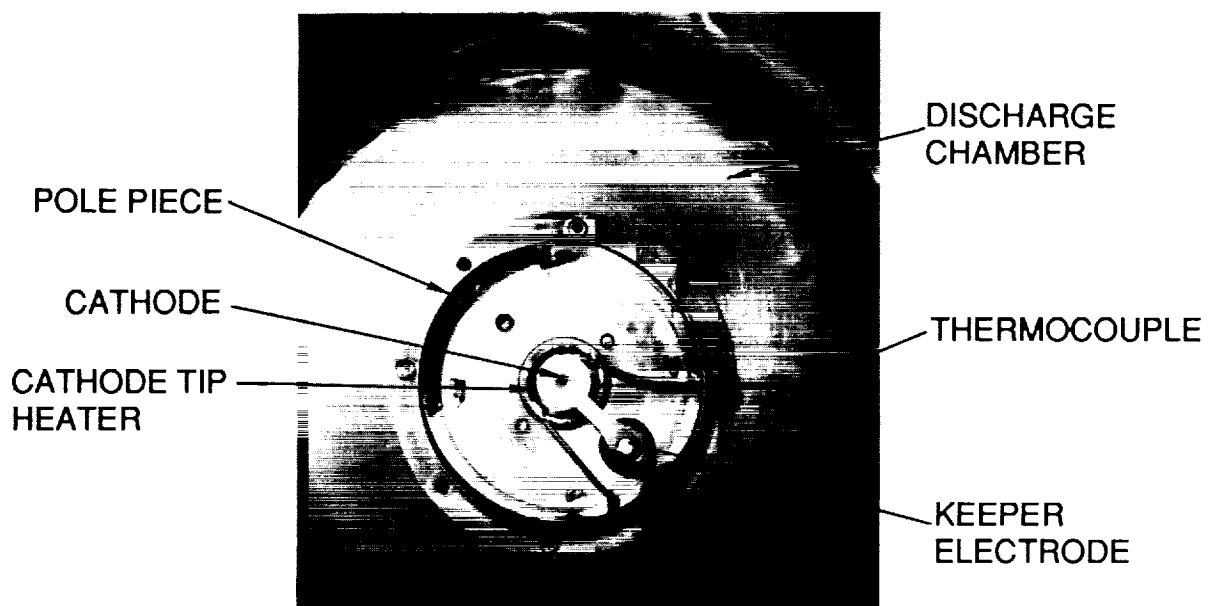


Figure 2.2.3. Photograph of the life-test cathode components.

The cathode tube, molybdenum flange, stainless-steel flange, flexible propellant line, keeper electrode, keeper isolator shadow shields, and molybdenum and tantalum anode face plates were ultrasonically cleaned in acetone and then ethyl alcohol for 15 minutes each. Components were then blown dry with helium and weighed. During the assembly of the cathode, the insert was never touched directly; rather, it was placed into the cathode barrel by pushing on the pigtail leads welded to the upstream end of the insert, and the section of pigtail leads touched by cotton gloves were later clipped off. The insert was exposed to atmosphere for a total of 2.75 hours; this represents the amount of time required to weigh the insert, assemble the cathode, and install the cathode into the vacuum tank. After installation, a flow of the argon/nitrogen gas mixture was established through the cathode at a rate of 15 sccm. A tantalum keeper electrode was placed downstream of the cathode, as shown in Fig. 2.2.4.



**Fig. 2.2.4** Photograph of an end view of the cathode, keeper electrode, polepiece, and discharge chamber.

The procedure used in Ref. 16 was followed to condition and start up the cathode, with two exceptions:

1. The 3-hour heating cycle at 500°C was initiated by ramping up to this temperature over a time period of about 5 hours. It is theorized that ramping up to 500°C slowly may allow time for hydrides in the insert to bake out. In the 5000-hour xenon test, this temperature was achieved within approximately 15–30 minutes.
2. Cathode start-up was initiated by application of 585 volts to the keeper; there was no power supply available to start the cathode-keeper discharge at low voltage.

### 2.2.3 Cathode No. 1 Operation

Much difficulty was encountered in trying to operate the cathode with the keeper geometry shown in Fig. 2.2.4. The cathode was easy to start, but was difficult to operate. The discharge was so noisy that it continuously tripped out the anode power supply. With a total of 5.4 hours of run time on the cathode, it was decided to change the keeper to a more standard configuration. The vacuum tank was opened, while an argon/nitrogen flow of approximately 18 sccm was established through the cathode. A photograph of the anode face plate is shown in Fig. 2.2.5. It is clear from this photograph that the cathode plume was asymmetrically impinging at the 10:00 o'clock position. It is likely that the plume was affected by the cathode keeper electrode, but it is not clear at this time why the keeper should affect the plume in this manner.

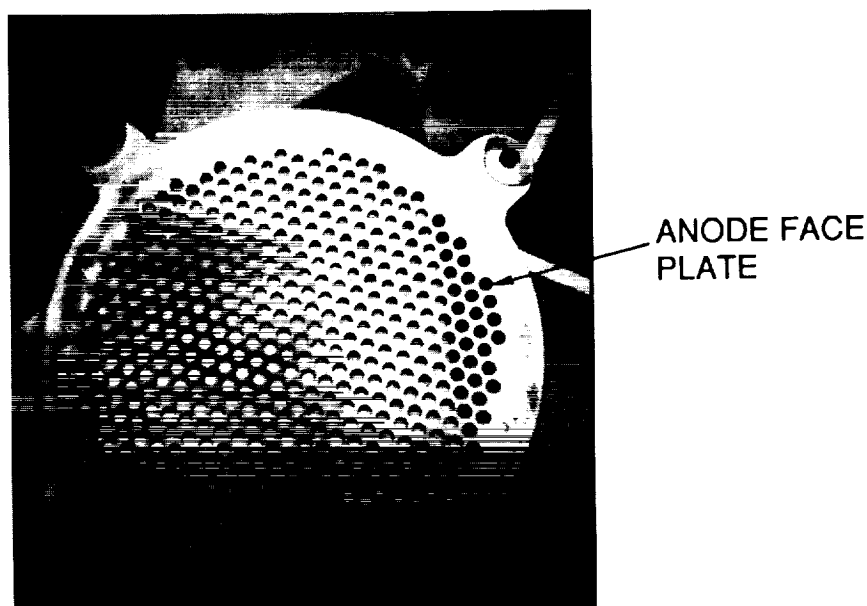


**Fig. 2.2.5** Photograph of the molybdenum anode face plate. (Note the discoloration on the upper left side of the face plate.)

A new keeper was fabricated from tantalum and placed as shown in Fig. 2.2.6. The tank was closed and pumped down to a base pressure of  $5.3 \times 10^{-7}$  torr. The cathode started easily on this new keeper, but the keeper and cathode discharge continued to be noisy and erratic. There were seemingly no combinations of cathode current or flow rate that resulted in stable operation for very long.

Finally, a standard J-series keeper electrode, thinned slightly for better viewing of the cathode orifice plate, was installed. The cathode operated better than with previous keeper geometries. It is not understood why the keeper should have such an effect on the discharge chamber operation. By the time the cathode had accumulated 220 hours of operation (at currents

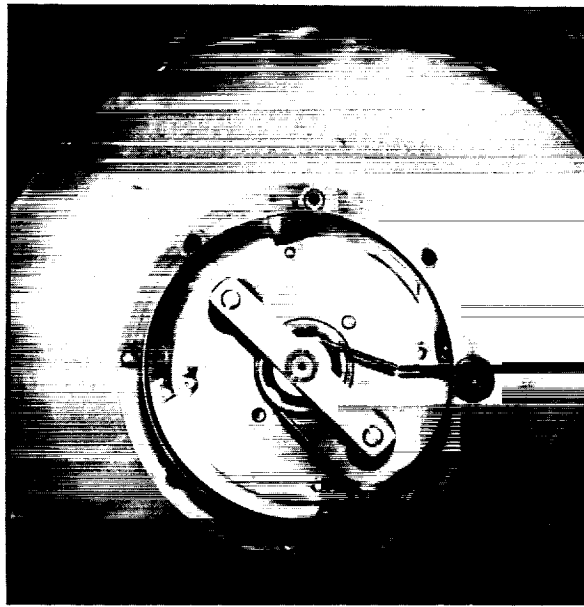


**Fig. 2.2.6 Photograph of new keeper electrode geometry.**

between 10–20 A) it had experienced several exposures to atmosphere and shutdowns of the vacuum system. Due to the exposures to atmosphere, it was decided to continue the test only up to 500 hours of operation in order to obtain additional operating experience while a replacement cathode was being fabricated.

The cathode was operated for an additional 463 hours at discharge currents ranging from 9–25 A; the discharge current was set to limit the orifice plate temperature to 1200°C or less. At run hour 275, the cathode operated at emission currents as high as 21 A with an orifice plate temperature of 1195°C. However, as more operating hours were put on the cathode, the orifice plate temperature increased, for a fixed emission current. At approximately run hour 550, the orifice plate temperature began to increase at a significant rate. By the end of the testing (run hour 683), the cathode could not be operated in a stable mode, and the orifice plate temperature, for an emission current of 18.7 A, had increased to 1340°C. Due to this excessive operating temperature, testing was terminated.

In Fig. 2.2.7 a scanning electron micrograph ( SEM ) of the cathode orifice plate after 683 hours of operation on the argon/nitrogen mix is shown. Substantial deposits of tungsten (darker grey) and tantalum or tungsten (whitish deposit) can be seen surrounding the orifice. Extreme magnification of the tungsten and tantalum/tungsten deposits are shown in Figs. 2.2.8–9. The tantalum deposit was due probably to erosion of the keeper electrode. The tungsten deposits which have an ordered crystalline structure were due undoubtedly to the high operating temperature of the cathode.

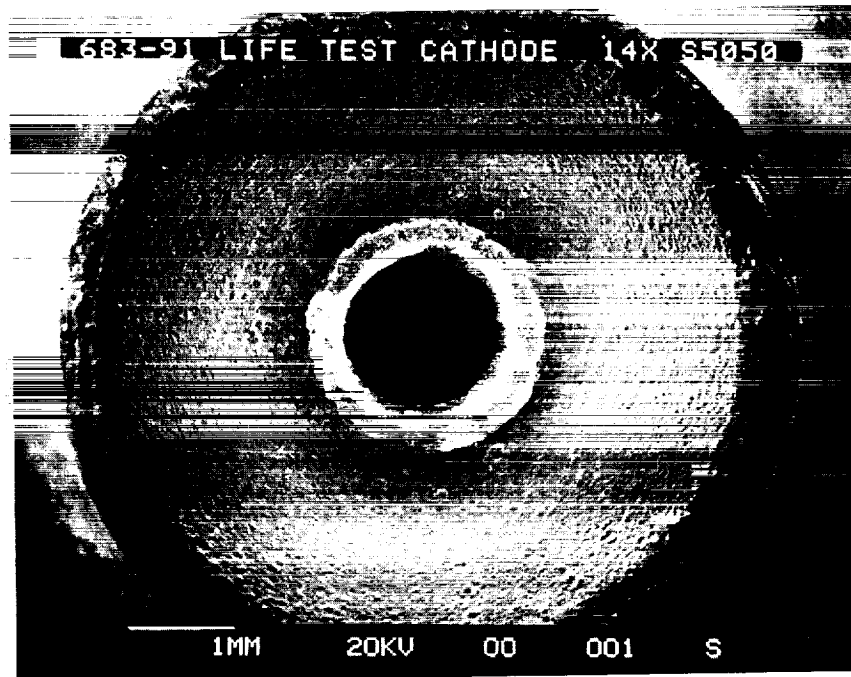


Fig. 2.2.7 Scanning electron micrograph (SEM) photograph of the cathode orifice plate.

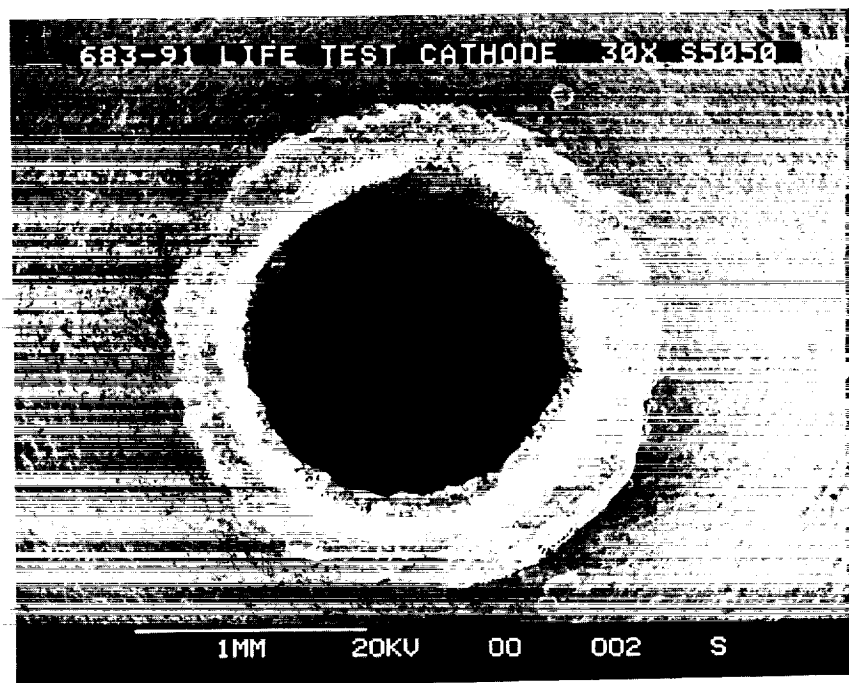
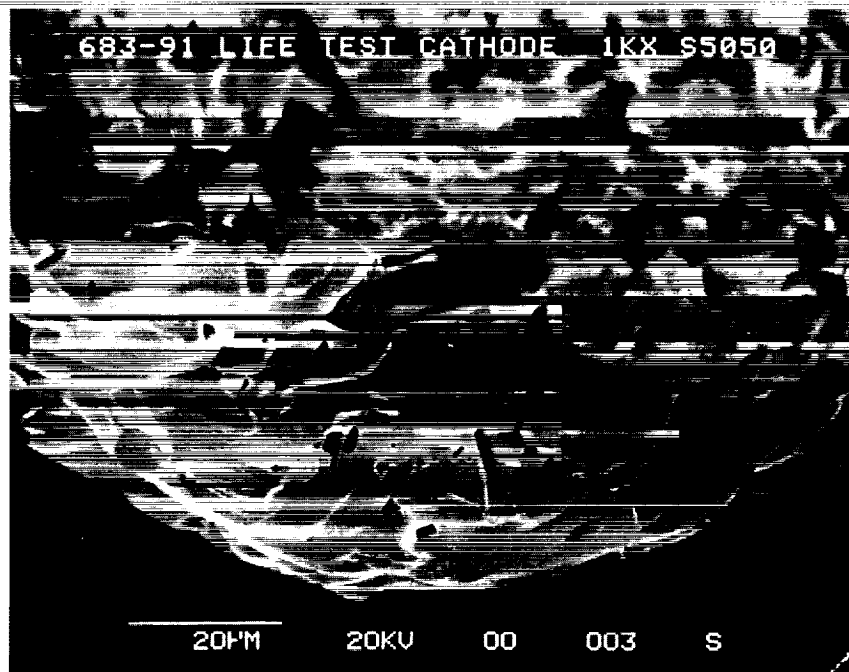
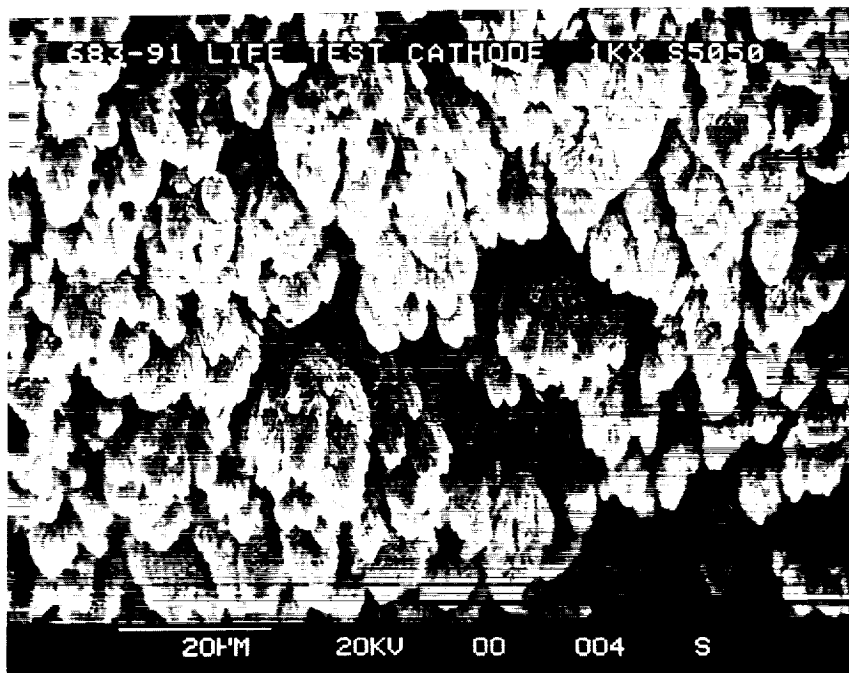


Fig. 2.2.8 SEM photograph of deposits surrounding the cathode orifice.



**Fig. 2.2.9a** SEM photograph of tungsten deposits surrounding the cathode orifice.



**Fig. 2.2.9b** SEM photograph of tungsten and tantalum deposits surrounding the cathode orifice.

The reasons for the excessive cathode operating temperatures observed in this test are not known. However, to remove nitrogen as a factor of concern, it was decided to perform a new test on another cathode using a pure argon propellant. If cathode testing on pure argon is successful, endurance testing of cathodes on a mixture of argon and nitrogen will be resumed.

#### 2.2.4 Cathode No. 2 Assembly

A major experimental concern is the integrity of the propellant system; cathode tests must be conducted with no atmospheric gas leaks into the propellant system. The propellant system is pressurized above atmospheric pressure from the gas supply bottle to the micrometer valve. Under normal operation, a large pressure drop is encountered across the micrometer valve resulting in pressures of a few torr at the downstream end.

The leak rate of atmospheric gases into that portion of the propellant feed system which is below atmospheric pressure (from the micrometer valve to the cathode propellant line vacuum flange) was measured in the following manner. A cap was connected to the propellant line inside the vacuum tank that attaches to the flex line, and the tank was then closed and pumped down to a pressure of less than  $10^{-6}$  torr with the valves open to pump out the propellant lines. Next, all valves except for HV-3 and the micrometer valve were closed; in this way a leak rate of air into the propellant system (between hand valve HV-2 to the flex line in the vacuum tank) could be measured by recording the increase in pressure with time as measured by the capacitance manometer. A plot of the pressure increase over time is shown in Fig. 2.2.10. By estimating the propellant line volume, a total leak rate can be calculated. The data from approximately 45.25 hours and 1050 hours of this testing indicated that the leak rate was between  $6.5 \times 10^{-6}$  sccm and  $4.5 \times 10^{-5}$  sccm, respectively. These values approach the minimum purity levels of the argon itself, and it can be therefore assumed that there is no leakage of air into the propellant lines, or that the leak rate is acceptably low.

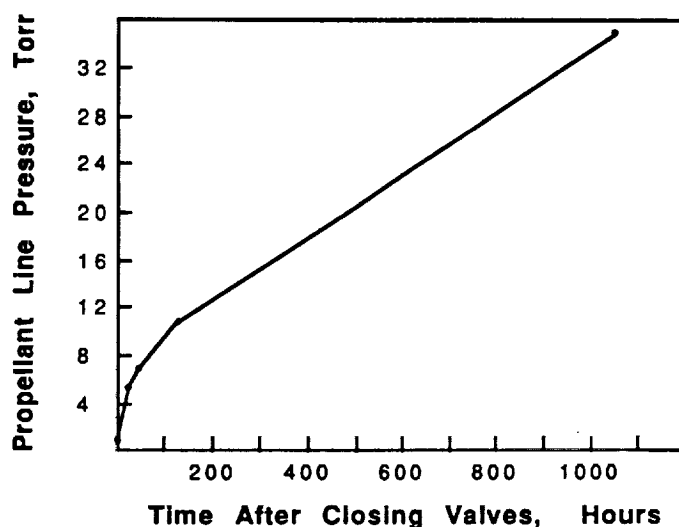


Fig. 2.2.10 Plot of increase in propellant line pressure with time during extended leak check.

Another cathode was assembled using the assembly procedures discussed previously. Residue-free rubber gloves, used for flight hardware assembly at JPL, were worn when handling the cathode. The insert was exposed to air for 1.58 hours; an additional 35 minutes was required to complete the cathode/facility assembly and to pump down the vacuum tank to high vacuum. This cathode will be tested in FY 1992.

## 2.3 Discharge Chamber Erosion Studies

Tests conducted at JPL since 1987 have shown that adding nitrogen to the xenon propellant reduces the erosion rates of components in the discharge chamber of an ion engine<sup>21-24</sup>. It has long been assumed that the observed reductions in component erosion rates were due to formation of sputter-resistant surface nitrides; in this theory, the base metal forms a nitride at the surface whose erosion rate is lower than the base metal. However, in 1979 LeRC suggested that desorption of chemisorbed surface nitrogen was the dominant mechanism for reduced erosion rates observed in the screen grid of mercury ion engines. This mechanism involves the adsorption of a surface layer of nitrogen and desorption of this nitrogen surface layer by ion bombardment. The surface layer generally consists of a single layer of nitrogen atoms or molecules that are held to the metal surface by covalent bonds.

Appendix B contains a paper, "Metal and Metal Nitride Erosion Rates in a Divergent Field Ion Engine," presented at the 22<sup>nd</sup> IEPC, held at Viareggio, Italy, October 17-21, 1991, which summarizes the results of a continuing investigation of the effects of the addition of small quantities of nitrogen on ion engine discharge chamber erosion. The erosion rates of various metals and metal nitrides are presented as a function of the percentage of nitrogen added to the argon propellant. The two mechanisms, chemisorption and surface nitriding, are discussed in attempts to account for the reduced erosion rates observed in these and other tests. The tests conducted showed that tantalum and titanium nitride erosion rates are greater than the base metal, but that the erosion rates of the base metals, and possibly the metal nitrides, could have been affected by vacuum facility gases. Analyses indicate that reduced screen grid erosion rates may be attributable to chemisorption of surface nitrogen; however, it is difficult to attribute reduced erosion rates observed at the cathode side of the baffle to chemisorption, due to the estimated ion energies and current densities, and the desorption rates of chemisorbed nitrogen.

## 2.4 Carbon/Carbon Grid Development

Numerous mission analyses have shown that the use of high-power ion propulsion significantly benefits planetary exploration and lunar/Mars piloted and cargo missions<sup>26-28</sup>. Most of the missions described in Refs. 26-28 require a large number of ion engines; the number of engines required in an Ion Propulsion System (IPS) is determined by the power which can be processed by each engine, and by the useful engine lifetime. To reduce the number of engines in the IPS requires development of engines that operate at higher power levels and for longer periods of time.



The performance of an ion thruster is due chiefly to the design of the ion extraction grids. Fundamentally, the maximum beam current that the grids can extract for a fixed specific impulse is limited by space-charge effects, electron back-streaming, and electrical breakdown (arcing) between the grids. These effects themselves are related to the hole alignment between the screen, accelerator, and decelerator grids, and to the grid-to-grid separation distances. Simply put, the better the holes in the grids line up, and the closer the grids can be spaced to each other, the more current the optics can extract out of the ion engine discharge chamber.

The problems inherent in increasing the thrust density of ion engines are grid erosion and thermal grid distortion, which changes the grid separation distances. Grid erosion, due to ion sputtering of the grid surfaces-to-grid, becomes more severe as the thrust density increases because there are more ions to erode the grids. Thermal distortion is due to non-uniform heating, and the resulting thermal expansion, of the grid electrodes because of radial and grid-to-grid temperature gradients.

Currently, state-of-the-art grids are fabricated from molybdenum sheets. To mitigate the grid distortion problems, the grids are dished by hydroforming; a typical J-series ion engine grid is dished approximately 0.8 in. over the 12-in. diameter<sup>29</sup>. With this technology molybdenum grids have been fabricated up to 50 cm in diameter<sup>30,31</sup>.

However, there are limits to dished molybdenum grid technology. For example, it is difficult to dish the grids uniformly across the entire diameter of the grid, which leads to a non-uniform grid gap. In addition, the dishing process may cause grid-to-grid hole misalignment. Because of the finite coefficient of thermal expansion for molybdenum, thermal distortion can still occur. Finally, recent test data indicate that the first life-limiting mechanism in an ion engine is sputter erosion of the accelerator grid by charge-exchange ions whose energies depend upon the voltage applied to the accelerator grid and are typically in the range of 300–1000 eV.

Carbon/carbon may be superior to molybdenum for use as a grid material. The materials properties of carbon/carbon, shown in Figs. 2.4.1 and Fig. 2.4.2 can be adjusted to provide a near-zero coefficient of thermal expansion over a temperature range of approximately 500°C. This means that the grids will not distort thermally as the dished molybdenum grids, and can therefore be used as flat sheets. Hole alignment between the screen, accelerator, and decelerator grids may therefore be superior due to the elimination of the need to compensate the hole alignment for dished grids. In addition, the sputter yield of carbon is almost an order of magnitude lower than molybdenum<sup>13</sup>. These materials properties of carbon/carbon may permit the fabrication of ion engine grids which can process more power and have longer operating life times than current state-of-the-art grids fabricated from molybdenum. An experimental program was initiated to find a vendor to fabricate the grid blanks and machine the holes. Three processes for grid hole fabrication were identified: electric discharge machining, laser machining, and computer-numerically controlled machining. Boeing Aerospace Defense and Space was selected to laser-machine the holes in the carbon/carbon grid blanks based on their demonstrated capability to machine carbon/carbon grids with an open area fraction of approximately 60%. A company recommended by Boeing, B.F. Goodrich/Supertemp, was subsequently selected as the

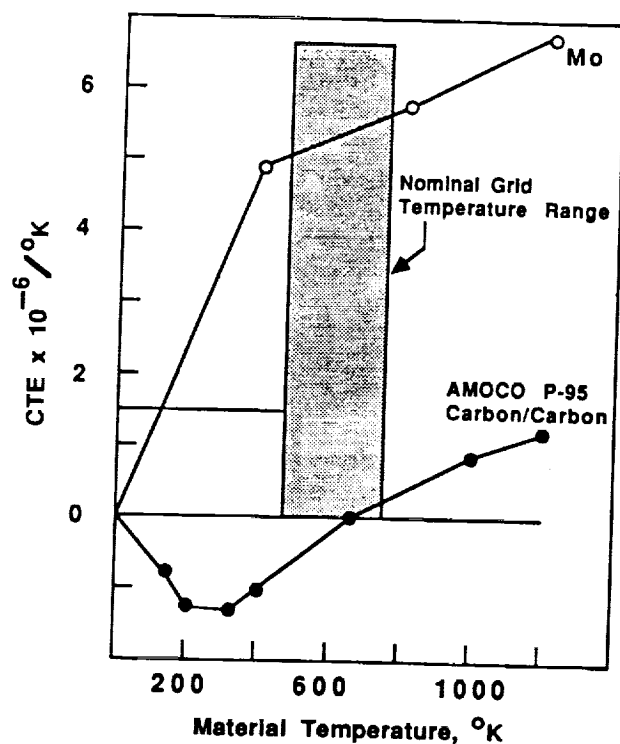


Fig. 2.4.1 Plot of coefficient of linear expansion as a function of temperature for carbon/carbon and molybdenum.

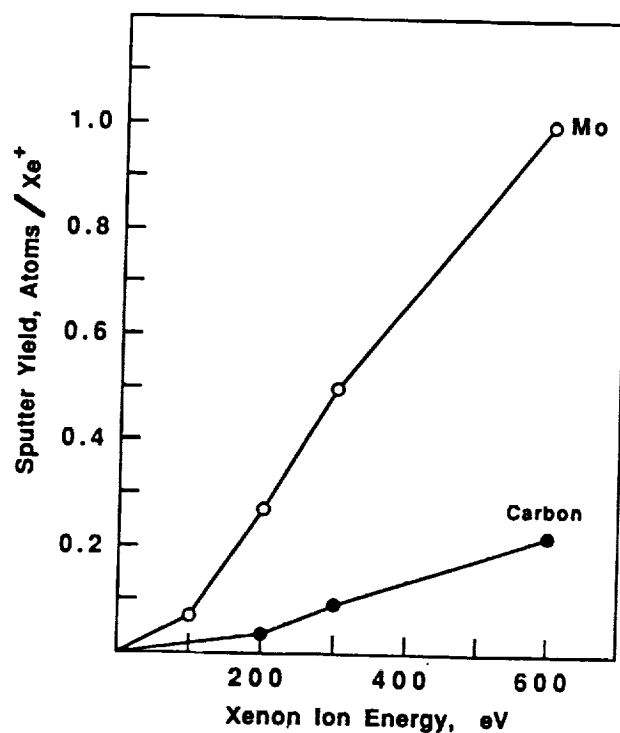


Fig. 2.4.2 Plot of sputter yield as a function of xenon ion energy for carbon/carbon and molybdenum.

vendor to fabricate the grid blanks. A contract was initiated with Boeing to laser machine the holes into a complete screen/accelerator/decelerator 15-cm-diameter grid set.

Development of carbon/carbon grid technology will continue in FY 1992. Different fiber types and hole fabrication techniques will be investigated. The materials properties of the carbon/carbon sheets, including the coefficient of thermal expansion, surface smoothness, and ion etch rate, will also be investigated. Finally, techniques to measure grid distortion during ion engine operating will be assessed.

## **2.5 Divergent-Field Thruster Performance**

The 30-cm-diameter, xenon, ring-cusp engine endurance tested in Ref. 9 exhibits excellent performance as a result of only a relatively brief optimization period. It was of interest to compare the performance of the 30-cm-diameter divergent-field thruster (formerly of the J-series design), which was the product of an extensive optimization effort with mercury propellant, to that of the ring-cusp engine. The measured performance values for the two thrusters are given in Table 2.5.1 for operation at the conditions of the 890-hour endurance test of Ref. 9. Surprisingly, the performance values of the two engines are comparable. The other major concern for the divergent-field thruster is that of baffle erosion. It appears likely, however, that the addition of 1 or 2% of nitrogen to the xenon propellant would enable a sufficiently low baffle erosion rate for operation at 5 kW (as opposed to the 10-kW operating point used in Ref. 10).<sup>21,22,24</sup>

## **2.6 Multi-Orifice Hollow Cathode**

The operation of orificed hollow cathodes at discharge currents greater than approximately 20 A results in the production of energetic ions (with energies of tens of electron-volts) that can cause severe sputtering damage of engine components near the cathode.<sup>16,17,32</sup> Hollow cathode currents in excess of 20 A, however, are required for the operation of high power ( $\geq 5$ -kW ion engines). In an attempt to minimize the effects of the cathode jet at high emission currents, a multi-orifice cathode shown schematically in Fig. 2.6.1 was designed and fabricated. This cathode has three symmetrically located orifices placed on the cylindrical section of the tungsten orifice plate. The intent of this design is to reduce the magnitude of the current through each orifice by a factor of three relative to a conventional, single-orifice cathode operating at the same total current level.

Only very preliminary tests of the multi-orifice cathode have been performed to date. The tests were performed in a 30-cm divergent-field thruster (formerly a J-series thruster) with the baffle and baffle support structure removed. Two axial positions of the downstream end of the cathode were tested, one corresponding to approximately the nominal cathode position for the J-series engine, and the other approximately 20 mm downstream of this position. A flat disk of

**Table 2.5.1 Ion Engine Performance Comparison**

	Ring-Cusp (Ref. 9)	Divergent Field
Discharge Voltage (V)	26.9	28.5
Screen Grid Voltage (V)	1517	1503
Accelerator Grid Voltage (V)	-331	-340
Total Accelerating Voltage (V)	1860	1843
Neut. Common-to-Ground Voltage (V)	-15.4	-11.7
Discharge (anode) current (A)	22.0	23.3
Beam Current (A)	3.19	3.21
Neutralizer Keeper Current (A)	2.8	4.4
Accelerator Grid Current (mA)	17.4	53.0
Corrected Facility Pressure (Pa)	$1.7 \times 10^{-3}$	$4.7 \times 10^{-3}$
Main Flow Rate (equivalent A)	3.09	2.89
Cathode Flow Rate (equivalent A)	0.29	0.28
Neutralizer Flow Rate (equivalent A)	0.32	0.23
Ingested Flow Rate (equivalent A)	0.05	0.20
Beam Voltage (V)	1529	1491
Net-to-Total Voltage Ratio	0.82	0.81
Discharge Losses (W/A)	158	180
Total Propellant Efficiency Corrected for Ingestion Only	0.85	0.89
Discharge Chamber Propellant Efficiency Corrected for Ingestion Only	0.93	0.95
Assumed Total Thrust Correction Factor	0.96	0.95
Thruster Input Power (W)	5510	5550
Thruster Beam Power (W)	4880	4770
Calculated Thrust (N)	0.20	0.19
Thrust-to-Power Ratio (mN/kW)	36.0	34.8
Specific Impulse (s)	3840	4000

molybdenum was positioned just upstream of the cathode orifices and served as the keeper/starter electrode. The upstream end of the cathode tube was attached to the propellant feed system through the use of a 6.35-mm-diameter Swagelok fitting, as shown in Figures 2.6.2a and 2.6.2b.

Engine operation with the cathode positioned 20 mm downstream of the nominal J-series cathode position resulted in very poor engine operation. It appeared that a very peaked radial plasma density profile was produced which limited the ion current extraction capability of the accelerator system to less than 3.2 A. At a beam current of 3.2 A and a discharge current of 21 A, the center portion of the grids were observed to glow a dull red. This region was approximately 5 cm in diameter. During a high voltage recycle, a blue cathode plume could be seen extending from the cathode to the red glow on the grids.

For engine operation with the cathode positioned at the nominal J-series cathode position the situation was significantly different. The engine ran well, reasonable discharge voltages could be achieved, and the performance was acceptable as indicated in Fig. 2.6.3. This figure has been reproduced from Ref. 16. A representative operating point for the 30-cm-diameter divergent-field thruster with the multi-orifice cathode is indicated on the figure. It is seen that in this case the performance lies between that obtained for operation with and without a baffle with a conventional cathode as measured by Patterson and Rawlin.

## **2.7 High-Power Ion Engines**

A design approach for the near-term development of 100-kW class ion engines is given in Appendix C.

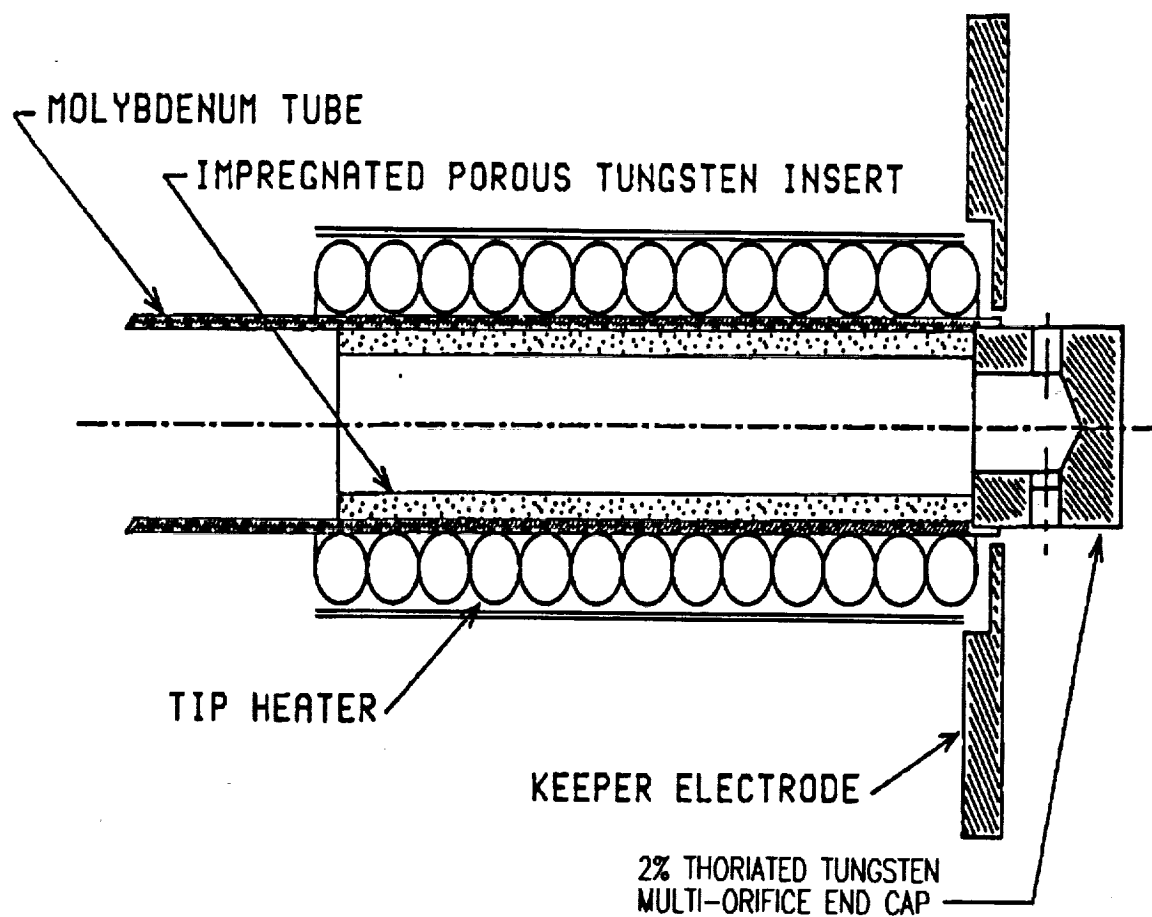


**Fig. 2.6.1a Schematic of multi-orifice cathode.**

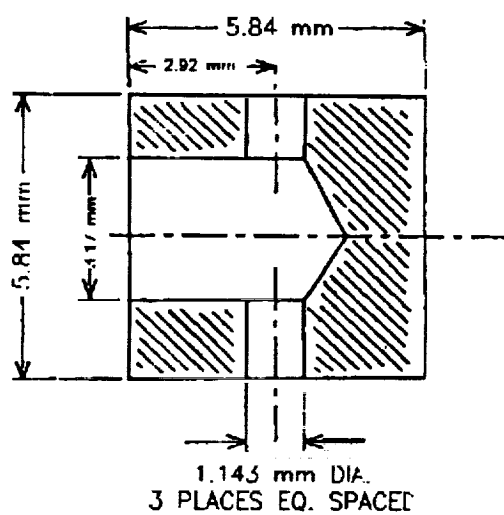


**Fig. 2.6.1b Multi-orifice cathode endcap.**

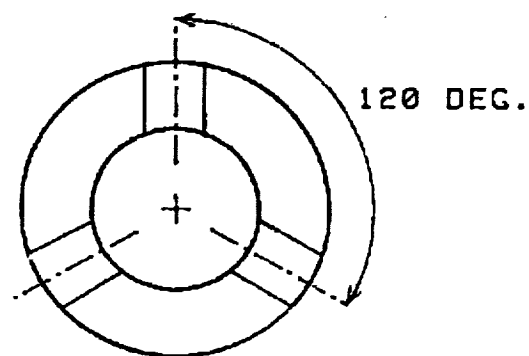


**Fig. 2.6.1c Multi-orifice cathode end view.**

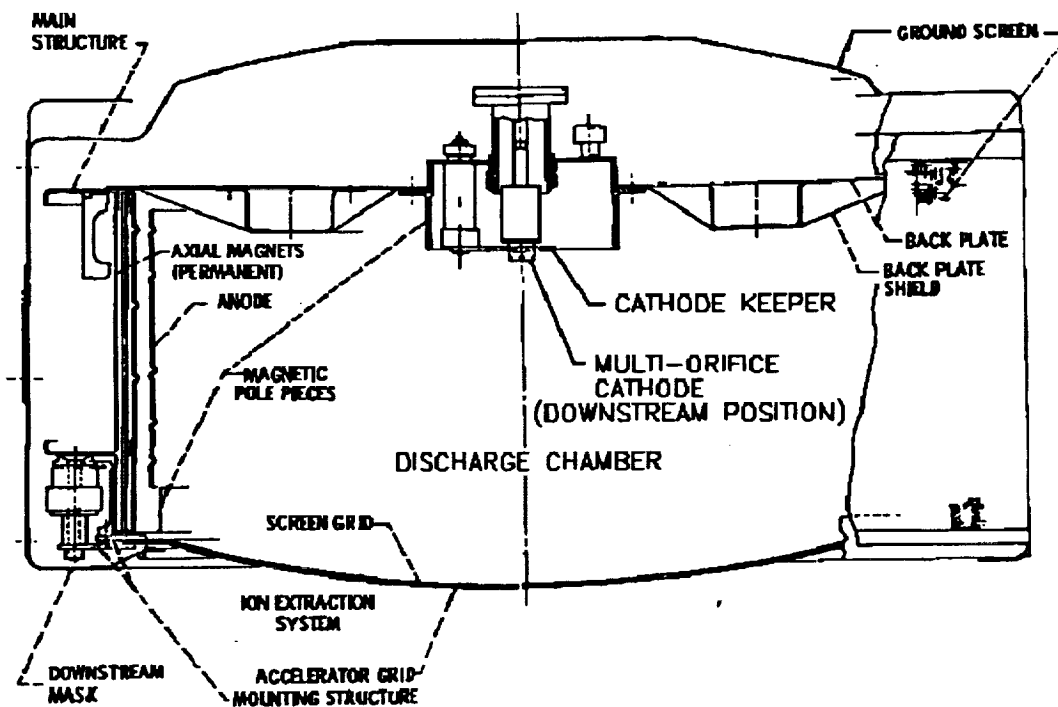


Fig. 2.6.2a Schematic of downstream multi-orifice cathode position.

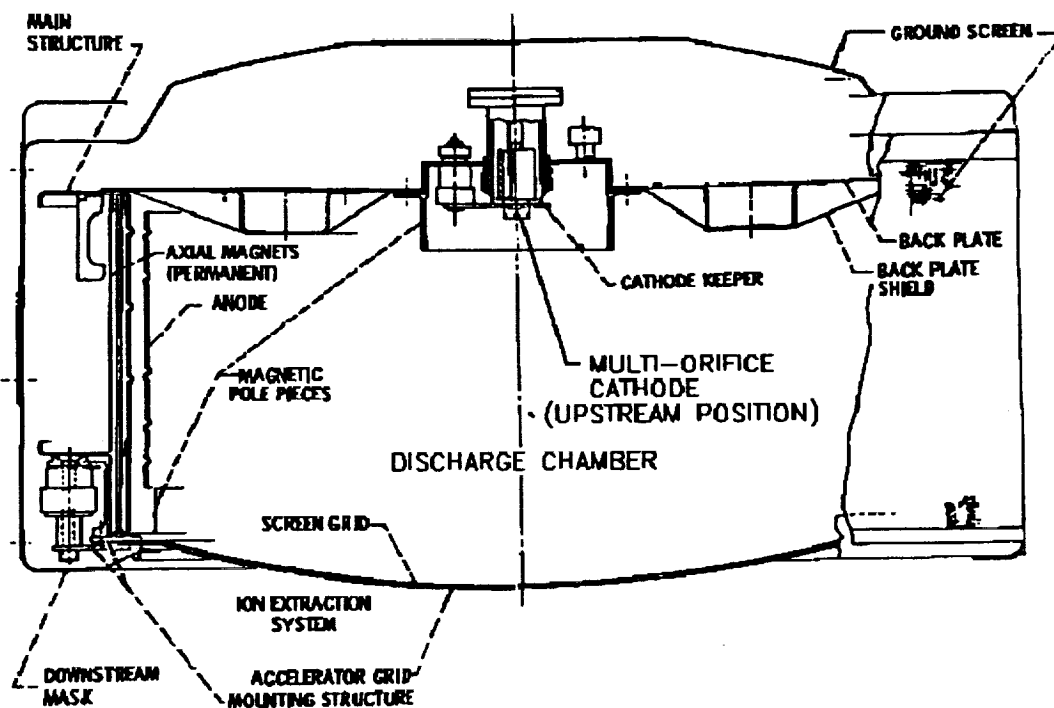


Fig. 2.6.2b Schematic of upstream multi-orifice cathode position.

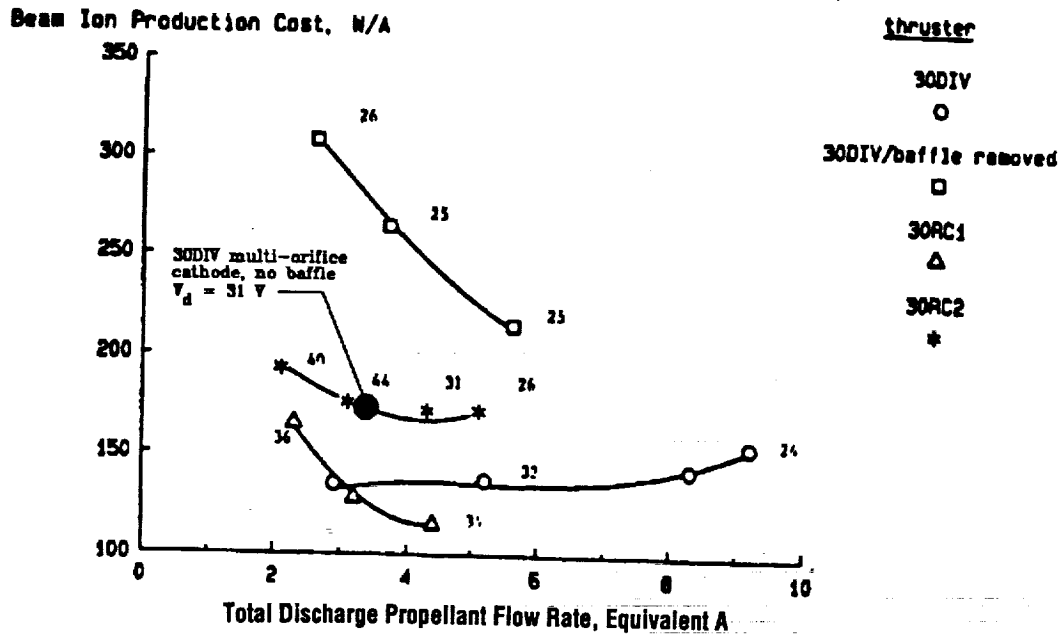


Fig. 2.6.3 Thruster performance with the multi-orifice cathode and the baffle removed falls between that for operation with and without the baffle using a conventional hollow cathode (from Ref. 10).

### 3. Magnetoplasmadynamic (MPD) Thruster Technology

*Thomas J. Pivrotto, Keith D. Goodfellow, and James E. Polk*

#### 3.1 Operation of an Applied-Field MPD Thruster

A schematic diagram of the MPD thruster is shown in Fig. 3.1.1. The 2% thoriated tungsten cathode was 1.91 cm in diameter and was used with both a 60-deg cone tip, as shown, and with a hemispherical tip. The anode/nozzle had an initial throat diameter of 1.27 cm as shown. Both G-90 graphite and pure tungsten were used to make anode/nozzles. High-purity boron nitride was used for the insulators and a molybdenum threaded cap was used to hold everything together. Propellant leaks were prevented by using Grafoil gaskets. The gaseous propellant was introduced into the engine through the cathode attachment fitting and flowed into the plenum chamber through the annular gap between the cathode shaft and the insulators.



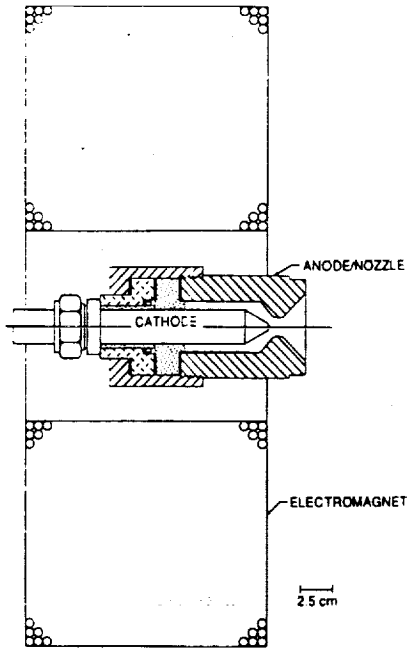


**Fig. 3.1.1 Schematic of MPD thruster.**

The electromagnet, also shown in Fig. 3.1.1, was wound from 0.95-cm-diameter, 0.08-cm wall-thickness, pure-copper refrigeration tubing. The resulting solenoid had an inside diameter of 18 cm, an outside diameter of 51 cm and had 17 layers of conductor with 16 turns per layer. Woven fiberglass tubing was used for electrical insulation and the solenoid was cooled by passing water through the conductor tubing. The front face and inside cylindrical surfaces of the solenoid were protected from radiant heat from the archhead by water-cooled copper sheet. The calculated and measured magnetic field flux densities are compared in Fig. 3.1.2.

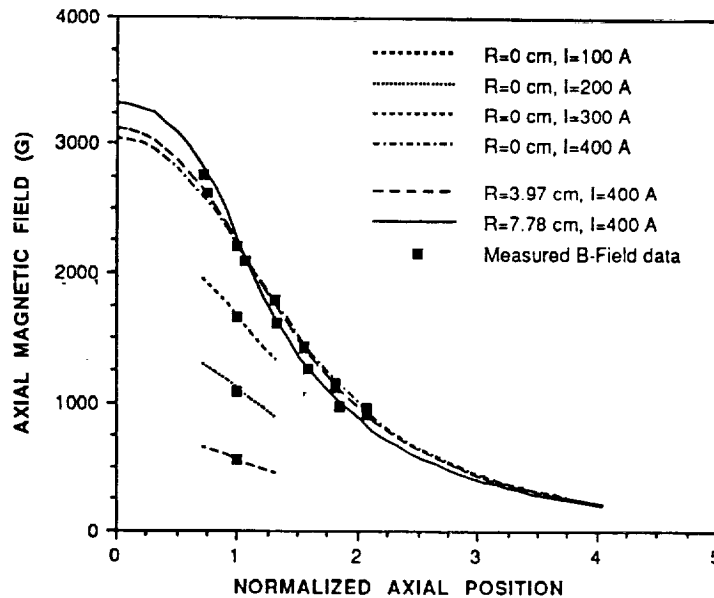


**Fig. 3.1.2 Plot of calculated and measured magnetic-field strength.**

A unique dual-beam thrust stand is shown schematically in Fig. 3.1.3 and pictorially in Fig. 3.1.4. Both the electromagnet and arched were suspended from a water-cooled framework that was an integral part of the vacuum tank header. The electromagnet was supported by two 1.27-cm-diameter stainless steel tubes that also carried the electromagnet cooling water to and from the solenoid windings and the water-cooled solenoid shield. These two tubes were in a plane that was perpendicular to the thrust direction and acted as the flexures in the system. As the electromagnet developed thrust, through the interaction between its axial and radial magnet field components and the electric currents flowing in the plasma, these two tubes were bent slightly and the amount of bending was measured with a Linear Variable Differential Transformer (LVDT). The LVDT output was calibrated by applying weights horizontally along the electromagnet centerline with a pulley system. This calibration was accomplished in situ after the vacuum tank has been evacuated.

The arched and its heavy copper bus bars were suspended from a single 1.27-cm-diameter stainless steel tube, which was also used to carry the propellant gas to the thruster. The measurement of deflection and appropriate calibrations of the arched system was essentially the same as that of the electromagnet. The electric power to both the electromagnet and arched was transferred to the thrust stand through pools of mercury.

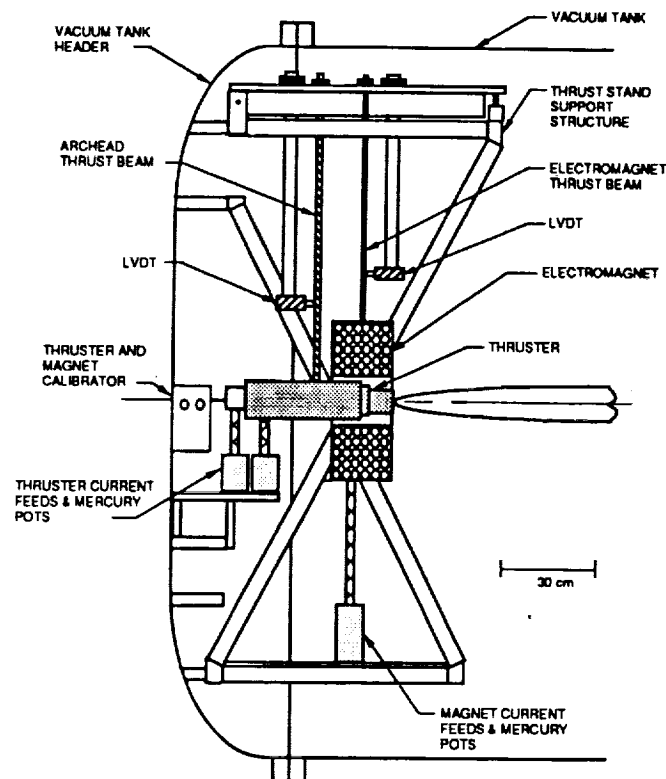


**Fig. 3.1.3 Schematic of MPD thruster dual-beam thrust stand.**

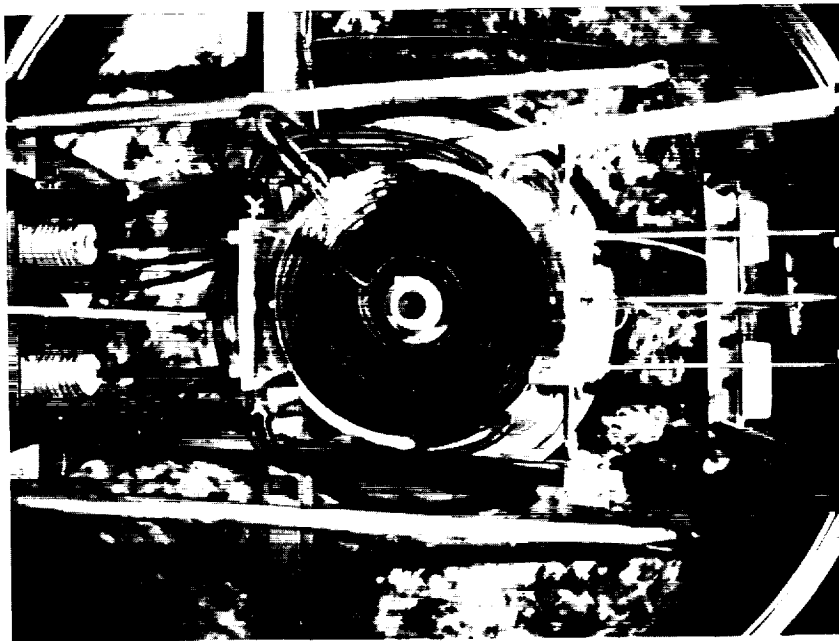
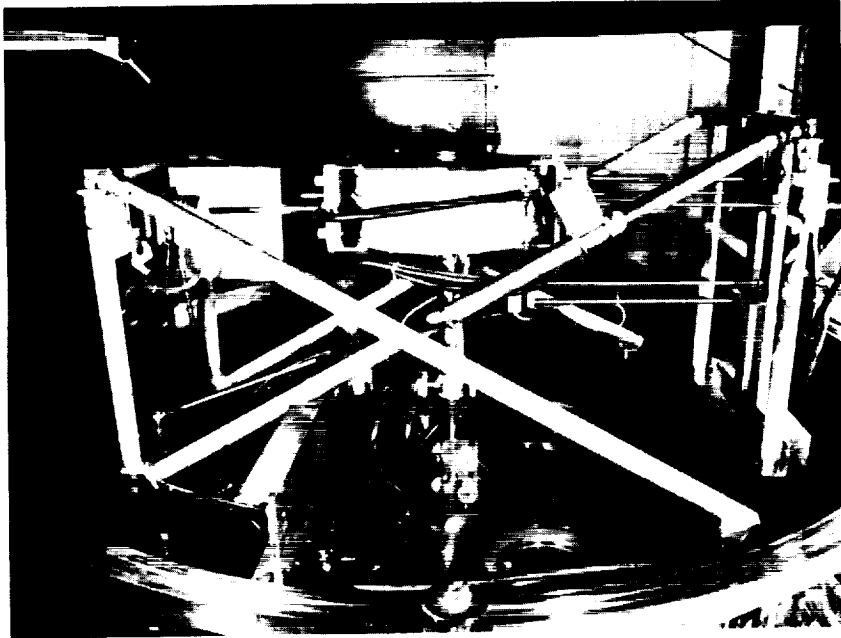


Fig 3.1.4 Photograph of side view and front view of thrust stand.

A reliable, easy-to-use data acquisition system was needed for the MPD thruster experiment. The existing system was over 10 years old, and both the software and the hardware needed upgrading. The upgrade path selected was one in which a desktop computer was to be used with commercially available interface boards. Two methods were considered: developing specialized in-house software, or purchasing a commercial package. The commercial package solution was selected because the development time would significantly be reduced, modifications would be easier, and assistance was available from the JPL Data Acquisition Group. Several commercial packages were considered for both IBM PC-type computers and for Macintosh computers. A Macintosh-based system (LabView) was selected because of its versatility and ease of use. The MPD experiment is often modified and the system must be easy to modify (both hardware and software). LabView is an icon-oriented program that is easy to modify and is self documenting. In addition, many of the basic data acquisition software features (such as data collection and display and interface protocols) are supplied with the software.

The new system is capable of taking data at two different rates simultaneously. Data with long time constants (such as temperatures) are sampled at one rate while data with short time constants (such as current and voltage) are sampled at another rate, allowing the capturing of relevant data without creating an unnecessarily large data file. The data are displayed numerically. In addition, select channels can be displayed in "strip-chart" format on the computer screen. This allows the operator to see both the instantaneous values and the trends. The system is also capable of monitoring the experiment and terminating it if select parameters are out of range.

This experimental system was operated for a total run time of 59.6 hours with typical runs lasting from 2 hours to as long as 7 hours. A preliminary attempt to measure thrust on both the arched and solenoid, with ammonia vapor as the propellant, is shown in Fig. 3.1.5. The ammonia mass flow rate was approximately 0.050 g/s and the magnetic field strength, measured at the cathode tip, was set at 638 and 1110 gauss. Due to the unavailability of our large vacuum pumping plant during this test, the vacuum-tank back pressure was measured to be between 120 and 130 mtorr. The reason for the large amount of data scatter is not known at this time and is being investigated. The stated ammonia mass flow rate was obtained, as an approximation, from an uncalibrated mass flow meter. Calibrations will be performed in the near future and performance calculations will then be made.

All cathodes used in these experiments were made of 2% thoriated tungsten and were 1.91 cm in diameter. However, two tip configurations were used: a 60-deg included angle cone with a rounded tip and a 0.95-cm radius hemisphere. Testing with the conical tip and at power levels up to 50 kW produced severe cathode tip melting. A photograph of two such cathode tips, after about 8 hours of testing each, is shown in Fig. 3.1.6. Clear evidence of surface melting is evident. Figure 3.1.7 shows an illustration of a typical cathode profile before and after testing. The post-test cathode tip angle is approximately 45 deg. This indicates that the cathode tip was eroded significantly during operation until it reached a geometry that was compatible with the operating conditions. The final configuration is surprisingly close to the hemispherical shape. This result, along with a thermal analysis, provided the basis for selecting a hemispherical cathode tip.

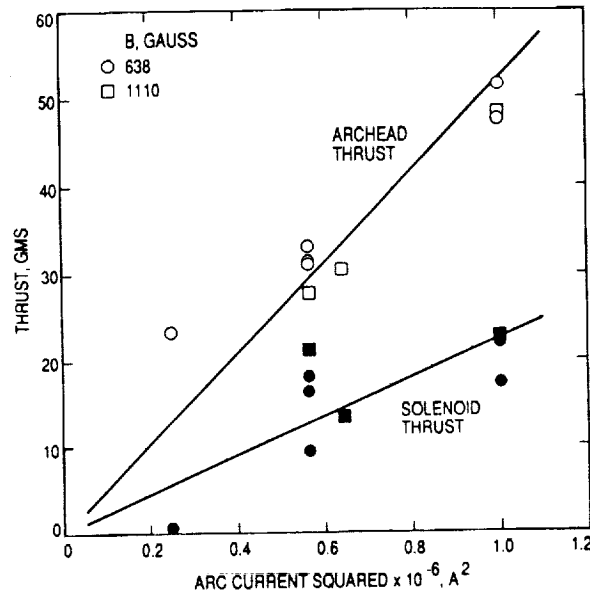


**Fig. 3.1.5 Plot of MPD thrust data.**

One of the cathode tips shown in Fig. 3.1.6 and illustrated in Fig. 3.1.7 has been sectioned and analyzed with the aid of an SEM. The preliminary results indicate that: (a) the long-term arc attachment area was within approximately 0.2 cm of the cathode tip, (b) molten tungsten from the attachment area flowed back along the conical surface, possibly driven by gas-dynamic force from a recirculation zone at the tip, (c) evidence for current emission on the cylindrical surface of the cathode was also found, and (d) thoria was found on the tip surface, indicating that the supply had not been depleted after approximately 8 hours of operation.

A hemispherical cathode tip shape has since been tested at power levels up to 80 kW in a series of 7 runs for a total time of 26.5 hours. A head-on picture of that cathode is shown in Fig. 3.1.9. Although the surface has been roughened by the discharge no evidence of melting can be detected. Also, it was found that the starting and operating characteristics of the thruster are similar for both types of cathode tips.

The anode/nozzle also was affected by the long-term steady-state operation. The principal effect was an erosion of the nozzle throat. Initially the throat had a 0.79 cm radius of curvature, a diameter of 1.27 cm, a 50-deg half-angle entrance cone and a 45-deg half-angle exit cone. Two such nozzles were made of G-90 graphite and a third of pure tungsten. All three nozzles suffered essentially the same type and degree of erosion, although the graphite sublimated, leaving no residual material, while the tungsten nozzle left molten tungsten in the exit cone. One of the graphite nozzles has been sectioned and is shown in Fig. 3.1.9. Note that a slight throat remains. This seems to be an asymptotic configuration that each of the three nozzles eroded to after several hours of operation each. The pure tungsten nozzle also apparently eroded to the same shape, as is suggested in Fig. 3.1.8.

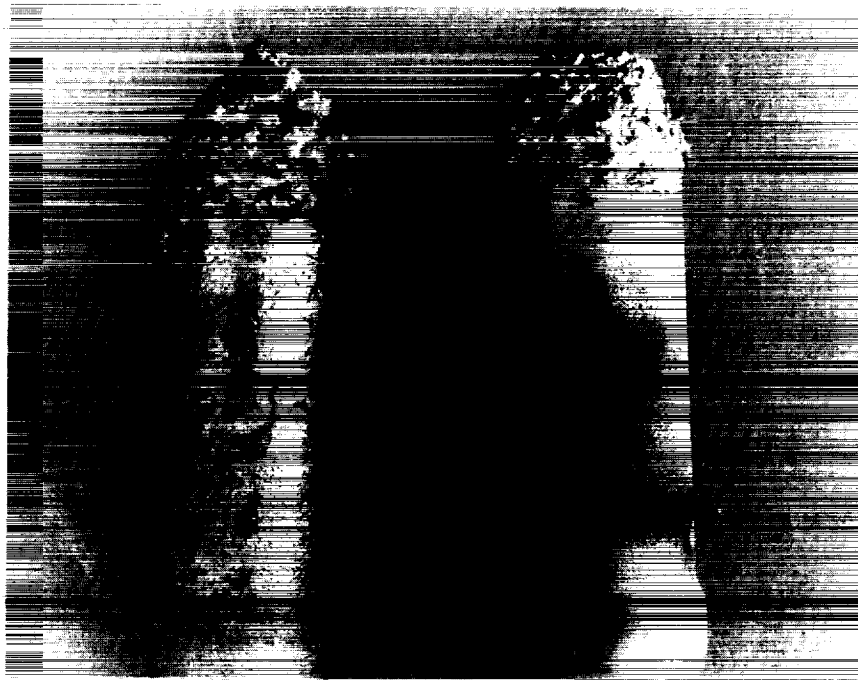


**Fig. 3.1.6** Photograph of experimental cathode tips after testing.

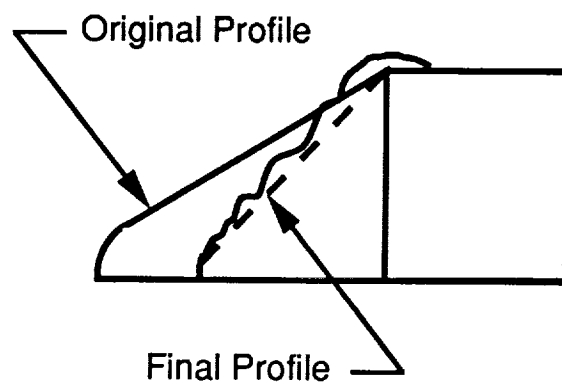


**Fig. 3.1.7** Illustration of pre-test and post-test cathode geometries.

Although each nozzle throat opened up to about 3.2 cm from the original 1.27 cm, the starting and operating characteristics were essentially unchanged. This was unexpected; the high plenum chamber pressure, resulting from the small throat diameter, was thought necessary to prevent arc attachment at the cathode root. This turned out not to be a problem with this design, even after the throat had opened up.

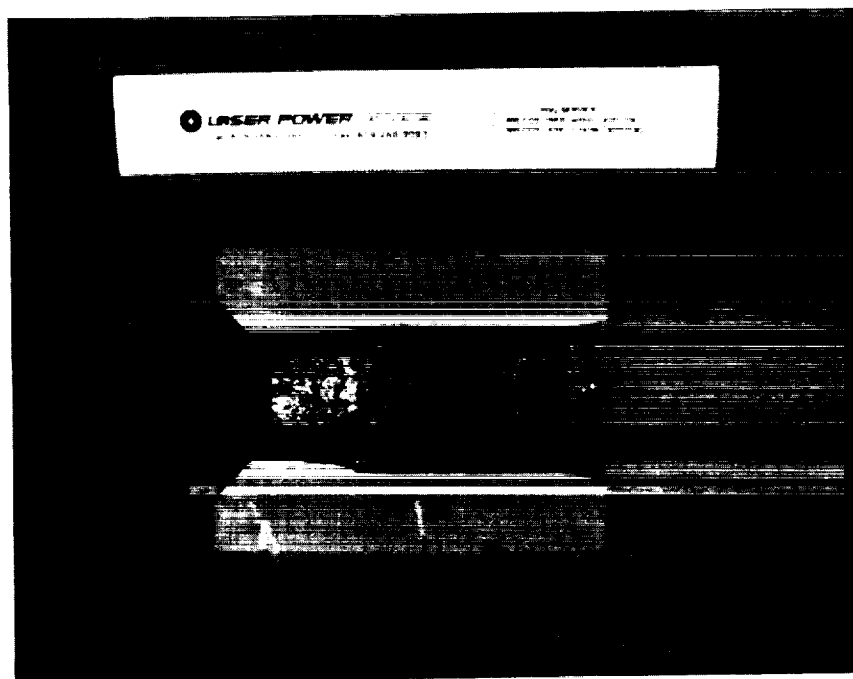


**Fig. 3.1.8** Photograph of MPD thruster cathode tip and eroded throat.

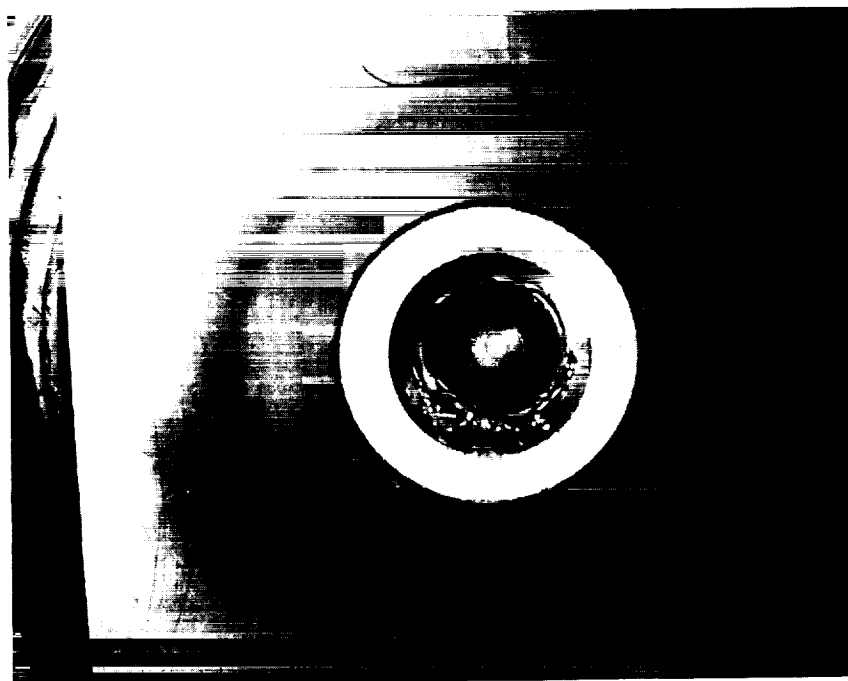


**Fig. 3.1.9** Photograph of the sectioned graphite nozzle.

## 3.2 Diffuser Evaluation

It is a well-known fact that vacuum-tank ambient pressure can have an adverse effect on several of the thrust-producing mechanisms as well as on the measurement of thrust, in all forms of electric propulsion devices. For example, in thermal devices such as arcjets, a high background pressure will interfere with the nozzle expansion processes, will contribute to cooling through natural and forced convection and may interfere with thrust stand operation because of possible impingements of fluid currents on sensitive thrust stand elements. These same processes can disturb applied-field MPD thruster measurements as well. In addition, background gas entrainment and acceleration in the engine plume and effects on plasma conductivity are considerations. Because of these potentially adverse effects, testing with adequate background pressure levels in electric propulsion test facilities is critical to the ultimate development of electric propulsion engines.

A literature survey of background pressure effects on self- and applied-field MPD engine performance can be found in Ref. 33. For self-field MPD thrusters, no indications of adverse effects were observed when vacuum-tank pressures were below one mtorr. For applied-field engines it was found that high background pressure could either degrade performance by interfering with one or more thrust-producing mechanisms or enhance performance by entrainment and acceleration of residual vacuum chamber gases. These effects depend on type and flow rate of propellant gas used, background gas type, and pressure. For example, with a hydrogen flow rate of 3.5 mg/s and nitrogen as the background gas, the vacuum-tank pressure had to be kept below about 8 mtorr to avoid adverse effects on performance measurements. For ammonia propellant at various flow rates and with a variety of background gases, a pressure below 0.3 mtorr was required.

If steady-state vacuum tank pressures of these magnitudes are to be maintained by continuous pumping only, the facility costs, and for long term life testing (a practical necessity for all electric propulsion devices) the operating costs, can become prohibitive. For example, the installation cost of a modern diffusion pump is approximately  $\$12 \times 10^6$  per gm/s of hydrogen and  $\$15 \times 10^6$  per gm/s of ammonia vapor. Cryopumping of hydrogen or dissociated ammonia would be even more expensive for full-scale engine life testing. The only known method of reducing the required pump capacity would be to take advantage of the directed kinetic energy in the test engine plume. This can be done by considering the engine as part of an ejector pumping system and/or directing the high energy plume into a diffuser designed to decelerate the exhaust gases while maintaining as much of the original stagnation pressure as is possible.

A review of the literature indicated that ejector/diffuser design methods and/or data for ambient pressures below one torr do not exist. Extrapolations from the existing high-pressure data were therefore used as a starting point and several preliminary designs have been fabricated and tested with high power arcjets and moderate power applied-field MPD engines. Examples of some relevant results of these tests are shown in Figs. 3.2.1 and 3.2.2. Data obtained from a 30-kW class arcjet engine are shown in Fig. 3.2.1. These data were obtained in the facility shown in Fig. 3.2.3, using the engine design shown in Fig. 3.2.4. The vacuum tank pressure was measured with a Baratron pressure gauge calibrated in the range of 1–1000 mtorr. The initial test was made without the diffuser but with the engine plume directed at the inlet to the water-



cooled elbow shown in Fig. 3.2.3. The propellant was ammonia so that with zero arc power the diffuser passed pure ammonia vapor and with arc power the gas was a mixture of nitrogen and hydrogen with possibly some residual ammonia vapor if dissociation was incomplete. Therefore, for arc power greater than zero the tank pressure increases, partly because of a decrease in mean molecular weight (increase in the volume rate of flow due to dissociation), and partly due to an increase in gas temperature. Note that since the engine is facing into the open elbow, some recovery of stagnation conditions must be occurring.

Next, a water-cooled constant diameter diffuser with a 14.9-cm ID and a length of 53.7 cm was installed as shown in Fig. 3.2.3. The mouth of this diffuser was 6.4 cm from the engine exit plane. With this diffuser, a vacuum tank pressure decrease of 50 mtorr, independent of arc power, was experienced. Again, the vacuum tank pressure increase with arc power is attributed to increased dissociation and gas temperature. With this diffuser, a secondary effect may be that

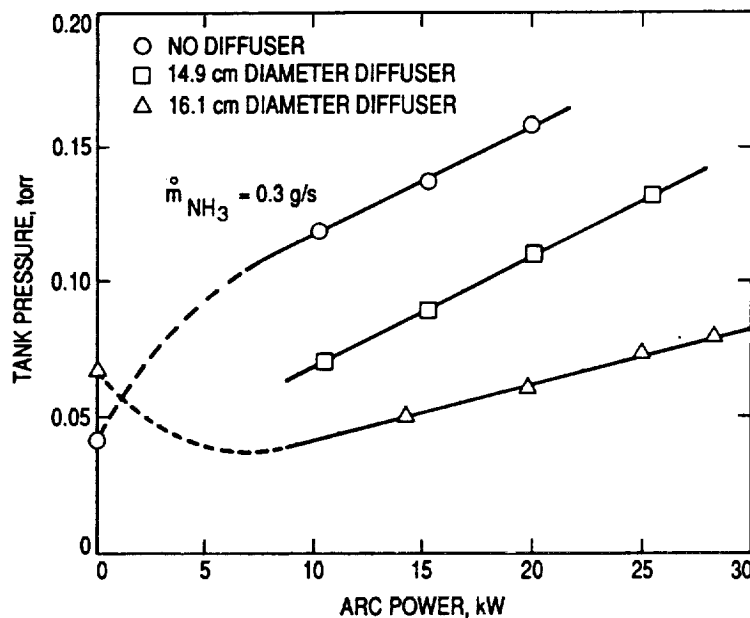


Fig. 3.2.1 Plot of arcjet diffuser data.

the arcjet plume could expand beyond the diffuser entrance and not be completely captured. To alleviate this potential problem, a second diffuser that was slightly larger in diameter and length was fabricated, installed and tested. This new diffuser had an internal diameter of 16.1 cm, a length of 60 cm and its mouth was coincident with the arcjet exit plane. The results of this test are also shown in Fig. 3.2.1. For this test, the zero arc power data point is higher than the corresponding point for the no-diffuser case. This increase in vacuum tank pressure represents the loss of pumping speed (decrease in system conductance) due to the diffuser impedance. However, once the arc is turned on, and regardless of the dissociation and elevated gas temperature, the measured vacuum tank pressure is dramatically reduced from the no-diffuser test and the amount of reduction increases with arc power (increased exhaust velocity). Hence, for this final arcjet diffuser design, the ejector/diffuser effect overcomes dissociation, elevated temperatures and plume ballooning effects and its use results in a very large reduction in vacuum

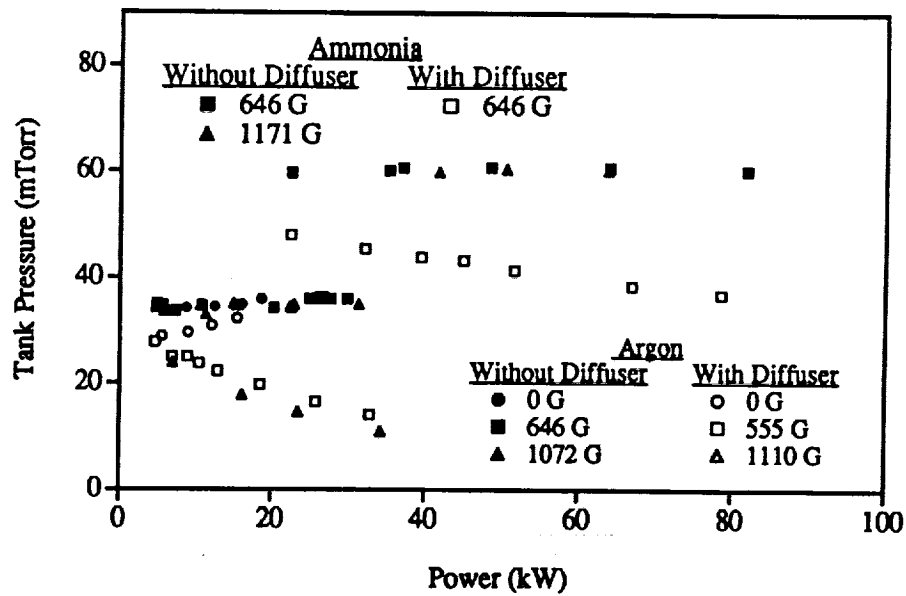


Fig. 3.2.2 Plot of MPD thruster diffuser data.

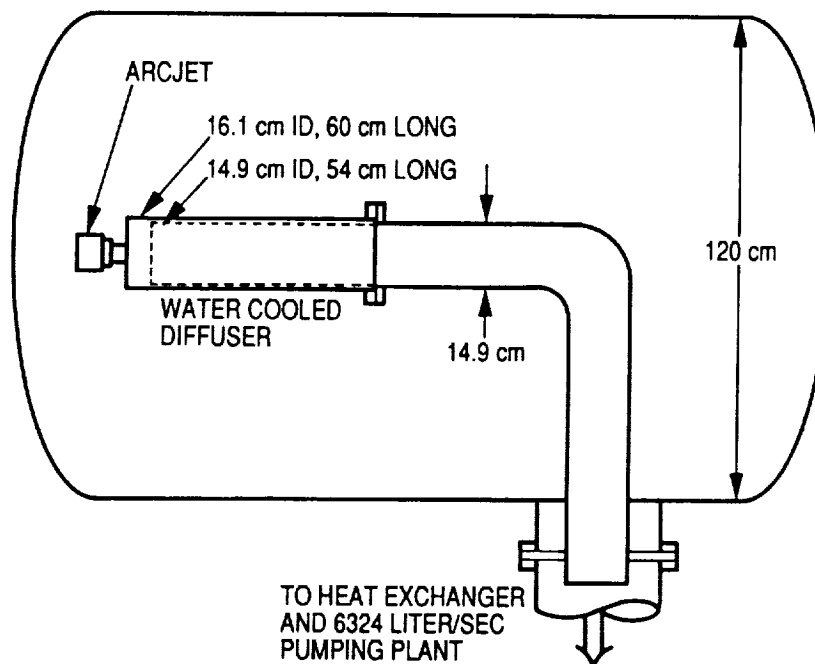
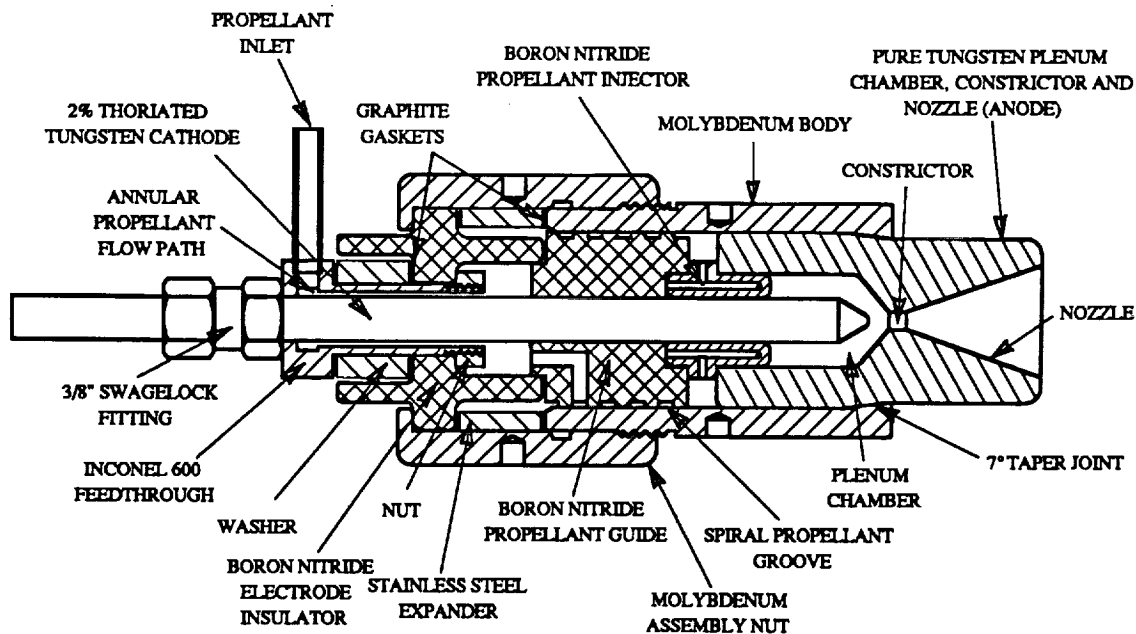


Fig. 3.2.3 Schematic of the arcjet test facility and diffuser installation.



**Fig. 3.2.4 Schematic of the arcjet engine.**

tank back pressure. This means that the investment in pumping plant installation and operating cost could be reduced by more than a factor of two in any proposed new arcjet test facility.

Because of these encouraging results with arcjets a similar, constant diameter, ejector/diffuser design was investigated with our applied-magnetic-field MPD engine test facility. The design chosen is shown schematically in Fig. 3.2.5. Because a greater plume expansion was expected from the lower back pressures and the use of a magnetic nozzle, a larger diffuser mouth was used in this facility than in the arcjet facility. The design, shown in Fig. 3.2.5, is a water-cooled, 46-cm-diameter by 123-cm-long cylindrical section followed by a 41-cm-long cone as a transition to a 25 cm diameter vacuum line. A 6320 liter/s mechanical pumping plant was used to pump on the diffuser outlet, and a 1230-liter/s mechanical pumping plant was used to continue pumping on the vacuum tank, directly. The mouth of the diffuser was located 3 cm from the engine exit plane in order to provide visual access to the plume.

The data obtained with this ejector/diffuser is shown in Fig. 3.2.2. Argon, at a constant mass flow rate of 0.09 g/s, was used as the propellant; the arc power was varied between 5 and 35 kW; and the magnetic-field strength, measured at the cathode tip, was varied between 0 and 1110 gauss. The initial tests were conducted without the diffuser installed. The internal vacuum line was removed from the vacuum tank and both pumping plants were used to pump on the tank itself. Vacuum tank pressure measurements, obtained with a calibrated Baratron gauge, were made as a function of arc power and magnetic field strength and are shown as filled data points in Fig. 3.2.2. These data indicate that the pressure is independent of magnetic field strength and rises only slightly with arc power. Since these tests were performed in a large tank, the exhaust gas temperature most likely was equilibrated with the tank walls before it arrived at the two pump out ports. The slight rise in vacuum tank pressure with arc power could then have been

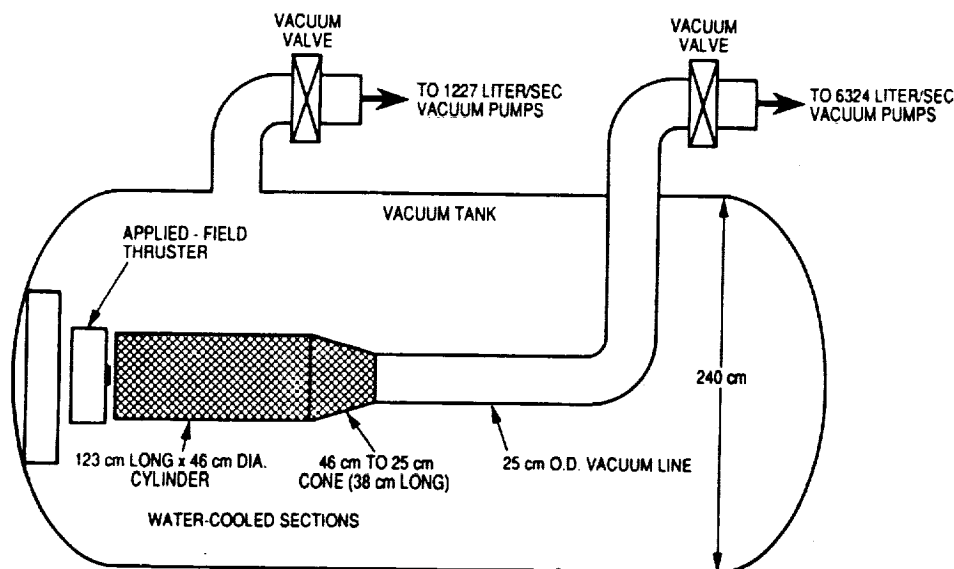


**Fig. 3.2.5 Schematic of MPD thruster diffuser installation.**

caused by a slight rise in temperature at the pump out ports.

Next the ejector/diffuser was installed as shown in Fig. 3.2.5, and essentially the same test parameters were repeated. These data are shown as open data points in Fig. 3.2.2. Without the magnetic field and at low power, the vacuum tank pressure was reduced by the diffuser, but as the arc power was increased the tank pressure also increased as it did for the arcjet tests shown in Fig. 3.2.1. This result may have been caused by expansion of the plume and elevated gas temperatures which negated most of the diffuser/ejector effect. With the addition of the diffuser and vacuum line, the conductance of that part of the pumping system was much decreased, but the ejector/diffuser effect was still great enough to overcome these and produce a moderate reduction in tank pressure.

When the magnetic field was turned on, a dramatic new result appeared. The vacuum tank pressure was reduced further and continued to drop with increasing arc power and magnetic field strength. These results seem to indicate that as the exhaust velocity is increased by either increasing the arc power or applied magnetic field strength, or both, the ejector/diffuser effect increases, resulting in a reduced vacuum tank pressure. Increasing the applied-field strength also appears to focus the plume into a narrower jet, so a higher fraction may be intercepted by the diffuser inlet. This effect continued at lower mass flow rates and higher arc power and magnetic field strength. The greatest indicated effect to date was a vacuum tank pressure of 6 mtorr with 0.07 g/s of argon, 40 kW of arc power and a magnetic field strength of 1360 gauss.

All indications seem to suggest that at still a higher arc power and/or magnetic field strength, the diffuser will lower the vacuum tank pressure further. At a pressure of one mtorr, or less, it will become possible to turn on our three diffusion pumps, thus adding  $130 \times 10^3$

liters/s for hydrogen to our pumping capacity. Hence, with a sufficiently high plume velocity, the ejector/diffuser effect can: (1) overcome the added impedance of the diffuser and vacuum line, (2) overcome the elevated gas temperature at the entrance to the pump out system, and (3) effectively reduce the vacuum tank pressure to a regime low enough to make accurate engine electrode temperature measurements.

### **3.3 Electrode Thermal Modeling**

Radiation-cooled MPD thrusters are preferable to liquid-cooled thrusters for space applications because of the simpler design and higher efficiency<sup>34</sup>. However, in radiation-cooled thrusters the maximum operating power can be severely limited by the thruster thermal design. Recent experiments at JPL have shown severe thruster melting even at moderate powers (less than 50 kW). A better understanding of the thruster thermal characteristics is therefore essential for thruster development. In FY 1991, MPD thruster thermal analyses consisted of three phases: selection of an appropriate thermal model, cathode tip analysis, and overall thruster analyses.

#### **3.3.1 Thermal Model Selection**

The MPD thruster thermal environment requires a special type of thermal model. The large temperature gradients present in the thruster (about 3000 K drop over about 20 cm) severely complicate the thermal model since the material properties change significantly and nonlinearly over this temperature range. The model must therefore contain temperature-dependent material properties (primarily thermal and electrical conductivities). In addition, nonlinear temperature dependent boundary conditions are also required because of the surrounding plasma. These effects require the use of a "nonlinear" thermal model which significantly increases the complexity of the analysis. Two methods were considered for addressing this problem. First, the development of an in-house thermal model designed specifically to address this problem, and second, the purchase of a commercial modeling package. While the development of a special code would better address the problems unique to this situation, the development time required for such a model can be extensive, and therefore a commercial modeling package appeared to be the best approach.

Both the hardware and the software had to be selected. More than 10 commercial finite-element models (FEM) were investigated and 5 were examined in detail. Only two of these (MSC/NASTRAN and AFEMS) contained suitable nonlinear capabilities. The second consideration was whether a mainframe or a desktop computer would be used. A cost estimate of the two systems (i.e., using an existing MSC/NASTRAN and VAX computer combination or purchasing software and using a PC computer) revealed that mainframe system costs far exceeded the PC system costs. In addition the execution speed of the PC system was significantly faster. However, the PC system did have a smaller memory capability, but for this effort, this was not significant. MSC/NASTRAN also offers a PC-based version of their mainframe model. Since this model was designed to operate on mainframes, it does not take advantage of PC specific features and is therefore somewhat limited. The other PC-based package is AFEMS by FEM Engineering. This package has recently been developed specifically for PC use. Of these two packages, AFEMS was selected because it is designed specifically for a PC-based operation and has incorporated recent FEM software algorithm improvements. Preliminary tests of the code

have revealed it to be versatile and easy to use, and the results are described in the following sections.

### 3.3.2 Cathode Tip Thermal Model

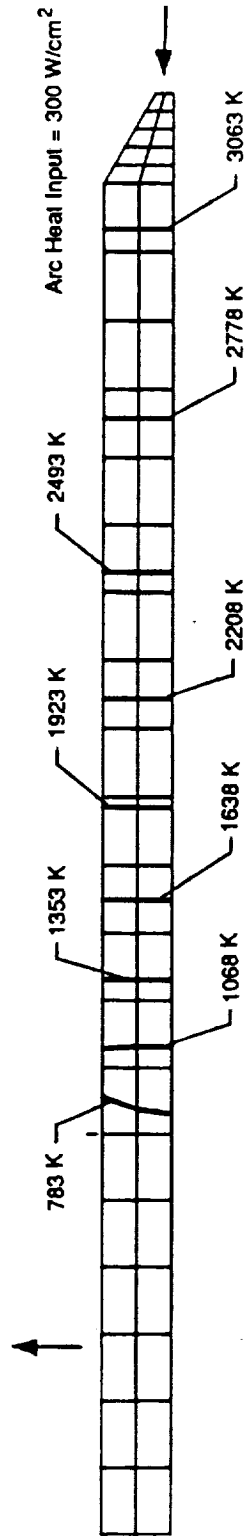
The severe cathode tip melting observed in recent experiments (Figs. 3.1.6 and 3.1.7) prompted an analysis of the heat transfer in the tip region.<sup>35</sup> Two configurations were considered: a flattened conical tip and a flattened hemispherical tip. A one-dimensional analytical model was developed to obtain a first-order approximation. Then a two-dimensional axisymmetric model was developed using the AFEMS software. The details of these models are described in the paper "An Experimental and Numerical Investigation of an Applied-Field Magnetoplasma-dynamic Space Propulsion Engine," by Pivrotto and Goodfellow, which is reproduced in Appendix D. The one-dimensional model provided a good first approximation of the average axial temperature drop, but overestimated the temperature drop along the outside surface and underestimated the temperature drop along the centerline as would be expected. The axial temperature drop for the conical tip was typically about 2.5 times the temperature drop for the hemispherical tip with equivalent heat loads. Therefore, for equivalent operating conditions, the conical geometry produces significantly higher tip temperature and is consequently more susceptible to melting. For this analysis, a fixed value heat load was applied uniformly over the flattened portion of the tip. In reality there is probably a significant portion of the current (and heat transfer) to the side of the cathode. Also, in reality the heat load to the surface will depend on the surface temperature and the properties of the surrounding plasma sheath. This analysis is only appropriate for predicting trends and gross effects and not for the precise determination of temperature profiles within the cathode. The development of the required cathode sheath model is the second portion of this program and is described later.

### 3.3.3 Preliminary Electrode Thermal Models

Preliminary thermal models for both the cathode and the anode electrodes were completed to estimate the overall electrode thermal conditions; that is, the thermal boundary conditions that were appropriate for these geometries and material properties. The cathode results are shown in Fig. 3.3.1. The model included a constant heat flux of  $300 \text{ W/cm}^2$  uniformly distributed over the flat portion of the tip, temperature-dependent conduction radially from the base area, temperature dependent-thermal conductivity and internal heat generation (from Ohmic heating). For this case the cathode base temperature was 550 K and the tip temperature was 3350 K. From the experiments for operation at 30 kW, the cathode base temperature is estimated to be 900 K and the tip temperature to be between 3000 and 3500 K. For the conical tip cathodes, the tip temperature clearly exceeded 3660 K and melted on some occasions, as seen in the photograph of the two conical cathode tips in Fig. 3.1.6. The large L/D (length/diameter) ratio for the cathode severely limits the allowable heat load at the tip, because it is effectively thermally choked. That is, cooling of the cathode base is ineffective, and the cathode tip region must have effectively a zero net heat flux (cooling balances heat loads). An accurate model of the heat loads at the tip is therefore very important.

The preliminary thermal model of the anode is shown in Figure 3.3.2. This model includes a constant radial heat flux of  $600 \text{ W/cm}^2$  distributed over throat area, temperature dependent-conduction radially from the base area, radiation from the other external surfaces,

Temperature Dependent Heat Conduction = 50 ( $T_s - 500$ ) W/cm<sup>2</sup>



Ohmic Heating = 10 W/cm<sup>3</sup>

Nonlinear Thermal Conductivity

**Fig. 3.3.1 Example of cathode temperature distribution.**

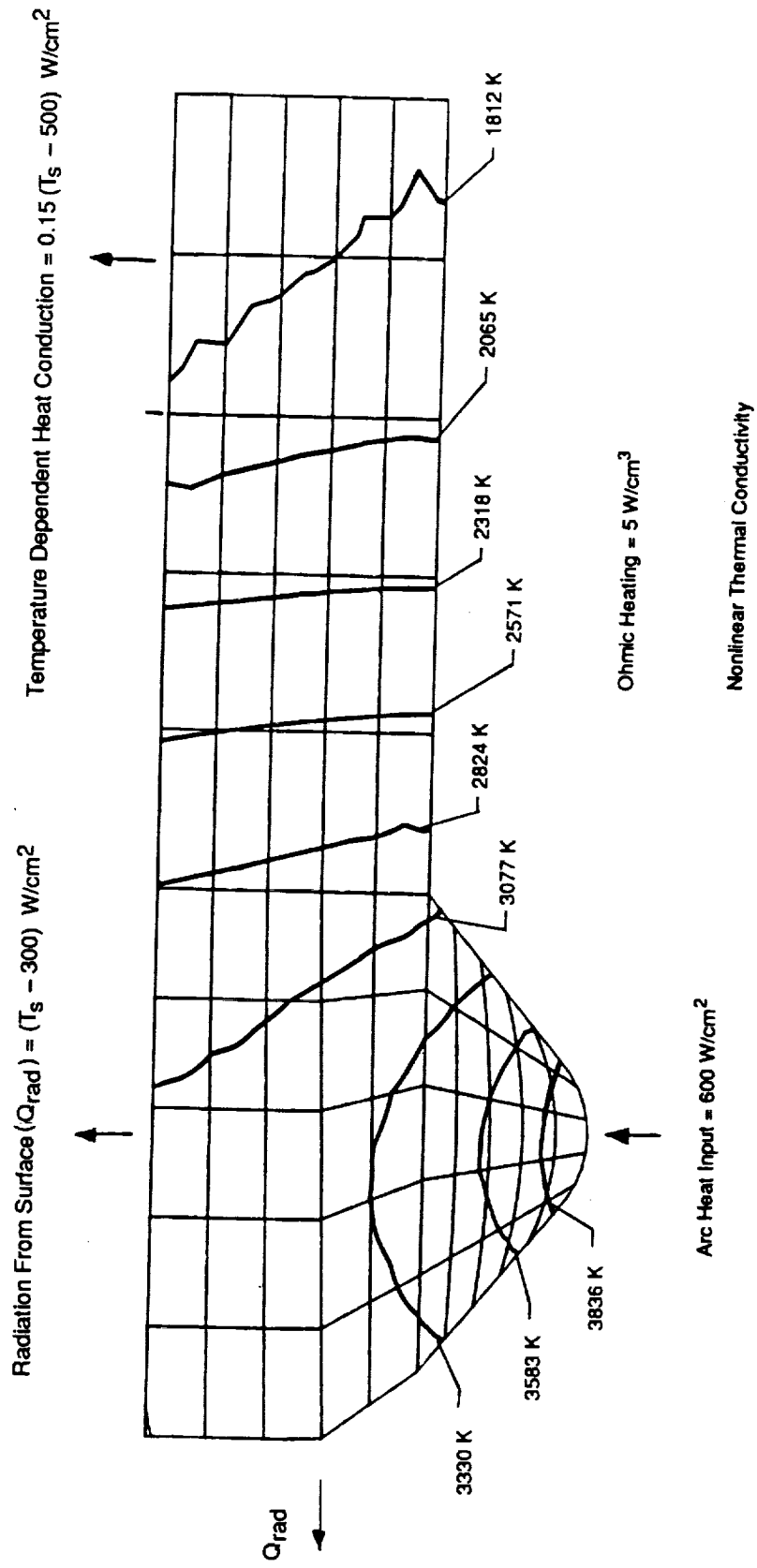


**Fig. 33.2 Example of anode temperature distribution.**



temperature-dependent thermal conduction, and internal heat generation (from Ohmic heating). While the cathode can be effectively approximated by a one-dimensional model, the anode can not. For this case the anode base temperature was about 900 K and the throat temperature was over 4000 K, clearly indicating that the heat load for this geometry is too large. These conditions may be similar to those of the experimental thruster which experienced severe melting in the throat and the throat diameter enlarged from 1.27 cm to about 3.18 cm uniformly. The uniform melting suggests that the heating was uniformly distributed and not localized.

Most of the same simplifications used for the cathode tip model are used for these models. To improve these models, a more comprehensive understanding of the boundary conditions, in particular for the heat loads associated with the current attachment at both electrodes is needed. Both the heat flux and the attachment area are unknown. The values selected for the preliminary cases were based on estimates obtained from the experimental data. For both electrodes, a range of heat load values was investigated to estimate what heat loads were physically feasible for these geometries since the actual heat loads were unknown. The examples presented here are two that appeared to be the most applicable. The number of cases computed was limited by time required for a steady-state solution to be achieved. Typically, more than 10 hours of computer time were required for each case. Development of a cathode sheath model has been initiated this year and will be continued next year in order to better determine the electrode thermal boundary conditions.

### 3.4 Cathode Sheath Model

A plasma sheath region forms between the main body of plasma and the electrodes in contact with it and connects the plasma characteristics with those of the electrodes. A model of this region connects plasma temperatures and number densities with the electrode temperature and heat flux. Also included are the current density and the sheath voltage drop. The objective, given information about the plasma near the electrodes, is to predict current density and heat flux to the surface.

Many models for the cathode sheath are available, but many are too extensive for our purposes. For this analysis, the model must be simple, but yet return the essential physical processes. A simple model is required because it will be combined with the cathode thermal model and eventually with a plasma flow model. A complex model would require excessive solution time. Various forms of good simple models were found in the literature<sup>35-38</sup>. The two best candidates were the models by Prewett and Allen<sup>36</sup>, and by Bade and Yos<sup>38</sup>.

The Prewett and Allen model of the cathode sheath region is a one-dimensional model with three species (ions and electrons from the plasma and thermionic electrons). The ions and the thermionic electrons are monoenergetic while the plasma electrons are considered to be Maxwellian. The solution consists of solving the continuity and energy equations for each species along with the Poisson equation for electrostatics. The Richardson equation is used to determine the thermionic electron current which is augmented with the Schottkey effect for electrical extraction of electrons from the material. The Schottkey effect is included by calculating the electric field at the cathode surface. The Bade and Yos model is similar to the

Prewett and Allen Model but does not include the plasma electrons (which can be considered negligible for large sheath voltages ( $>10$  volts)).

The Bade and Yos model does, however, include a model for an ionization zone at the sheath/plasma boundary that is necessary to match the ion current values for the plasma and the sheath. The ion current in the sheath is significantly larger than for the plasma where the electrons carry most of the current. The ionization zone produces "extra" ions that enter the sheath in order to satisfy this condition. The energy for the ion production is provided by the high energy thermionic electrons accelerated across the sheath.

It was decided for our model to combine the ionization zone model from the Bade and Yos work with the Prewett and Allen sheath model. Both models were modified to include additional terms that were found to be significant for the description of the MPD thruster cathode sheath layer. A new model was formulated that included these additional terms in the two base models. This model is being developed now and will be presented in detail in the FY 1992 publication. Given the plasma electron temperature and pressure, the sheath voltage, and the cathode temperature for a particular cathode material and propellant, the model calculates the current density and the heat flux to the cathode surface. Conversely, the current density could be given and the sheath voltage calculated, but this method is significantly more difficult numerically.

To obtain a complete model of the cathode, the thermal and sheath models must be combined. The sheath model supplies the necessary boundary conditions for the thermal model and the thermal model supplies the sheath model with the surface temperature.

### 3.5 Cathode Surface Studies

An optical technique, based on an available 8.89 cm in QUESTAR field model telescope, has been developed and used to take short-exposure, high-resolution photographs of the MPD electrodes while the thruster was operating. The telescope was necessary because the nearest, suitable, vacuum tank window was approximately 4 m from the MPD electrodes. With this system, a "head-on" photograph of the 1.91-cm-diameter cathode was obtained in which the image diameter was 1.59 cm. These images could then be expanded without loss of resolution to a diameter of approximately 12 cm for analysis. Photographs obtained with this technique are shown in Figs. 3.5.1 and 3.5.2. These pictures, taken with an exposure time of 1 ms, show axisymmetric patterns of color and intensity. In Fig. 3.5.1 a ring of tiny dark spots is evident. Based on post test analysis of the cold electrodes, it turns out these dark spots represent the growth of tungsten crystals out of the surface of the cathode. In long-term arcjet testing, it has been found that this type of crystal growth can reach lengths of a millimeter and interfere with arcjet operation. It has been found in the current experiments that these crystals appear under certain operating conditions and disappear under other conditions. Not enough testing has been done to delineate what conditions promote crystal growth. However, by using this optical technique, it is possible to watch for crystal growth under a variety of operating conditions.

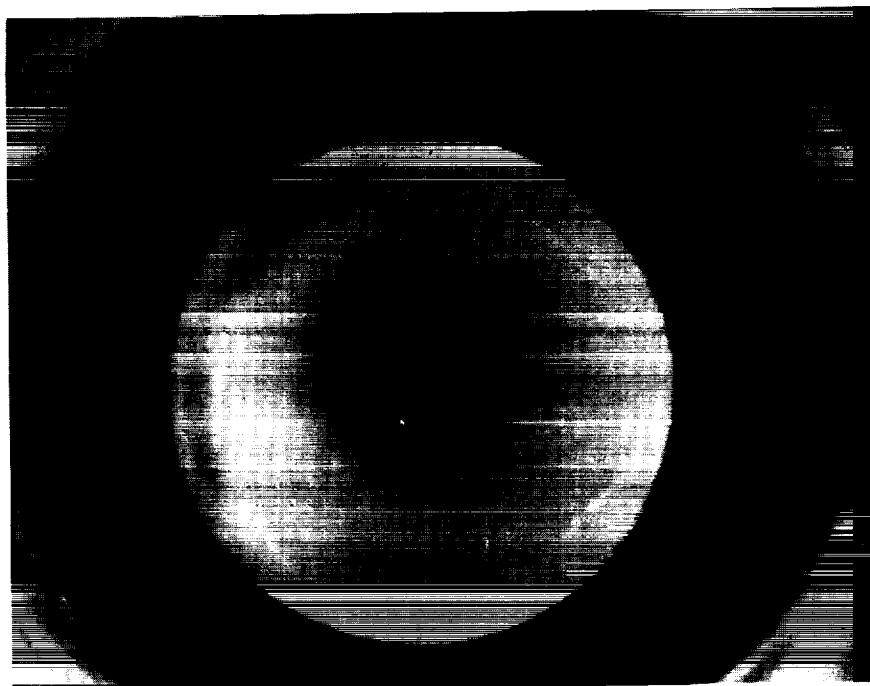


**Fig. 3.5.1** Photograph of hot cathode tip showing axisymmetric patterns.

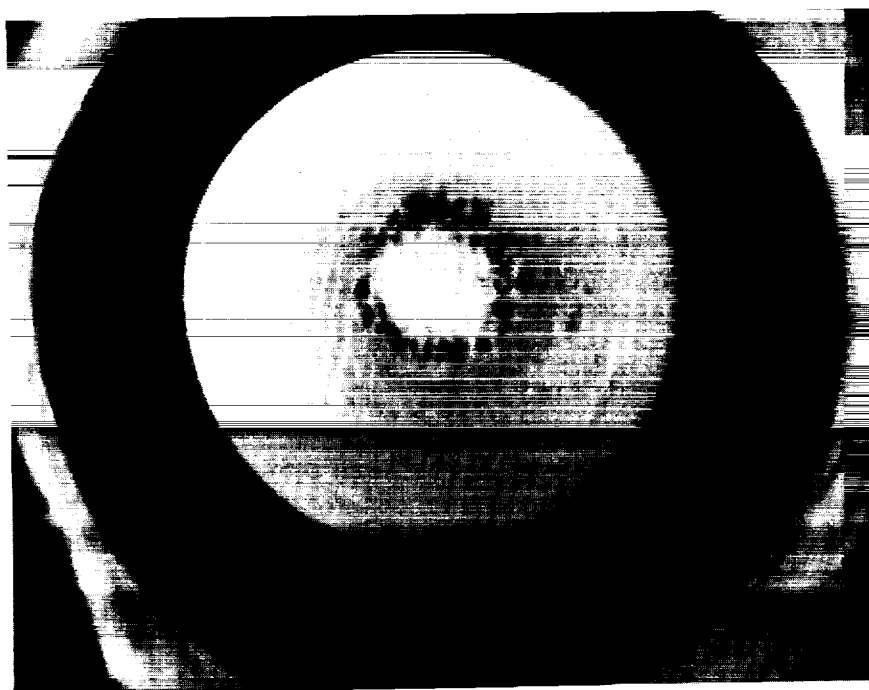


**Fig. 3.5.2** Photograph of hot cathode tip showing formation of crystals in a ring pattern.

### 3.6 Cathode Test Facility

Because MPD thrusters are relatively low thrust devices, extremely long operating times are required to achieve the necessary total impulses. Therefore, component endurance is one of the primary concerns in engine design. The cathode currently appears to be the life-limiting component, so a major focus of the effort at JPL is on the study of high current cathode phenomena. The long-term goal is the development of a cathode capable of operating reliably at 10,000 A for 5000 hours, which represents a level of technology appropriate for long-duration missions. Achieving this ambitious goal depends on obtaining a detailed understanding of cathode wear mechanisms, cathode thermal behavior and mass transport in the surrounding gas, as well as the capability to test candidate cathode designs.

A new, dedicated facility has been designed and is currently being constructed to provide the experimental support for the cathode development program. The facility will enable the following tasks:

1. Collection of cathode thermal data to validate the cathode thermal model.
2. Diagnosis of the near-cathode plasma environment to define the boundary conditions for the thermal model.
3. Development of improved cathode designs.
4. Investigation of new cathode materials.
5. Performance of cathode endurance tests at high current levels.

The facility requirements were defined by these tasks and the need to adequately simulate the cathode environment in MPD thrusters.

The facility consists of the vacuum tank pictured in Fig. 3.6.1, a Roots blower and mechanical roughing pump, a closed-loop cooling system, and arc power supplies. Figure 3.6.2 shows a schematic of the laboratory layout. The vacuum chamber is approximately 0.5 m in diameter and 2 m long and is composed of three water-cooled stainless steel segments that are electrically isolated from each other. Each segment has a port on each side and one on the top. A 1.3-m-long steel extension bolted to the rear of the tank contains a loose coil of finned copper tubing to act as a beam dump. A 7.6-cm-diameter stainless steel tube was inserted through the coiled copper tubing to ensure optical access along the tank centerline. The anode will be mounted to a plate bolted between the first and second segments, effectively making the first segment the discharge chamber. The cathode will be mounted to the chamber door, which is mounted on a set of rails extending from the tank entrance.

The chamber will be pumped by a 200-cfm Roots blower and a 50-cfm mechanical pump. The pressures attainable with this system as a function of flow rate for argon and hydrogen are plotted in Fig. 3.6.3. The pressure found in the cathode region of MPD thrusters ranges from about 1 torr to several hundred torr. These pressures can be achieved in this facility with reasonable gas flow rates. A particular pressure higher than the best achievable can be obtained by throttling the pump line or bleeding in additional gas.

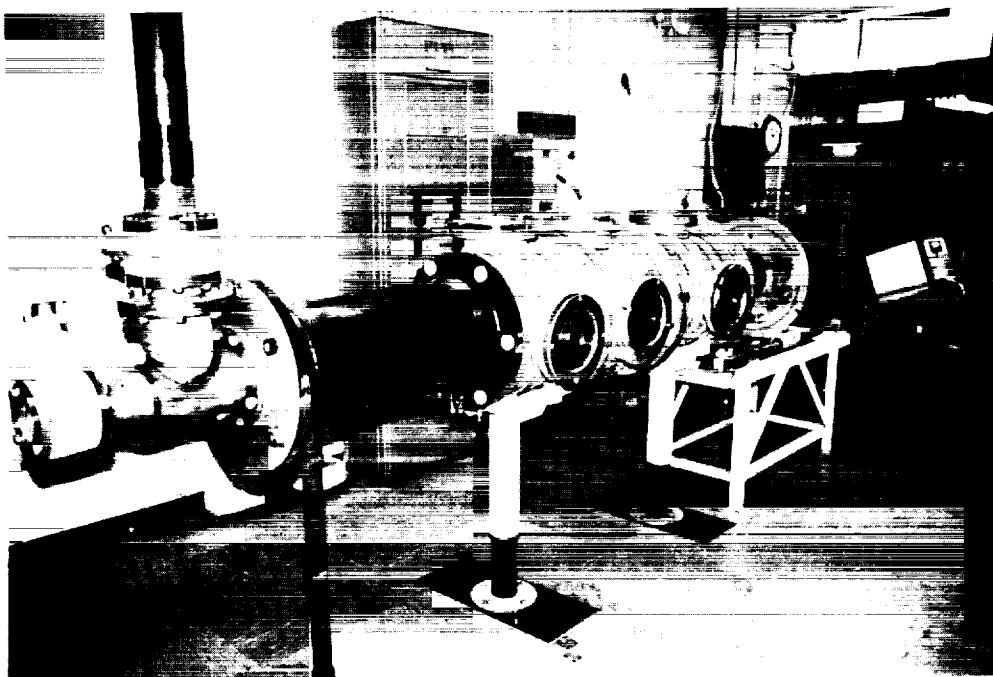


**Fig. 3.6.1** Photograph of vacuum chamber for cathode test facility.

The chamber, beam dump, anode and cathode will be cooled with a closed-loop water cooling system composed of a plate and frame heat exchanger and a cooling tower. The system has been sized to dissipate 130 kW. Power for the discharge will initially be supplied by three Westinghouse arc power supplies. Each is capable of providing about 200 A at 70 V. Later our existing Miller power supplies will be connected, providing up to 3000 A at 80 V continuously or 4000 A at 80 V for 20 minutes.

### **3.7 Investigation of Alkali Metal Propellants**

MPD thrusters using gaseous propellants such as hydrogen, argon, or ammonia have demonstrated only marginal performance and are subject to excessive cathode erosion. Several approaches to addressing these issues for gaseous propellants are being pursued. However, experience in the United States in the 1960s and early 1970s and in the Soviet Union suggests that the use of alkali metals as propellants may significantly improve engine performance and electrode endurance. A critical review of the available literature was conducted to evaluate the potential advantages and problems associated with alkali metal propellants and was summarized in the paper "Alkali Metal Propellants for MPD Thrusters," by Polk and Pivrotto, which is reproduced in Appendix E.

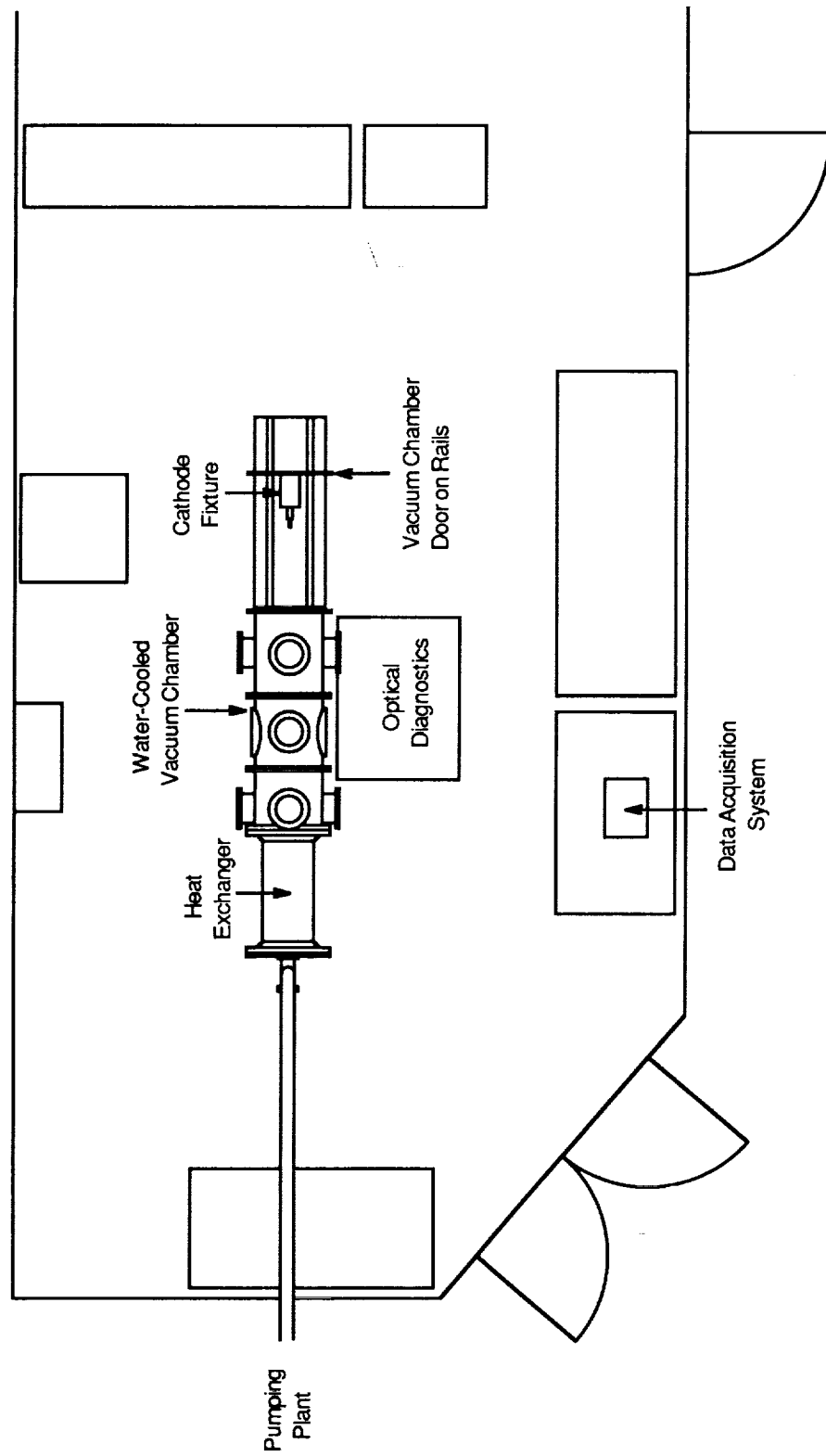


**Fig. 3.6.2 Schematic of laboratory layout.**

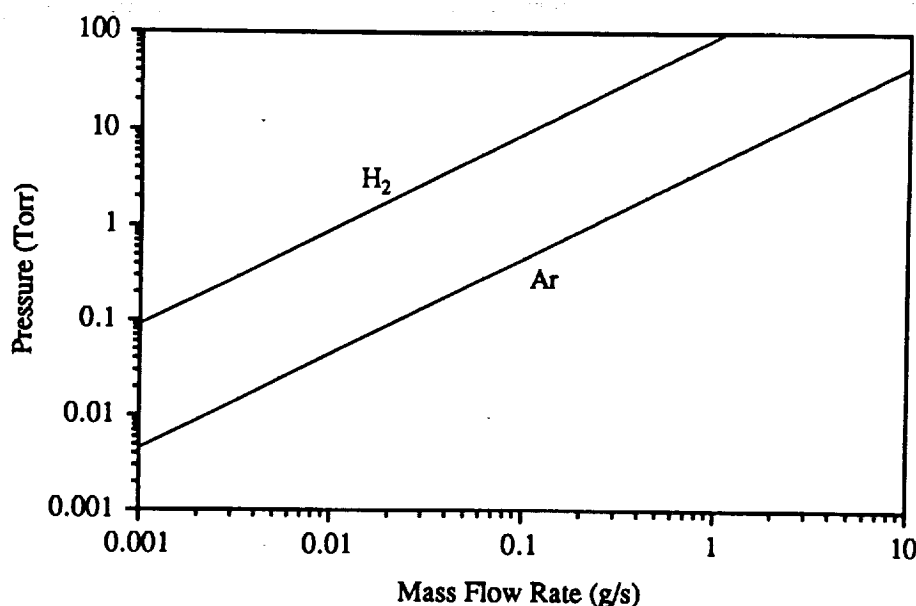


**Fig. 3.6.3 Plot of vacuum system performance.**

The primary purpose of this review was to determine if sufficient justification exists to initiate a renewed experimental examination of alkali metal propellants. A critical review of the experimental programs conducted at the Giannini Scientific Corporation, Electro-Optical Systems, Los Alamos National Laboratory, AVCO Corporation, and in the Soviet Union revealed considerable evidence indicating that efficiencies as high as 60–70% can be achieved at specific impulses of 5000–7000 s with lithium. The experimental procedures were also reviewed, but no sources of gross systematic bias that could invalidate this general conclusion were identified. Anecdotal evidence of improved cathode lifetime was also found.

The properties of the alkali metals were also examined to determine if the observed gains in performance and lifetime could be justified on sound physical bases. The alkali metals all have low first ionization potentials. In addition, the second ionization potential and the first excited state of the ion are very high for lithium. There is, therefore, little double ionization and very little energy required to produce single ions. This results in reduced frozen flow losses, which might explain some of the efficiency gains observed experimentally. The high thermal efficiencies measured in the experiments suggest that the alkali metals also have some impact on the anode thermal losses which plague gas-fed MPD engines. A more sophisticated analysis of the anode region would be required to verify this, however.

The alkali metals are also very effective in lowering the work function when adsorbed on the surface of refractory metal cathodes. A reduction in the work function allows lower operating temperatures, resulting in lower cathode erosion rates. A model of alkali metal adsorption used

to determine the thermionic emission capabilities of a tungsten cathode as a function of surface temperature and alkali metal vapor pressure and temperature is presented in the paper.

The impact of alkali metal propellants on test facility requirements and other spacecraft systems was also examined. One demonstrated advantage of alkali metals is that they are easily pumped. The low vapor pressure metals simply condense on the vacuum chamber walls at room temperature. Facility pumping requirements with alkali metals are therefore much less demanding. One of the largest costs in a full-scale multimegawatt engine development program will be the construction of a facility with adequate pumping capability, and the use of condensable propellants may enable an otherwise unaffordable test program.

The alkali metals are extremely reactive and exothermically react with water or water vapor to form hydrogen, so they represent a potential combustion hazard. In addition, the alkali metal hydroxides formed in these reactions are caustic, so care must be taken when operating and cleaning a test facility.

The greatest risk in the development of alkali metal-fed engines is the potential for spacecraft contamination. The plumes of MPD thrusters have not been sufficiently well-characterized to estimate the backflow of particles. However, even for modest fluxes, high surface temperatures are required to prevent the bulk condensation of alkali metals. Several strategies for minimizing the contamination potential from condensable propellants are discussed in the paper.

The conclusion of the review of alkali metal propellant experience was that an investment in an experimental program is justified. Alkali metals, particularly lithium, appear to provide the greatest leverage of any current approach in bridging the gap between MPD thruster capabilities and mission requirements. The experimental program priorities should include:

1. The development of a reliable alkali metal propellant flow metering system, a thruster, and a test facility.
2. Establishment of proper handling procedures to guarantee the safe use of alkali metals.
3. Verification of previous performance measurements.
4. Investigation of cathode operation in an alkali metal vapor environment.
5. Characterization of the plume in conjunction with the development of plume modeling capability to assess the spacecraft contamination potential.

Once these preliminary tasks have been completed, the engine should be scaled to the appropriate power level and adequate endurance demonstrated.



## 4. References

1. Yen, C. L., and Sauer, C. G., "Nuclear Electric Propulsion for Future NASA Space Science Missions," IEPC-91-035, October 1991.
2. Sauer, C., "Application of Solar Electric Propulsion to Future Planetary Missions," AIAA-87-1053, May 1987.
3. Collett, C. R., and Poeschel, R. L., "A 10,000 Hour Endurance Test of a 700 Series 30-cm Engineering Model Thruster," AIAA-76-1019, November 1976.
4. Collett, C. R., and Bechtel, R. T., "An Endurance Test of a 900 Series 30-cm Engineering Model Ion Thruster," AIAA-76-1020, November 1976.
5. Trump, G., James, E. L., Bechtel, R. T., and Vetrone, R., "An Electric Propulsion Long Term Test Facility," AIAA-79-2080, November 1979.
6. Bechtel, R. T., and James, E. L., "Preliminary Results of the Mission Profile Life Test of a 30-cm Hg Bombardment Thruster," AIAA-79-2078, November 1979.
7. James, E. L., and Bechtel, R. T., "Results of the Mission Profile Life Test First Test Segment: Thruster J1," AIAA-81-0716, April 1981.
8. Bechtel, R. T., Trump, G. E., and James, E. J., "Results of the Mission Profile Life Test," AIAA-82-1905, November 1982.
9. Patterson, M. J., and Verhey, T. R., "5-kW Xenon Ion Thruster Lifetest," NASA-TM-103191, July 1990; also AIAA-90-2543, 1990.
10. Patterson, M. J., NASA Lewis Research Center, Cleveland, Ohio, personal communication, September 1990.
11. Rawlin, V. K., "Internal Erosion Rates of a 10-kW Xenon Ion Thruster," AIAA-88-2912, July 1988.
12. Wilber, P. J., Monthly progress report to NASA LeRC for the Advanced Electric Propulsion Research Grant to Colorado State University, September 7, 1991.
13. Matsunami, N., Yamamura, Y., Itikawa, Y., Itoh, N., Kazumata, Y., Miyagawa, S., Morita, K., Shimizu, and Tawara, H., "Energy Dependence of the Yields of Ion-Induced Sputtering of Monatomic Solids," IPPJ-AM-32, September 1983.
14. Bechtel, R. T., "The 30 cm J-Series Mercury Bombardment Thruster," AIAA-81-0714, April 1981.

15. Rawlin, V. K., "Operation of the J-Series Thruster Using Inert Gas," NASA-TM-82977, November 1982.
16. Brophy, J. R., and Garner, C. E., "A 5000 Hour Xenon Hollow Cathode Life Test," AIAA-91-2122, June 1991; also Appendix A in JPL Publication 92-10, Jet Propulsion Laboratory, Pasadena California (this publication).
17. Brophy, J. R., and Garner, C. E., "Tests of High Current Hollow Cathodes," AIAA-88-2913, July 1991.
18. Brophy, J. R., "Near-Term, 100-kW Class Ion Engines," AIAA-91-3566, September 1991; also Appendix C in JPL Publication 92-10, Jet Propulsion Laboratory, Pasadena California (this publication).
19. Gilland, J. H., Myers, R. M., and Patterson, M. J., "Multimegawatt Electric Propulsion System Design Considerations," AIAA-90-2552, July 1990.
20. Frisbee, R. H., Blandino, J. J., and Leifer, S. D., "A Comparison of Chemical Propulsion, Nuclear Thermal Propulsion, and Multimegawatt Electric Propulsion for Mars Missions," AIAA-91-2332, June 1991.
21. Garner, C. E., Brophy, J. R., and Pless, L. C., "Metal and Metal Nitride Erosion Rates in a Divergent Field Ion Engine," IEPC-91-097, October 1991; also Appendix B in JPL Publication 92-10, Jet Propulsion Laboratory, Pasadena California (this publication).
22. Garner, C. E., Brophy, J. R., Pless, L. C., and Barnett, J. W., "The Effect of Nitrogen on Xenon Ion Engine Erosion," AIAA-90-2591, July 1990.
23. Garner, C. E., Pless, L. C., and Torres, E. R., "Techniques for Reduced Spalling and Increased Operation Life of Xenon Ion Engines," AIAA-89-2714, July 1989.
24. Garner, C. E., Brophy, J. R., and Aston, G., "The Effects of Gas Mixtures on Ion Engine Erosion and Performance," AIAA-87-1080, May 1987.
25. *Grade GTA*, Catalog No. 63590, Union Carbide Corp., P.O. Box 94637, Cleveland, Ohio.
26. Vincente, F., Karras, T., Brewer, L., and Gore, R., "Electric Propulsion Applications Enabled by Space Nuclear Power," AIAA-89-2595, July 1989.
27. Nock, K. T., "TAU-A Mission to a Thousand Astronomical Units," AIAA-87-1049, May 1987.
28. Gilland, J. H., "Synergistic Use of High and Low Thrust Propulsion Systems for Piloted Missions to Mars," AIAA-91-2346, June 1991.
29. Dulgeroff, C. R., and Poeschel, R. L., "Retrofit and Verification Test of 30 cm Ion Thruster," NASA-CR-165233, January 1980.

30. Rawlin, V. K., and Millis, M. G., "Ion Optics for High Power 50-cm-dia Ion Thrusters," AIAA-89-2717, July 1989.
31. Rawlin, V. K., "Performance of Large Area Xenon Ion Thrusters for Orbit Transfer Missions," NASA-TM-102049, May 1989.
32. Friedly, V. J., "Hollow Cathode Operation at High Discharge Currents," NASA-CR-185238, April 1990.
33. Sovey, J. S., and Mantenicks, M. A., "Performance and Lifetime Assessment of MPD Arc Thruster Technology," NASA-TM-101293, 1988; also AIAA-88-3211, 24th Joint Propulsion Conference, Boston, Massachusetts, July 11-13, 1988.
34. Auweter-Kurtz, M., Kurtz, H., Merke, W., Schrade, H., Sleziona, C. and Wegmann, T., *High Power Steady State MPD Thruster Final Report*, IRS-90-P4, Institute for Spacecraft Systems, University of Stuttgart, Stuttgart, Germany, March 1990.
35. Pivirotto, T. J., and Goodfellow, K. D., "An Experimental and Numerical Investigation of an Applied-field Magnetoplasma-dynamic Space Propulsion Engine," IEPC-91-074, 22nd International Electric Propulsion Conference, Viareggio, Italy, October 14-17, 1991; also Appendix D in JPL Publication 92-10, Jet Propulsion Laboratory, Pasadena California (this publication).
36. Prewett, P. D., and Allen, J. E., "The Double Sheath Associated with a Hot Cathode," *Proceedings of the Royal Society of London*, Vol. 348, pp. 435-446, 1976.
37. Neumann, W., *The Mechanism of the Thermoemitting Arc Cathode*, Akademie-Verlag Press, Berlin, Germany, pp. 20-45, 1987.
38. Bade, W. L., and Yos, J. M., *Theoretical and Experimental Investigation of Arc Plasma-Generation Technology*, ASD-TDR-62-729, Part 2, Vol. 1, 1963.





**AIAA-91-2122**

**A 5,000 Hour Xenon Hollow Cathode Life Test**

J. Brophy, C. Garner  
Jet Propulsion Laboratory  
Pasadena, California

**AIAA/SAE/ASME/ASEE  
27th Joint Propulsion Conference  
June 24-26, 1991 / Sacramento, CA**

## A 5,000 HOUR XENON HOLLOW CATHODE LIFE TEST

John R. Brophy\* and Charles E. Garner\*  
*Jet Propulsion Laboratory*  
*California Institute of Technology*  
*Pasadena, CA 91109*

A 6.35 mm diameter hollow cathode was successfully operated for a total of 5,024 hours at an emission current of 25 A. Over this time the cathode orifice diameter eroded from 1.80 mm (0.071") to 2.08 mm (0.082"), resulting in a final emission current to orifice diameter ratio of 12 A/mm. Post-test analyses revealed tungsten deposits on the interior surface of the insert and x-ray diffraction analyses of the insert suggest complete depletion of the original impregnate. The successful completion of the scheduled 5,000 hr test, however, suggests that chemical reactions which use the reaction products originating from the depletion of the original impregnate serve to produce free barium and significantly extend the life of the cathode at an operating temperature substantially above 1,100 °C. Analyses of material sputtered from the walls and anode of the test apparatus provide physical evidence in support of a cathode jet phenomena in which energetic ions are produced during hollow cathode operation at emission currents above 20 A.

## Introduction

The power-limited, low thrust nature of ion propulsion necessitates very long engine burn times to accomplish typical missions of interest. Engine burn times of 10,000 to 15,000 hours are typically required for deep space missions. The hollow cathode, which is a key component of ion engines, must be capable of reliable, long term operation. Hollow cathodes have been under development for ion engines since the middle 1960's<sup>1</sup> and have been the subject of numerous studies and endurance tests.<sup>1-37</sup> The vast majority of these investigations performed up until the early 1980's used mercury as the working fluid, although some early studies also used cesium. With mercury vapor, cathode operation was found to be very reliable, and a useful life-time greater than 25,000 hours was demonstrated<sup>18</sup> with a 6.35-mm diameter hollow cathode operating at a discharge current of 10.5-11.5 A.

More recently ion engine research and development efforts have centered on the use of rare gases (argon, krypton and xenon) rather than mercury. Along with this switch from mercury is the present trend toward operation at higher engine power and thrust levels. These higher

power operating regimes require significantly greater cathode emission currents. There is little long term, hollow cathode operating experience with rare gases, especially at emission currents above 15 A. Most notably a 6.35-mm dia. hollow cathode was operated at an emission current of 6.3 A for approximately 4,000 hours, and a similar cathode (but with a larger orifice diameter) was operated for 900 hours at an emission current of approximately 19 A.<sup>35</sup> In both of these tests, which used xenon gas, the cathodes were tested as part of full-up engine life tests. In other tests, a 12.7-mm dia. hollow cathode was operated on argon for 1,000 hrs at an emission current of 100 A.<sup>29</sup> A more detailed summary of inert gas hollow cathode testing is given by Verhey and MacRae.<sup>37</sup>

There have been no tests of a rare gas hollow cathode, at an emission current required for a 5 kW class xenon ion engine, in which the test duration was a significant fraction of the engine design life time (typically 10,000 hrs<sup>33</sup>). Therefore, the present program was initiated to perform a 5,000 hour test of a 6.35-mm dia. xenon hollow cathode at an emission current of 25 A. The 25 A emission current level was selected to be a more severe test of a cathode similar to that which would be required to operate at an

\*Member of the Technical Staff, Electric Propulsion and Plasma Technology Group; Member AIAA.

"Copyright © 1991 by the American Institute of Aeronautics and Astronautics, Inc. with permission"

emission current of approximately 19 A in the 5 kW engine under development at NASA LeRC.<sup>35</sup> The test duration of 5,000 hours was selected to be half of the engine design life, with the expectation that major design deficiencies may be uncovered in this time span. Ultimately, cathode tests of 10,000 hours or longer will be required.

## Apparatus and Procedure

### The Cathode

The cathode used in this test is shown schematically in Fig. 1. The body of this cathode consists of a 6.35-mm diameter by 57.12-mm long molybdenum tube with a nominal wall thickness of 0.38 mm. This tube is electron beam welded to a 2.54-mm thick molybdenum flange at the upstream end, and a 2 % thoriated tungsten orifice plate (shown in Fig. 2) is electron beam welded to the downstream end. The orifice plate is 1.52 mm thick with a minimum orifice diameter of 1.80 mm. A 56 degree half-angle chamfer is machined into the downstream face of the orifice plate.

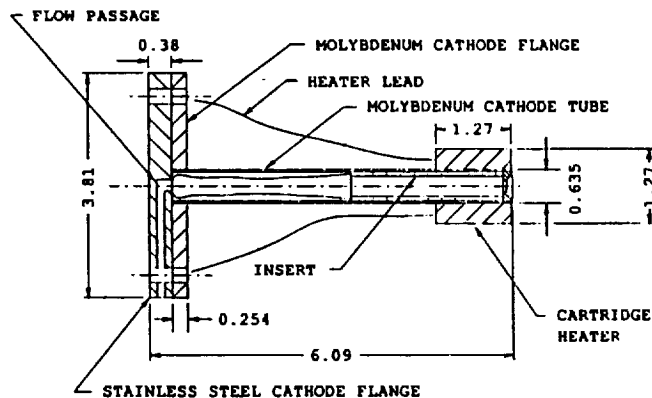


Fig. 1 Life-test cathode schematic (dimensions in centimeters).

A 12.7-mm diameter by 12.7-mm long cartridge heater assembly is used for the cathode tip heater. This heater assembly consists of a molybdenum wire potted in aluminum oxide surrounded by a molybdenum cup. The cartridge heater is friction fitted over the downstream end of the cathode tube. The downstream end of the cartridge heater is positioned approximately 0.25 mm upstream of the end of the cathode. One of the molybdenum heater leads is crimp connected to a copper lead using the crimp portion of a nickel lug. This entire lead assembly is insulated using ceramic beads. The other molybdenum heater lead is connected directly to the stainless steel cathode flange with a stainless steel screw. No radiation

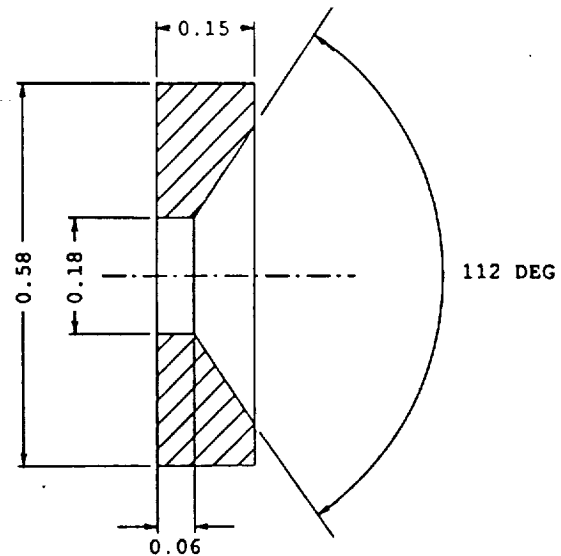


Fig. 2 Cathode orifice plate (dimensions in centimeters).

shielding is used around the heater assembly. It is expected that with good thermal contact between the cathode and the cartridge heater, the downstream face of the heater will act as a radiation fin and facilitate cooling of the cathode at high emission currents.

A 3.2-mm diameter stainless steel tube is welded into the stainless steel cathode flange, and a gas passage is machined into this flange as shown in Fig. 1. A gas tight seal between the stainless steel and molybdenum flanges is provided by a Grafoil gasket and a knife edge machined into the downstream surface of the stainless steel flange. Leak tests using nitrogen indicate that this configuration is leak tight at pressures up to at least  $2.0 \times 10^5$  Pa (15 psig). These leak tests are performed by plugging the cathode orifice with a shaped elastomer and then submerging the entire assembly in water. The internal cathode pressure during operation is on the order of  $2.7 \times 10^3$  Pa (20 torr) so this seal arrangement is leak tight at a pressure two orders of magnitude higher than required. A photograph of the unassembled cathode is given in Fig. 3.

The cathode insert indicated in Fig. 1 consists of an 80 % dense porous tungsten cylinder impregnated with a barium-calcium-aluminate oxide mix with a molar ratio of 4:1:1, and is identical to the inserts used in other recent tests.<sup>20,22</sup> The insert is 25.4-mm long and has a wall thickness of 0.76 mm. A Mo-Re collar is brazed to the upstream end of the insert to provide a transition material from the tungsten insert to the three rhenium leads which are brazed to this collar. The insert is placed into the

cathode tube with the downstream end of the insert touching the upstream face of the orifice plate. The insert leads are clipped so that they extend slightly beyond the upstream surface of the molybdenum cathode flange. The assembly process of tightening the bolts which hold the stainless steel and molybdenum flanges together compresses the insert leads and firmly holds the insert against the orifice plate. The cathode tube was cleaned in acetone and then in alcohol prior to the insertion of the cathode insert. During the assembly of the cathode and installation of the cathode into the vacuum test facility, the insert was exposed to air for a total of 2 hours and 15 minutes.

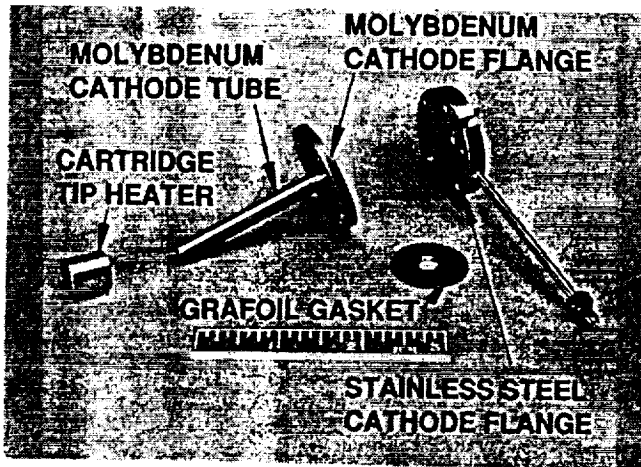


Fig. 3 Life-test cathode components.

### Test Facility

The cathode test facility, which is shown in Fig. 4, consists of a 0.91-m diameter by 2.1-m long stainless steel vacuum tank with two 0.25-m diameter oil diffusion pumps. The cathode is mounted in a J-Series ion engine style cathode pole piece assembly with the baffle and baffle support legs removed. The standard J-Series thruster keeper assembly is used for the starter electrode. The cathode pole piece assembly is bolted to a stainless steel plate which also supports the disk-shaped anode positioned 130 mm downstream of the cathode. A cylindrical, tantalum foil enclosure attached to the stainless steel plate facilitates pressurization of the region between the cathode and the anode, permitting operation at lower cathode flow rates. The anode was fabricated from a SERT II thruster style, flat molybdenum ion extraction grid with tantalum foil spot welded to the side facing away from the cathode, and is radiation cooled.

Two W-5%Re/W-26%Re thermocouples were attached to the downstream face of the cartridge tip heater.

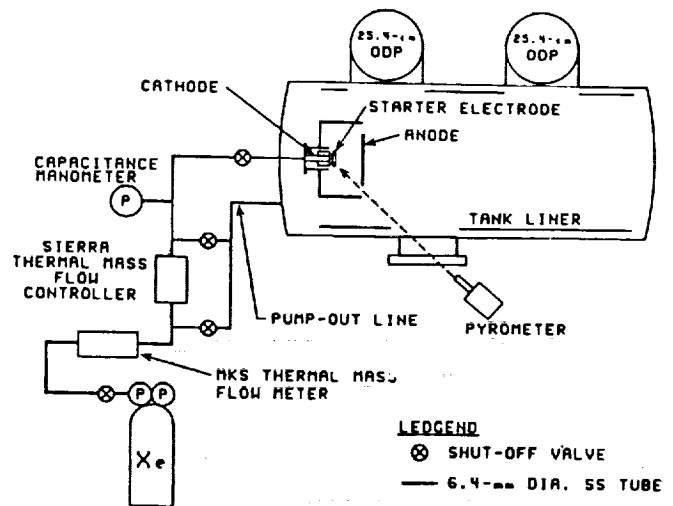


Fig. 4 Cathode life-test facility schematic.

These thermocouples were attached by first spot-welding tantalum foil to the molybdenum heater surface. The thermocouples were then spot-welded to the tantalum. A second layer of tantalum foil was spot-welded over the thermocouples to secure them in place. In addition, a disappearing-filament type optical pyrometer is used to measure the temperature of the cathode as indicated in Fig. 4. The optical pyrometer was calibrated by placing a standard lamp with a 2 % thoriated tungsten filament in the vacuum system at the location of the cathode. The calibration was accomplished by viewing the lamp through the vacuum tank window over the same optical path used in the life test.

The xenon feed system consists of approximately 1.8 m of 6.35-mm diameter stainless steel tubing followed by 15 cm of 1.59-mm diameter stainless steel tubing which terminates at the stainless steel cathode flange. All tubing pieces and fittings were cleaned in acetone and rinsed in alcohol prior to assembly. A new MKS, Inc., 0-20 sccm, thermal mass flow meter is used to measure the xenon flow rate into the cathode. Downstream of this flow meter, a thermal mass flow controller from Sierra Instruments is used to control the xenon flow rate. This arrangement permits measurement of the flow rate independent of the action of the flow controller. It also eliminates possible thermal feed-back effects from the solenoid valve in the flow controller from affecting the flow sensor. Furthermore, this arrangement always results in the same pressure downstream of the MKS flow meter, regardless of the pressure to which the flow controller is exhausting. A capacitance manometer positioned downstream of the flow controller is used to measure the cathode internal pressure.



during operation. The capacitance manometer was calibrated immediately prior to installation in the gas feed system.

A separate pump-out line is included in the feed system to facilitate removal of contaminant gases from the feed lines. This pump-out line is connected into both sides of the flow controller to provide a large diameter path for the gas. Four shut-off valves are included in the feed system to permit isolation of different feed system components. The entire feed system was subjected to two series of leak tests. In the first, the two pump-out line shut-off valves were closed along with the shut-off valve to the cathode. The feed lines were then pressurized to  $2.45 \times 10^5$  Pa (35 psig) and carefully checked for leaks using a soap-like bubble solution. No leaks of xenon gas out of the system were detected. The second set of leak tests was designed to look for air leaks into the feed system for those components which would be operated at pressures less than atmospheric pressure during normal operation. In this case the feed system was pumped out to high vacuum for several days, then all of the shut-off valves were closed and the pressure increase indicated by the capacitance manometer over another period of several days was recorded. From these data a maximum leak rate into the propellant feed system was estimated to be  $2 \times 10^{-7}$  standard  $\text{cm}^3/\text{s}$ .

Both the flow controller and the flow meter were carefully calibrated prior to the initiation of the life test. The new MKS thermal mass flow meter was calibrated at the manufacturer's facility on the east coast of the United States using nitrogen and a secondary calibration standard. The flow meter was then shipped to JPL where it was subsequently taken to the manufacturer's facility on the west coast and recalibrated on both nitrogen and xenon using a primary volumetric calibration standard. Next, the flow meter was calibrated in-house at JPL on nitrogen and xenon using a secondary volumetric calibration standard (i.e. a "bubble" volume calibration kit from the Hastings corporation).

The results of these calibrations are shown in Figs. 5 and 6. The comparison between the calibrations performed with the MKS primary calibration standard and the Hastings calibration kit is given in Fig. 5 for nitrogen. These data indicate that the Hastings calibration kit agrees well with the primary standard calibration. The calibrations with the Hastings kit were performed on two separate days with no difference in the results. In addition, the calibration on nitrogen at the MKS facility indicated that the flow meter's calibration had not changed (within the manufacturer's tolerance of 0.8 % of full scale) as a result of being shipped from the east coast to the west coast.

The data in Fig. 6 indicate the flow meter's response

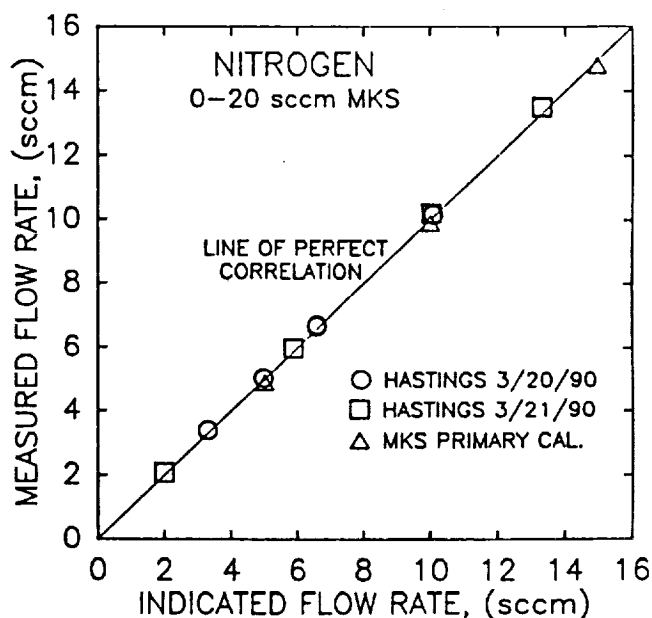


Fig. 5 Comparison of flow meter calibrations using nitrogen.

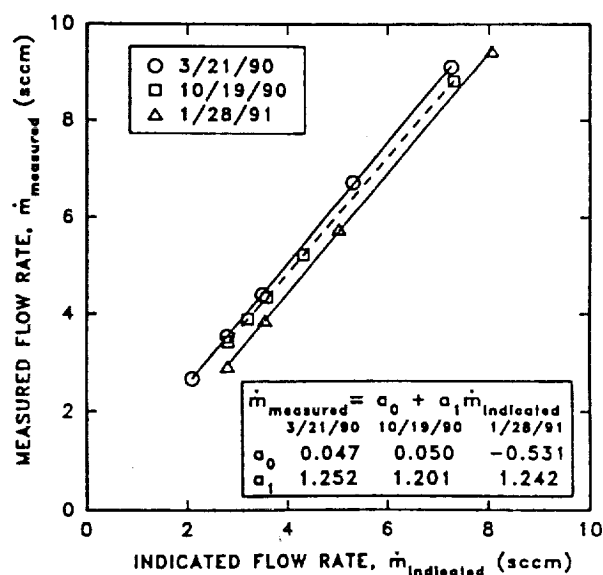


Fig. 6 Flow meter calibrations on xenon over a time period of nine months.

to xenon gas over the range of flow rates of interest for calibrations performed at three different dates. A straight line curve fit to the calibration data taken on 3/21/90

indicates a slope of 1.22 and an intercept of 0.171. The slope of 1.22 differs from the manufacturer's recommended correction factor for xenon of 1.32 by a significant amount. After seven months and more than 4,000 hours of operation, the flow meter was recalibrated. The results of this calibration performed on 10/19/90 indicate a slope of 1.20 and an intercept of 0.029. These calibration data indicate a shift in the flow meter response after seven months of continuous operation that amounts to approximately 5 % of the flow rate. The shift is in the direction that the actual flow rate is 5 % less than the indicated flow rate. A final calibration was performed after an additional three months on 1/28/91. These data indicate a further zero shift, but essentially no change in slope from the original 3/21/90 calibration.

Three power supplies are used to start and run the cathode: a tip heater supply, a starter supply, and the anode supply, all of which are 60 Hz laboratory supplies. The starter supply is actually a parallel combination of two separate supplies. One of which is a high voltage supply capable of 900 V at 100 mA, and the other is a 35 V, 10 A supply with current regulation. Both the tip heater and starter supplies are only used to start the cathode. During normal operation only the current regulated anode supply is used. A calibrated 100 mV, 30 A current shunt is used to measure the discharge current. Voltage sensing leads connected to the anode and cathode inside the vacuum system are used to measure the discharge voltage.

Commercial heater elements were installed on the vacuum tank liner in order to bake the tank liner out at  $>100^{\circ}\text{C}$  for 30 hours prior to the beginning of the test. This bake-out procedure resulted in an ultimate tank pressure of  $9.3 \times 10^{-5}$  Pa ( $7 \times 10^{-7}$  torr) at the start of the test. After 4,000 hours of nearly continuous high vacuum operation the no-flow tank pressure had decreased to approximately  $6.7 \times 10^{-5}$  Pa ( $5 \times 10^{-7}$  torr). A computer data acquisition and control system is used run to the life test and enables long duration, unattended operation.

### Start-Up Procedure

The following procedure is used to condition the insert and start the cathode. The insert conditioning is accomplished by first setting the xenon flow rate to the normal run condition (4.0 sccm). The tip heater current is then set to 4.0 A and the cathode is heated to approximately  $500^{\circ}\text{C}$  (as indicated at the orifice plate) for 3 hours. After 3 hours the heater power is removed and the cathode is allowed to cool for 30 minutes. The cathode heater current is then set to 7.0 A and the cathode is heated to  $>1050^{\circ}\text{C}$  for 1 hour. After 1 hour the cathode is again allowed to cool for 30 minutes after which the tip heater

current is set to 7.5 A to heat the cathode to  $>1100^{\circ}\text{C}$ . The cathode is heated under these conditions for 30 minutes before attempting to initiate the discharge.

## Results

### Operational Data

A summary of the cathode life test operating history is given in Table 1. The first five shutdowns indicated in this table were ultimately traced to a faulty anode power supply. The faulty power supply was an SCR regulated Sorenson supply which resulted in rather noisy operation of the cathode, as indicated in Figs. 7 and 8. Current oscillations, as indicated in Fig. 7, were typically  $\pm 2.0$  and  $-3.5$  A around a nominal value of 25.1 A, with a frequency of approximately 80 kHz. The corresponding voltage oscillations are shown in Fig. 8 where the average voltage is 19 V with spikes to greater than 65 V. These data were taken with a xenon flow rate of 4.0 sccm. After 123 hours of operation, the faulty Sorenson power supply was replaced with a transistor regulated Hewlett-Packard supply.

Operation on the Hewlett-Packard power supply was significantly less noisy than with the Sorenson supply, as indicated in Figs. 9 and 10. This figure shows a discharge current oscillation of  $\pm 0.75$  A with a frequency of 5 kHz. A higher frequency oscillation (approximately 100 kHz) superimposed on this 5 kHz oscillation is also evident from this oscilloscope trace. Discharge voltage spikes, with occasional peaks to  $+30$  V, were also detected at this frequency. The switch from the Sorenson to the Hewlett-Packard power supply also resulted in a decrease in orifice plate temperature of approximately  $50^{\circ}\text{C}$ .

With the exception of the first 123 hours, the entire test was conducted with the Hewlett-Packard supply, and the discharge current oscillations shown in Fig. 9 remained unchanged until approximately 4,000 hours of operation. At this time a low frequency oscillation (330 Hz) appeared. The magnitude of this oscillation was  $\pm 4$  A for the current and  $\pm 2$  V for the discharge voltage as indicated in Figs. 11 and 12. The very high frequency (100 kHz) oscillations were still present at this time, but the 5 kHz oscillations had disappeared. By increasing the xenon flow rate from 4.0 sccm to 5.0 sccm the low frequency oscillations were eliminated. Operation at the higher flow rate, however, resulted in an anode voltage of only 12 V. By run hour 4,700 the cathode could again be operated at an indicated flow rate of 4.0 sccm without the appearance of the 330 Hz oscillations. At the end of the test (after 5,024 hours of operation) there appeared to be very little noise in either the discharge current or voltage as indicated in Figs. 13 and 14.

ORIGINAL PAGE IS  
OF POOR QUALITY

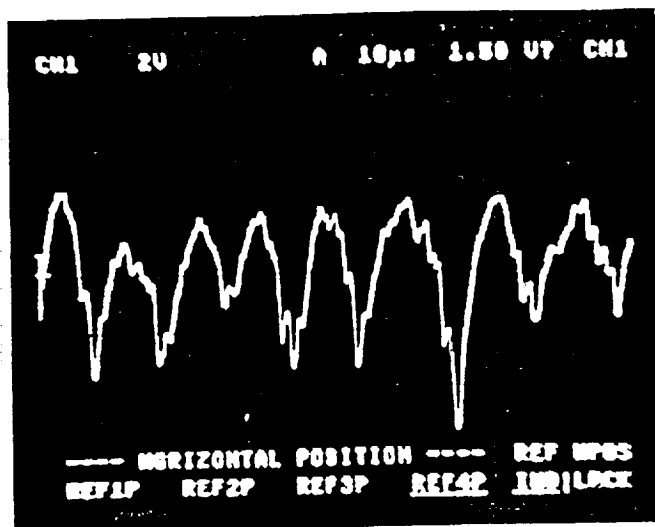


Fig. 7 Discharge current oscillations with Sorenson anode power supply; 2 A per major division.

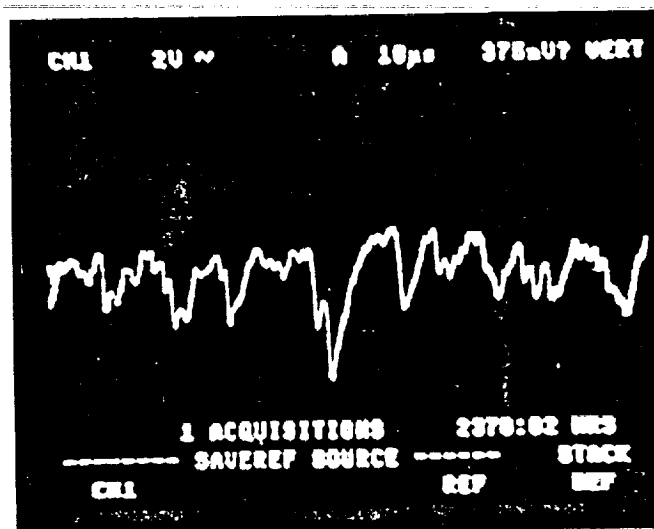


Fig. 9 Discharge current oscillations with Hewlett-Packard anode power supply; 2 A per major division.

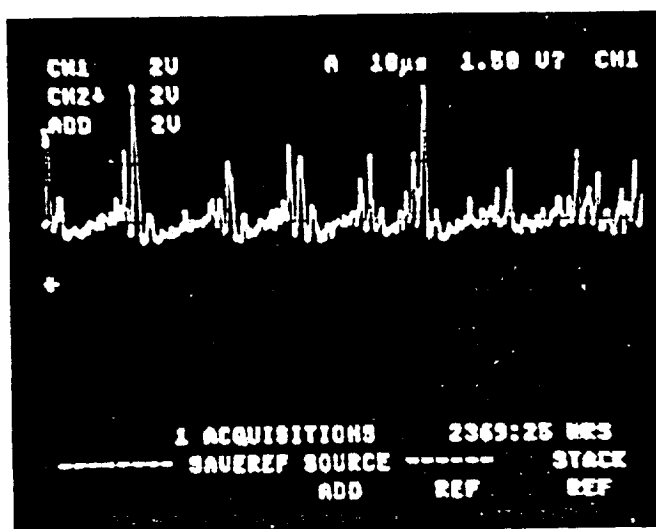


Fig. 8 Discharge voltage oscillations with Sorenson anode power supply; 20 V per major division.

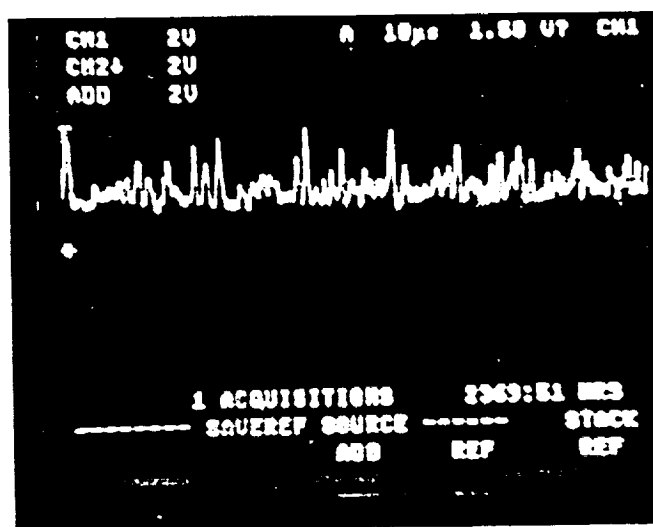


Fig. 10 Discharge voltage oscillations with Hewlett-Packard anode power supply; 20 V per major division.

Shutdown number 7 resulted from a nearby lightning strike which momentarily removed power from the diffusion pump high vacuum valves, causing them to close. The computer detected the resulting increase in tank pressure and shut down the cathode. Shutdown number 9 occurred when both the primary and the backup printers failed and the computer responded by turning off the cathode. Shutdowns 8, 10 and 11 resulted from failures in the data acquisition hardware, which, when detected by the computer, caused the computer to shut down the test. A software change to increase the tolerance to data acquisition system errors eliminated these shutdowns.

Of the 20 shutdowns which occurred in the course of the 5,000 hour test, 11 occurred in the first 750 hours. Shutdown number 12 occurred as a result of a broken belt in one of the two mechanical pumps backing the diffusion pumps. Shutdown number 13 resulted from another lightning strike which again momentarily removed power from the laboratory. The 14th shutdown was a result of operator error. This error occurred near the depletion of the 1000 liter bottle of xenon used in the test. The high pressure side of the regulator indicated zero pressure, but the low pressure side still indicated  $2.5 \times 10^5$  Pa (35 psig). In an attempt to determine the remaining bottle pressure,

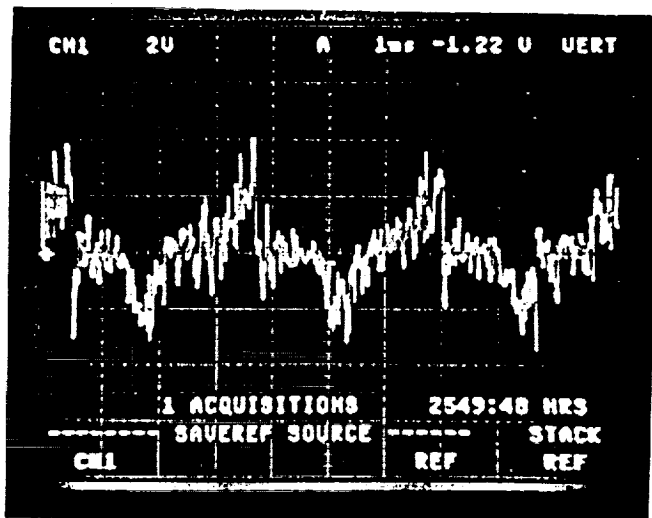


Fig. 11 Low frequency (330 Hz) discharge current oscillations; 2 A per major division.

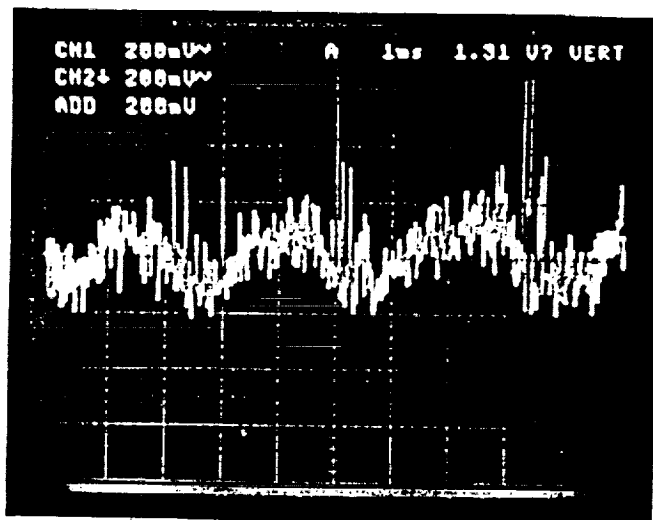


Fig. 12 Low frequency (330 Hz) discharge voltage oscillations; 2 V per major division.

the regulated pressure setting was increased until it reached the supply pressure. The flow controller, however, could not respond adequately to the change in upstream pressure, resulting in a momentary decrease in the flow rate to the cathode. This decrease in flow rate resulted in a discharge voltage which exceeded the maximum allowable voltage level set in the computer, causing the computer to shut down the cathode.

The 15th, 17th and 19th shutdowns were manual

shutdowns required to change xenon bottles. Shutdown number 16 was caused by failure of the Sierra thermal mass flow controller. The flow controller failure was such that it slowly decreased the xenon flow rate over a period of several hours. As the flow rate decreased, the discharge voltage increased. When the discharge voltage exceeded the maximum allowable voltage level, the computer shut down the cathode. Finally, shutdown number 18 was the result of a windstorm which knocked out the laboratory facility power.

Also evident in the data in Table 1 are the conditions required to restart the cathode following a shutdown. The first 11 times the cathode was restarted, covering a period of 743 hours of operation, the cathode started very easily, and with relatively low voltages applied to the starter electrodes. All of these restarts were performed with the normal 4.0 sccm xenon flow rate through the cathode. No conditioning procedure was used prior to these restarts since the cathode was maintained at high vacuum with continuous xenon flow throughout each shutdown. The lightning strikes which caused shutdowns 7 and 13 occurred during normal working hours and high vacuum operation was restored within minutes. The 12th restart required the application of 900 V to the starter electrode to ignite the cathode.

Clearly evident in these data is the trend toward increasing restart difficulty with operating time. The only exception is restart number 14, which required 300 V applied to the keeper. This restart, however, was accomplished within minutes of the cathode shutdown, and the cathode did not cool off significantly before the restart. All other restarts were performed beginning with a cold (i.e. room temperature) cathode. The last five cathode restarts required a 200 torr gas pulse to force the transition from the low current high voltage glow discharge mode to the high current arc mode. In this case, the application of 900 V to the keeper electrode resulted in a 900 V, 10 mA glow discharge which would not transition to the arc mode. To force this transition, the starter supply was turned off and the shut-off valve leading to the cathode was closed until the pressure indicated by the capacitance manometer indicated 200 torr. At this time the shut-off valve was opened rapidly and the starter supply was turned on to 900 V. This procedure caused the immediate establishment of a 2.0 A arc discharge to the starter electrode which was then easily transferred to the anode electrode. It should be noted that the cathode tip heater used in the life test did not cover the full axial length of the insert. It is not known what effect, if any, this heater configuration may have had on the observed increase in start-up difficulty over the course of the test. A longer heater element, however, would probably be capable of heating the upstream end of

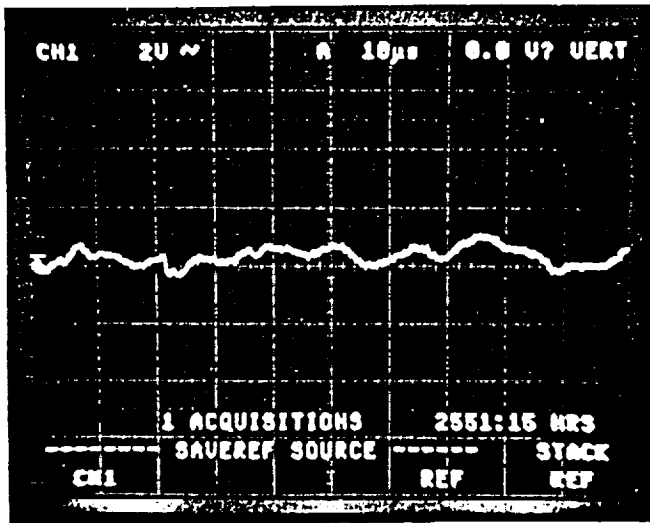


Fig. 13 Discharge current oscillations at the end of the life-test; 2 A per major division.

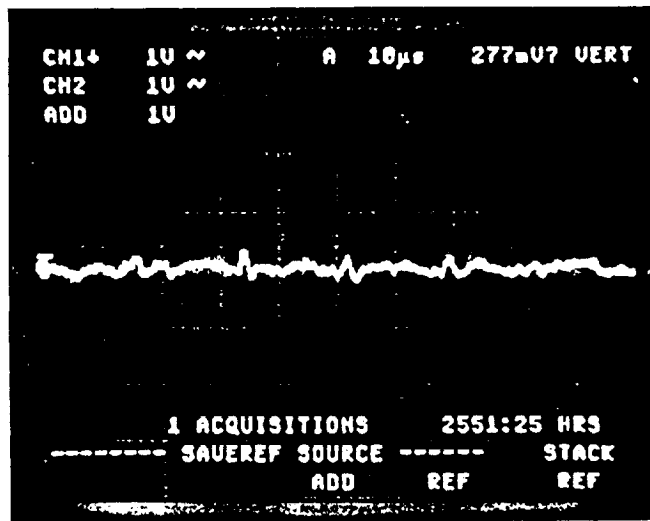


Fig. 14 Discharge voltage oscillations at the end of the life-test; 10 V per major division.

the cathode to temperatures greater than was possible with the present configuration, perhaps facilitating cathode start-up due to the liberation of free barium from the upstream end of the cathode even after the cathode has been run for extended periods of time.

A photograph of the cathode in operation is given in Fig. 15 and shows a close-up of the cathode orifice plate. This photograph was taken after 4,046 hours of operation and indicates the view of the cathode which the test

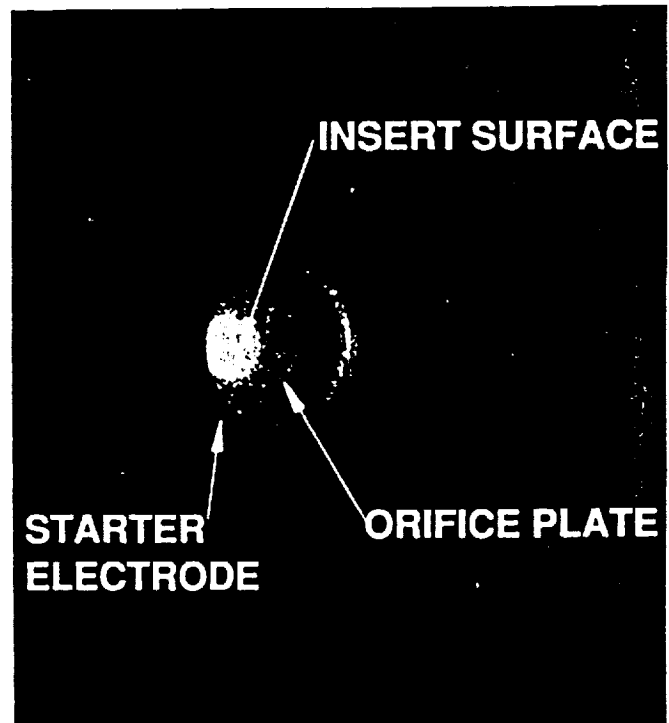


Fig. 15 Close-up of cathode orifice plate during operation at run-hour 4,046.

operator sees through the optical pyrometer. The orifice plate is clearly visible through the aperture in the starter electrode. Orifice plate temperatures are normally taken at a radial location corresponding to the midpoint of the visible portion of the orifice plate. Temperature measurements indicate a significant radial temperature gradient along the orifice plate. The optical pyrometer was also used to measure the temperature of the insert itself. The emitting surface of the insert can be clearly seen through the cathode orifice as indicated in this photograph. Furthermore, the insert surface appears considerably brighter than the orifice plate. This photograph also indicates that after 4,046 hours of operation, the starter electrode does not appear to be significantly eroded, and no material deposits on the interior diameter of the cathode orifice are evident.

The variation in the orifice plate temperature as measured by the optical pyrometer is given in Fig. 16 as a function of cathode run time. The decrease in orifice plate temperature resulting from the change in power supplies at run hour 123 is clearly evident in this figure. Also evident is that subsequent to the change in anode power supplies, the orifice plate temperature remained essentially constant at approximately 1125°C until run hour 1,000. From 1,000

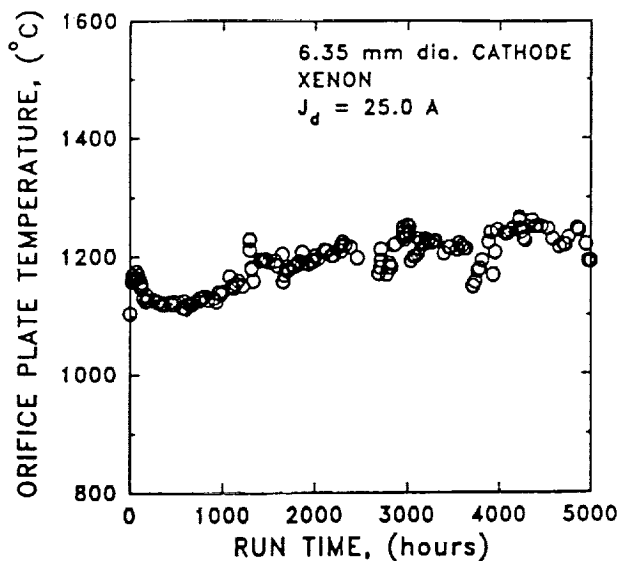


Fig. 16 Variation in orifice plate temperature over the life-test as measured by the optical pyrometer.

hours to approximately 3,000 hours the orifice plate exhibits a gradual increase in temperature with a slope of 29 °C/chr. These data indicate an occasional significant decrease in orifice plate temperature. These decreases are accompanied by decreases in the temperatures of the cathode flange and cathode support plate as indicated by thermocouples located there, as well as by changes in the discharge voltage. The orifice plate temperature was approximately constant over the last 1,000 hours of the test.

Beginning after run hour 2950, measurements of the insert brightness temperature were made using the optical pyrometer looking at the insert surface through the cathode orifice. Comparison of the insert and orifice plate brightness temperatures are given in Fig. 17 covering the time period from 3,000 to 5,000 hours of cathode operation. The insert and orifice plate temperatures appear to be relatively well correlated, indicating that the insert temperature measurement is real. The unexpected feature of these data, however, is the magnitude of the insert brightness temperature. Models of the insert barium depletion rate (as discussed in a subsequent section) predict a very short life time for insert operation at the temperatures indicated in this figure.

The anode current and voltage over this same time period are given in Fig. 18. The anode power supply is operated in the current regulating mode so that a constant 25 A anode current is maintained. The exception to this are the two periods of unstable cathode operation occurring

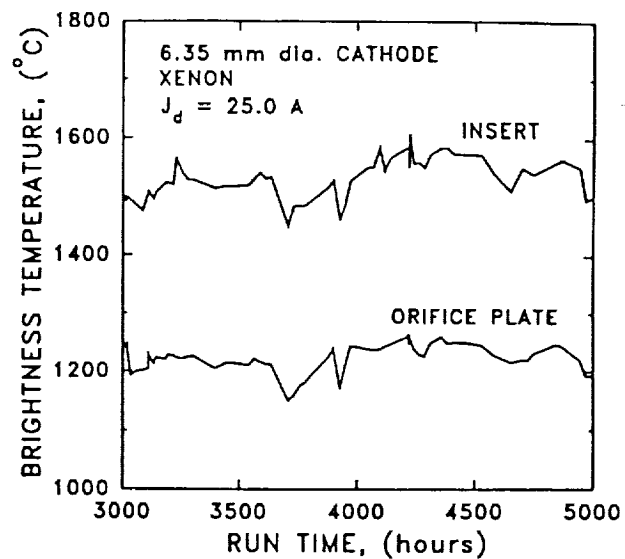


Fig. 17 Brightness temperature of the downstream end of the insert as measured by the optical pyrometer.

around 4,000 hours and 4,500 hours, respectively. The large spikes in the anode current correspond to cathode restarts in which the cathode was operated at less than 25 A for a short time. On the compressed time scale of Fig. 18 these short time intervals appear as spikes. At the beginning of the life test the discharge voltage was between 19 and 21 volts. After approximately 900 hrs the discharge voltage dropped to 18 V and remained there for 500 hrs. At roughly run hour 1400 the discharge voltage decreased to between 15 and 16 volts. This discharge voltage level was maintained for the next 1400 hrs, after which the discharge voltage began a gradual increase back to around 18 V. The discharge voltage spike at run hour 3069 corresponds to the flow controller failure. The other spikes correspond to cathode shutdown/restart events.

The xenon flow rate, as measured by the MKS thermal mass flow meter, and the interior cathode pressure are given in Figs. 19 and 20, respectively. Again, the spikes in the data represent short duration operation at other flow rate settings. The cathode pressure data indicate a slight, gradual increase in the interior pressure. The temperature of the stainless steel cathode flange as a function of run time is given in Fig. 21. In general, the cathode flange temperature also shows a gradual increase with time.

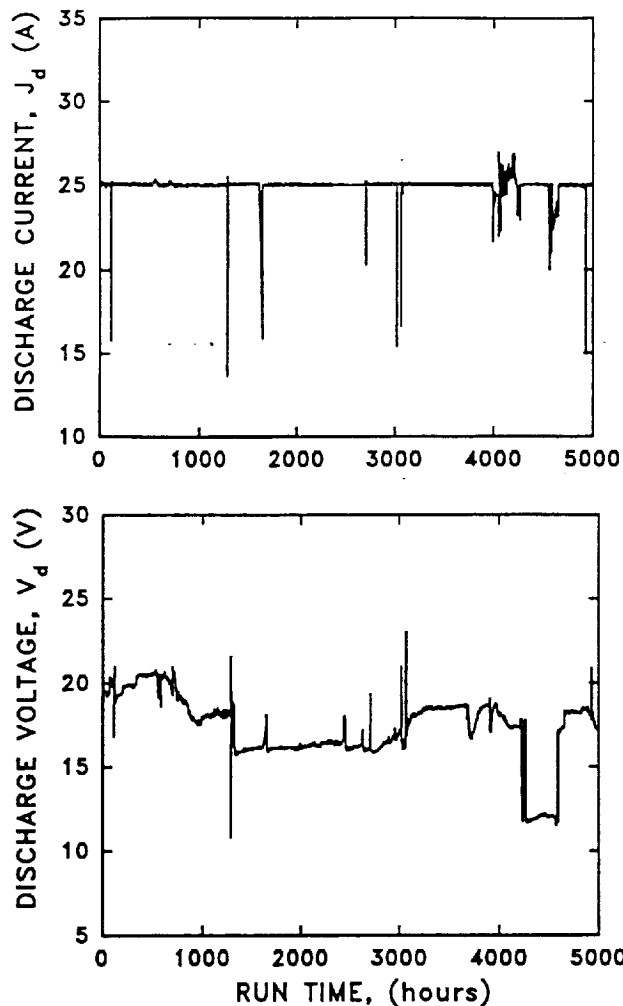


Fig. 18 Anode current and voltage during the life-test.  
Post-Test Analyses

The most surprising result from the life test was the appearance of a substantial amount of sputter-deposited material which had flaked-off from the walls of the discharge enclosure and collected at the bottom of the enclosure as indicated in Fig. 22. EDAX analyses of this debris indicated that most of the flakes were comprised primarily of tantalum (80%) and molybdenum (20%). Both the cylindrical discharge enclosure and the cathode pole piece were lined with tantalum foil. The anode and the starter electrode were molybdenum. The anode was also backed by a tantalum foil liner. Therefore, since most of the materials exposed to the cathode discharge plasma were tantalum and molybdenum, it is not surprising that the EDAX analyses indicated the flakes were comprised of these materials. What is surprising is that there was any significant sputtering at all. Published<sup>38</sup> values for the

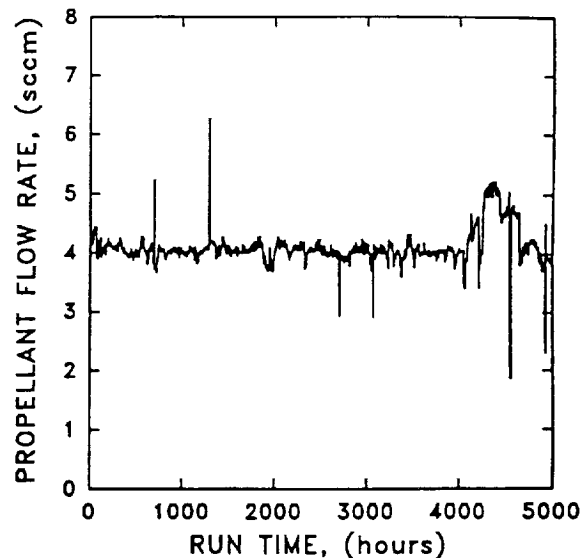


Fig. 19 Measured xenon flow rate during the life-test.

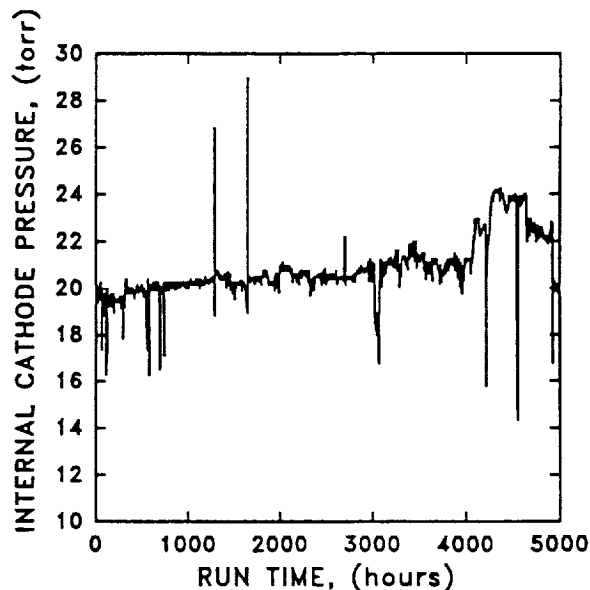


Fig. 20 Interior cathode pressure during the life-test.

sputtering thresholds of tantalum (30 V) and molybdenum (27 V) by xenon ions are significantly greater than the discharge voltage level (15 to 20 V) during the test, suggesting that there should have been little or no sputtering of these materials. The appearance of flaked-off sputter-deposited material at the bottom of the discharge enclosure was first noticed after only 500 hours of cathode operation.

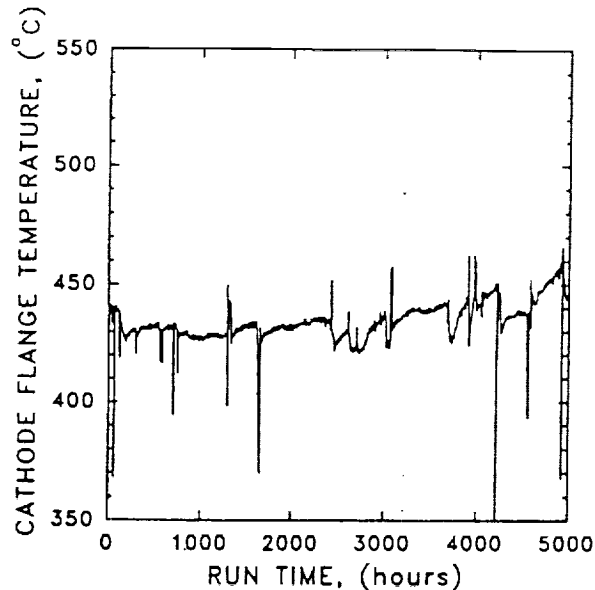


Fig. 21 Temperature of the stainless steel cathode flange during the life-test.

Even more significantly, sputter-deposited material peeled from the outer regions of the anode exhibited a surface covered with cone formations as shown in Fig. 23. The formation of such cones can occur if the surface is being sputtered by ions from the plasma while simultaneously material sputtered from another location is deposited on the surface.<sup>39</sup> This implies that there must be ions in the plasma which are energetic enough to sputter materials which are at anode potential. Energetic ions are known to be produced by operation of hollow cathodes at emission currents greater than 20 A<sup>34</sup> in what is generally referred to as the cathode jet phenomena.<sup>29</sup> The results from the present test lend additional experimental support for the existence of this cathode jet, but do not shed any additional light on the mechanism responsible for its formation.

A close-up photograph of the cathode and starter electrode at the end of the 5,000 hour test is shown in Fig. 24. The two tungsten/rhenium thermocouples which were originally attached to the downstream face of the cartridge tip heater are also visible. These thermocouples both failed approximately 500 hours into the test. The downstream (visible) surface of the molybdenum starter electrode appears to have been recrystallized.

There were no material deposits in the cathode orifice at the end of the test. This is significantly different from observations made both in-house and elsewhere<sup>35</sup> that cathodes tested as part of a complete engine exhibit significant deposits of tungsten around the ID of the cathode orifice. Such deposits have been observed for

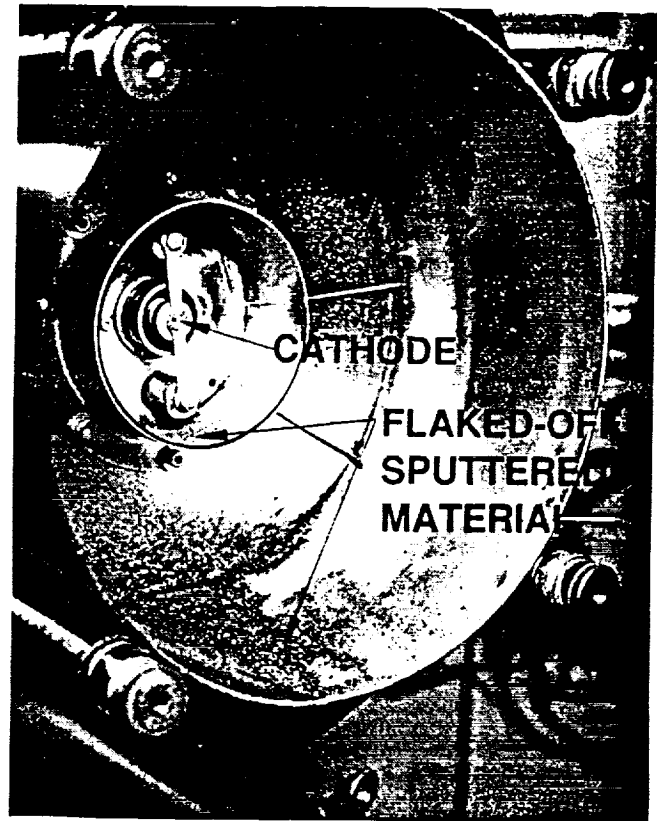


Fig. 22 Post-test condition of the discharge enclosure showing a substantial amount of sputter-deposited material.

cathodes operating in both ring-cusp and divergent-field engine configurations. The explanation for the observed difference in orifice deposits between the present cathode life test and those cathodes tested in complete engines is not apparent. However, this difference does underscore the fact that long duration tests of cathodes by themselves, although important, cannot guarantee adequate cathode life in the engine itself. This can only be accomplished by performing complete engine life-tests.

**Starter Electrode:** A photograph of the starter electrode at the end of the test is given in Fig. 25. At the start of the test this electrode had a uniform thickness of 1.52 mm. It is clear from Fig. 25 that the starter electrode has been eroded from the downstream side, presumably by sputtering. The starter electrode potential was typically 1 or 2 volts above cathode potential throughout the test. Near the center of the electrode it appears that the original thickness has been reduced by a factor of two by the end of the test. This corresponds to an erosion rate on the





Fig. 23 SEM photograph of sputter-deposited material removed from the anode showing the formation of cone-like surface features.

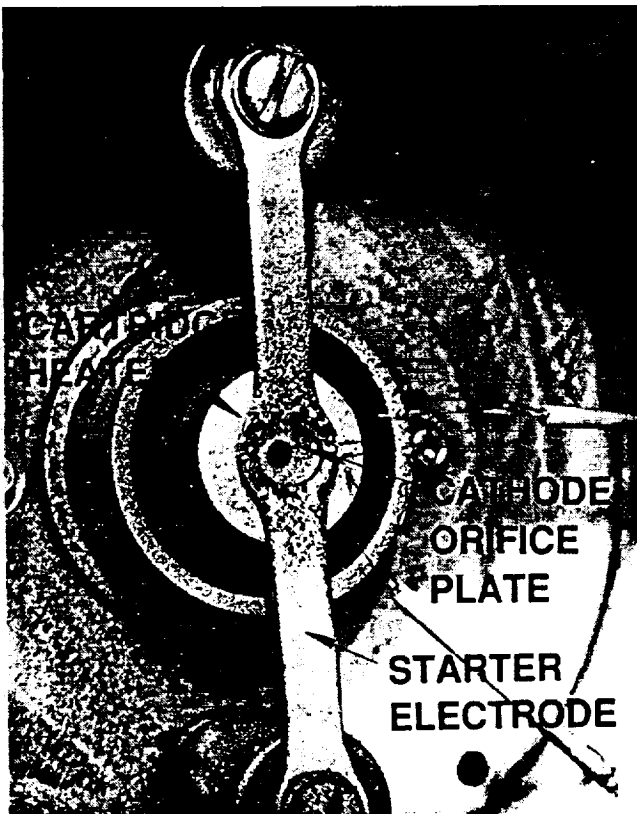


Fig. 24 Post-test condition of the cathode and starter electrode.

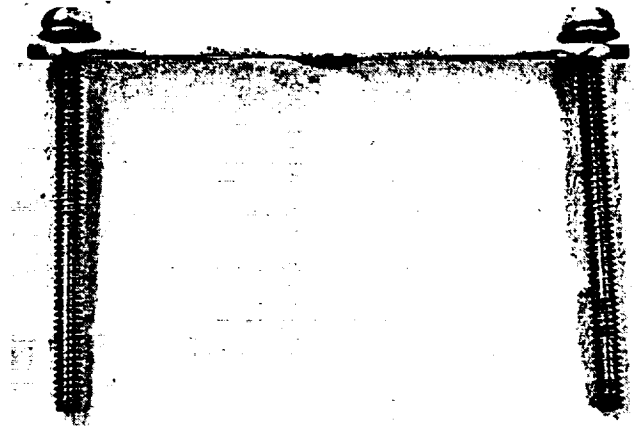


Fig. 25 Edge view of the starter electrode at the end of the life-test.

order of 1500 angstroms/hr, which is substantially greater than that of most other ion engine discharge chamber components.<sup>40</sup> Erosion rates of this magnitude have only been observed at one other location in the discharge chamber of divergent-field thrusters, and that is at the upstream side of the baffle which separates the cathode from the main discharge chamber.<sup>40</sup> It is likely that the same mechanism which causes the high baffle erosion rates in the divergent-field thruster is also responsible for the high erosion rate of the starter electrode observed in this test, as well as the high starter electrode erosion rate observed by Patterson and Verhey.<sup>35</sup>

**Cathode Orifice Plate:** SEM photographs of the cathode orifice plate before and after the 5,000 hour test are shown in Fig. 26. The initial orifice diameter was 1.80 mm (0.071"). At the end of the test the orifice diameter, as determined from the SEM photograph, was 2.08 mm (0.082"). This corresponds to a ratio of emission current to orifice diameter at the end of the test of 12.0 A/mm, which is exactly the criteria specified by Kaufman<sup>41</sup> for acceptable cathode tip life-time.

SEM photographs of the orifice plate-to-cathode tube electron-beam welds before and after the test are shown in Fig. 27. After 5,000 hours the weld has a "shingled" appearance, and it is not known if the weld is still leak tight. No leak tests were attempted at the end of the test in order to not compromise the post test condition of the insert.

A high magnification SEM photograph of the surface of the tungsten orifice plate is shown in Fig. 28. The most interesting feature in this figure is the abundance of voids in the surface with sizes ranging from roughly 1 to 10 microns. It has been suggested that these voids represent

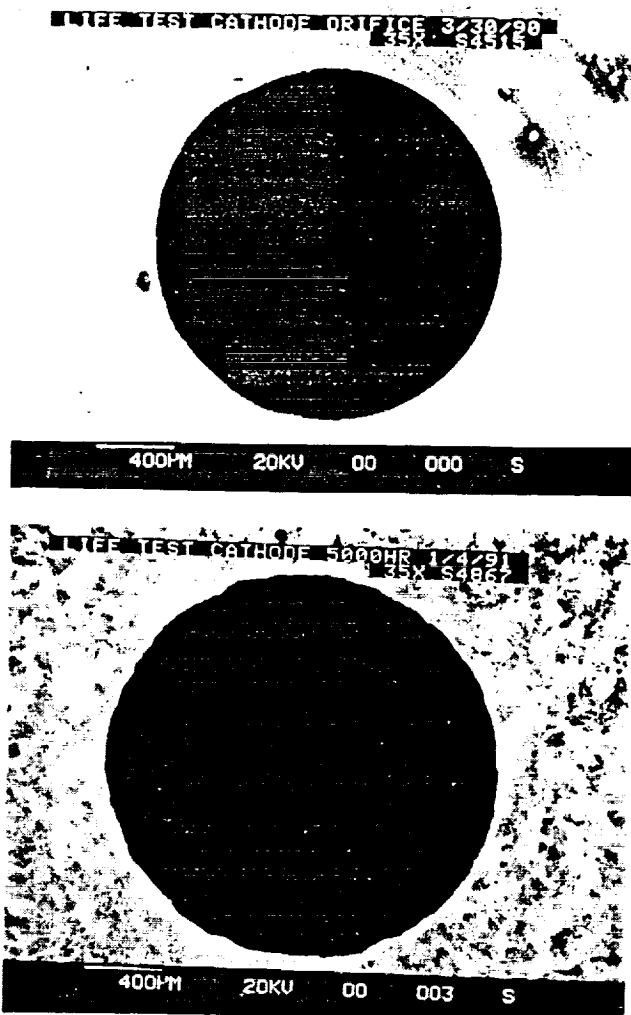


Fig. 26 SEM photograph of the cathode orifice before (top) and after (bottom) the life-test.

the locations where the thorium from the original 2 % thoriated tungsten material had accumulated and subsequently evaporated.

**Cathode Insert:** The cathode and cartridge tip heater assembly was cut in half lengthwise using a silicon-carbide cutting tool with no lubrication. The resulting cut width was approximately 0.74 mm. The two halves of the cathode are shown in Fig. 29. Most notable in this photograph are the material deposits located approximately 3 to 6 mm upstream of the orifice plate. EDAX analyses of this material indicate that it is essentially pure tungsten. There are no obvious locations on the insert from which this tungsten could have originated, never-the-less the insert itself is still believed to be the source of the tungsten.

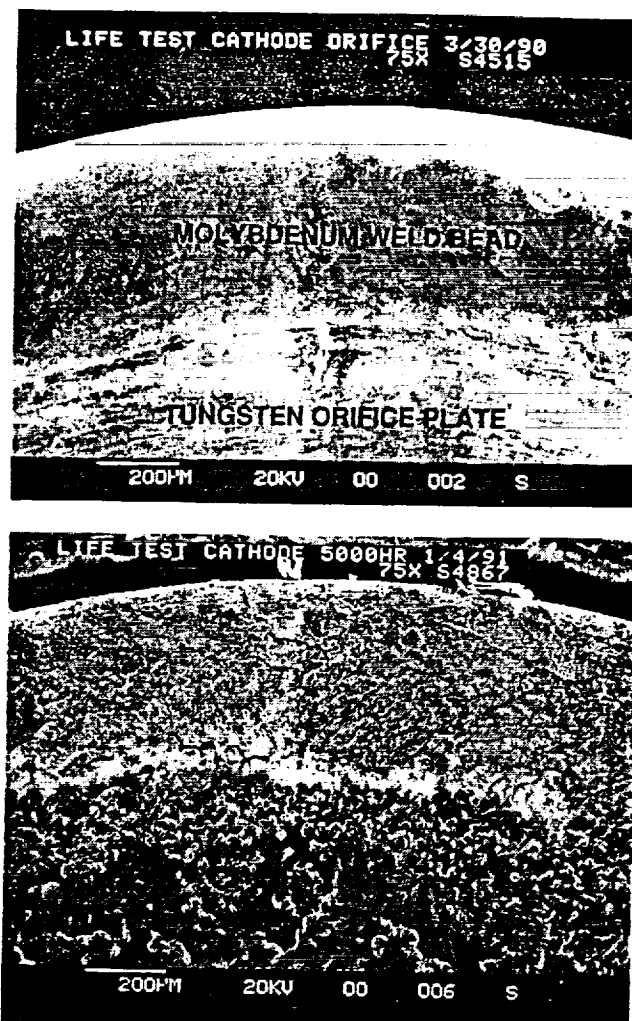


Fig. 27 SEM photographs of the orifice plate-to-cathode tube weld before (top) and after (bottom) the life-test.

There are actually two different deposit sites, one covering the region approximately 3 to 4 mm upstream of the orifice plate and the other from 4 to 6 mm upstream. The material deposited in the 4 to 6 mm region is very fragile and is easily separated from the rest of the insert. The material deposited over the 3 to 4 mm region is firmly attached to the insert, has a surface appearance similar to the first 3 mm of the insert, and is noticeably shinier than the rest of the insert surface. The maximum thickness of the deposit was estimated to be approximately  $0.7 \pm 0.2$  mm. The deposit appears to be axisymmetric, resulting in a reduction in the interior diameter of the insert at this location. The original ID of the insert was 3.81 mm (0.150"). Using the approximate deposit thickness the minimum ID of the insert was calculated to be 2.41 mm (0.095") at the location of the deposits. This represents a 60 % reduction in cross-sectional area, however, this area

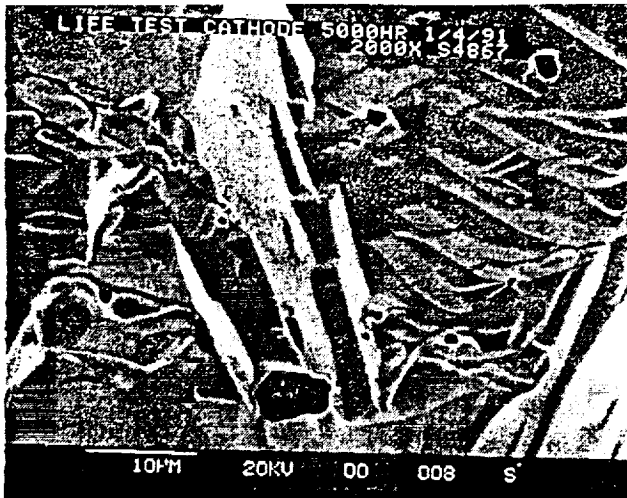


Fig. 28 SEM photograph (2000X) of the cathode orifice plate after the life-test showing numerous surface voids.

is still 34 % greater than the area of the orifice at the end of the test.

The ID of the molybdenum cathode tube which was not covered by the insert was covered by a brown film. EDAX analyses of this film indicated it to be a very thin layer of molybdenum oxide. The thinness of the layer suggests that the source of oxygen was not from a leak in the flow system, but may have been from the insert's oxide impregnant.<sup>42</sup>

X-ray diffraction analyses were performed on the insert as a function of axial position along the insert. To accomplish this one half of the insert was cut into six half-disk shaped slices (again using a silicon carbide cutting tool with no lubrication). The slice thicknesses are shown in Fig. 30. Each of these slices was ground-up into a power using titanium-carbide tooling prior to performing the x-ray diffraction analysis. This procedure was necessary in order to obtain quantitative information regarding the relative amounts of the chemical compounds in the insert. The x-ray diffraction analyses were performed in air.

The procedure of cutting the insert into slices also freed the insert from the molybdenum cathode tube, leaving behind a residue on the tube ID. A summary of the EDAX analyses of this residue is given in Table 2. At the downstream end of the tube, the residue between the insert and the molybdenum tube consists largely of tungsten, barium and oxygen, most likely in the form of  $BaWO_4$ . (The distribution by weight for  $BaWO_4$  would be 48%, 35% and 16% for W, Ba and O, respectively.) Trace

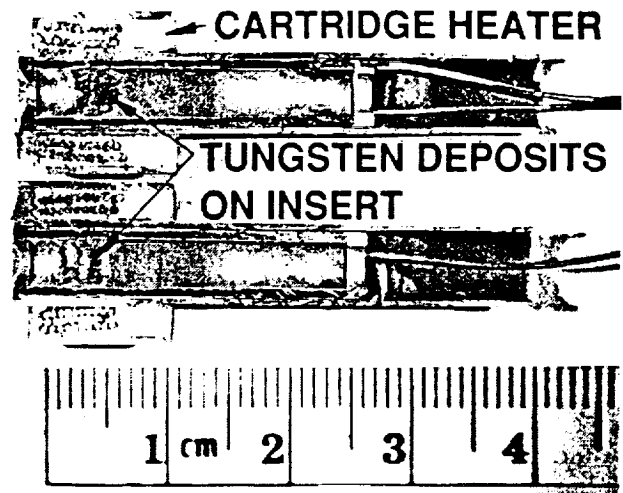
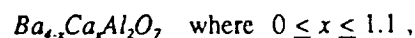


Fig. 29 Life-test cathode cut in half axially showing deposits on the insert.

amounts of calcium and aluminum are also present. The residue under the upstream end of the insert consists primarily of rhenium. The only sources of rhenium in the cathode are the pig-tail leads brazed to the upstream end of the insert.

The results from the x-ray diffraction analyses of the ground-up insert slices is given in Table 3 and plotted in Fig. 31. These data indicate the relative percentages of all materials in the insert except tungsten: the insert is typically 80% tungsten, and this constituent of the insert has been ignored in the data in Table 3. The diffraction analyses indicate the presence of only four compounds in the insert. No trace of  $BaO$  was found, even though the cathode was operating normally when the test was voluntarily terminated. This evidently is not an unexpected result.<sup>43</sup>

A new, unused insert, identical to the one used in the 5,000 hr test was cut into slices and analyzed according to the same procedures used for the life-test insert. X-ray diffraction analyses of this new insert revealed small quantities of  $BaO$  and  $CaO$ . No aluminum oxide compounds were identified. This again is the expected result.<sup>43</sup> The original impregnant is actually a complex barium calcium aluminate compound of the form



and the x-ray diffraction patterns, which change as a function of  $x$  are not generally available.<sup>43</sup> The diffraction analyses revealed diffraction patterns which could not be

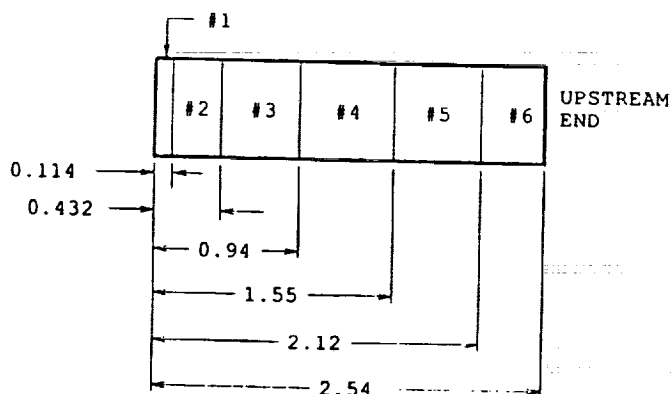


Fig. 30 Insert slices for x-ray diffraction analyses.

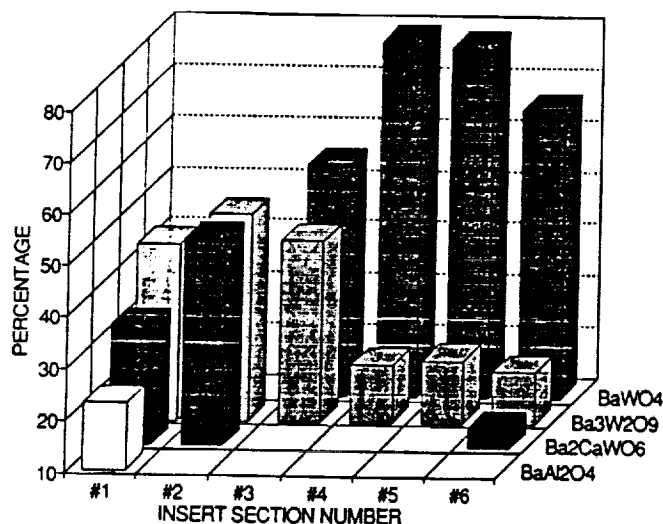


Fig. 31 Results of x-ray diffraction analyses on the insert slices (ignoring pure tungsten).

identified, but which may correspond to the  $Ba_{4-x}Ca_xAl_2O_7$  compounds. These patterns did not correspond to the known diffraction patterns of  $Ba_3CaAl_2O_{12}$  and  $BaCa_2Al_2O_{15}$ . These unidentified patterns were not present in the life-test insert x-ray diffraction analyses.

#### Discussion of Cathode Insert Life

A cathode life time model, developed in Ref. 23, gives the fraction of barium lost from the insert as a function of insert temperature and operating time according to the equation

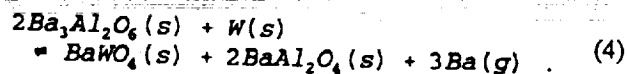
$$\frac{q}{q_0} = B e^{-a/\tau} t^{1/2} \quad (1)$$

where  $a$  and  $B$  are constants with the values<sup>23</sup>

$$a = 1.61 \times 10^4 \text{ [K]} \quad (2)$$

$$B = 400 \text{ [hr}^{-1/2}\text{]} \quad (3)$$

In general the chemical reaction for the production of barium on a hot tungsten surface is given by<sup>10</sup>



If this is the only reaction producing free barium, then only half of the initial barium can be used. The other half becomes locked-up in  $BaWO_4$  and  $BaAl_2O_4$ . However, because of other possible reactions, inserts made of impregnated porous tungsten may be capable of dispensing between 1/3 and 2/3 of the total impregnated barium.<sup>10</sup> Thus, the most optimistic life time prediction would be obtained from Eq. (1) by assuming that 2/3 of the initial barium is available to lower the surface work function.

Assuming that the insert is at the brightness temperature of 1500 °C, as indicated in Fig. 17, and assuming that this temperature controls the insert life, then Eq. (1) predicts an insert life of only 321 hours to deplete 2/3 of the total barium ( $q/q_0 = 0.67$ ). However, the cathode was successfully operated for 5,000 hours. Equation (1) implicitly assumes that all of the barium that is evaporated from the surface is immediately lost from the cathode. However, as stated in Ref. 10, if the barium can be prevented from permanently condensing on non-emitting cathode surfaces, then a greatly increased insert life should result. This can be accomplished if these other cathode surfaces are maintained at or above 300 °C, and preferably above 400 °C.<sup>25</sup> In the present life test cathode, the temperature of the stainless steel flange at the back of the cathode is typically 430 °C or greater, as indicated in Fig. 21, suggesting that the cathode life could be considerably greater than that predicted by Eq. (1). In this case, the barium that is evaporated from the insert may migrate to other cathode surfaces, but the temperature of these surfaces is such that the barium is prevented from condensing. Eventually, the barium may return to the insert surface. Under these circumstances, barium is lost from the cathode only through the cathode orifice.

It is unlikely, however, that this non-condensing feature of the life test cathode is sufficient to account for the difference in predicted and demonstrated cathode life times by itself. Other possibilities include:

1. A strong axial temperature gradient along the 25.4

mm insert length, resulting in an average insert life which is considerably greater than that determined by the temperature at the downstream end.

2. Barium reaction and evaporation rates at high temperatures that are significantly different than those represented by the constants in Eqs. (2) and (3). The life time predictions from Eq. (1) are very sensitive to the value of the constant which appears in the exponential function.
3. Chemical reactions other than that described by Eq. (4) which take place at high temperatures to produce a low work function coating on the insert.

Each of these possibilities will probably contribute to the final explanation of the cathode life-time demonstrated in the present test. However, the third possibility is the most interesting and possibly the most significant.

The normal operating temperature range for cathodes impregnated with a 4:1:1 molar ratio of barium calcium aluminate is 1,000 to 1,100 °C. Long duration operation at temperatures greater than 1,100 °C will result in complete conversion of the barium calcium aluminate into other compounds, such as those on the right-hand-side of Eq. (4). The higher the insert temperature, the more rapid is this conversion.

At temperatures of at or above 1,500 °C, however, other chemical reactions become possible.<sup>43</sup> At these temperatures either  $BaAl_2O_4$  or  $Ba_2CaWO_6$  may react to liberate free Ba, but the details of this chemistry are not well understood.<sup>43</sup> The melting temperature for  $BaAl_2O_4$  is approximately 2170 °C, which is significantly above the 1500 °C melting temperature for the barium calcium aluminate impregnant. This leads to the possibility of impregnated cathodes which can operate for long periods of time at temperatures significantly above 1,100 °C. This possibility is significant not only for the development of high-current hollow cathodes for ion engines, but also as a foundation from which long-lived magnetoplasmadynamic (MPD) thruster and arcjet cathodes may be developed. Clearly there is a need for increased understanding of impregnated, hollow cathode operation at high temperatures.

### Conclusions

A program was initiated to test a 6.35-mm diameter hollow cathode for 5,000 hours at an emission current of 25 A. The test duration of 5,000 hours was selected to be half of the ion engine design life-time of 10,000 hours with

the expectation that major design deficiencies would be uncovered in this time period. The cathode life-test was voluntarily terminated after 5,024 hours of operation at 25 A, resulting in a total demonstrated emission capability of 125,600 A-hrs.

Substantial sputtering of the test apparatus components facing the cathode was observed despite operation at a discharge voltage of  $\leq 20$  V throughout the test. Evidence for sputtering of materials at anode potential was also found. These sputtering symptoms are consistent with the existence of a cathode jet, comprised of energetic ions, which may be created during operation at emission currents greater than 20 A.

Optical measurements of the insert temperature during the life-test indicated temperatures which are far too high to be consistent with long term cathode operation. Yet the cathode successfully operated for more than 5,000 hours with little change in discharge voltage. Chemical reactions using the reaction products from the original impregnant may be responsible for the liberation of free barium at temperatures well in excess of 1,100 °C. The possibility of long-life operation for impregnated cathodes at temperatures significantly above 1,100 °C may greatly benefit the development of not only high-current hollow cathodes for ion engines, but may also be a foundation from which long-lived MPD thruster and arcjet cathodes can be developed.

### Acknowledgements

The work described in this paper was performed by the Jet Propulsion Laboratory, California Institute of Technology, under contract with the National Aeronautics and Space Administration. "Approved for public release; distribution unlimited."

### References

- <sup>1</sup>Kemp, R. F. and Sellen, J. M. Jr., "Investigation of Cesium and Mercury Discharge Neutralizers," in "Research on Ion Beam Diagnostics," J. M. Sellen, Jr. and R. F. Kemp, eds., NASA CR-54692, 1966.
- <sup>2</sup>Rawlin, V. K. and Kerslake, W. R., "Durability of the SERT II Hollow Cathode and Future Applications of Hollow Cathodes," NASA TM X-52532, 1969.
- <sup>3</sup>Csiky, G. A., "Investigation of a Hollow Cathode Discharge Plasma," AIAA Paper No. 69-258, March 1969.
- <sup>4</sup>Philip, C. M., "A Study of Hollow Cathode Discharge Characteristics," AIAA Paper No. 70-1087, 1970.
- <sup>5</sup>Goldstein, R., Pawlik, E. V., and Wen, L., "Preliminary Investigations of Ion Thrusters Cathodes," JPL Technical Report 32-1536, August 1971.

- <sup>6</sup>Weigand, A. and Nakanishi, S., "A Survey of Kaufman Thruster Cathodes," NASA TM X-67918, October 1971.
- <sup>7</sup>Hudson, W. R. and Weigand, A. J., "Hollow Cathodes with BaO Impregnated Porous Tungsten Insert and Tips," AIAA Paper No. 73-1142, 1973.
- <sup>8</sup>Mirtich, M. J., "Investigation of Hollow Cathode Performance for 30-cm Thrusters," AIAA Paper No. 73-1138, October 1973.
- <sup>9</sup>Wintucky, E. G., "A 20,000 hr Endurance Test of a Structurally and Thermally Integrated 5-cm Diameter Ion Thruster Main Cathode," AIAA Paper No. 75-368, 1975.
- <sup>10</sup>Mirtich, M. J. and Kerslake, W. R., "Long Lifetime Hollow Cathodes for 30-cm Mercury Ion Thrusters," AIAA Paper No. 76-985, 1976.
- <sup>11</sup>Collett, et. al., "Thruster Endurance Test," NASA CR-135011, May 1975.
- <sup>12</sup>Collett, C. R. and Bechtel, R. T., "An Endurance Test of a 900 Series 30-cm Engineering Model Ion Thruster," AIAA Paper No. 76-1020, November 1976.
- <sup>13</sup>Nakanishi, S., "A 15,000-Hour Cyclic Endurance Test of an 8-cm Diameter Mercury Bombardment Ion Thruster," AIAA Paper No. 76-1022, November 1976.
- <sup>14</sup>Sovey, J. S., "Characteristics of a 30-cm Diameter Argon Ion Source," AIAA Paper No. 76-1017, 1976.
- <sup>15</sup>Mantienieks, M. A. and Wintucky, E. G., "5200 Cycle Test of an 8-cm Diameter Hg Ion Thruster," NASA TM-78860, April 1978.
- <sup>16</sup>Fearn, D. G., "Cyclic Life-Test of an Ion Thruster Hollow Cathode," *J. Spacecraft*, Vol. 15, No. 3, June 1978.
- <sup>17</sup>Rehn, L., and Kaufman, H. R., "Correlation of Inert Gas Hollow Cathode Performance," AIAA Paper No. 78-707, April 1978.
- <sup>18</sup>Mantienieks, M. A., Mercury Ion Thruster Component Testing," AIAA Paper No. 79-2116, 1979.
- <sup>19</sup>Poeschel, R. L. and Beattie, J. R., "Primary Electric Propulsion Technology Study," NASA CR-159688, November 1979.
- <sup>20</sup>Siegfried, D. E., "A Phenomenological Model of Orified Hollow Cathodes," NASA CR-168026, December 1982.
- <sup>21</sup>Stillwell, R. P., Robinson, R. S., Kaufman, H. R., and Cupp, R. K., "Experimental Investigation of an Argon Hollow Cathode," AIAA Paper No. 82-1890, November 1982.
- <sup>22</sup>Bechtel, R. T., Trump, G. E., and James, E. J., "Results of the Mission Profile Life Test," AIAA Paper No. 82-1905, November 1982.
- <sup>23</sup>Beattie, J. R., "Extended Performance Technology Study: 30-cm Thruster," NASA CR-168259, June 1983.
- <sup>24</sup>Kudo, I., Machida, K., and Toda, Y., "10,000-Hours Neutralizer Hollow Cathode Endurance Test," IEPC 84-38, presented at the International Electric Propulsion Conference, Tokyo, Japan, May 1984.
- <sup>25</sup>Ninoo, H., "Gas Pressure and Electron Density in the Active Zone Level of Hollow Cathode Arc Discharges," NASA TM-77468, April 1984.
- <sup>26</sup>Schatz, M. F., "Heaterless Ignition of Inert Gas Ion Thruster Hollow Cathodes," AIAA Paper No. 85-2008, Sept. 1985.
- <sup>27</sup>Kudo, I., Murakami, H., Toda, Y., and Machida, K., "Recycle Test of an Ion Thruster Main Cathode," International Symposium on Space Technology and Science, 15th, Tokyo, Japan, May 1986, Proceedings Volume 1 (A87-32276 13-12).
- <sup>28</sup>Rawlin, V. K. et. al., "High Current Hollow Cathodes for Ion Thrusters," AIAA Paper No. 87-1072, May 1987 (view graphs only).
- <sup>29</sup>Brophy, J. R. and Garner, C. E., "Tests of High Current Hollow Cathodes for Ion Engines," AIAA Paper No. 88-2913, July 1988.
- <sup>30</sup>Rawlin, V. K., "Internal Erosion Rates of a 10-kW Xenon Ion Thruster," NASA TM 100954, July 1988.
- <sup>31</sup>Gair, S. A. and Harris, P. T., "A Review of the Cathode Construction for the RAE 10/25 mN Thruster," IEPC-88-078, October 1988.
- <sup>32</sup>Maslyany, N. V., Pridantzev, V. F., Prisnyakov, V. F., and Khitko, A. V., "Parametric Investigations of the Hollow Cathodes for Ion Thrusters," IAF-88-260, 39th Congress of the International Astronautical Federation, October 1988.
- <sup>33</sup>Beattie, J. R., Matossian, J. N. and Robson, R. R., "Status of Xenon Ion Propulsion Technology," *J. Propulsion*, Vol. 6, No. 2, March-April 1990, pp. 145-150.
- <sup>34</sup>Friedly, V. J., "Hollow Cathode Operation at High Discharge Currents," NASA CR-185238, April 1990.
- <sup>35</sup>Patterson, M. J. and Verhey, T. R., "5kW Xenon Ion Thruster Lifetest," AIAA Paper No. 90-2543, July 1990.
- <sup>36</sup>Fearn, D. G., Singfield, A., Wallace, N. C., Gair, S. A., and Harris, P. T., "The Operation of Ion Thruster Hollow Cathodes using Rare Gas Propellants," AIAA Paper No. 90-2584, July 1990.
- <sup>37</sup>Verhey, T. R. and MacRae, G. S., "Requirements for Long-life Operation of Inert Gas Hollow Cathodes -- Preliminary Results," AIAA Paper No. 90-2586, July 1990.
- <sup>38</sup>Stuart, R. V. and Wehner, G. K., "Sputtering Yields at Very Low Bombarding Ion Energies," *J. Applied Physics*, Vol. 33, No. 7, 1962.
- <sup>39</sup>Robinson, R. S., "Physical Processes in Directed Ion Beam Sputtering," NASA CR-159567, March 1979.
- <sup>40</sup>Garner, C.E., Brophy, J. R., Pless, L.C., and Barnett, J. W., "The Effect of Nitrogen on Xenon Ion Engine

Erosion," AIAA Paper No. 90-2591, July 1990.

<sup>41</sup>Kaufman, H. R., "Technology of Electron-Bombardment Ion Thrusters," in *Advances in Electronics and Electron Physics*, Vol. 36, Academic Press, Inc., 1974.

<sup>42</sup>Personal communication, L. E. Lowry, Space Materials Science and Engineering Section, Jet Propulsion Laboratory, January 1991.

<sup>43</sup>Personal communication, W. Olinger, Georgia Institute of Technology, January 1991.

Table 1 Cathode Life Test Summary

Shutdown #	Run Time (hrs)	Test Segment Duration (hrs)	Explanation	Restart Conditions	
				Orifice Plate Temperature (°C)	Start Voltage Required (V)
1	40	40	Low anode voltage detected by the computer. Faulty anode power supply.	1143	25
2	62	22	Faulty anode power supply.	1047	22
3	114	52	Faulty anode power supply.	1047	18
4	121	7	Faulty anode power supply.	1047	35
5	122	1	Faulty anode power supply.	1024	35
6	123	1	Manual shutdown to change anode power supply.	1029	35
7	295	172	Lightning strike caused momentary facility power outage. Computer shutdown cathode.	1041	35
8	558	263	Data acquisition system failure. Computer shutdown cathode.	1052	50
9	581	23	Failure of primary and back-up printers. Computer shutdown cathode	1048	50
10	697	116	Data acquisition system failure. Computer shutdown cathode.	1041	80
11	743	46	Data acquisition system failure. Computer shutdown cathode.	1047	80
12	1289	546	Mechanical pump belt broke. Operator error led to computer shutdown of cathode.	1153	900
13	1649	360	Lightning strike caused momentary facility power outage. Computer shutdown cathode.	1085	900
14	2704	1055	Operator error led to computer shutdown of cathode.	1050	300
15	3020	316	Xenon bottle changed. Gas pulse required to restart (200 torr).	1050	>900
16	3069	49	Flow controller failure. Computer shutdown cathode. Cathode exposed to air for approximately 5 minutes. Gas pulse required to restart (200 torr).	1050	>900
17	4221	1152	Xenon bottle changed. Gas pulse required to restart (200 torr)	1050	>900



Shutdown #	Run Time (hrs)	Test Segment Duration (hrs)	Explanation	Restart	Conditions
				Orifice Plate Temperature (°C)	Start Voltage Required (V)
18	4562	341	Windstorm caused facility power outage, computer shutdown cathode. Gas pulse required for restart (200 torr)	1050	>900
19	4927	365	Xenon bottle changed. Gas pulse required for restart (200 torr)	1050	>900
20	5024	97	End of test.	----	----

Table 2 Summary of Residual Deposits on Molybdenum Tube

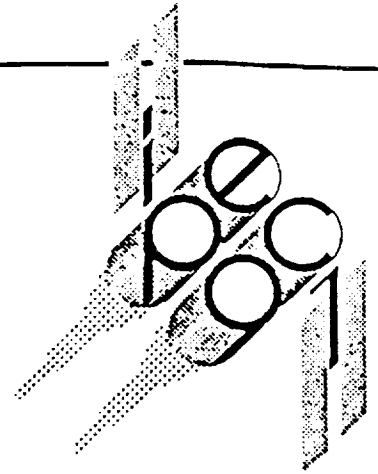
POSITION*	WT %						
	W	Mo	Re	Al	Ca	Ba	O
1	35.1	1.7	---	1.9	---	44.3	16.9
2	39.9	3.0	---	2.7	3.2	31.9	19.3
3	45.1	2.0	---	1.4	2.0	31.0	18.5
4	43.6	1.0	---	2.4	2.4	32.9	18.5
5	1.9	34.5	63.6	---	---	---	---
6	9.7	48.7	41.6	---	---	---	---

\*Positions correspond to locations underneath the insert slices identified in Fig. 31.

Table 3 Post 5,000 hr Test Insert Constituents

POSITION	RELATIVE PERCENT BY WEIGHT			
	BaAl <sub>2</sub> O <sub>4</sub>	Ba <sub>2</sub> CaWO <sub>6</sub>	Ba <sub>3</sub> W <sub>2</sub> O <sub>9</sub>	BaWO <sub>4</sub>
1	44	33	23	---
2	50	50	---	---
3	45	55	---	---
4	21	---	---	79
5	22	---	---	78
6	20	14	---	66





**IEPC-91-097**

**METAL AND METAL NITRIDE EROSION  
RATES IN A DIVERGENT FIELD ION ENGINE**

C. Garner, J. Brophy, and L. Pless  
Jet Propulsion Laboratory  
California Institute of Technology  
Pasadena, California

**AIDAA/AIAA/DGLR/JSASS 22nd International  
Electric Propulsion Conference**

October 14-17, 1991 / Viareggio, Italy

# METAL AND METAL NITRIDE EROSION RATES IN A DIVERGENT FIELD ION ENGINE

Charles E. Garner\*, John R. Brophy\*\*, and L.C. Pless+

*Jet Propulsion Laboratory  
California Institute of Technology  
Pasadena, Ca 91109*

## ABSTRACT

Erosion measurements were performed in a 30-cm diameter divergent-field ion engine modified for operation on argon propellant. The erosion rates of tantalum, tantalum nitride, titanium, and titanium nitride badges placed in the discharge chamber were measured as a function of the percentage of nitrogen (by mass) added to the argon propellant. The erosion rates of the metals tantalum and titanium were lower than those of the corresponding metal nitrides, both when the ion engine was operated on pure argon propellant, and when the engine was operated on a mixture of argon and nitrogen (3% by mass). In addition, the erosion rates of the metal nitrides were also reduced when nitrogen was added to the argon propellant.

## INTRODUCTION

Ion engine operating life is limited, in-part, by ion sputter erosion of surfaces in the discharge chamber which are at or near cathode potential. Internal engine components subject to ion sputtering include the screen grid, the cathode starter electrode (keeper), and in the J-series ion engine, the baffle and pole piece assembly. For several reasons, inert gases have replaced mercury as the propellants of choice for interplanetary and earth-orbital ion propulsion systems. Erosion rates within the ion engine discharge chamber, however, are expected to be greater with inert gas propellants than the corresponding rates with mercury. This is due primarily to the higher sputter yields of the inert gases as compared to mercury.

Data on erosion and wear rates within the discharge chamber of ion engines operated on inert gases are limited. During the 5 kW, xenon ring-cusp thruster wear test recently conducted at the NASA Lewis Research Center (LeRC), the cathode starter electrode was severely eroded within 890 hours.<sup>1</sup> In high current hollow cathode testing conducted at JPL, significant erosion of the pole

piece and other components was observed in the vicinity of the hollow cathode operated on argon at 100 amperes,<sup>2</sup> in spite of the low discharge voltage (less than 24 volts) which was used in the test. In 1988 a screen grid life of 7000 hours<sup>3</sup> was inferred from a 10 kW xenon thruster life evaluation test; however, there was a good deal of uncertainty in the screen grid life estimate.

In 1987, J-series ion thruster erosion testing<sup>4</sup> revealed unexpectedly high erosion rates and highly peaked erosion profiles on the cathode side of the baffle, a result substantiated by later tests<sup>3</sup>. During testing of a high current hollow cathode<sup>2</sup> it was observed that a well-defined and collimated plume was produced by the cathode when it was operated at a high emission current. A section of the anode face plate 15 cm downstream of the cathode was eroded, even though this face plate was at anode potential. As a result of this testing it was suggested that a cathode jet having ion energies of tens of eV might be the mechanism responsible for the high erosion rates observed at the cathode side of the baffle<sup>2</sup>. At sufficiently high discharge currents this cathode jet might result in increased screen grid erosion.

Techniques which could be used to reduce discharge chamber erosion include reducing the discharge voltage, which reduces the energy of the sputtering ions, and reducing the propellant utilization efficiency (propellant utilization efficiency is defined as the fraction of the neutral propellant flow which is ionized and extracted as beam ions), which reduces the fraction of multiply charged ions. However, it may be desirable to operate ion engines at the highest possible discharge voltage and propellant utilization to reduce the number of neutrals escaping from the discharge chamber. These neutrals are responsible for the creation of charge-exchange ions which can erode the accelerator grid at unacceptably high rates.<sup>1</sup> Thus, internal component erosion may be traded against accelerator grid erosion.

Previous testing of J-series mercury ion engines indicated that the presence of certain facility background gases reduced molybdenum screen grid erosion.<sup>5-7</sup> Subsequently it was proposed<sup>8</sup> that small quantities of nitrogen added to the mercury propellant could reduce discharge chamber component erosion and extend the useful life of the engine. Preliminary data<sup>4,9,10</sup> have suggested that the addition of small quantities of nitrogen to the xenon propellant reduces erosion within the

\* Member of the Technical Staff, Electric Propulsion and Plasma Technology Group. Member AIAA.

\*\* Supervisor, Electric Propulsion and Plasma Technology Group. Member AIAA.

+ Member of the Technical Staff, Electric Power Systems Section.

discharge chamber of xenon ion engines. It was proposed<sup>6</sup> that the mechanism responsible for the reduced erosion rates observed when nitrogen or other facility gases are present within the discharge chamber is the formation of sputter-resistant oxides or nitrides that have lower ion sputter erosion rates than the native metal. However, there are no sputter yield data for metals and metal nitrides in the 30-60 eV range. Subsequently, it was suggested<sup>7</sup> that desorption of chemisorbed nitrogen was the dominant mechanism for reduced ion engine discharge chamber erosion rates observed in these and other tests.

In reference 10 are definitive analyses to verify the formation of tantalum nitride in the ion engine discharge chamber. However, there are some aspects of data<sup>4,9,10</sup> obtained from previous testing which do not support the theory that erosion reduction is due to formation of sputter-resistant metal nitrides:

(1) No definitive evidence was found for existence of molybdenum nitride<sup>4,9,10</sup>, despite reduced molybdenum erosion rates measured from badges placed at the screen grid and discharge side of the baffle.

(2) The greatest erosion reduction has been measured at the cathode side of the baffle, where badges are eroded by high-energy ions in the cathode jet<sup>2</sup>. Differences in ion sputter yields of different materials generally decrease with increasing ion energy, therefore if the mechanism for erosion reduction is formation of sputter-resistant nitrides, the erosion rate reduction factor at the cathode face of the baffle should be reduced, relative to other locations in the discharge chamber where badges are presumably eroded by lower energy ions.

This paper presents the results of a continuing investigation of the effects of the addition of small quantities of nitrogen on ion engine discharge chamber erosion. The erosion rates for various metals and metal nitrides are presented as a function of the percentage of nitrogen added to the argon propellant. Finally, the two mechanisms, chemisorption and sputter-resistant metal nitrides, are discussed to account for reduced erosion rates observed in these and other tests.

## EXPERIMENTAL PROCEDURE

Erosion tests were performed using a 900-series 30 cm ion engine discharge chamber modified for use with argon propellant. The 900-series ion engine, which is very similar to the J-series ion thruster, employs an axially diverging magnetic field in the discharge chamber to increase engine efficiency. The engine was operated without beam extraction in a stainless steel vacuum chamber 0.7 meters in diameter and 1.4 meters in length, and pumped by silicone-based oil diffusion pumps. Vacuum tank pressure was measured using an ionization

gauge tube and controller. The no-load tank pressure prior to flowing argon into the ion engine was typically  $1.6\text{--}2.5 \times 10^{-4}$  Pa ( $1.9 \times 10^{-6}$  torr). Tank pressure during engine operation was typically  $2.8 \times 10^{-2}$  Pa ( $2.1 \times 10^{-4}$  torr). No cold liner was used to trap water vapor and other volatile gases in the vacuum chamber.

Polished erosion badges were placed in a badge holder made from 302 stainless-steel, which was mounted to a tantalum baffle in the discharge chamber at the location shown in Fig. 1. The same tantalum baffle was used in all tests. The tantalum baffle and all the tantalum erosion badges used in the experiments were machined from a single sheet of electron-beam melted tantalum.

Tantalum nitride and titanium nitride samples were cut from 6.35 mm thick discs of solid metal nitride that were originally fabricated for use as sputter targets in the microelectronics industry. The metal nitride targets were formed by sintering tantalum or titanium powders in an ammonia-rich atmosphere. Tantalum nitride and titanium nitride were selected because of their high melting points and low chemical reactivity at high temperatures<sup>11,12</sup>. Since these materials were already nitrides, it was expected that their materials properties, such as sputter yield, would not change when nitrogen was added to the propellant. TaN and TiN materials characteristics are listed in Table 1.

The polished erosion badges were masked using 0.076 mm thick tantalum foils having a cross-shaped pattern 2.0 mm wide and 20.0 mm in length to expose the underlying badge material to the discharge chamber plasma (Fig. 2). Data were taken both at the center corner, where it is assumed that all badges are exposed to identical plasma conditions, and at locations of the cross-shaped pattern farthest from the center.

Material erosion rates were determined by measuring the trench depth eroded into unmasked portions of the erosion badges by discharge chamber ions. A profilometer capable of resolving surface features as low as 20 angstroms was used to measure trench depths. Trench depths from the profilometer traces were determined as follows: The uneroded surface height (baseline height) of the sample was determined as an average of peaks and trough heights in the uneroded region of the sample (Fig. 3). The same procedure was used for the etched regions, with only a 0.32 mm long region considered for purposes of determining the trench depth of the sample. This 0.32 mm region is 13 mask thicknesses away from the mask edge; previous experimental data<sup>4</sup> suggest that this is a suitable distance to minimize mask effects on the etch rates of the erosion badges. Furthermore, it is far enough away from the sample edge such that there is no spurious data due to roll-off at the badge edges.

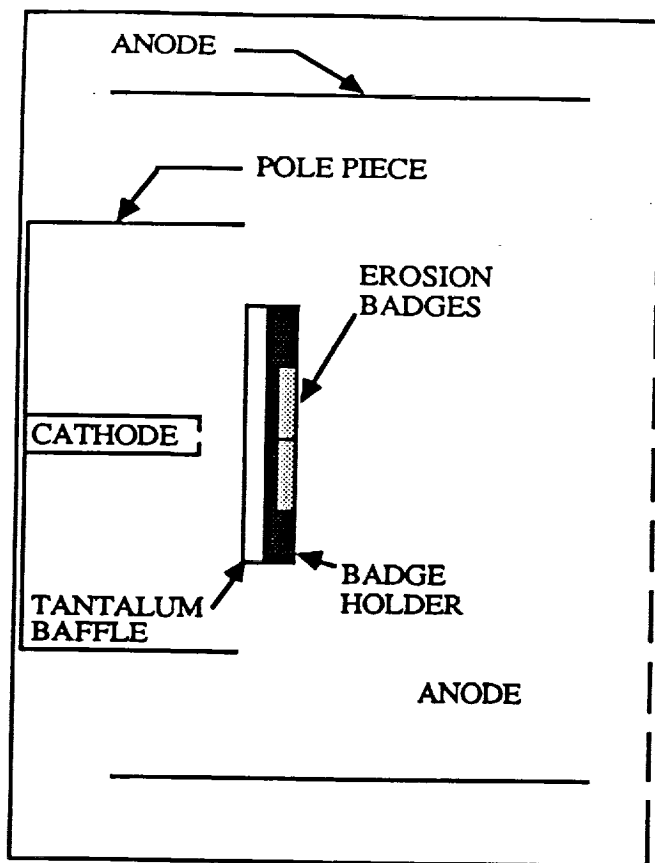


Figure 1. Schematic diagram of the ion engine discharge chamber showing the locations of erosion badges.

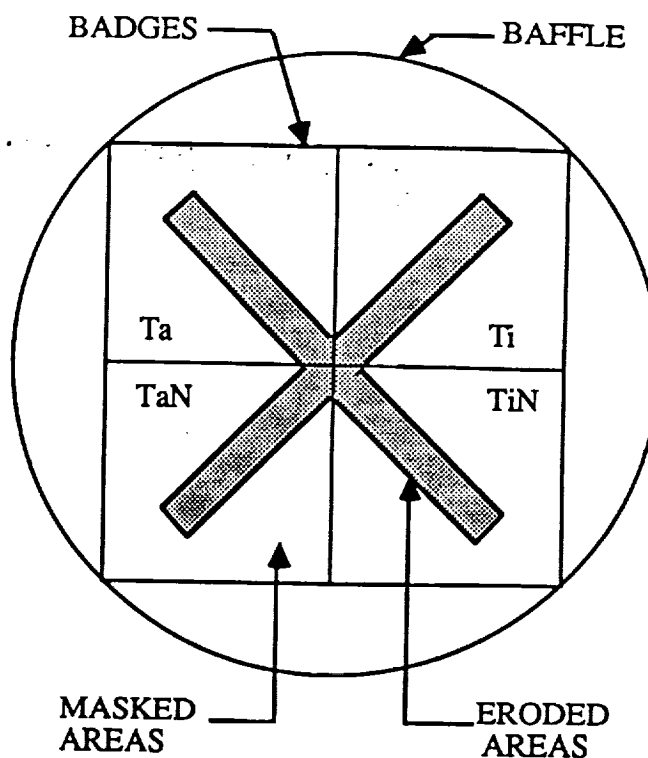


FIGURE 2. Tantalum mask and erosion badges used for erosion testing.

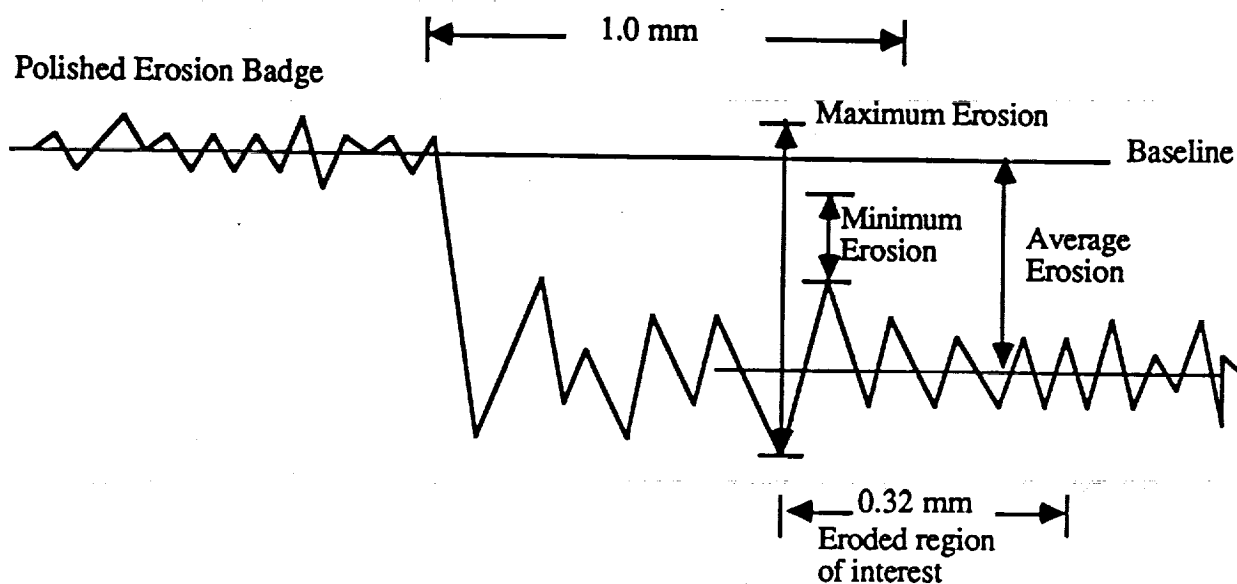


Fig. 3. Simulated profilometer trace used to determine the depth of the trench eroded into the erosion badge by discharge chamber ions.

TABLE 1. MATERIALS PROPERTIES OF TA NITRIDE AND TI NITRIDE.

MATERIAL	COLOR	DENSITY g/cm <sup>3</sup>	MELTING POINT °C	ELECTRICAL RESISTIVITY μΩ-cm
Ta Nitride	Grey	16.3*	2980	80
Ti Nitride	Golden Yellow	5.4	2950	200

\* Value supplied by vendor Material Safety Data Sheet.

The average erosion rate was determined subjectively by estimating an average surface location between the peaks and troughs in the eroded region, and then calculating the difference in heights between this subjective estimate and the baseline. Uncertainties in the erosion depth measurements were determined by adding the peaks in the baseline to the troughs in the eroded region to determine the maximum erosion rate, and troughs in the baseline to peaks in the eroded region to determine the minimum erosion rate. The erosion badges were polished to the specifications shown in Table 2.

Table 2. Erosion Badge Polishing Specifications

Badge Material	Surface Roughness Angstrom
Molybdenum	± 350
Tantalum	± 500
Ta Nitride	± 7500
Titanium	± 2000
Ti Nitride	± 25000

The uncertainties in the erosion rate measurements were due primarily to the formation of deep valleys and high peaks in the portions of the badges exposed to the discharge plasma ions (Fig. 3). Because the discharge was operated for only 54-110 hours during each test, and because of the formation of peaks and valleys in the eroded region, there is a significant amount of uncertainty in some of the erosion data. The test periods were selected to allow many experimental conditions to be investigated. This technique could be used with longer duration tests to greatly reduce the measurement uncertainties. Long-duration discharge chamber erosion studies were beyond the scope of this work and are a topic for future investigations.

The engine cathode flow rates were controlled by a manual micrometer valve, and main flow rates were

controlled by an electronic flow controller. Research-grade bottles of both pure argon and argon containing between 2.95-3.05% nitrogen by mass were procured. After the propellant system was assembled, the mass flow meters were calibrated in-house on the pure argon or argon/nitrogen mixture using a bubble volumeter. A curve fit was used to interpolate between the calibration points.

Backflow of argon or nitrogen into the ion engine was calculated using the method developed by Wilbur et al.<sup>13</sup> The largest source of error in the uncertainty analysis of the argon and nitrogen engine flow was the backflow calculation. This was due to uncertain knowledge of the local tank wall temperature, which affects the rate at which facility gases (primarily argon, nitrogen and water vapor) backflow into the thruster. Tank wall temperatures were measured with thermocouples at two locations during testing. The backflow of nitrogen and argon, both a function of tank pressure, were calculated and added to the values of argon or nitrogen injected into the engine through the propellant system.

A computer data acquisition and control system monitored the tank pressure, engine discharge voltage and current, and engine propellant flow rates. Typical engine operating conditions are shown in Table 3. The discharge voltage was typically  $40.0 \pm 0.2$  V. In some instances the discharge voltage varied by  $\pm 0.75$  V; larger voltage variations that occurred within a time band of approximately 2 seconds were not measured due to limitations in the data acquisition system.

Table 3. Ion Engine Operating Conditions Used for Erosion Testing

Discharge Current	(A) :	20.1
Discharge Voltage	(V) :	40.0
Cathode Flow Rate	(sccm) :	9.8
Main Flow Rate	(sccm) :	10.3
Tank Pressure (no load)	(torr)	$1.8 \times 10^{-6}$
Tank Pressure (engine on)	(torr)	$2.1 \times 10^{-4}$

The erosion tests were conducted in the following manner. Erosion badges were placed in the discharge chamber, with the polished face of the badges facing the screen grid. At this location, the erosion badges should be eroded by plasma ions with an energy of approximately 40 eV; it is estimated that about 10% of the plasma ions are doubly-charged with an energy of approximately 80 eV. The vacuum tank was then pumped to  $2.1 \times 10^{-4}$  Pa with the propellant lines open to vacuum up to the propellant tank valve such that the propellant lines were at high vacuum. Next, propellant was flowed into the engine, and the ion engine discharge chamber plasma initiated. The run time clock was started when the plasma conditions were adjusted to those listed in Table 3; this typically required an operating time of less than 10 minutes at conditions different from those listed in Table 3.

The tests were run for periods of 54-110 hours. After a minimum cool-down period of 3.5 hours, the vacuum tank was vented to atmosphere and the erosion badges were removed from the engine and replaced with a new set of erosion badges.

## RESULTS AND DISCUSSION

Table 4 describes the pertinent test parameters and the order in which the tests were conducted.

Table 4. Ion Engine Plasma Chamber Erosion Testing

Test #	Test Duration (Hrs)	%N <sub>2</sub> Added To Argon	Materials Tested
1	53.6	0	Ta, TaN, Ti, TiN, Mo
2	60.7	0	Ta, TaN, Ti, TiN
3	80.8	3.0	Ta, TaN, Ti, TiN
4	108.8	3.0	Ta, TaN

The effects on component erosion rates of adding small quantities of nitrogen to the argon propellant are depicted graphically in Figs. 4-5. Data are for erosion rates at the center of the baffle. There is significant uncertainty in some of the data due to the surface profiles created by ion bombardment of the erosion badges during engine operation, and to the short duration of the tests. The data for tantalum and tantalum nitride from Test # 3 are not shown; it is believed that deposits from the mask which arose from poor contact affected the data. The mask contact with the titanium and titanium nitride, however, was good.

The data shown in Table 5 that were taken at a location approximately 9 mm from the center showed no significant differences relative to data taken at the baffle center. It appears that on the discharge face of the baffle, the erosion rate is uniform over an area of diameter 20.0 mm or more.

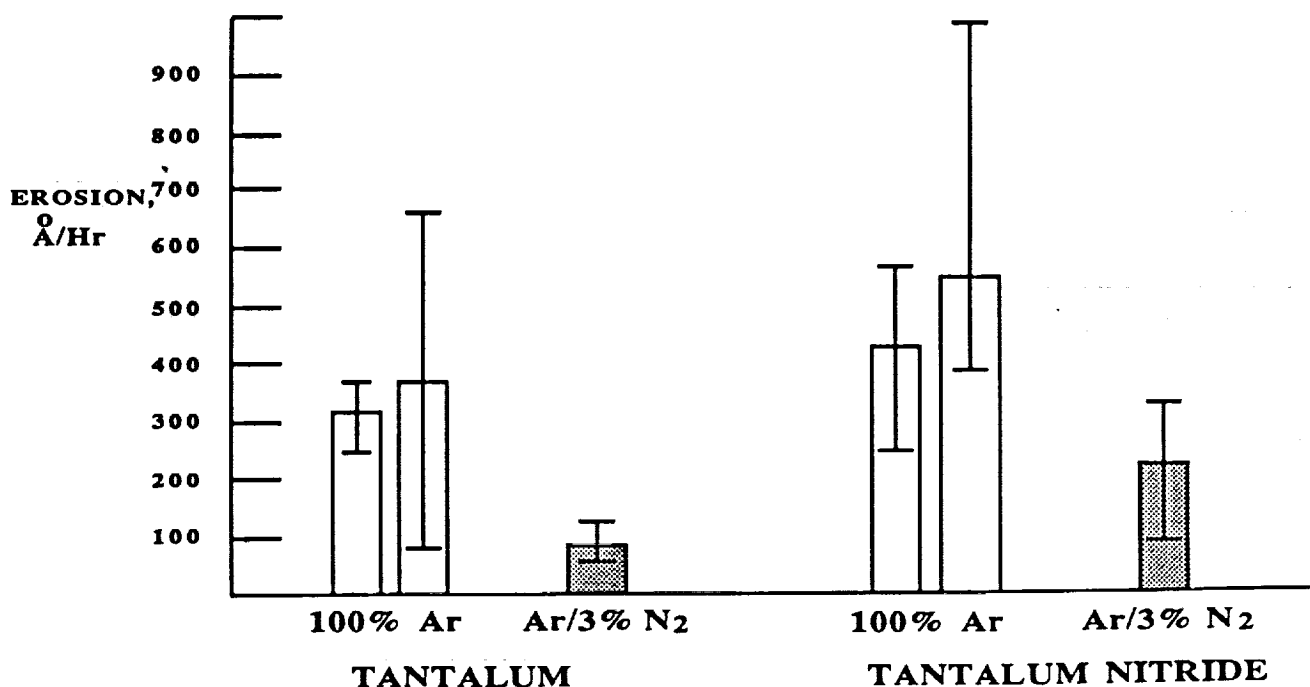


Figure 4. Erosion rates of tantalum and tantalum nitride, both on pure argon and an argon/nitrogen mixture.



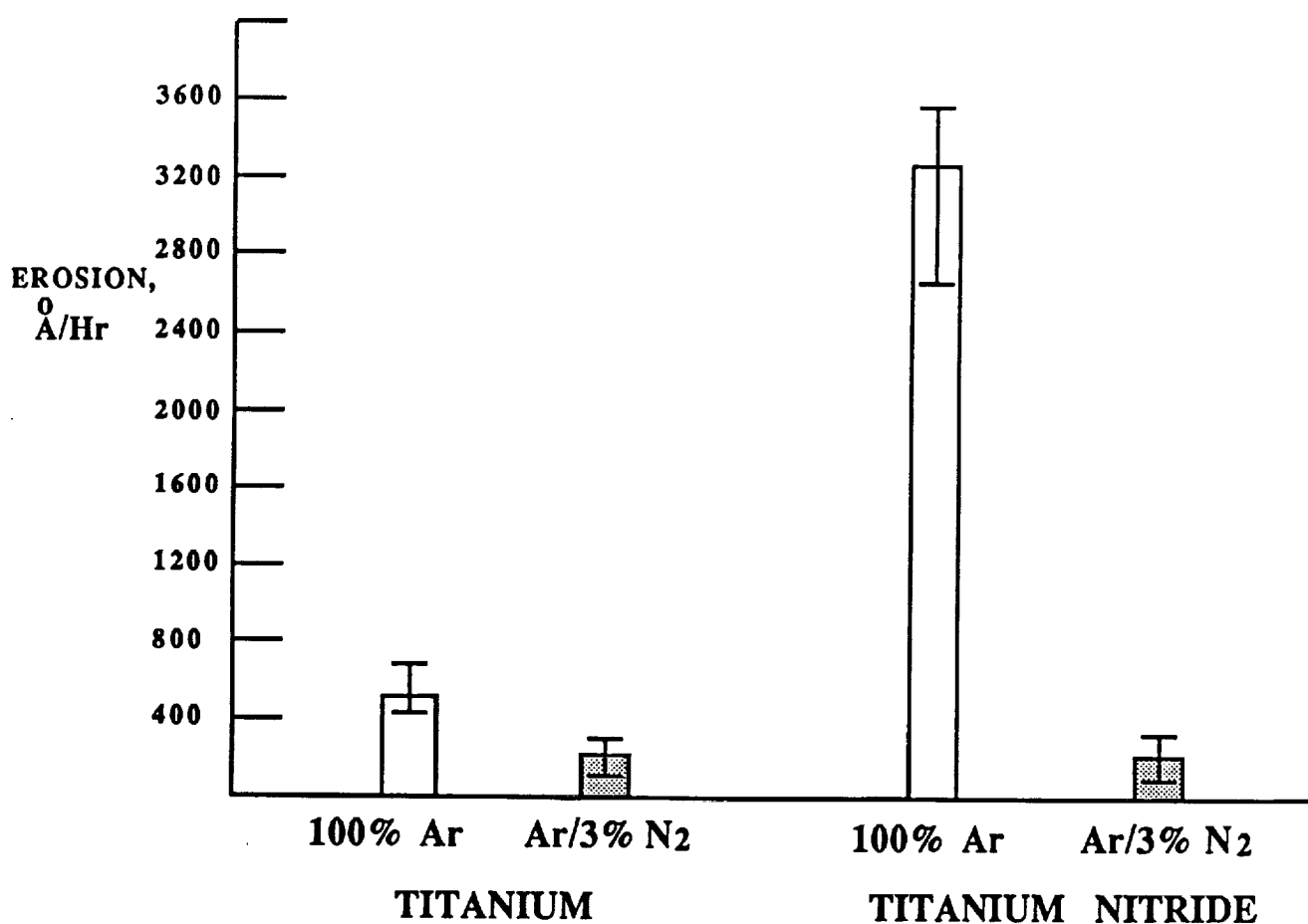


Figure 5. Erosion rates of titanium and titanium nitride, both on pure argon and an argon/nitrogen mixture.

TABLE 5. COMPARISON BETWEEN EROSION RATES AT BADGE CENTER AND AT 9 MM DISTANT FROM CENTER.

MATERIAL	TEST #	DISTANCE FROM CENTER mm	EROSION RATE		
			MIN ○ Å/Hr	AVE ○ Å/Hr	MAX ○ Å/Hr
Tantalum	4	Center	87	97	108
"	"	9	92	101	124
Ta Nitride	4	0	83	221	331
"	"	9	92	207	239

TABLE 6. SPUTTER YIELD ESTIMATES FOR EROSION BADGES  
PLACED AT THE DISCHARGE SIDE OF THE BAFFLE.

TEST #	SAMPLE MATERIAL	% N2 IN ARGON	SPUTTER YIELD CALCULATED 1X10 <sup>-3</sup>	SPUTTER YIELD FROM Ref. 14 1X10 <sup>-3</sup>
1	Molybdenum	0	4.4	6.0 <sup>i</sup>
1	Tantalum	0	1.0	2.1 <sup>i</sup>
1	Ta Nitride	0	1.8	*
2	Tantalum	0	0.84	2.1 <sup>i</sup>
2	Ta Nitride	0	1.1	*
2	Titanium	0	0.97	6.0 <sup>i</sup>
2	Ti Nitride	0	2.4	*
3	Titanium	3	0.41	6.0 <sup>i</sup>
3	Ti Nitride	3	0.16	*
4	Tantalum	3	0.27	*
4	Ta Nitride	3	0.55	*

<sup>i</sup> interpolated from curve fit

\* data not available

The sputter yields of the materials listed in Table 6 were calculated by estimating the ion current density to the erosion badges (app. 9.1 mA/cm<sup>2</sup>). Comparisons of the sputter yields obtained in these tests to those given in Ref. 14 are also listed in Table 6. Considering the great amount of uncertainty in sputter yields of materials at low ion energies, the agreement between the erosion tests made using pure argon and the data in Ref. 14 are quite reasonable, except for the sputter yield calculation for titanium.

When the engine was operated on pure argon, the erosion rates of tantalum and titanium were lower than their corresponding nitrides, with tantalum having the lowest erosion rate and titanium nitride having the highest. When the engine was operated on the argon/nitrogen mix, the erosion rates of all materials tested decreased, relative to the tests conducted on pure argon. Again, tantalum had the lowest erosion rate of the materials tested. Titanium nitride showed the most significant erosion reduction when nitrogen was added to the argon; its erosion rate was reduced by a factor of 15.

In all experiments the discharge voltage and current were held approximately fixed at the values listed in Table 3. In addition, a performance degradation analysis performed in Ref. 10, along with careful monitoring of ion engine operating parameters (with beam extraction) demonstrated that there is at most only a small degradation

in ion engine performance when small quantities of nitrogen (0-2% by mass) are added to the xenon propellant. Since no erosion studies have been conducted with an ion engine on a thrust stand, and since no materials have been used which are not affected by the presence of nitrogen in the propellant, it can not be definitively stated that no changes in plasma conditions occur when nitrogen is added to the propellant. However, it is clear that (1) the erosion rates of all materials tested in this work and in previous works were reduced when nitrogen was added to the propellant, and (2) there are no known mechanisms in which adding nitrogen to the propellant could appreciably change the energies or densities of propellant ions bombarding surfaces in the discharge chamber that are at cathode potential.

If it is accepted that propellant ion energies and current densities in the discharge chamber remain unchanged whether or not nitrogen is added to the propellant, then the erosion reductions observed in this and other tests are due to either the formation of sputter-resistant metal nitrides, or to some other mechanism. The results presented here indicate clearly that, at approximately 40 eV the metal nitride erosion rates are greater than the metal erosion rates; therefore, the mechanism responsible for the reduced discharge chamber component erosion rates can not be the formation of surface nitrides that have a lower erosion rate than the pure metal.

The data are far from conclusive, however, due to the uncertainties in the erosion rate measurements and to the fact that the erosion rates of the base metals may have been affected by gases (primarily nitrogen or water vapor) in the vacuum facility that back-flowed into the discharge chamber through the grid holes. In addition, it is not clear that eroding a metal nitride is an adequate simulation to the situation which exists when a metal is eroded in the presence of atomic or ionic nitrogen.

### ALTERNATIVE MECHANISMS

A mechanism to account for reduced erosion rates in this and other works is proposed in reference 7 and detailed in reference 15. This mechanism involves the adsorption of a surface layer of nitrogen and desorption by inert-gas ion bombardment. Adsorption is defined as the process in which a gas forms a layer on a surface. Two types of adsorption are distinguished: chemisorption, in which the gas atoms are held by covalent bonds, and physisorption, in which they are held by van der Waals forces. In chemisorption, a single layer of adsorbed atoms is held to the surface by a (normally) weak covalent bond. Nitrogen chemisorbed on the surfaces of single-crystal molybdenum and tungsten have a surface binding energy of about 6.5 eV<sup>15</sup>; the propellant ions in the discharge chamber have sufficient energy to remove these surface nitrogen atoms via ion sputtering.

Chemisorption as a mechanism to reduce erosion rates in an ion engine can be evaluated if the sputter yields of base metal, chemisorbed nitrogen, and ion energies and current densities are known. Unfortunately ion energies, current densities, and sputter yields of both the base metals or chemisorbed nitrogen are not generally available. However, reasonable approximations of sputter yields and ion energies and current densities can be inferred from various sources. Test data on the effects of the addition of nitrogen on xenon ion engine erosion are presented in references 9 and 10. A separate discussion will be presented for molybdenum screen badge and tantalum baffle erosion.

### MOLYBDENUM SCREEN BADGE

In reference 10, molybdenum screen badges placed near the screen grid were eroded at a rate of 250 angstroms per hour. Assuming an ion current density of approximately 10 mA/cm<sup>2</sup>, and a double/single ion current ratio of 0.09, the sputter yields for singly and doubly charged xenon ions on molybdenum are  $3.4 \times 10^{-4}$  and  $8.5 \times 10^{-3}$  respectively. Some experimental data on the sputtering of chemisorbed nitrogen from tungsten or molybdenum are presented in references 15 and 16. Argon, krypton, and xenon ion energies range from 25-5000 eV; data from these references were used to infer chemisorbed nitrogen sputter yields from molybdenum and

tantalum at low ion energies. Based on these data, chemisorbed nitrogen sputter yields from molybdenum were assumed to be one-half that of tungsten.

In reference 8 a model was developed to predict the arrival rates of N, N<sub>2</sub>, N<sub>+</sub>, and N<sub>2</sub><sup>+</sup> to surfaces inside the discharge chamber. Calculations made using this model show that the arrival rate of nitrogen atoms and/or ions was sufficient to provide complete ( $0.8-1.6 \times 10^{15}/\text{cm}^2$ ) surface coverage of the molybdenum surface. In reference 10, when 2% nitrogen by mass was added to the xenon propellant, the erosion rate of the molybdenum was reduced from 250 angstroms per hour, down to 15 angstroms per hour.

This information and the assumptions made above on sputter yields and ion energies and current densities were utilized to perform calculations on the relative arrival and removal rates of chemisorbed nitrogen at the molybdenum surface. These calculations show that the chemisorbed nitrogen layer could substantially reduce the net erosion rate of the underlying molybdenum, and that chemisorption could have been the mechanism responsible for the reduced erosion rates of the molybdenum screen badges when nitrogen was added to the xenon propellant.

In an ion engine, metals with a chemisorbed nitrogen surface layer may have a smaller effective sputter yield because incoming propellant ions must desorb surface nitrogen. As the concentration of nitrogen increases, surface coverage increases until it is complete and the addition of more nitrogen has little or no effect on the erosion rate of the component. The data on molybdenum screen grid erosion obtained in reference 10 can qualitatively be described by chemisorption; however, because of the lack of hard data on sputter yields, nitrogen arrival rates, sticking coefficients, and ion energies and current densities, there is a good deal of uncertainty in these calculations.

Since the mechanism for erosion reduction observed in ion thruster discharge chambers may be desorption of surface nitrogen and not formation of sputter-resistant nitrides, the nitrogen in the discharge chamber must be continuously replenished. From a systems point of view, the simplest way to accomplish that is to mix the nitrogen with the propellant, as was done in these tests. The only deleterious effects on the propulsion system are possible contamination of the neutralizer or discharge chamber hollow cathodes. Tests are underway at present to life test a hollow cathode on an argon and 3% nitrogen mixture. If deleterious effects on the physical chemistry of hollow cathodes occur, then a nitrogen gas purifier can be placed in the propellant lines that branch to the hollow cathodes.

## TANTALUM BAFFLE

The same analyses described above was applied to erosion data measured at the cathode side of the baffle. In reference 10 the cathode side of the tantalum baffle was eroded at a rate of approximately 775 angstroms per hour when the engine was operated on pure xenon, and 20 angstroms per hour when 2% by mass nitrogen was added to the xenon. This high erosion rate on pure xenon operation is due undoubtedly to high velocity ions in the cathode jet<sup>2</sup>.

The first problem in this evaluation is that the ion energies and current densities at the cathode side of the baffle are not known. There are two ways in which the xenon ion energy and current density at the cathode side of the baffle were estimated. The first made use of the cathode jet data from reference 17; in the second method xenon sputter yields on tantalum were estimated using yield data for argon and mercury.

Data from reference 17 indicate that, for a cathode with a 1.1 mm diameter orifice and an emission current of 11.8 A, the xenon ion energy and current density were approximately 25 eV and 5 mA/cm<sup>2</sup>. The sputter yield required for 775 angstroms per hour of erosion (the amount observed in reference 10) would be approximately  $3 \times 10^{-3}$ . This value is unlikely; references 18 and 19 provide sputter yield data for argon and mercury ion bombardment of tantalum. Xenon on tantalum sputter yields are not known, but can be approximated by assuming that the sputter yields for tantalum under xenon bombardment are half-way between the values for argon and mercury. At 25 eV, a value of  $1 \times 10^{-4}$  is obtained, which is a factor of 30 below the value calculated above. It is therefore assumed that the xenon ion current density and energy at the cathode side of the baffle must have been much higher than 25 eV and/or 5 mA/cm<sup>2</sup>.

For purposes of this scoping calculation, we will assume that the tantalum baffles used in reference 10 were eroded by a cathode jet with an ion energy of 60 eV and a current density of 12.5 mA/cm<sup>2</sup>. In addition, it is assumed that chemisorbed nitrogen sputter yields are identical to those found in reference 16 for tungsten. Assuming that under steady-state conditions there exists full surface coverage, and a nitrogen sputter yield of 0.13 (inferred from reference 16), the xenon ion current density required to remove one monolayer of surface nitrogen per second is approximately 1.3 mA/cm<sup>2</sup>. The total xenon ion current arriving at the surface, however, is estimated to be 12.5 mA/cm<sup>2</sup> and implies that the nitrogen current density must be very high, with a sticking probability approaching unity, to get the very low erosion rates observed in reference 10 when nitrogen was added to the xenon.

It is difficult to attribute such a large (factor of 30 or more) reduction in erosion at the cathode side of the baffle to chemisorption, given the nitrogen sputter yields on tungsten and estimates of the ion energies and current densities at that location. There is data to indicate, however, that yields for nitrogen removed from a surface where a nitride was formed can be substantially lower than chemisorbed nitrogen sputter yields.<sup>20</sup> Yields for nitrogen sputtered from molybdenum which was nitrized by 100 eV N<sub>2</sub><sup>+</sup> ions were found to be a factor of 5 or more lower than chemisorbed nitrogen sputter yields. In addition, the nitrogen was trapped up to 8 monolayers below the surface. These data suggest that a possible mechanism for reduced erosion rates at the cathode side of the baffle is the formation of surface nitrides, notwithstanding the data on metal nitride erosion rates presented in this paper.

## CONCLUSIONS

Significant reductions in the erosion rates of tantalum, titanium, tantalum nitride, and titanium nitride were observed when nitrogen (3% by mass) was added to the argon propellant. The effect is most pronounced for titanium nitride, followed by tantalum, tantalum nitride, and titanium.

The erosion rates of the metals tantalum and titanium were lower than those of the corresponding metal nitrides, both when the ion engine was operated on pure argon propellant, and when the engine was operated on a mixture of argon and nitrogen (3% by mass). These data, coupled with data from other erosion tests, are inconsistent with the theory that reduced erosion rates observed when adding nitrogen to the propellant are due to the formation of sputter-resistant metal nitrides. The erosion rates of the base metals, however, may have been affected by backflow of facility gases into the discharge chamber.

A mechanism to account for reduced erosion rates at locations downstream of the baffle was suggested in reference 7 and involves the desorption of chemisorbed surface nitrogen by inert-gas ion bombardment. Since the binding energy of the nitrogen is less than that for the metal, nitrogen should be preferentially sputtered. These processes, when the surface nitrogen is continuously replenished, as is the case when the nitrogen is mixed with the propellant in an ion engine, may have a significant effect on the effective sputter yield of metals in ion engine discharge chambers. In an ion engine, metals with a chemisorbed nitrogen surface layer may have a smaller effective sputter yield because incoming propellant ions must desorb surface nitrogen. As the concentration of nitrogen increases, nitrogen surface coverage increases until it is complete and the addition of more nitrogen has little or no effect on the erosion rate of the component. At the cathode side of the baffle, however, it is difficult to attribute such large (factor of 30 or more) reductions in

erosion to chemisorption, given the nitrogen sputter yields on tungsten and estimates of the ion energies and current densities of ions in the cathode jet.

## ACKNOWLEDGEMENTS

The authors would like to thank Alison Owens and Robert Toomath for their assistance in completing this work. The work described in this paper was carried out by the Jet Propulsion Laboratory, California Institute of Technology, under a contract with the National Aeronautics and Space Administration. "Approved for public release; distribution unlimited."

## REFERENCES

- (1) Michael Patterson, NASA LeRC, personal communication, (May 1990).
- (2) Brophy, J.R. and Garner, C.E., "Tests of High Current Hollow Cathodes for Ion Engines", AIAA-88-2913, (1988).
- (3) Rawlin, V.K. "Internal Erosion Rates of a 10 kW Xenon Ion Thruster", AIAA-88-2912, (1988).
- (4) Garner, C.E. et al. "The Effects of Gas Mixtures on Ion Engine Erosion and Performance", AIAA-87-1080, (1987).
- (5) Beattie, J.R. "A Model for Predicting the Wearout Life Time of the LeRC/Hughes 30-CM Mercury Ion Thruster", AIAA-79-2079, (1979).
- (6) Rawlins, V.K. and Manteniaks, M.A. "The Effects of Facility Background Gases on Internal Erosion of the 30-CM Mercury Ion Thruster", NASA-TM-73803, (1978).
- (7) Manteniaks, M.A. and Rawlins, V.K. "Sputtering in Mercury Ion Thrusters", NASA-TM-79266, (1979).
- (8) Wilbur, P.J. "A Model for Nitrogen Chemisorption in Ion Thrusters", AIAA-79-2062, (1979).
- (9) Garner, C.E. et al. "Techniques for Reduced Spalling and Increased Operating Life in Xenon Ion Thrusters", AIAA-89-2714, (1989).
- (10) Garner, C.E. et al. "The Effect of Nitrogen on Xenon Ion Engine Erosion", AIAA-90-2591, 1990.
- (11) Othmer, Donald F. Encyclopedia of Chemical Technology, Vol. 15, John Wiley and Sons, New York, New York, (1981), Pgs 873-886.
- (12) Bever, M.B. Encyclopedia of Materials Science and Engineering", V4, Pergamon Press, (1982), pg 3208.
- (13) Wilbur, P.J. "Mercury Ion Thruster Research-1977 Annual Report", NASA CR-135317, (Dec. 1977), pgs 142-149.
- (14) Noriaki Matsunami et al. "Energy Dependence of the Yields of Ion-Induced Sputtering of Monatomic Solids", IPPJ-AM-32, September 1983.
- (15) Winters, H.F. "Sputtering of chemisorbed nitrogen from single-crystal planes of tungsten and molybdenum", Phys Rev B 35 5 2174 (1987).
- (16) Winters, H.F. and Sigmund, P. "Sputtering of chemisorbed gas (nitrogen on tungsten) by low-energy ions", J. Appl. Phys. 45 (11) 4760 (1974).
- (17) V. J. Friedly and P. J. Wilbur, "High Current Hollow Cathode Phenomena", AIAA-90-2587 (1990).
- (18) Askerov, S.G. and Sena, L.A. "Cathode Sputtering of Metals by Slow Mercury Ions", Sov. Phys.-Sol. State 11 (6) 1288 (1969).
- (19) Stuart, R.V. and Wehner, G.K. "Sputtering Yields at Very Low Bombarding Ion Energies", J. Appl. Phys. 33 (7) 2345 (1962).
- (20) D. A. Baldwin et. al. "Low Energy (< 100 eV) Sputtering of Thin Molybdenum Nitride Films", Surf. Sci. 130 361 (1983).





**AIAA-91-3566**

**Near-Term, 100-kW Class Ion Engines**

J. Brophy  
Jet Propulsion Laboratory  
California Institute of Technology  
Pasadena, California

**AIAA/NASA/OAI Conference on  
Advanced SEI Technologies  
September 4-6, 1991 / Cleveland, OH**

## Near-Term, 100-kW Class Ion Engines

John R. Brophy\*  
*Jet Propulsion Laboratory*  
*California Institute of Technology*  
*Pasadena, CA 91109*

A design approach for large area, high power ion engines is presented. This approach conceptually divides a single engine into a combination of smaller discharge chambers (or segments) configured to operate as a single large area engine. This segmented ion thruster (SIT) approach is shown to enable the immediate development of 100-kW class argon ion engines for operation at a specific impulse of 10,000 s. A combination of six 30-cm diameter ion chambers operating as a single engine can process over 100 kW. Such a segmented ion engine could be built today and would operate from a single power processor unit. The segmented engine design approach may also enable the development of megawatt class ion engines. Potential benefits of the segmented ion thruster design include: mitigation of the span-to-gap problem central to the development of large area, high power ion engines; reduction in hollow cathode emission current requirements; improved fault tolerance; and reduced vacuum system pumping speed requirements for engine development testing.

### Nomenclature

$D_b$	= beam diameter
$e$	= electronic charge ( $1.6 \times 10^{-19}$ coul.)
$E$	= accelerator system electric field
$E_{max}$	= maximum electric field
$f_b$	= beam flatness parameter
$J_A$	= accelerator grid impingement current
$J_b$	= beam current
$J_{nk}$	= neutralizer keeper current
$l_e$	= effective acceleration length
$M_{Ar}$	= atomic mass of argon
$M_{Xe}$	= atomic mass of xenon
$NPPH$	= normalized perveance per hole parameter for xenon ( $2.84 \times 10^{-9}$ A/V <sup>3/2</sup> )
$N_s$	= number of chambers in the segmented ion thruster
$R$	= net-to-total voltage ratio
$R_s$	= span-to-gap ratio
$T$	= thrust
$V_{nk}$	= neutralizer keeper voltage
$V_T$	= total voltage between the grids
$\gamma$	= total thrust loss factor
$e_b$	= discharge loss (eV/beam ion)
$\phi_s$	= screen grid open area fraction

### Introduction

High power ion propulsion systems have been shown to be capable of providing substantial benefits for the Space Exploration Initiative.<sup>1-7</sup> For ion propulsion to fulfill this promise, however, requires the development of ion engines which can process input powers on the order of hundreds to thousands of kilowatts at specific impulses in the range 7,000 to 10,000 seconds with useful lifetimes of 10,000 hours.

From 1961 to approximately 1981 most ion engine research focused on the use of mercury propellant. A 150-cm diameter mercury ion engine was operated at input powers as high as 130 kW with a specific impulse of 8,150 seconds and an overall efficiency of 70%.<sup>8</sup> In other work a mercury ion engine was operated at specific impulses greater than 16,000 seconds.<sup>9</sup> The J-Series<sup>10</sup> mercury ion thruster, which was designed for a maximum input power of 2.7 kW at a specific impulse of 3,000 seconds, was developed to nearly flight readiness for use in the Solar Electric Propulsion Stage (SEPS).

Since 1981 most ion propulsion research has centered on the use of noble gas propellants, with engine sizes ranging from 10 cm to 50 cm.<sup>11-19</sup> The 30-cm diameter J-

"Copyright © 1991 by the American Institute of Aeronautics and Astronautics, Inc. with permission"

\*Member of the Technical Staff, Member AIAA



Series thruster has been operated at input powers up to 17 kW with a specific impulse of 4,400 seconds using xenon propellant,<sup>17</sup> and a 50-cm diameter thruster has been operated at up to 20 kW at a specific impulse of 4,600 seconds also with xenon.<sup>17</sup>

Ion engines operate by ionizing the propellant gas through electron bombardment and then accelerating the resulting positive ions electrostatically. The magnitude of the applied high voltage which accelerates the ions and the ion charge-to-mass ratio determine the exhaust velocity. Typically greater than 85% of the input power is processed by the positive high voltage supply which accelerates the ions. Most of the remaining 15% of the input power goes to creating the ions and is supplied by a separate discharge power supply as indicated in the generic power supply schematic shown in Fig. 1.

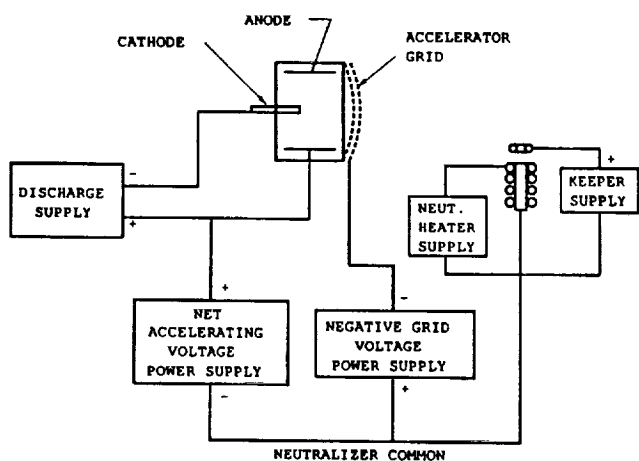


Fig. 1 Generic ion engine power supply schematic.

The attractive feature of ion propulsion is that the electrostatic acceleration process is almost 100% efficient. In practice the acceleration efficiency is typically 99.7%. This nearly lossless acceleration mechanism promises to enable the development of ion engines which can process megawatts of input power while maintaining reasonable engine component temperatures without active cooling. It also is responsible for the high overall engine efficiencies characteristic of ion propulsion. Furthermore, this feature almost guarantees that the effort expended in scaling ion engines up to the megawatt power level will be rewarded with an engine efficiency that is close to that of current projections.

This paper describes an approach to high power ion engine design which enables near-term development of

noble gas ion engines capable of processing hundreds of kilowatts of input power at specific impulses in the range 7,000 to 10,000 seconds. The use of this design approach to scale ion engines up to the megawatt level is also discussed.

### Ion Engine Scaling

Space charge effects in the accelerator system of ion engines place an upper limit on the thrust density (and hence power density) which ion engines can achieve at a given specific impulse. Therefore, to increase the power and thrust capabilities of an ion engine it is necessary to increase the area of the ion accelerator system while maintaining a constant thrust density. For conventional ion engines with a circular cross section, increasing the accelerator system area is accomplished by increasing the engine diameter. This has led to the development of engines sizes ranging from 5 to 150 cm in diameter over the past 30 years.

To maintain a constant thrust (and power) density as the engine diameter is increased requires that the grid-to-grid separation remain constant. This requirement results in increasing values of the grid span-to-gap ratio, i.e., the ratio of accelerator system diameter to the grid separation. The current state-of-the-art, 30-cm diameter, ion accelerator system has a span-to-gap ratio of approximately 500. The maximum achievable span-to-gap ratio is limited by mechanical constraints imposed by fabrication and handling procedures, as well as by thermal effects which serve to alter the grid separation during engine operation.

A conventional circular ion engine using argon propellant and operating at a specific impulse of 10,000 seconds would require a beam diameter of approximately 2.2 m to process one megawatt. Assuming a maximum electric field between the grids of 3000 V/mm, this thruster would require the development of an accelerator system with a span-to-gap ratio of about 1700. This is a factor of 3.4 beyond the state-of-the-art, and would have to be developed for an engine diameter which is more than a factor of seven greater than the present 30 cm thruster.

Aside from increasing the active grid area, the power processed by an ion engine may be increased by increasing the net accelerating voltage. For a given propellant this voltage determines the engine specific impulse. For the Space Exploration Initiative, specific impulses in the range 7,000 to 10,000 seconds are required. With argon propellant, this translates into net accelerating voltages which are roughly a factor of two higher than that typically used on the 30 cm thruster with

xenon propellant (which was designed for operation at specific impulses less than 4,000 seconds).

Finally, the use of lighter atomic mass propellants increases the current handling capability of the accelerator system at a given voltage, which in turn increases the power processed by the engine. Therefore, to scale ion engines up to megawatt power levels it is necessary to significantly increase the active accelerator system area, operate at high applied net accelerating voltages, and use light atomic mass propellants. The last two of these items must together be consistent with the specific impulse range required for the application of the high power engine.

### Segmented Engine Design

The development of 100-kW and megawatt class ion engines must be achieved primarily by scaling up the active grid area for beam extraction by one or two orders of magnitude from the current state-of-the-art. To overcome span-to-gap limitations associated with continuously increasing the diameter of the conventional circular ion engine, alternate engine geometries have been proposed including an annular engine configuration<sup>20</sup> and a rectangular engine design.<sup>21</sup> This paper describes a "Segmented Ion Thruster" (SIT) design in which multiple grid sets together with discrete ion sources (or segments) are used to increase the total active grid area per "engine." An example of a SIT design which uses six discrete ion sources is shown in Fig. 2. The total accelerator system area is six times the area of each individual ion source segment.

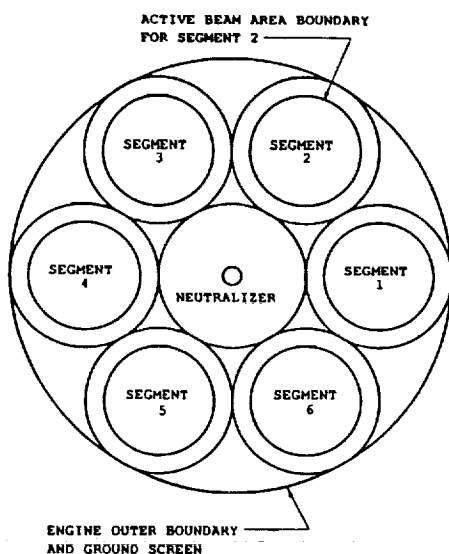


Fig. 2 Example of a segmented ion thruster (SIT) with six ion source chambers.

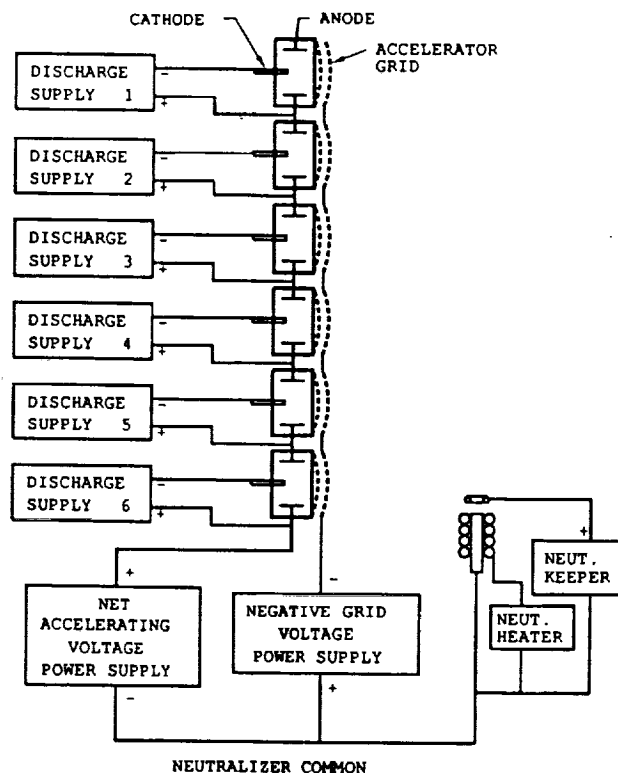


Fig. 3 Power supply schematic for the segmented ion thruster with six segments.

The six individual ion source segments are configured to operate as a single ion engine from a single power processor unit as suggested in Fig. 3. Multiple discharge power supplies, as indicated in this schematic, are used to individually control the emission current from each cathode. A similar arrangement of multiple discharge supplies was used to operate the 1.5-m diameter, 130-kW mercury ion engine.<sup>6</sup> Heater power supplies for the segment cathodes are not shown because the individual discharge supplies could be used to heat the cathodes for start-up. Similarly, separate cathode starter power supplies are not shown. The high voltage required to start the cathode is assumed to come from a boost supply which is included in the discharge supply. A single positive net accelerating voltage power supply, a single negative grid high voltage power supply and a single set of neutralizer power supplies complete the power processor unit for the segmented ion thruster.

Although not shown in Fig. 3, in practice each of the segments would be electrically isolated from the others through its own high voltage propellant isolators and insulating standoffs. If a high voltage fault (such as a

screen to accelerator grid short) should develop in one segment, that segment would be shut down and then isolated from the high voltage power supplies through the use of relays. Thus, failure of one segment would not result in complete failure of the engine, but would instead only decrease the engine thrust by the factor  $(N_s - 1)/N_s$ .

The SIT design may, in some sense, be considered as the third step in ion engine evolution to higher power levels. The lowest power ion sources are made with accelerator systems that consist of a single aperture. Child's law limits the total current that can be extracted from this single aperture for a given applied voltage, and typical power levels are tens of watts. The second generation of ion sources make use of multiple aperture accelerator systems. The current per hole is still limited by Child's law but multiple holes are used to significantly increase the total current. For multiple aperture grid systems the total current is limited by the achievable span-to-gap ratio and by the maximum electric field which can be sustained between the grids. With multiple aperture grid systems steady-state ion engine power levels of up to 130 kW have been demonstrated.

The third step makes use of multiple grid sets per engine. Span-to-gap and electric field considerations still limit the current per grid set but multiple grid sets are used to significantly increase the total beam current. Total engine power levels of substantially greater than 100 kW should be relatively easily achievable. This engine configuration is somewhat analogous to a multicylinder automobile engine. An alternate analogy is that of segmented mirrors used in the development of large optical telescopes.

The segmented engine design approach is feasible largely because of the use of noble gas propellants rather than mercury. This is due to the substantial simplification of the propellant flow control system for noble gas propellants relative to that for mercury. It should also be noted that as far as the high voltage power supplies are concerned, the segmented ion thruster configuration is electrically indistinguishable from more conventional non-segmented configurations. That is, the positive high voltage power supply which accelerates the ions cannot tell that the ions originate from separate discharge chambers.

The SIT approach enables large total accelerator system areas to be achieved through the use of smaller, more manageable, individual ion source components. The use of relatively small ion chamber diameters mitigates the span-to-gap problem central to the development of large area, high power ion engines. Furthermore, each segment has a dedicated hollow cathode which operates at a

fraction of the total engine discharge current (depending on the number of segments in the engine). This decreased discharge current requirement and the use of one cathode per ion chamber has the following additional advantages relative to other high power ion engine design approaches: it minimizes the cathode-jet problem of high current hollow cathodes, it mitigates the plasma uniformity problem characteristic of large diameter engines or unusual engine geometries, and it eliminates the starting problems associated with the use of multiple cathodes in a single discharge chamber.

### Performance Projections

Ion engine performance projections were made using the equations given in Ref. 22 with appropriate modifications for the SIT configuration. Briefly the beam current for a given SIT configuration, assuming argon propellant, is calculated from a perveance expression in the following form,

$$J_b = N_s f_b \phi_s (NPPH) \left( \frac{D_b}{l_s} \right)^2 \sqrt{\frac{M_x}{M_a}} V_T^{3/2}, \quad (1)$$

where  $N_s$  is the number of segments in the SIT configuration and  $D_b$  is the active beam diameter of each segment. The value for the normalized perveance per hole parameter,  $NPPH$ , was selected to provide the best fit to experimental perveance data for 30-cm diameter ion engines operating on xenon.<sup>21</sup> The square root of the ratio of xenon to argon atomic masses corrects Eq. (1) for the use of argon instead of xenon. The total voltage,  $V_T$ , and effective acceleration length,  $l_s$ , in Eq. (1) are calculated for each case to be consistent with assumptions made for the maximum span-to-gap ratio, the maximum electric field between the grids, the allowable range of the net-to-total voltage ratio, and the desired specific impulse. Once the beam current is calculated from Eq. (1) the thrust and input power are calculated as follows,

$$T = N_s \gamma J_b \sqrt{\frac{2M_a V_T R}{e}}, \quad (2)$$

and,

$$P_e = N_s J_b \left( V_T R + e_b + V_c + \frac{J_A}{J_b} (1-R) V_T \right) + N_s J_{nk} V_{nk}. \quad (3)$$

The SIT approach is applicable to any individual chamber size and any number of chambers per engine. Possible SIT engine configurations with 3, 4, 6 and 8

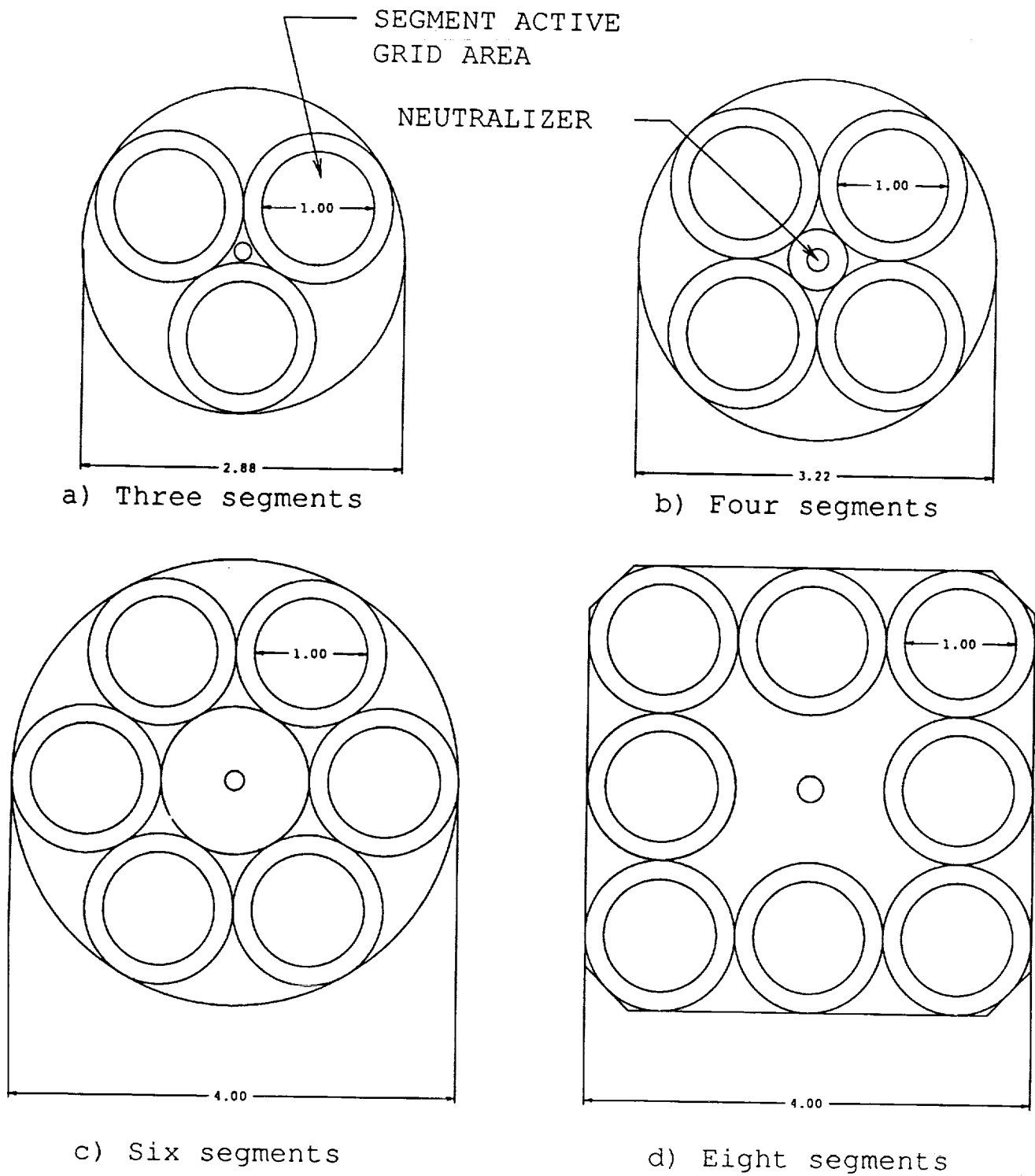


**Fig. 4 Segmented ion engine configurations.**

chambers are shown in Fig. 4. Projected SIT engine performance values are given in Table 1 for individual segment sizes of 30, 50, 75 and 100 cm diameter. The first two columns in this table refer to SIT configurations with six segments per engine, in the last two columns eight segments per engine are used. The first column in this table refers to relatively conservative engine performance which could be achieved using six state-of-the-art 30-cm diameter chambers. This SIT configuration has a total grid area equivalent to a 70-cm diameter circular engine. The maximum total engine input power for this configuration is projected to be 101 kW with an overall efficiency of 69% at a specific impulse of 10,000 seconds. Each of the six segments must process one sixth of this power, or 16.7 kW each. For each segment this is accomplished by operating with a beam current of 4.73 A at a beam voltage of 3360 V. Assuming a discharge voltage of 45.0 V and a discharge loss of 175 eV/ion, the discharge current per chamber is only 18.2 A. These parameters are well within the current state-of-the-art for 30-cm diameter ion sources. The J-Series thruster has been operated at beam currents up to 5.9 A with argon propellant,<sup>23</sup> and at input power levels of up to 17 kW with xenon.<sup>17</sup> The total thruster beam current is 6 times 4.73 A, which is 28.4 A, and greater than 95 kW (28.4 A x 3360 V) of the input power is contained in the exhaust.

Thus, with this approach a 100 kW argon ion engine could be built today using existing technology. Furthermore, building and testing such an engine now will provide the necessary experience for the development of larger, higher power segmented ion engines in the future.

Projected performance data for the 6 x 30-cm segmented engine are given in Table 2 over the range of specific impulses from 7000 to 10,000 s, and the input power versus  $I_{sp}$  from this table is plotted in Fig. 5.

The second column in Table 1 indicates the projected performance which could be achieved through the use of a 6 x 50-cm segmented ion engine. Specifically, this engine, which would consist of six 50-cm diameter ion sources of the type currently under development,<sup>17</sup> can process over a quarter of a megawatt at a specific impulse of 10,000 s. Operation of 50-cm diameter chambers with argon propellant at a specific impulse of 10,000 s will require the development of an accelerator system with a span-to-gap ratio of only 338, which is significantly less than the state-of-the-art for 30-cm thrusters, and less technologically demanding than the accelerator systems currently under development for the 50-cm chamber.<sup>24</sup> Furthermore, the use of relatively high applied voltages means that the accelerator system electrodes can be more robust (i.e., thicker) than those designed for closer grid spacings and lower voltages. With this approach near

term development of a 0.25 MW argon ion engine appears to be possible.

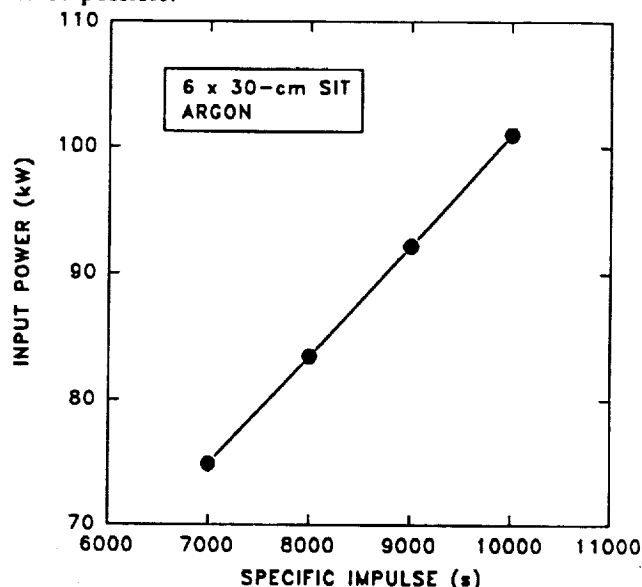


Fig. 5 Variation of input power as a function of specific impulse for the 6 x 30-cm SIT.

The third column in Table 1 gives the performance of an 8 x 75-cm segmented thruster. For operation with argon at a specific impulse of 10,000 s and a maximum electric field of 2600 V/mm, assigning the span-to-gap ratio equal to the present state-of-the-art (i.e. 500) results in a chamber diameter of approximately 75 cm. The use of eight 75-cm chambers results in an ion engine which can process over 800 kW and produce a thrust of greater than 10 N. Each 75-cm chamber requires a discharge current of 130 A assuming a discharge voltage of 40 V. A 12.7-mm diameter hollow cathode has been operated on argon at emission currents of up to 150 A for as long as 24 hours and at 100 A for 1,000 hours.<sup>25</sup>

The development of such an engine will require scaling the existing 50-cm diameter ion chamber up to 75-cm. In particular, the development of a 75-cm diameter, high voltage accelerator system with a span-to-gap ratio of 500 will be required, and long duration tests of hollow cathodes operating with emission currents greater than 100-A will be necessary. The significance of the segmented design approach is that an 800-kW argon ion engine (with a specific impulse of 10,000 s) could be built without requiring the development of an ion accelerator system which has a span-to-gap ratio that is greater than the current state-of-the-art. (Note, the effective span-to-gap-ratio of this engine design is 1400, based on an effective engine diameter of 2.12 m.) Furthermore, hollow cathodes have already been tested at emission currents necessary to support development of such an engine. Thus, the development of 800-kW class

**Table 1 Projected Performance of Segmented Ion Thrusters**

	6 x 30-cm SIT	6 x 50-cm SIT	8 x 75-cm SIT	8 x 100-cm SIT
Number of Segments	6	6	8	8
Segment Diameter (cm)	30	50	75	100
Specific Impulse (s)	10,000	10,000	10,000	10,000
Maximum Power into Engine (kW)	100	289	844	1640
Engine Efficiency	0.69	0.70	0.70	0.70
Thrust (N)	1.42	4.10	12.0	23.2
Propellant Flow Rate (g/s)	0.014	0.042	0.12	0.24
Propellant Efficiency	0.80	0.80	0.80	0.80
Total Grid Area (m <sup>2</sup> )	0.383	1.11	3.53	6.28
Equivalent Diameter (m)	0.70	1.19	2.12	2.83
Engine Mass (kg)	50	120	300	440
Each Segment				
- Input Power (kW)	16.7	48.2	106	205
- Beam Current (A)	4.7	13.6	29.7	57.6
- Discharge Current (A)	18.2	59.3	130	252
- Discharge Voltage (V)	45.0	40.0	40.0	40.0
- Grid Gap ( $E_{max} = 2600$ V/mm) (mm)	1.4	1.4	1.5	1.4
- Beam Voltage (V)	3360	3360	3360	3360
- Total Voltage (V)	3730	3730	3730	3730
- Span-to-Gap Ratio	200	338	500	700
- Screen Hole Diameter (mm)	2.2	2.2	2.2	2.2
- Screen Grid Thickness (mm)	0.56	0.56	0.63	0.56
- Discharge Propellant Efficiency	0.85	0.85	0.85	0.85

argon ion engines appears to be a readily achievable goal.

The power density of this engine is no greater than that of the 30-cm diameter J-Series ion engine operating at 17 kW, and at this power level the J-Series thruster was demonstrated to be self-radiating. Consequently, the 8 x 75-cm segmented engine will not require active cooling even at 800 kW. The engine specific mass is projected to

be less than 0.4 kg/kW.

The forth column in Table 1 gives the projected performance for an 8 x 100-cm segmented ion engine. In this case the engine consists of eight 100-cm diameter ion chambers, which together can process a maximum input power of 1.6 MW and produce a thrust of 23 N at a specific impulse of 10,000 s. The span-to-gap ratio

Table 2 Projected Performance versus  $I_{sp}$  for 6 x 30-cm Segmented Ion Engine

	$I_{sp} = 7000$ s	$I_{sp} = 8000$ s	$I_{sp} = 9000$ s	$I_{sp} = 10000$ s
Input Power (kW)	74.9	83.5	92.2	101
Thrust (N)	1.43	1.43	1.43	1.43
Total Engine Efficiency	0.66	0.67	0.68	0.69
Total Beam Current (A)	40.6	35.5	31.6	28.4
Beam Voltage (V)	1650	2150	2720	3360
Grid Gap* (mm)	0.69	0.90	1.14	1.40
Total Propellant Flow Rate (g/s)	0.0209	0.0182	0.0162	0.0146

\* Assumes a maximum electric field of 2600 V/mm

required for the accelerator system of each 100-cm diameter chamber is 700 (the effective span-to-gap ratio based on the equivalent circular engine diameter is over 2000). The discharge current for each chamber is 250 A. Both the span-to-gap ratio and the discharge current requirements are beyond the current state-of-the-art, but not by enormous amounts.

Thus, the development of a 1.6 MW argon ion engine appears to be a technically reasonable objective, and one which would require only reasonable extensions to the state-of-the-art for key engine components using the SIT design approach. This would require scaling the chamber diameter by a factor of 2 from the existing 50-cm chamber and increasing hollow cathode current capability from the 100-150 A range to 250 A. From Fig. 3, such an engine would fit within a square 4-m on a side and have a mass of approximately 440 kg (for a specific mass of approximately 0.3 kg/kW). Power density considerations dictate that the engine would be self-radiating at 1.6 MW. The overall engine efficiency would be approximately 70%.

Operation of the 8 x 100-cm thruster at specific impulses less than 10,000 s will result in decreased power handling capability (if the maximum span-to-gap ratio is maintained at 700) or will require development of 1-m diameter accelerator systems with significantly greater span-to-gap ratios as shown in Fig. 6 and Tables 3 and 4.

#### Engine Performance and Life Testing

Development of high power ion engines will require both performance and life testing. Life testing places greater demands on the vacuum test facility because of the necessity to perform long duration tests at very low

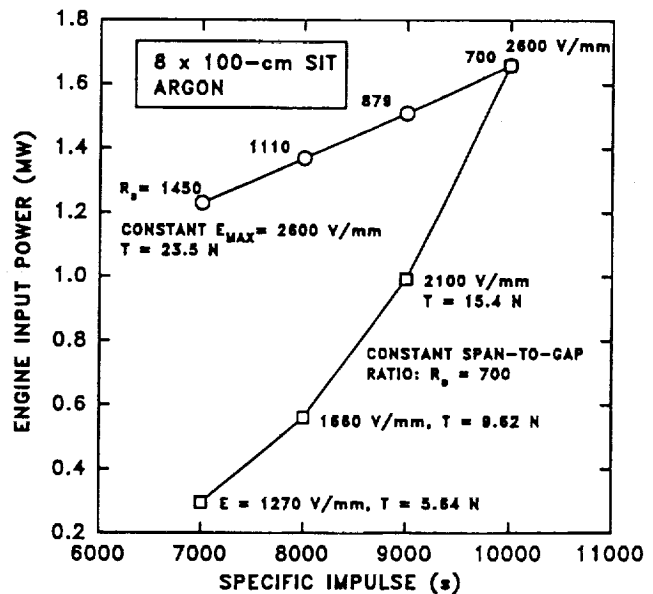


Fig. 6 Performance variation with specific impulse for the 8 x 100-cm SIT with constant  $E_{max}$  and constant  $R_s$  assumptions.

pressures. Vacuum system pressures less than  $10^{-5}$  torr during engine operation are required to minimize accelerator grid erosion due to facility induced charge-exchange ions. To life test a 100-kW argon ion engine at a pressure of  $5 \times 10^{-6}$  torr requires a pumping speed of  $1.2 \times 10^6$  liters/s, life testing a 1.6-MW engine requires  $2.0 \times 10^7$  liters/s. Ion engine performance testing, on the other hand, can generally be done at vacuum system pressures as high as  $3 \times 10^{-5}$  torr so that pumping speed

**Table 3 Projected Performance for 8 x 100-cm SIT at  $E_{max} = 2600$  V/mm**

	Isp = 7000 s	Isp = 8000 s	Isp = 9000 s	Isp = 10000 s
Input Power (MW)	1.23	1.37	1.51	1.66
Thrust (N)	23.5	23.5	23.5	23.5
Total Engine Efficiency	0.66	0.67	0.68	0.69
Total Beam Current (A)	666	583	518	466
Total Discharge Current (A)	2914	2550	2270	2040
Grid Gap (mm)	0.69	0.90	1.14	1.40
Span-to-Gap Ratio	1450	1110	879	712
Accelerator System Electric Field (V/mm)	2600	2600	2600	2600
Total Propellant Flow Rate (g/s)	0.342	0.300	0.266	0.240

**Table 4 Projected Performance for 8 x 100-cm SIT with Constant Span-to-Gap Ratio**

	Isp = 7000 s	Isp = 8000 s	Isp = 9000 s	Isp = 10000 s
Input Power (MW)	0.295	0.560	0.992	1.66
Thrust (N)	5.64	9.62	15.4	23.5
Total Engine Efficiency	0.66	0.67	0.68	0.69
Total Beam Current (A)	160	239	340	466
Total Discharge Current (A)	699	1040	1490	2040
Grid Gap (mm)	1.40	1.40	1.40	1.40
Span-to-Gap Ratio	700	700	700	700
Accelerator System Electric Field (V/mm)	1270	1660	2110	2600
Total Propellant Flow Rate (g/s)	0.082	0.123	0.175	0.240



requirements for performance testing are generally only about one sixth that required for life testing.

For the segmented ion thruster, most of the development work can be performed at the segment level. Major life limiting design deficiencies can be identified by life testing individual segments. Life testing at the segment level reduces the pumping speed requirement by  $1/N$ , relative to life testing the complete engine. Ultimately the complete engine will have to be performance tested and segment-to-segment interactions identified. A life test of the complete engine may not be necessary depending on the extent of these interactions.

### Reliability

The segmented ion thruster design approach is capable of enabling the near-term development of 100-kW class ion engines and may enable the development of megawatt class engines, but at the expense of increased engine and power processor complexity. It should be noted, however, that increased complexity does not always result in reduced reliability. The benefits of the segmented design, i.e., reduced span-to-gap requirements, reduced cathode emission current requirements, increased fault tolerance and reduced vacuum system pumping speed requirements, must be weighed against the increased complexity. Presumably there is some number of segments per engine at which the increased complexity offsets the benefits of the segmented engine design. It is not obvious whether this number is as small as two or perhaps greater than ten. Segmented engine designs with as many as eight segments are presented in this paper and are believed to be reasonable. A detailed reliability analysis of a segmented ion engine versus a conventional engine configuration would be required to resolve this issue.

### Arcing

Ion accelerator system operation at voltage differences of a few thousand volts between electrodes 1.4 mm apart with plasmas on both sides of the electrodes will occasionally produce a high current low voltage arc discharge between these electrodes. To clear this low voltage arc and restore normal engine operation, it is necessary to remove the voltages from the electrodes for some period of time (typically on the order of one second) and then reapply these voltages. This capability for high voltage "recycling" is built into the design of the high voltage power supplies for ion engines. Recycling rates are generally a function of the electric field stress between the electrodes and the current density of ions extracted.

It would also seem likely that the recycle rate is a function of the total active grid area, all else being equal. Thus, one may expect that a large area ion engine may recycle more frequently than a smaller one under identical operating conditions.

Extended tests of 30-cm diameter xenon ion engines with electric field stresses of 2300 to 2400 V/mm have resulted in average recycle rates of between 1.5 and 2.4 recycles/hour.<sup>16,26</sup> If the recycle rate scales with active grid area then the 6 x 30-cm SIT thruster may have a recycle rate of between 9 and 15 recycles/hour. This rate is high, but not unreasonably so. Scaling the recycle rate with beam area up to the 8 x 100-cm SIT size results in a recycle rate of between 135 and 216 recycles/hour. This is one recycle every 17 to 26 seconds. This is clearly an unacceptable recycling rate, however, the recycling rates from Refs. 16 and 24, upon which this conclusion is based, may be artificially high as a result of operation at relatively high vacuum chamber pressures which significantly increased the erosion rates of the accelerator grids in these tests. Never-the-less, much additional work will be required to determine the variation of recycle rates with grid area.

### Conclusions

A segmented ion thruster (SIT) design consisting of multiple discharge chambers and ion accelerator systems is presented as a method by which 100-kW class ion engines could be developed today using components from existing 30-cm diameter ion engines. Furthermore, this design approach may enable the development of megawatt class ion engines by reducing the performance requirements of key engine components, such as the ion accelerator system and the main discharge hollow cathode. Benefits of the segmented ion thruster design approach include: reduction in the required accelerator system span-to-gap ratio for large area engines, reduction in the required hollow cathode emission current, mitigation of the plasma uniformity problem associated with the development of large area ion engines, increased tolerance of accelerator system faults, and reduction in the vacuum system pumping speed required for engine development testing. The optimum number of segments per engine must be determined through a trade off between these benefits and the engine and power processor system complexities which increase with the number of segments. Useful, megawatt class ion engines must have high voltage recycle rates that are comparable to present state-of-the-art engines. That is, ion accelerator systems must be developed in which the recycle rate per unit grid area is significantly less than that demonstrated in recent long

duration engine tests.

### Acknowledgments

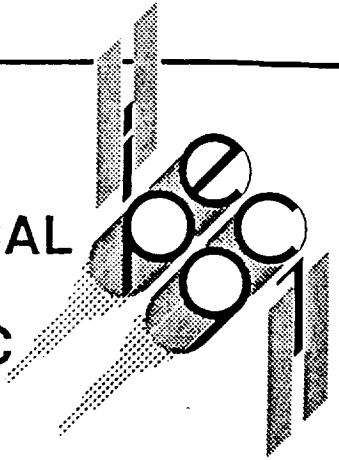
The work described in this paper was carried out by the Jet Propulsion Laboratory, California Institute of Technology, under contract with the National Aeronautics and Space Administration.

### References

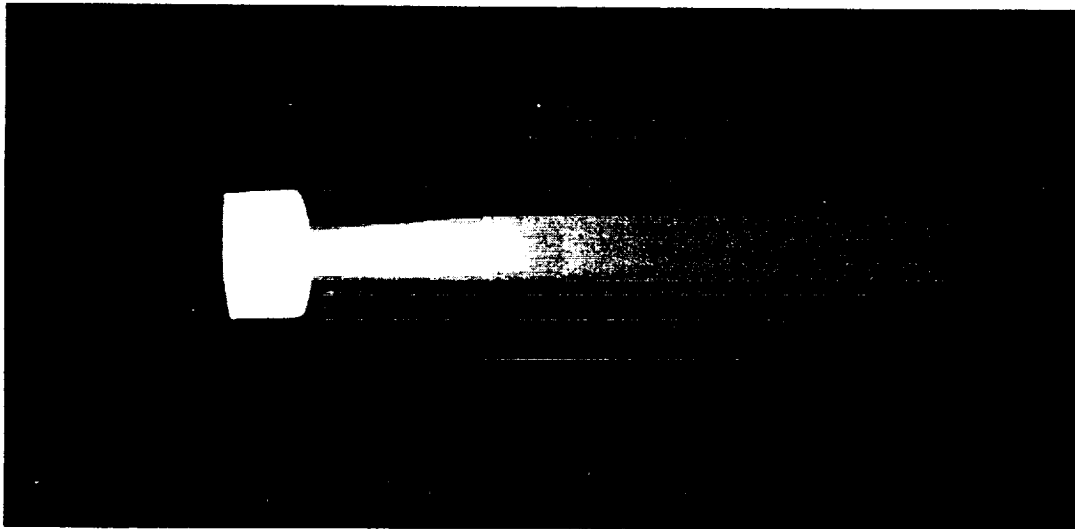
- <sup>1</sup>Brophy, J. R. and Barnett, J. W., "Benefits of Electric Propulsion for the Space Exploration Initiative," AIAA Paper No. 90-2756, July 1990.
- <sup>2</sup>Gilland, J. H., Myers, R. M., and Patterson, M. J., "Multimegawatt Electric Propulsion System Design Considerations," AIAA Paper No. 90-2552, July 1990.
- <sup>3</sup>Frisbee, R. H., et al., "Advanced Propulsion Options for the Mars Cargo Mission," AIAA Paper No. 90-1997, July 1990.
- <sup>4</sup>Hack, K. J., et al., "Evolutionary Use of Nuclear Electric Propulsion," AIAA Paper No. 90-3821, Sept. 1990.
- <sup>5</sup>Galecki, D. L. and Patterson, M. J., "Nuclear Powered Mars Cargo Transport Mission Utilizing Advanced Ion Propulsion," NASA TM 100109, July 1987.
- <sup>6</sup>Gilland, J. H., "Synergistic Use of High and Low Thrust Propulsion Systems for Piloted Missions to Mars," AIAA-91-2346, June 1991.
- <sup>7</sup>Frisbee, R. H., Blandino, J. J., and Leifer, S. D., "A Comparison of Chemical Propulsion, Nuclear Thermal Propulsion, and Multimegawatt Electric Propulsion for Mars Missions," AIAA-91-2332, June 1991.
- <sup>8</sup>Nakanishi, S. and Pawlik, E. V., "Experimental Investigation of a 1.5-m-diam. Kaufman Thruster," *J. Spacecraft*, Vol. 5, No. 7, July 1968, pp. 801-807.
- <sup>9</sup>Byers, D. C., "An Experimental Investigation of a High-Voltage Electron-Bombardment Ion Thruster," NASA TM X-52429, May 1968.
- <sup>10</sup>Bechtel, R. T., "The 30 cm J Series Mercury Bombardment Thruster," AIAA Paper No. 81-0714, April 1981.
- <sup>11</sup>Fearn, D. G., "The Control Philosophy of the UK-10 and UK-25 Ion Thrusters," AIAA Paper No. 90-2629, July 1990.
- <sup>12</sup>Latham, P. M., Martin, A. R., and Bond, A., "Design, Manufacture and Performance of the UK-25 Engineering Model Thruster," AIAA Paper No. 90-2541, July 1990.
- <sup>13</sup>Bassner, H., "Status of the Space Testing Programs of the RF-Ion Thruster RIT-10," AIAA Paper No. 91-1889, June 1991.
- <sup>14</sup>Groh, K. H., et al., "Inert Gas Performance of the RIT 35 Main Propulsion Unit," IEPC-88-098, presented at the 20th International Electric Propulsion Conference, Garmisch-Partenkirchen, Germany, October 1988.
- <sup>15</sup>Beattie, J.R. and Matossian, J.N., "Xenon Ion Propulsion for Stationkeeping and Orbit Raising," IEPC-88-052, presented at the 20th International Electric Propulsion Conference, Oct. 1988.
- <sup>16</sup>Patterson, M. J. and Verhey, T. R., "5 kW Xenon Ion Thruster Life Test," AIAA Paper No. 90-2543, July 1990.
- <sup>17</sup>Patterson, M. J. and Rawlin, V. K., "Performance of 10-kW Class Xenon Ion Thrusters," AIAA 88-2914, July 1988.
- <sup>18</sup>Nakamura, Y., Matsumoto, M., Kitamura, S., and Miyazaki, K., "Discharge Performance of a 12 cm Cusp Xenon Ion Thruster," IEPC 88-061, presented at the 20th International Electric Propulsion Conference in Garmisch-Partenkirchen, Germany, October 1988.
- <sup>19</sup>Yamagiwa, Y., et al., "A 30-cm Diameter Xenon Ion Thruster -- Design and Initial Test Results," IEPC 88-095, presented at the 20th International Electric Propulsion Conference in Garmisch-Partenkirchen, Germany, October 1988.
- <sup>20</sup>Aston, G. and Brophy, J. R., "A 50-cm Diameter Annular Ion Engine," AIAA-89-2716, July 1989.
- <sup>21</sup>Gilland, J. H., Myers, R. M. and Patterson, M. J., "Multimegawatt Electric Propulsion System Design Considerations," AIAA-90-2552, July 1990.
- <sup>22</sup>Brophy, J. R. and Aston, G., "A Detailed Model of Ion Propulsion Systems," AIAA Paper No. 89-2268, July 1989.
- <sup>23</sup>Rawlin, V. K., "Operation of the J-Series Thruster Using Inert Gas," NASA TM 82977, November 1982.
- <sup>24</sup>Brophy J. R. and Gamer, C. E., "Tests of High Current Hollow Cathodes for Ion Engines," AIAA-88-2913, July 1988.
- <sup>25</sup>Rawlin, V. K., "Ion Optics for High Power 50-cm-dia Ion Thrusters," AIAA Paper No. 89-2717, July 1989.
- <sup>26</sup>Rawlin, V. K., "Internal Erosion Rates of a 10-kW Xenon Ion Thruster," AIAA Paper No. 88-2912, July 1988.

**IEPC 91-074**

**AN EXPERIMENTAL AND NUMERICAL  
INVESTIGATION OF AN APPLIED-  
FIELD MAGNETOPLASMADYNAMIC  
SPACE PROPULSION ENGINE**



**Thomas J. Pivrotto and Keith D. Goodfellow  
Jet Propulsion Laboratory  
California Institute of Technology  
Pasadena, California**



**AIDAA/AIAA/DGLR/JSASS 22nd International  
Electric Propulsion Conference**

**October 14-17, 1991 / Viareggio, Italy**

AN EXPERIMENTAL and NUMERICAL INVESTIGATION of an APPLIED-FIELD  
MAGNETOPLASMA DYNAMIC SPACE PROPULSION ENGINE

Thomas J. Pivrotto and Keith D. Goodfellow

Jet Propulsion Laboratory  
California Institute of Technology  
Pasadena, California  
USA

ABSTRACT

In order to enhance the exploration of our solar system the basic cost of such operations must be reduced. One major reduction would come from the development of more propellant efficient primary and secondary space propulsion systems. Electric propulsion devices promise to accomplish this reduction in basic operating cost by greatly reducing the mass of propellant required in space. One such device, the Applied Field Magnetoplasmadynamic (MPD) thruster, is being studied and some preliminary results on diffuser effects in MPD test facilities, on thermal modeling of the engine cathode and on thrust measurements are presented here.

1. INTRODUCTION

The eventual robotic and/or human exploration of our solar system will require enhancement and development of a broad spectrum of technologies, including primary and secondary space propulsion. Indeed, one of the major impediments to this human advancement is the basic cost of transportation in space and this cost is overwhelmingly determined by the shear weight of the propellant needing to be moved from place-to-place. Therefore, a very large advance can be made toward the eventual success of this mission by the development of propellant efficient space propulsion systems.

One very promising approach is the substitution of electrical energy for chemical energy in our thruster technology, whenever this becomes feasible. Feasibility is guaranteed for any mission that requires a large nuclear or solar electrical power source for mission primary objectives. However, even without this need, the potential saving in needed propellant mass is so great that the net mass saving for some select missions, after the entire power supply mass is charged to the propulsion system, is still very attractive.

Of the many different concepts for deriving thrust from a propellant accelerated by electrical means, the single concept that can utilize electrical power levels in the hundreds to thousands of kilowatts is a magnetoplasmadynamic (MPD) thruster. Work on these devices has been ongoing, and at a low level, since 1965. This work has been impeded by a lack of understanding of the physical processes occurring, both in the plasma and in the engine components, when the temperatures, electric currents and electric/magnetic fields become very high, as they must if this device is to become efficient and practical.

This paper reports on the preliminary results of some ongoing research on one

particular type of MPD, called an Applied Field Magnetoplasmadynamic thruster. The applied field refers to an applied radial and axial magnetic field. Specifically, the results of measurements of the effectiveness of a diffuser to lower the engine test environmental pressure are presented. This work addresses one aspect of the problem of providing adequate and affordable test facilities for MPD developmental testing. In addition, some preliminary results from our attempt to model the heat flow and temperature distributions in the MPD cathode are presented and discussed. This is part of our effort to understand the flow of heat and resultant temperatures in all engine components under very severe conditions. Finally, a few experimental results from our unique duel beam thrust stand, are presented. This stand was designed and built to separately measure the thrust developed by the arched and by the applied field electromagnet, simultaneously.

2. DIFFUSER EFFECTS

It is a well known fact that vacuum tank ambient pressure can have an adverse effect on several of the thrust producing mechanism, as well as on the measurement of thrust, in all forms of electric propulsion devices. For example, in thermal devices such as arcjets, a high background pressure will interfere with the nozzle expansion processes, will contribute to cooling through natural and forced convection and can interfere with thrust stand operation because of possible impingements of fluid currents on sensitive thrust stand elements. These same interfering mechanism can be applicable to applied field MPD testing as well; and in addition, background gas entrainment and acceleration in the engine plume and effects on plasma conductivity would be additional considerations. Because of these potentially adverse effects, testing with adequate background pressure levels in electric propulsion test facilities is critical to the ultimate development of electric propulsion engines.

A literature survey of background pressure effects on self and applied field MPD performance can be found in Reference 1. For self field MPD's they found no indications of adverse effects when vacuum tank pressures were below one mtorr. For applied field MPD's it was found that high background pressure could either degrade performance by interfering with one or more thrust producing mechanism or enhance performance by entrainment and acceleration. These effects depend on type and flow rate of propellant gas used, background gas type and pressure. For example, with hydrogen flowing at 3.5 mg/s and nitrogen as background gas the vacuum tank pressure had to be kept below about 8 mtorr to avoid adverse effects on performance measurements.

For ammonia propellant at various flow rates and with a variety of background gases a pressure below 0.3 mtorr was required.

If these required steady state vacuum tank pressures are to be maintained by continuous pumping only, the facility costs, and for long term life testing (a practical necessity for all electric propulsion devices) the operating costs, can become prohibitive. For example, the installation cost of a modern diffusion pump is approximately  $\$12 \times 10^6$  per gm/sec of hydrogen and  $\$15 \times 10^6$  per gm/sec of ammonia vapor. Cryopumping of hydrogen or dissociated ammonia would be even more prohibitive for full scale engine life testing. The only known method of reducing the required pump capacity would be to take advantage of the directed kinetic energy in the test engine plume. This can be done by considering the engine as part of an ejector pumping system and/or directing the high energy plume into a diffuser designed to decelerate the exhaust gases while maintaining as much of the original stagnation pressure as is possible.

A review of the literature seemed to indicate that ejector/diffuser design methods and/or data for ambient pressures below one torr do not exist. Extrapolations from the existing, high pressure, data were used as a starting point and several preliminary designs have been fabricated and tested with high power arcjets and moderate power applied-field MPD engines. Examples of some relevant results of these tests are shown in Figures 1 and 2.

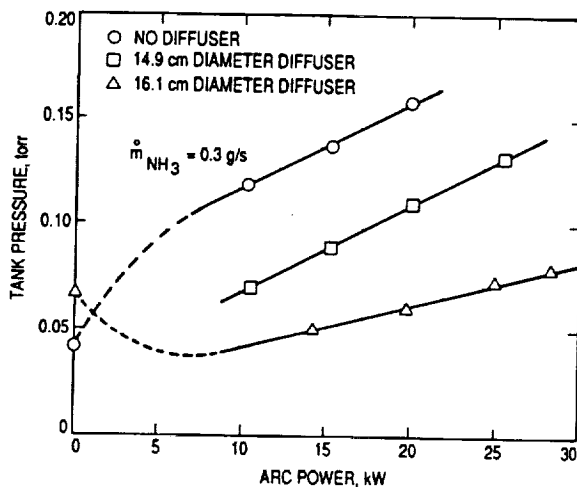


Figure 1. Arcjet Diffuser Data.

Data obtained from a 30 kW class arcjet engine is shown in Figure 1. This data was obtained in the facility shown in Figure 3, using the engine design shown in Figure 4. The vacuum tank pressure was measured with a Baratron pressure gauge calibrated in the range of one to one thousand mtorr. The initial test was made without the diffuser but with the engine plume directed at the inlet to the water cooled elbow shown in Figure 3. The propellant was ammonia so that with zero arc power the diffuser passed pure ammonia vapor and with arc power the gas was a mixture of nitrogen and hydrogen with possibly some residual ammonia vapor if

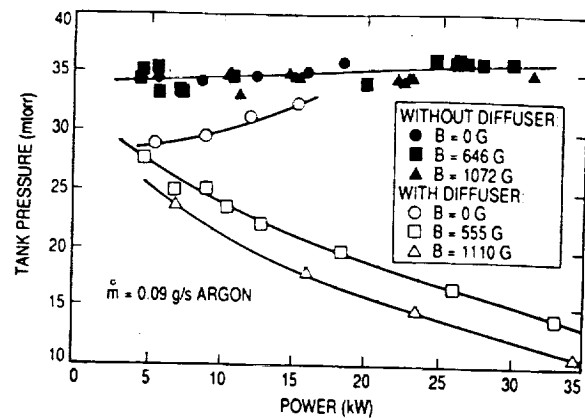


Figure 2. MPD Diffuser Data.

dissociation was incomplete. Therefore, for arc power greater than zero the tank pressure increases, partly because of a decrease in mean molecular weight (increase in the volume rate of flow due to dissociation), and partly due to an increase in gas temperature. Note that since the engine is facing into the open elbow, some recovery of stagnation conditions must be

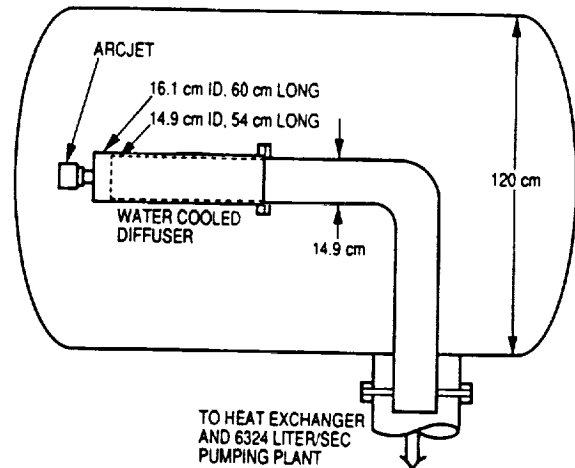


Figure 3. Arcjet Test Facility and Diffuser Installation.

occurring, resulting in a lowering of the tank pressure.

Next, a water cooled constant diameter diffuser with a 14.9 cm ID and a length of 53.7 cm was installed as shown in Figure 3. The mouth of this diffuser was 6.4 cm from the engine exit plane. With this diffuser, a vacuum tank pressure decrease of 50 mtorr, independent of arc power, was experienced. Again, the vacuum tank pressure increase with arc power is attributed to increased dissociation and gas temperature. With this diffuser, a secondary effect may also be that the arcjet plume could balloon out and not be completely captured by the diffuser mouth. To alleviate this potential problem, a second diffuser, slightly bigger in diameter and length was fabricated, installed and tested. This new diffuser had an internal diameter of 16.1 cm, a length of 60 cm and its mouth was coincident with the arcjet exit plane. The results of this test are also shown in Figure 1. For this test,

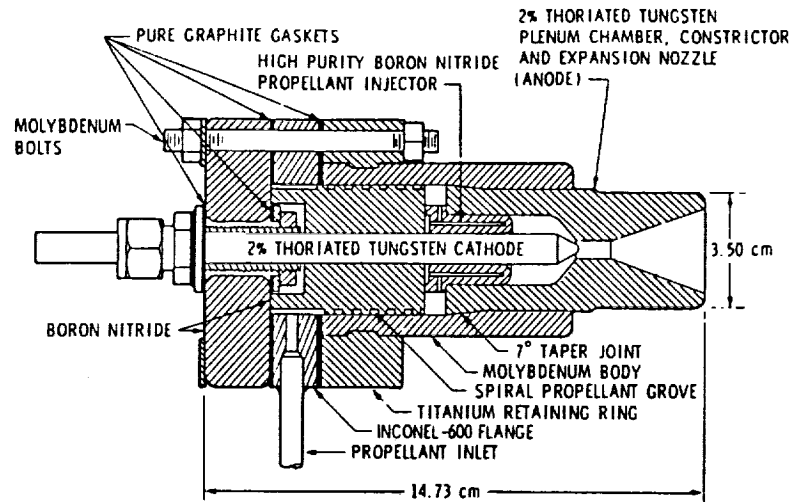


Figure 4. Arcjet Engine Schematic.

the zero arc power data point is higher than the corresponding point for the no diffuser case. This increase in vacuum tank pressure represents the loss of pumping speed (decrease in system conductance) due to the diffuser impedance. However, once the arc is turned on, and regardless of the dissociation and elevated gas temperature, the measured vacuum tank pressure is dramatically reduced from the no-diffuser test and the amount of reduction increases with arc power (increased exhaust velocity). Hence, for this final arcjet diffuser design, the ejector/diffuser effect overcomes dissociation, elevated temperatures and plume ballooning effects and its use results in a very large reduction in vacuum tank back pressure. This means that the investment in pumping plant installation and operating cost could be reduced by more than a factor of two in any proposed new arcjet test facility.

Because of these encouraging results with arcjets a similar, constant diameter, ejector/diffuser was attempted with our

applied-magnetic-field MPD engine test facilities. The design chosen is shown schematically in Figure 5. Since we were trying to achieve a lower vacuum tank pressure in our MPD facility, resulting in more ballooning of the plume, and since we were attempting to use a magnetic nozzle, again resulting in a further expansion of the engine plume we choose a much larger diameter to try first. The design, shown in Figure 5, was a water cooled 46 cm diameter by 123 cm long cylindrical section followed by a 41 cm long cone as a transition to a 25 cm diameter vacuum line. A 6324 liter/sec mechanical pumping plant was used to pump on the diffuser outlet and a 1227 liter/sec mechanical pumping plant was used to continue pumping on the vacuum tank, directly. The mouth of the diffuser was located 3 cm from the engine exit plane in order to provide visual access to the plume.

The data obtained with this ejector/diffuser is shown in Figure 2. Argon, at a constant mass flow rate of 0.09 g/s, was used as the propellant, the arc power was

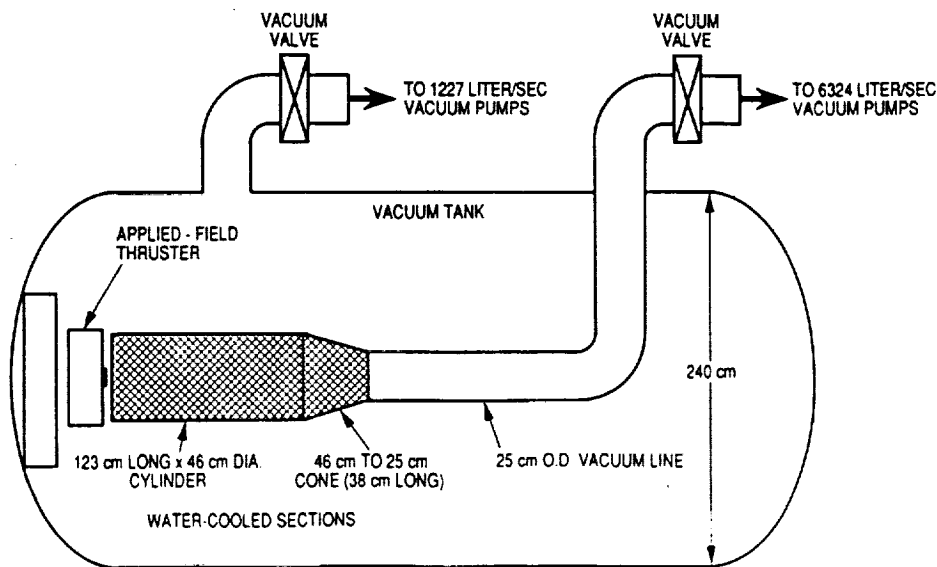


Figure 5. Schematic of MPD Diffuser Installation

varied between 5 and 35 kW and the magnetic field strength, measured at the cathode tip, was varied between 0 and 1110 gauss. The initial tests were conducted without the diffuser installed. The vacuum line was removed from the vacuum tank and both pumping plants were used to pump on the tank itself. Vacuum tank pressure measurements, obtained with a calibrated Baratron gauge, were made as a function of arc power and magnetic field strength and are shown as filled data points in Figure 2. Notice that the pressure is independent of magnetic field strength and rises only slightly with arc power. Since these tests were performed in a large tank the exhaust gas temperature most likely was equilibrated with the tank walls before it arrived at the two pump out ports. The slight rise in vacuum tank pressure with arc power could then have been caused by a slight rise in temperature at the pump out ports.

Next the ejector/diffuser was installed as shown in Figure 5, and essentially the same test parameters were repeated. This data is shown as open data points in Figure 2. Notice that without the magnetic field and at low power the vacuum tank pressure was reduced by the diffuser but as the arc power was increased the tank pressure also increased as it did for the arcjet tests of Figure 1. This result may have been caused by ballooning of the plume and elevated gas temperatures which canceled out most of the diffuser/ejector effect. Note that with the addition of the diffuser and vacuum line the conductance of that part of the pumping system was much increased, but the ejector/diffuser effect was still great enough to overcome these and still produce a moderate reduction in tank pressure.

When the magnetic field was turned on a dramatic new result appeared. The vacuum tank pressure was reduced further and continued to drop with increasing arc power and magnetic field strength. These results seem to indicate that as the exhaust velocity is increased by either increasing the arc power or applied magnetic field strength, or both, the ejector/diffuser effect increases, as is manifested by a reduced vacuum tank pressure. This effect continued at lower mass flow rates and higher arc power and magnetic field strength. The extreme, to date, was a measured vacuum tank pressure of 6 mtorr with 0.07 g/s of argon, 40 kW of arc power and a magnetic field strength of 1360 gauss.

All indications seem to suggest that at still higher arc power and/or magnetic field strength the diffuser will lower the vacuum tank pressure further. At a pressure of one mtorr, or less, it will become possible to turn on our three diffusion pumps, thus adding  $260 \times 10^3$  liters/sec to our pumping capacity. Hence, with a sufficiently high plume velocity, the ejector/diffuser effect can overcome the added impedance of the diffuser and vacuum line and overcome the elevated gas temperature at the entrance to the pump out system, and effectively reduce the vacuum tank pressure to a regime low enough to make meaningful engine voltage and thrust measurements.

### 3. CATHODE THERMAL MODEL

Radiation cooled MPD thrusters are preferable to liquid cooled thrusters for

space applications because of their simpler design and higher efficiency.<sup>1</sup> However, in radiation cooled thrusters the operating power can be severely limited by the thruster thermal design. Recent experiments at JPL have shown severe cathode tip melting even at moderate powers (less than 50 kW). A thermal analysis of the cathode tip region was completed to investigate this problem.

A one-dimensional heat transfer analysis was performed on the cathode tip to achieve a first-order approximation. Two tip geometries were considered, namely a flattened conical tip and a flattened hemispherical tip. The tip area is the same for both shapes and the dimensions are shown in Figure 6. The axial temperature drop

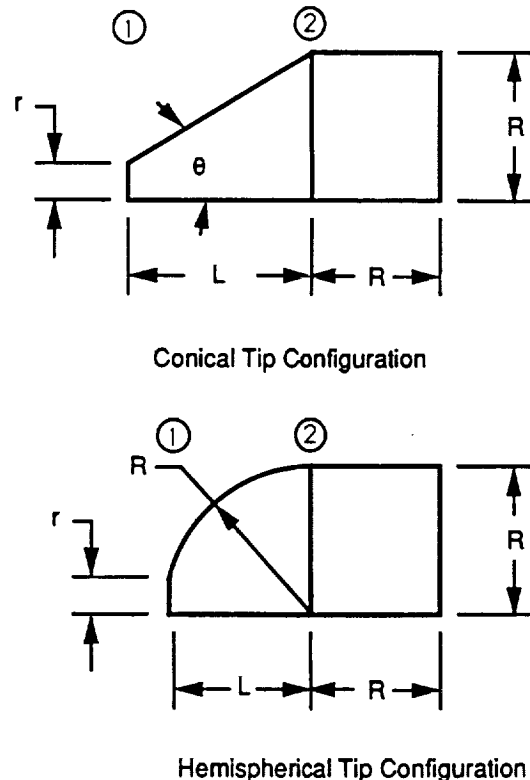


Figure 6. Cathode tip geometry.

across the tip can be obtained by integrating equation 1 along the axial direction with the appropriate cross-sectional area for the shape of interest. Since the cathode base temperature is usually fixed by the cooling capability of the thruster, the calculated cathode temperature drop can be used to estimate the tip temperature. It can then be determined whether or not the tip is likely to melt.

$$T_1 - T_2 = \Delta T = \frac{q}{k_c} \int_{x_1}^{x_2} \frac{dx}{A_c} \quad (1)$$

where  $q$  is the heat load (W),  $k_c$  is the thermal conductivity (constant), and  $A_c$  is the cross-sectional area.<sup>3</sup> The temperature drop for the conical and spherical tip geometries are given by equations 2 and 3 respectively. Values for the MPD thruster

Table 1. MPD Geometry Parameters

$r = 0.25 \text{ cm}$
$R = 0.95 \text{ cm}$
$\theta = 30^\circ$
$k_t = 1.0 \text{ W/cm K}$
$L_{\text{conical}} = 1.21 \text{ cm}$
$L_{\text{hemis}} = 0.916 \text{ cm}$

cathode geometry are given in Table I and the results are given in Table II.

$$\Delta T = \frac{q}{\pi k_t \tan(\theta)} \left( \frac{1}{r} - \frac{1}{R} \right) \quad (2)$$

$$\Delta T = \frac{q}{2\pi R k_t} \ln \left( \frac{R + (R^2 - r^2)^{1/2}}{R - (R^2 - r^2)^{1/2}} \right) \quad (3)$$

A two-dimensional analysis was also performed using a commercially available finite element analysis package. A base with a length equal to one radius was added to each tip shape to make the heat flux out of the base more uniform. A 1 kW heat load was applied uniformly across each tip. The resulting temperature contours for the constant thermal conductivity case are shown in Figures 7 and 8 for the conical and hemispherical tips respectively.

The large temperature gradients within the cathode require the use of temperature dependent properties for accurate results. The thermal conductivity as a function of temperature is shown in Figure 9.<sup>3</sup> The contours for the temperature dependent thermal conductivity case are shown in Figures 10 and 11. A comparison of the temperature drops for the various cases is

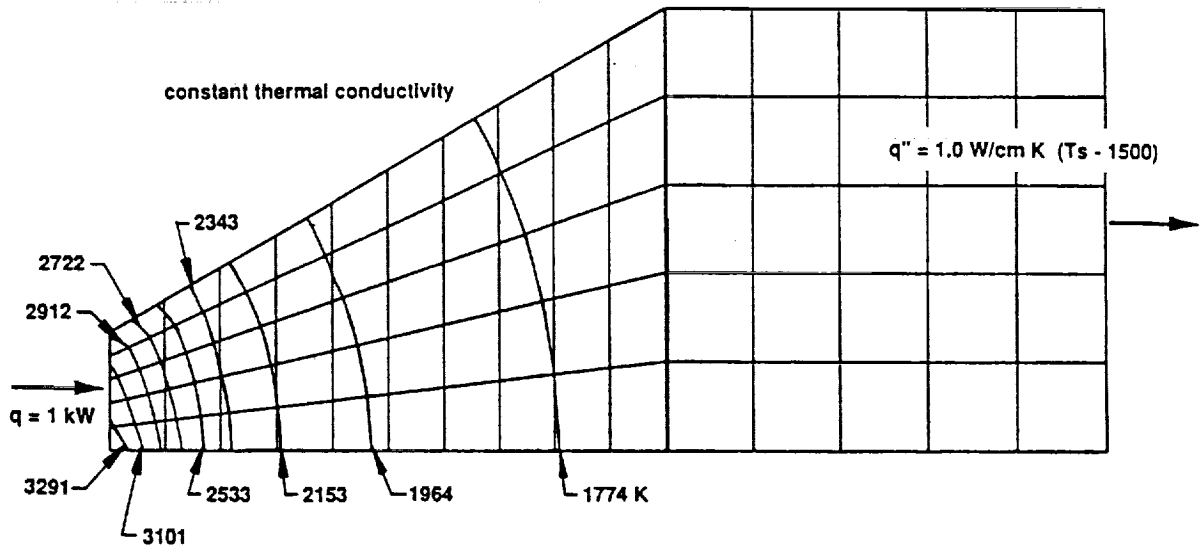


Figure 7. Conical tip temperature contours with constant thermal conductivity

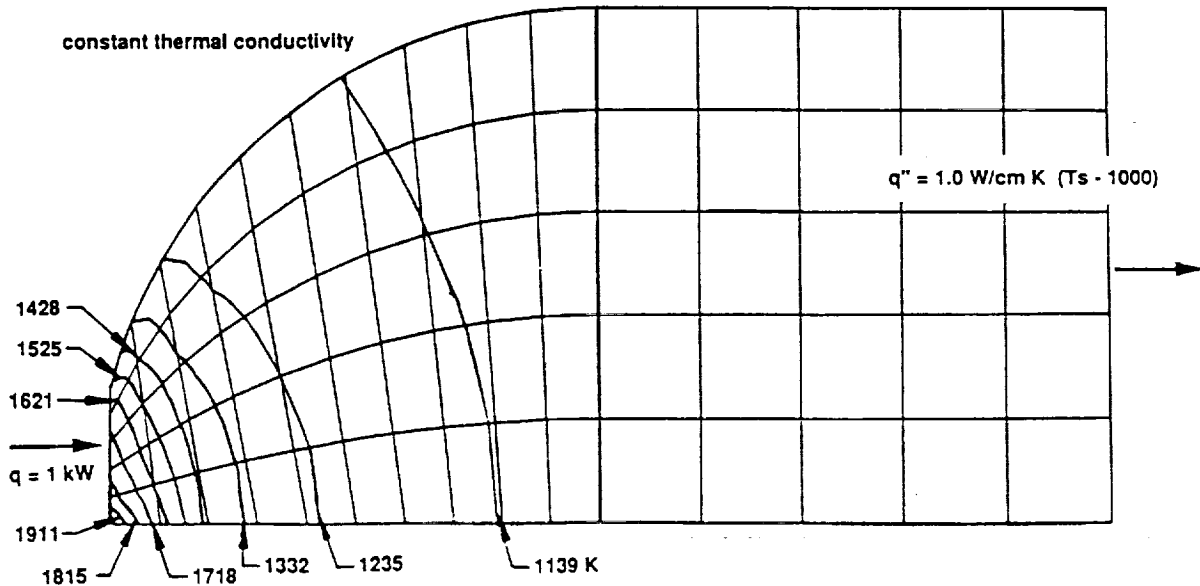


Figure 8. Hemispherical tip temperature contours with constant thermal conductivity



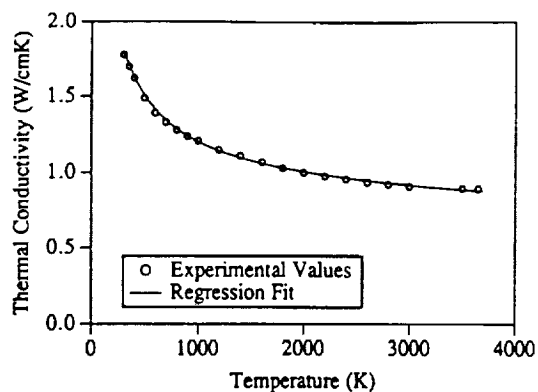


Figure 9. Thermal conductivity temperature dependence.

presented in Table II. Although different base temperatures were used for the two different shapes, the temperature drops are comparable. The lower base temperature was selected for the hemispherical tip so that all of the temperatures would be lower and the nonlinear conductivity effect would be larger and therefore providing a "worst case". With the same base temperature, the hemispherical tip temperature drops would be slightly smaller.

Comparing the temperature drops between the 2-D and 1-D analyses, it is apparent that the 1-D approximation is relatively good. Two temperature drops are given for the 2-D analysis, namely, along the centerline (center) and along the outer surface. The temperature drop predicted from the 1-D analysis falls between the inside and the

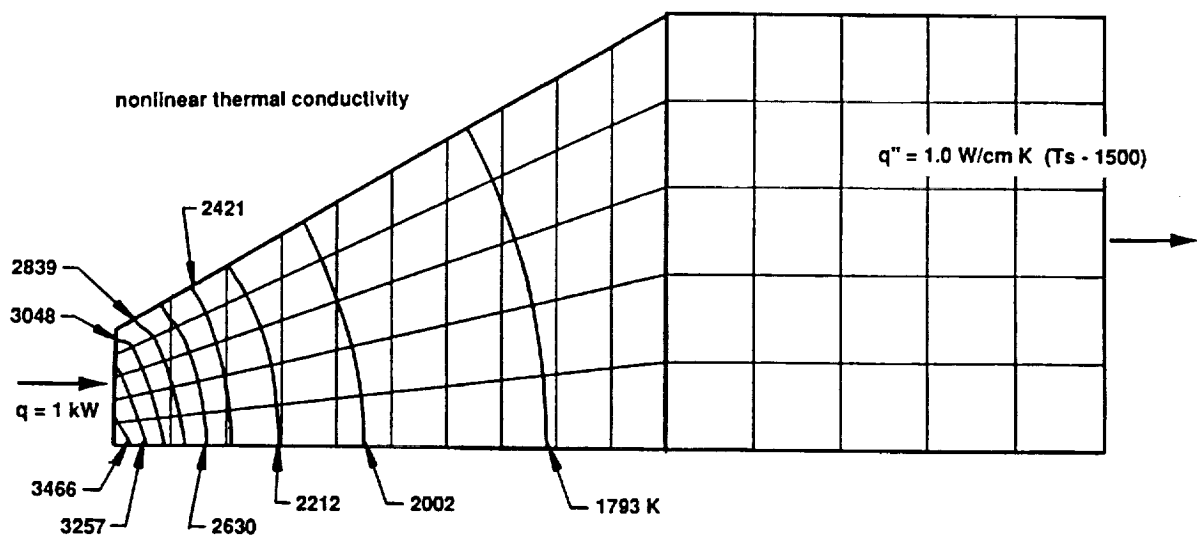


Figure 10. Conical tip temperature contours with temperature dependent thermal conductivity

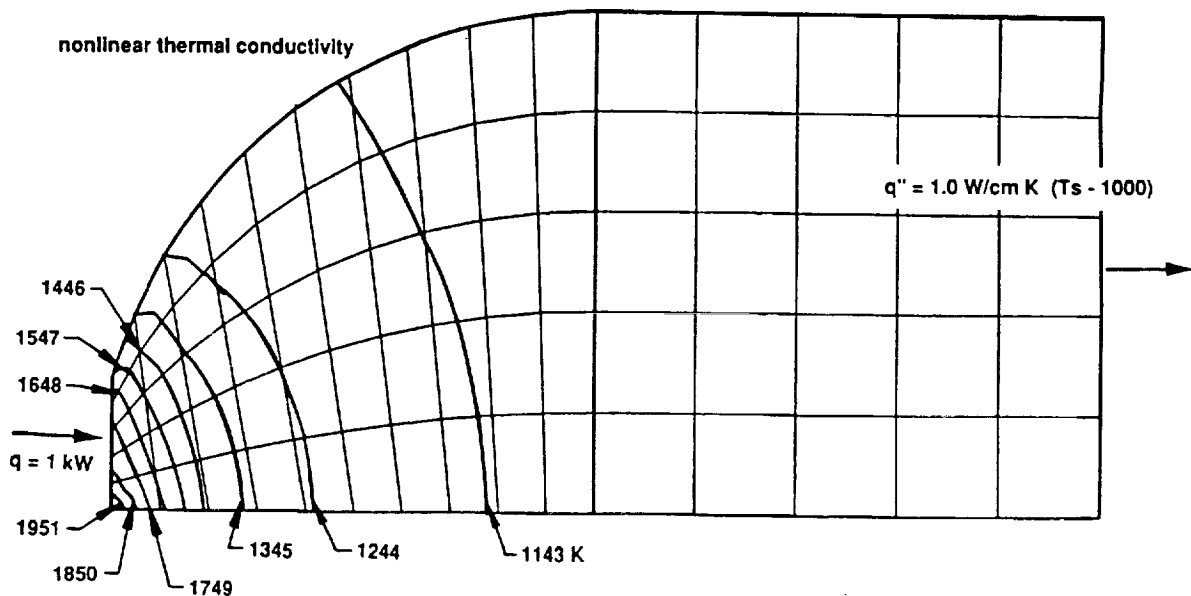


Figure 11. Hemispherical tip temperature contours with temperature dependent thermal conductivity

Table 2. Tip Geometry Temperature Drops

CASE		Conical Tip $\Delta T$	Hemispherical Tip $\Delta T$	$\Delta T_{con} / \Delta T_{hem}$
1-D		1625	674	2.41
2-D Constant $k_t$	Center	1762	897	1.96
	Outside	1194	451	2.65
2-D Variable $k_t$	Center	1952	939	2.08
	Outside	1295	468	2.77

outside values for both 2-D cases. Therefore, for predicting gross temperature drops within the cathode the 1-D analysis is acceptable. However, The large radial temperature gradients at the cathode tip can not be predicted with the 1-D model. The temperature at the centerline of the tip is significantly higher than the outside tip temperature. The 1-D model will only predict a rough average tip temperature, and can not predict the radial components since this is a 2-D effect. As can be seen in Figures 7, 8, 10 and 11, the temperature on the centerline at the tip can be significantly larger than the outside temperature. This may explain the crater formations observed at the tips of arcjet cathodes after long duration tests.<sup>5</sup> For equivalent base temperatures, the expected tip temperature for the hemispherical tip should be significantly lower than that for the conical tip; and therefore less susceptible to melting.

Testing of the MPD thruster even at moderate powers (up to 50 kW) produced severe cathode tip melting. Figure 12 shows a photograph of two conical cathode tips after testing with clear evidence of surface melting. Figure 13 shows an illustration of a typical cathode profile before and after testing. The post-test cathode tip angle is approximately 45°. This indicates that the cathode tip was eroded significantly during operation until it reached a geometry that was compatible with the operating

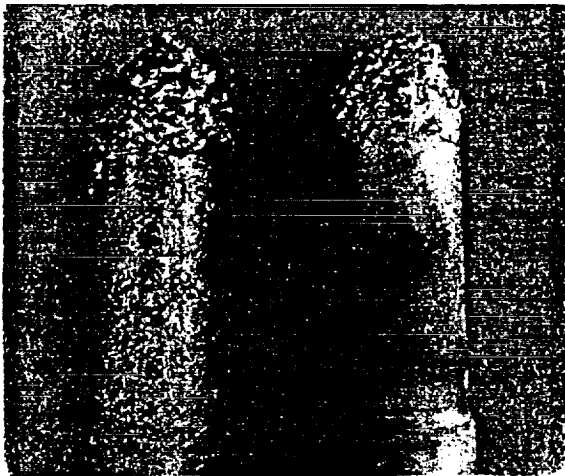
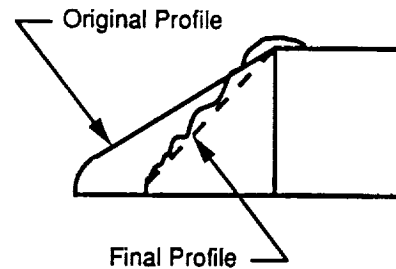


Figure 12. Experimental cathode tips after testing



Experimental Cathode Tip Variation

Figure 13. Illustration of pre-test and post-test cathode tip geometries.

conditions. The final configuration is surprisingly close to the hemispherical shape. This result, along with the analysis, provided the basis for selecting the spherical tip shape.

The spherical tip shape has since been tested up to 60 kW with no evidence of melting. Also, the starting and operating characteristics are similar with both tip shapes.

#### 4. THRUST STAND

An attempt is being made to develop a dual beam thrust stand capable of measuring, separately, the thrust component developed by the arthead and by the electromagnet, simultaneously. These measurements are an important part of our effort to understand how the applied magnetic field enhances the performance of these engines. A schematic of the thrust stand is shown in Figure 14. Both the electromagnet and arthead are suspended from a water cooled framework that is an integral part of the vacuum tank header. The electromagnet is suspended by two 1.27 cm diameter stainless steel tubes that also carry the electromagnet cooling water to and from the solenoid windings and water cooled solenoid shield. These two tubes are in a plane that is perpendicular to the thrust direction and act as the flexures in the system. As the electromagnet develops thrust, through the interaction between its axial and radial magnetic field components and the electric currents flowing in the plasma, these two tubes are bent slightly and the amount of bending is measured with a Linear Variable Differential Transformer (LVDT). The LVDT output is calibrated by applying weights horizontally along the electromagnet centerline with a pulley system. This calibration can be

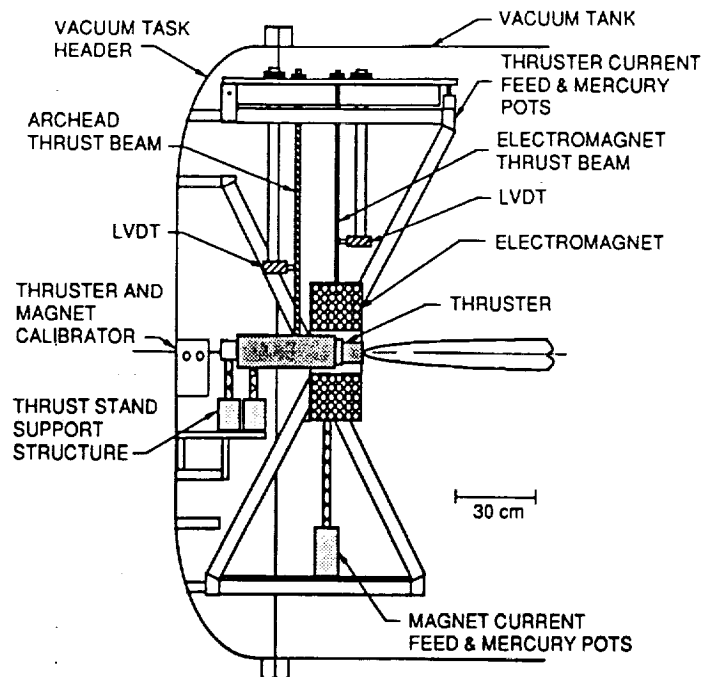


Figure 14. Schematic of MPD Dual Beam Thrust Stand.

accomplished, remotely, after the vacuum tank has been evacuated. The archhead and its heavy copper bus bars was suspended from a single 1.27 cm diameter stainless steel tube which was also used to carry the propellant gas to the engine. The measurement of deflection and appropriate calibrations of the archhead system was essentially the same as that of the electromagnet. The electric power to both the electromagnet and archhead was transferred onto the thrust stand through pots of mercury, as shown in Figure 14.

A preliminary attempt to measure thrust with this stand, while using ammonia vapor as the propellant, is shown in Figure 15. The ammonia mass flow rate was 0.050 g/s and the

magnetic field strength, measured at the cathode tip, was set at 638 and 1110 gauss. Due to the unavailability of our large

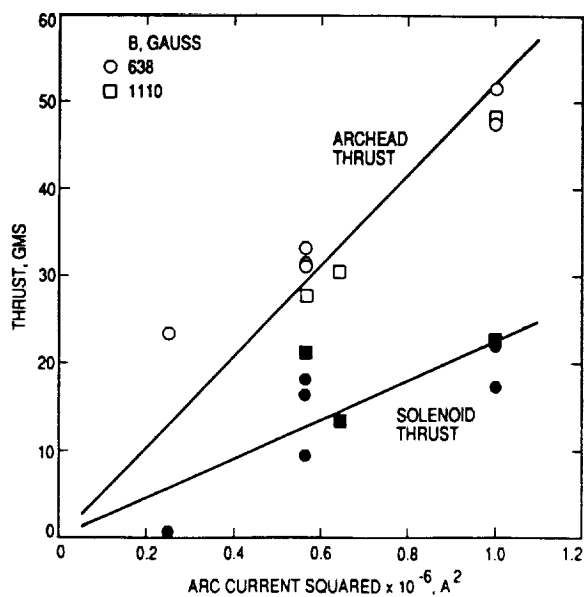


Figure 15. MPD Thrust Data.

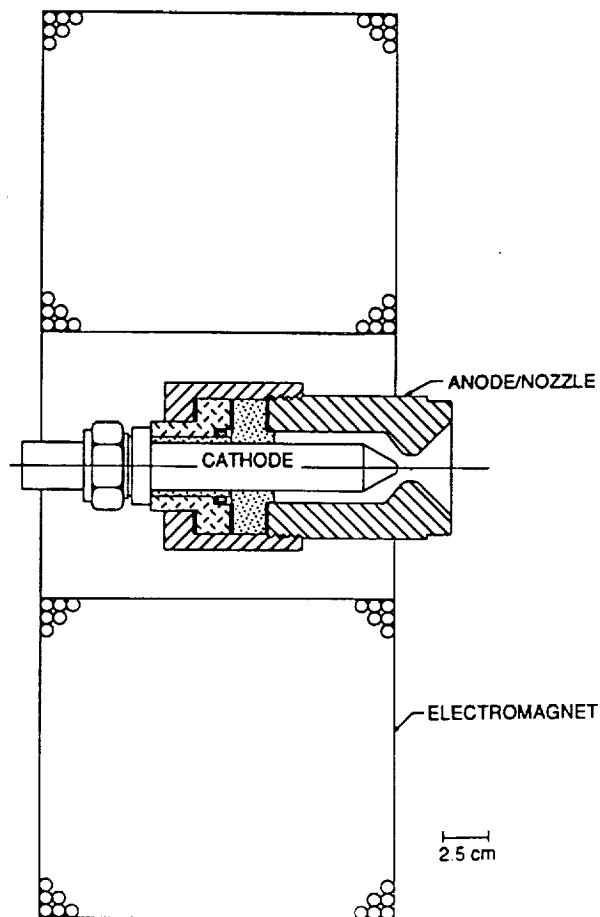


Figure 16. MPD Engine Schematic

vacuum pumping plant during this test the vacuum tank back pressure was measured to vary between 120 and 130 mtorr. The engine design used for this test is shown in Figure 16; however, the cathode tip was hemispherical and the throat diameter had been increased from the original 1.27 cm to 3.18 cm by erosion during previous testing. A photograph of the cathode tip and eroded throat is shown in Figure 17. The data obtained from this preliminary test is shown in Figure 15 as the arthead and solenoid thrust versus the square of arthead current with magnetic field strength as a parameter. The reason for the large amount of scatter is not known at this time and is being investigated. The results suggest that, for low arc current and magnetic field strength, the electromagnet increases the total thrust by 50 % or less. This is in qualitative agreement with the ammonia calculations published in Reference 6. These measurements will be continued to higher arc current and magnetic field strength and to lower ammonia mass flow rates.



Figure 17. Photograph of MPD Cathode Tip and Eroded Throat.

##### 5. ACKNOWLEDGMENTS

The work described in this paper was carried out by the Jet Propulsion Laboratory, California Institute of Technology, under

contract with the National Aeronautics and Space Administration. "Approved for public release; distribution unlimited."

The authors wish to thank William R. Thogmartin, Allison G. Owens and Robert L. Toomath for invaluable aid in the design, fabrication, instrumentation, checkouts and operation of all experimental hardware.

##### 6. REFERENCES

1. J. S. Sovey and M. A. Mantenicks, "Performance and Lifetime Assessment of MPD Arc Thruster Technology," NASA TM-101293 and paper AIAA-88-3211, 24th Joint Propulsion Conference, Boston, Massachusetts, July 11-13, 1988.
2. M. Auweter-Kurtz, H. Kurtz, W. Merke, H. Schrade, C. Sleziona and T. Wegmann, "High Power Steady State MPD Thruster Final Report," Institute for Spacecraft Systems, University of Stuttgart, IRS-90-P4. March 1990.
3. F. P. Incropera and D. P. DeWitt, Fundamentals of Heat Transfer, John Wiley & Sons, Inc., New York, 1981, pp. 75-79.
4. A. Goldsmith, T. E. Waterman and H. J. Hirschborn, Handbook of Thermophysical Properties of Solid Materials, Vol. I: Elements, The Macmillan Company, New York, 1961, pp. 675-688.
5. W. D. Deininger, A. Chopra, T. J. Pivrotto, K. D. Goodfellow and J. W. Barnett, "30-kW Ammonia Arcjet Technology," JPL publication 90-4, Feb. 1990.
6. "ARCJET TECHNOLOGY RESEARCH and DEVELOPMENT-FINAL REPORT," 3 June 1964 through 11 September 1965. Prepared by RESEARCH AND ADVANCED DEVELOPMENT DIVISION, AVCO CORPORATION, Wilmington, Massachusetts, for NASA Lewis Research Center, Cleveland, Ohio, NASA CR-54687, RAD-TR-65-37, Contract NAS 3-5900.



**AIAA 91-3572**

**Alkali Metal Propellants for  
MPD Thrusters**

J. E. Polk and T.J. Pivrotto  
Jet Propulsion Laboratory  
California Institute of Technology  
Pasadena, California

**AIAA/NASA/OAI Conference on  
Advanced SEI Technologies  
September 4-6, 1991 / Cleveland, OH**

# Alkali Metal Propellants for MPD Thrusters

J. E. Polk<sup>†</sup> and T.J. Pivrotto<sup>†</sup>  
*Jet Propulsion Laboratory  
California Institute of Technology  
Pasadena, California*

## Abstract

Experiments performed in the United States in the 1960's and early 1970's and in the Soviet Union with alkali metal-fuelled MPD thrusters indicate performance levels substantially better than those achieved with gaseous propellants. Cathode wear appears to be less in engines with alkali metal propellants also. A critical review of the available data indicates that the data are consistent and reliable. An analysis of testing and systems-level considerations shows that pumping requirements for testing are substantially decreased and reductions in tankage fraction can be expected. In addition, while care must be exercised in handling the alkali metals, it is not prohibitively difficult or hazardous. The greatest disadvantage seems to be the potential for spacecraft contamination, but there appear to be viable strategies for minimizing the impact of propellant deposition on spacecraft surfaces. Renewed examination of alkali metal-fuelled MPD thrusters for ambitious SEI missions is recommended.

## Introduction

The Space Exploration Initiative (SEI) is an ambitious vision of the human exploration of the solar system that will require significant advances on a number of technological fronts to realize. One of the key technologies in this undertaking is primary spacecraft

propulsion. The availability of high-performance advanced propulsion systems will to a large extent determine the cost and feasibility of achieving the goals of the Initiative. Nuclear Electric Propulsion (NEP) is a candidate system for the robotic planetary missions, lunar and Mars cargo missions, and piloted flights to Mars.

A recent study by Gilland [1] outlined the performance levels necessary for an NEP system to compete with alternatives such as advanced chemical propulsion with aerobraking or nuclear thermal propulsion in typical SEI missions. This study showed that electric power levels greater than a megawatt are required to achieve acceptable trip times for the cargo and piloted missions. The demonstrated capability of the magnetoplasmadynamic (MPD) thruster to process large amounts of power makes it an attractive choice for these missions. However, the savings in propellant mass or trip time compared to alternate propulsion schemes depend on the efficiency and specific impulse the MPD thruster is capable of delivering. For the lunar cargo mission an efficiency of at least 25% is necessary to be competitive for a power supply specific mass of 10 kg/kWe, and at least 40% if the specific mass was 20 kg/kWe. For the Mars cargo mission, an efficiency as low as 25% can be tolerated if the trip time can be extended to 800 days. However, for the Mars piloted mission, the demand for trip times on the order of one year drives the required efficiency to greater than 60%. In all cases the trip time and the initial mass in low earth orbit are substantially reduced if the efficiency is increased. The specific impulse was found to have a secondary impact on the competitiveness of electric propulsion systems. For the lunar cargo mission, a specific impulse of 2000-5000 s is sufficient, while for the Mars missions an

Copyright © 1991 American Institute of Aeronautics and Astronautics, Inc., with permission.

<sup>†</sup> Member of the Technical Staff, Member AIAA

$I_{sp}$  of 4000 s or more is required. In addition to these requirements on the performance of the NEP system, SEI missions place strong demands on thruster lifetime. To reduce the number of engines required to a reasonable number the lifetime must be on the order of 2000–8000 hours [2].

The performance and lifetime demonstrated in current research programs with gaseous propellants are at best marginal for these demanding SEI missions. Efficiencies of up to 20% at 3700 s specific impulse have been achieved with hydrogen propellant in a steady-state applied-field MPD thruster at 83 kW [3] and 22% at 950 s with argon in a steady-state self-field engine at 580 kW [4]. In multimewatt quasi-steady self-field thrusters efficiencies as high as 40% at specific impulses up to 5000 s have been attained [2]. While quasi-steady devices are important diagnostic tools, the high cathode erosion rates inherent in the cold cathode electron emission process render them useless for flight applications [5]. The cathode also appears to be the life-limiting component in steady-state thrusters. Erosion rates sufficiently low to allow several hundred hours of operation have been demonstrated [6,7], but the lifetime of current cathode materials is severely limited by evaporative mass losses [8]. Recent work with barium dispenser cathodes [9,10] has shown that lower operating temperatures can be achieved, but sustained operation for more than a few tens of hours has not yet been demonstrated.

The literature from US programs in the 1960's and early 1970's and from the Soviet Union suggests that substantial gains in performance and lifetime are possible with alkali metal propellants. Efficiencies from 50–60% at specific impulses of 5000–6000 s and reduced cathode operating temperatures and erosion rates have been reported. Based on this evidence, alkali metal-fed MPD thrusters appear capable of satisfying the demanding requirements of SEI missions. The justification for a renewed investigation of the alkali metal-fuelled MPD thruster must be based substantially on the validity of these reported results. However, it is difficult to assess the reliability of the performance and lifetime measurements conducted 20 years ago in the US laboratories, and evaluation of the Soviet program is hampered by the difficulty in obtaining English translations of publications and conference proceedings and the brevity

of the descriptions of experimental techniques in the available literature. The criticism must, under these circumstances, be based on an attempt to identify sources of systematic bias in the measurements as recorded by the researchers.

A discussion of the potential for biases in the performance measurements evolves from an examination of the derived performance indices' sensitivity to errors in the observable quantities. The primary performance parameters are defined by the relationships

$$I_{sp} = \frac{T}{\dot{m}g_0} \quad (1)$$

$$\eta = \frac{T^2}{2\dot{m}IV} \quad (2)$$

$$\eta_{th} = \frac{P_{beam}}{IV} \quad (3)$$

where the specific impulse is a function of the thrust  $T$ , the mass flow rate  $\dot{m}$  and the gravitational acceleration at the Earth's surface  $g_0$ ; the overall efficiency  $\eta$  is defined as the fraction of the total electric input power, given by the product of the arc current  $I$  and the voltage  $V$ , that appears as useful thrust power; and the thermal efficiency  $\eta_{th}$  is the ratio of the power deposited in the exhaust to the total input power. The thermal efficiency therefore represents an upper bound on the achievable overall efficiency. This definition of total efficiency neglects the power dissipated in the magnet for applied-field engines, but some effort has been expended in demonstrating that this portion of the power budget can be reduced to a negligible level [11,12]. These performance indicators are most susceptible to errors in the measurement of thrust, mass flow rate, and beam power. The overall efficiency is particularly sensitive to uncertainties in the thrust because of the quadratic dependence.

Statistical fluctuations in the measured quantities can be estimated from the scatter in the data provided there are a sufficient number of samples. When this scatter is well-defined, the mean behavior can be predicted or ranges of performance identified. However, conclusions based on the data may be compromised if there are systematic biases in the measured quantities, which may not be immediately apparent. Potential sources of systematic errors include tares in thrust balances from magnetic forces or cooling water circulation, thermal drift or hysteresis in thrust

stand motion, interactions with the test environment such as plume current pattern disturbances by material walls or entrainment of ambient gas in the exhaust, and biases in the mass flow rate determination or drift in the flow control. The reliability of the data depends primarily on the success of the experimenter in avoiding these errors.

The evidence for extended cathode life with alkali metal propellants is primarily anecdotal, consisting of subjective observations on the electrode state after long tests. However, there are some data on cathode temperature reductions achieved in alkali metal-fuelled engines and some erosion measurements that lend support to the subjective claims. The documentation of the experimental method is often insufficient to fully evaluate these data, however.

The primary purpose of this review is to determine whether it is worthwhile to resume experimentation with alkali metal propellants. First, the published results of testing with alkali metals will be summarized with a critical assessment of the reliability of the measurements. In addition, the observed performance and lifetime gains will be examined to determine if they can be justified on physical grounds. Finally, the impact of these propellants on testing requirements and other spacecraft systems will be discussed.

### Review of Experience with Alkali Metal Propellants

After Ducati's observation in 1963 [13] of the high exhaust velocities attainable by electromagnetic acceleration of a plasma, a number of laboratories in the United States and the Soviet Union started experimenting with the new class of accelerator. In the United States alkali metal propellants for applied field MPD engines were explored under NASA and Air Force sponsorship at Giannini Scientific Corporation in Santa Ana, California; Electro-Optical Systems (EOS), Pasadena, California; Avco Corporation Space Systems Division, Wilmington, Massachusetts; and Los Alamos National Laboratory in Los Alamos, New Mexico. Steady-state self-field and applied field thrusters with alkali metal propellants appear to have been studied by a number of organizations in the Soviet Union [14].

### The Giannini Scientific Corporation Experiments

Lithium and potassium were tested in engines similar to that shown in Fig. (1) [15]. The thoriated

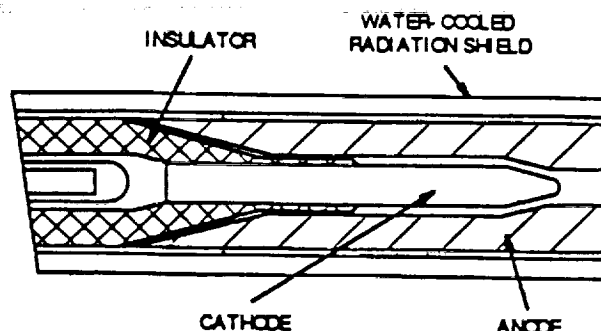


Figure 1: Radiation-cooled, applied field accelerator tested at the Giannini Scientific Corporation with lithium and sodium

tungsten cathodes all had a diameter of 0.792 cm, while the radiation-cooled tungsten anode throat diameter was varied from 0.635 cm to 1.117 cm. The propellant feed system was not described in this reference. The engines were tested in a chamber 0.4 m in diameter and 1.9 m long. The thrust measurements were not repeatable enough for publication, so only thermal efficiencies were reported. The thermal efficiency was calculated from the power deposited in two cooling circuits, one of which intercepted most of the beam power and another that was used to cool some engine components and absorb the power radiated by the anode. In tests ranging from 3 to 9 kWe with applied field strengths of 0.10 to 0.35 Tesla and flow rates from 0.5 to 3 mg/s the thermal efficiency of lithium was between 32% and 40%. For potassium under similar conditions the thermal efficiency varied from 27% to 37%. The efficiencies were observed to decrease with increasing throat diameter and increase slightly with increasing power at fixed mass flow rates and magnetic field strengths.

In a test of several hours duration with lithium propellant, an anode mass loss rate of 1.3 g/hr and a cathode mass gain of 0.8 g/hr were observed. In operation with lithium and potassium, insulator ero-



sion rates varied from 0.1 to 2.4 g/hr, depending on the cathode temperature.

### The Electro-Optical Systems Program

In a long and ambitious research program at Electro-Optical Systems on alkali metal-fuelled MPD thrusters, extending from the early sixties through 1967, a total of 26 configurations were studied. Work on the first 22 configurations are presented in [11] and the remaining 4 in [16]. A typical configuration, taken from [11], is shown in Fig. (2). For this de-

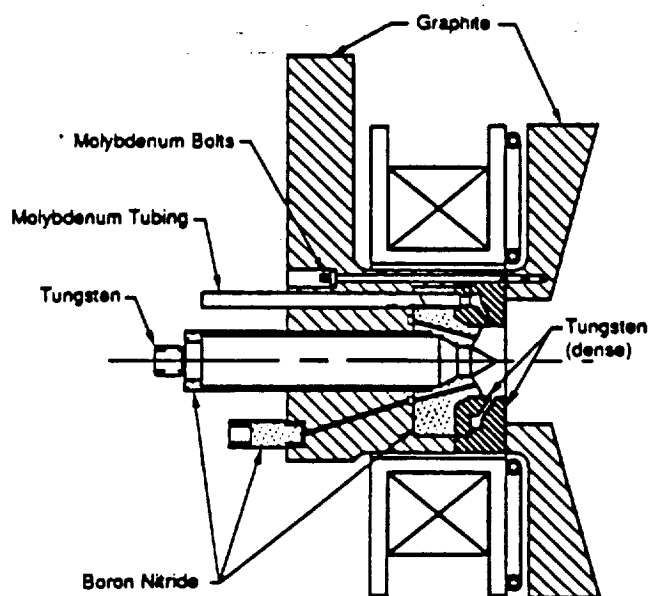


Figure 2: Radiation-cooled, applied field accelerator tested at Electro-Optical Systems, Inc.

vice the cathode diameter was 1.00 cm, the anode inner diameter (I.D.) 3.00 cm and the graphite radiator I.D. 5.00 cm. In later configurations one and two additional electromagnet coils were added, downstream of the anode, in order to extend the axial magnetic field. The materials of construction were, with a few exceptions, thoriated tungsten for both electrodes, boron nitride for the insulators and some main body parts, and graphite for the main supports and the anode radiator, when used. The principal

configuration changes were the point of lithium injection (either the cathode tip or the anode face or I.D.), anode I.D. (1.5 to 3.0 cm.) and shape, cathode tip configuration, and magnet coil I.D., location and number. These engines were tested at power levels ranging from 3.3 to 43.4 kWe.

One of the major required technologies was the lithium propellant transfer and metering system. In [11] the development of a bellows-type system is outlined. Several versions of this basic type were tested. Each consisted of a 7.62 cm O.D. bellows with a 12.70 cm usable expansion length, housed in a stainless steel cylindrical container. The bellows expansion rate was controlled by a screw-type linear actuator. In the first design pressurized argon was injected between the bellows and its housing to support the lithium-filled bellows and minimize sag and buckling. The linear actuator was then used to force the lithium out of the bellows and into the hot engine at a known rate. Vaporization occurred inside the hot electrode being used for propellant injection. A second variation of this scheme was to place the lithium between the bellows and its housing and to pressurize the inside of the bellows and force the lithium out at a known and controllable rate with the linear actuator. A third variation was to use the high pressure argon to expand or contract the bellows and to use the linear actuator as a brake to merely control the rate of expansion or contraction.

A second approach to this problem is presented in [16], in which the liquid lithium is contained in a heated stainless steel container and forced out with pressurized argon. The liquid lithium is forced up into a vaporizer that is attached to the engine anode. The heat of vaporization was obtained by conduction from the hot anode, hence the rate of vaporization (and propellant mass flow rate) depended on engine power. To measure mass flow rate a critical orifice was located at the vaporizer/anode joint and the argon pressure was used as a mass flow indicator.

Besides the lithium mass flow rate; arc power, magnetic field strength and total engine thrust were measured. The thrust stand used was an oil-cooled three leg parallelogram with flexures at each end of the legs. The thrust was resisted and sensed by a load cell. Arc and magnet power were brought onto the thrust stand through mercury pots and the cooling water, instrumentation and heater wires were flexible enough to

not effect the thrust measurements.

An example of the measured performance of this engine is shown in Fig. (3), taken from [17]. For

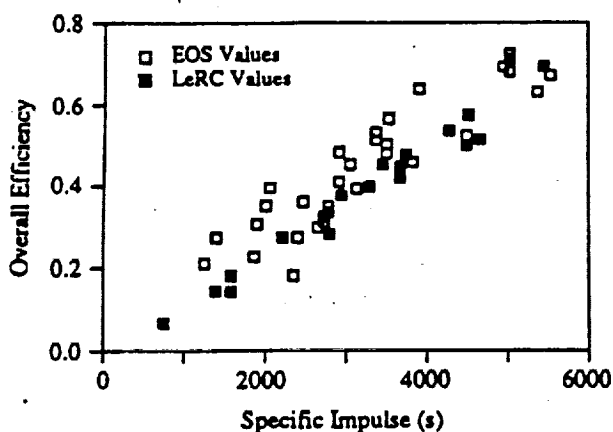


Figure 3: Comparison of lithium MPD thruster performance measurements conducted at EOS and NASA Lewis Research Center.

this data the magnetic field strength in the electrode region was 0.1–0.24 tesla and the flow rate set at 0.01 g/s. Measurements with the same geometry performed at the NASA Lewis Research Center are shown for comparison. The agreement between the two independent measurements is quite good. The maximum efficiency was approximately 70% at a specific impulse between 5000 and 6000 s. The performance of the engines with propellant injection in the anode was superior to the cathode-fed designs.

The thermal efficiency was measured by engine component calorimetry for each configuration tested. Values ranging from 31% to 76% were obtained. The variation was due to both configuration and operating condition changes.

One of the objects of the program was endurance testing of the lithium-fuelled arcjet [16]. A total of seven endurance tests were attempted, ranging in length from 0.5 to 111.5 hours. Of the 111.5 hours achieved in the most successful endurance test, 110.2 hours were with lithium and more than 100 hours of that were uninterrupted. The test was terminated voluntarily and examination of the engine after revealed that the electrodes were in "remarkably good

condition."

A similar radiation-cooled, applied-field engine was tested at EOS using sodium and potassium as propellants [18]. The performance with sodium varied from about 9% efficiency at 540 s specific impulse to approximately 34% at 2000 s, as shown in Fig. (4). In tests with potassium the efficiency was nearly con-

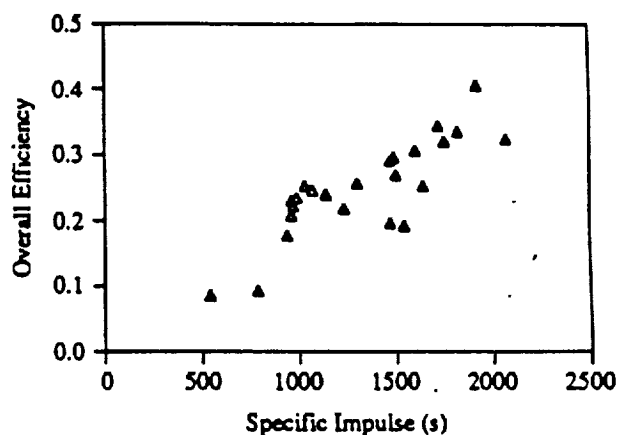


Figure 4: Performance obtained with a sodium applied-field accelerator at EOS.

stant at approximately 30% for specific impulses over 1200 s. Experiments were also conducted with bipropellant engines in which lithium was injected at the anode and hydrogen or nitrogen was introduced in the cathode region. The primary motivation for studying these designs was to attempt to force the arc to attach at the cathode tip to prevent insulator erosion.

The thermal efficiency of an EOS bipropellant accelerator with lithium supplied to the anode region and hydrogen through the cathode was measured by heat inputs to the engine cooling circuits and the chamber cooling circuit. These values were confirmed to within 10% by integrating the energy density measured with an enthalpy probe in the plume [19]. In addition, centerline velocities inferred by the time-of-flight of light intensity fluctuations in the plume were found to correlate well with the exhaust velocity calculated from thrust measurements. The confirmation of basic performance measurements by auxiliary diagnostic measurements in the exhaust lends considerable weight to the data.

In the large program at EOS considerable care was taken to quantify and minimize the impact of potential errors. Tares in the thrust stand due to cooling water flow and interaction of the magnet and engine currents with the tank and current leads were measured and corrected in the data reduction. Their analysis [18] indicated that interaction of the Hall currents in the exhaust with the fixed leads and tank could not significantly affect the thrust measurement. Thermal offsets in the thrust stand were found to be significant, so the null position was measured before and after each measurement at a particular operating point by turning off the engine. Hysteresis and drift in the transducer sensitivity were found to be negligible compared to the thermal drift. The total uncertainty in the thrust measurements was estimated to be  $\pm 1-2$  g. Experiments conducted at the Lewis Research Center were also performed on a pendulum thrust balance [17]. In these tests, however, the thrust was determined by measuring the change in thrust stand deflection when the exhaust was diverted and expelled normal to the thruster axis by a "thrust killer." These measurements were within 5% of the values obtained by correcting for current tares and thermal offset measured by turning off the thruster.

The possibility of mass entrainment from the ambient tank atmosphere was also explored in this program. Magnetic field probe measurements in the exhaust of a lithium engine have indicated that the discharge current path can extend downstream of the thruster exit plane by as much as a meter or more [20]. Measurements of velocity at different axial positions [19,20] suggest that considerable plasma acceleration occurs in this external interaction region, so neglecting the ingestion of ambient gases in the performance calculations can bias the results. The potential for spurious effects is in general smaller with condensable propellants than with gaseous propellants because low tank pressures are easier to achieve. Tests performed with lithium in the 2 m diameter by 2 m long EOS chamber indicated that the thrust and voltage were affected at chamber pressure levels greater than  $10^{-2}$  Torr, but appeared to be constant to pressures as low as  $5 \times 10^{-5}$  [11]. However, Moore admits that these experiments are not conclusive because the low tank pressures could not be sustained for very long. Tests conducted in another EOS

chamber at a pressure of  $10^{-7}$  Torr showed no significant change from the normal operating pressure [21]. These measurements are also ambiguous, because the extent of the interaction region could have been larger at the lower pressures, offsetting the decrease in available gas. The tests of an EOS lithium engine in the 4.5 m x 20 m chamber at NASA Lewis were conducted at a pressure of  $3 \times 10^{-4}$  Torr. The results agreed well with those obtained at EOS at pressure of approximately  $10^{-2}$  Torr.

The effects of entrainment were also studied by bleeding other gases into the chamber while operating the engine on alkali metal propellants. Tests with a lithium engine operating in an argon atmosphere at approximately 1 Torr showed a significant decrease in thrust and voltage [11]. Argon gas was also used in an experiment with a similar engine running on sodium, and the thrust was found to be constant below about  $10^{-3}$  Torr. Above that pressure the thrust initially decreased to about one-fourth the value found at low pressures, then increased to a maximum at about  $10^{-1}$  Torr [18]. Similar results were also obtained with potassium [22]. In all cases the performance was found to either remain constant with increasing pressure or decrease, so tank pressure effects appear to lead to conservative measurements of engine performance.

Another potential environmental effect is the perturbation of the exhaust plume current distribution by the tank walls. Moore [11] suggests that interactions with the tank wall could influence the performance measurements by limiting the extent of the current patterns, by electrostatic effects, or by shorting out part of the discharge. However, the agreement between the results obtained at EOS and in the large vacuum chamber at NASA LeRC suggest that this interaction has a minimal impact.

The mass flow rate of lithium, sodium and potassium was measured by the volumetric displacement of liquid fed to a vaporizer by a bellows-type piston for all performance measurements performed at EOS. The system was calibrated in bench tests by measuring the volumetric displacement rate of water from the reservoir and confirmed by measuring the total mass of metal displaced over a certain period. Uncertainties in the flow rate were caused primarily by changes in the density of the liquid metal due to fluctuations in the temperature and changes in the pres-

sure differential across the bellows. The stated error in an instantaneous measurement of the flow rate was 10% or 0.001 g, whichever quantity was larger. The average flow rate over several minutes or longer could be determined within 5%. This method was subsequently abandoned in favor of a vapor metering orifice for the endurance tests because of uncontrollable fluctuations in the bellows feed rate with time constants on the order of hours. It is not clear whether these fluctuations simply contributed to the random scatter in the data or could be responsible for systematic biases in the performance measurements.

### Los Alamos National Laboratory Program

Work on a lithium-fuelled, applied-field MPD thruster proceeded at Los Alamos Scientific Laboratory from 1967 to 1973. Almost all of the experimental work was performed on the configuration shown in Fig. (5), which was taken from [23]. The main fea-

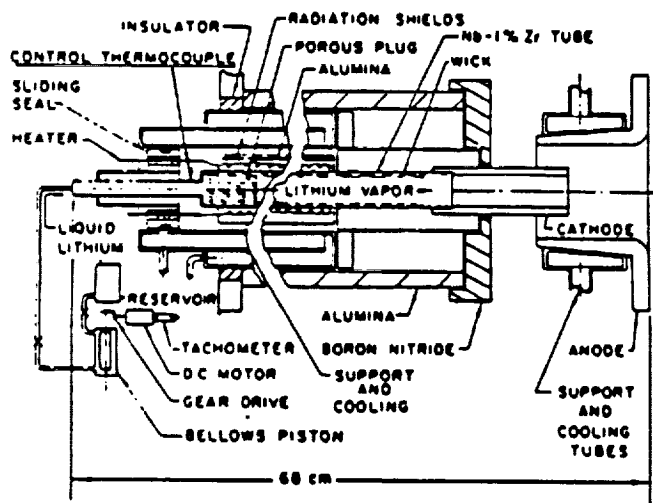


Figure 5: Lithium-fueled MPD thruster tested at Los Alamos National Laboratory.

tures of their design are a hollow tungsten cathode with a 1.1 cm I.D. and 1.9 cm outer diameter (O.D.) and a cylindrical tantalum anode with a 3.75 cm I.D. These two concentric electrodes were separately supported, with no insulator forming a discharge cham-

ber backplate between them. This unique arrangement eliminated the need for a troublesome insulator which was prone to cracking and erosion due to the alkali metal propellant. The liquid lithium was pushed out of a known volume by the expansion of a bellows-type piston, and into a separately heated vaporizer with a porous tungsten plug and a Nb-1 could be determined and controlled by the known expansion rate of the bellows. The lithium vapor then flowed out of the hollow cathode as a directed jet along the engine center line. This arrangement allowed for very stable arc operation with the discharge emanating from inside the cathode tube. Water-cooled electromagnets were used to apply a predominately axial magnetic field to the plasma in the discharge region. Axial field strengths as high as 0.48 tesla were generated. Most of the tests were performed at power levels below 25 kWe, although operation as high as 75 kWe was achieved. Later a similar configuration in which lithium vapor was injected through a circumferential slit in the anode as well as through the hollow cathode was tested [24].

The engine was initially tested in a vacuum chamber 0.9 m in diameter and 1.5 m long that was maintained at a pressure of  $2 \times 10^{-7}$  Torr [20]. It was subsequently tested in a larger tank measuring 6.5 m long by 2.4 m in diameter that was also maintained at about  $2 \times 10^{-7}$  Torr [23].

The earliest measurements of thrust performed in the smaller facility were based on the deflection of a wire screen suspended in front of the exhaust. The flow was assumed to be free-molecular and momentum transfer by atom or ion desorption from the wires at the surface temperature was considered in the data analysis. Results were published [20,25] for a range of applied field strengths at only one engine operating point, 350 A arc current at a flow rate of 33.5 mg/s. Under other conditions no valid results could be obtained because of thrust screen oscillations or current flow in the wires. The thrust was found to be relatively independent of lithium mass flow rate and linearly dependent on the product of arc current and applied magnetic field strength. This relationship of thrust with the product  $IB$ , was predicted in models discussed in references [20] and [26]. To obtain these results it was assumed that the major plasma-dynamic process was conversion of rotational energy supplied by  $J_r \times B$ , terms into axial kinetic energy

by expansion in a magnetic nozzle.

The exhaust velocity, or specific impulse calculated by Eq. (1), was found to increase linearly with the same  $IB$ , product divided by the lithium mass flow rate. The specific impulse in these experiments varied from 1500–2500 s. The uncertainty in the thrust measurement is not given in the references, but good agreement between the exhaust velocity inferred from the thrust measurements and Fabry Perot measurements of the centerline velocity was found. The comparison is shown in Fig. (6). In addition, ion energies

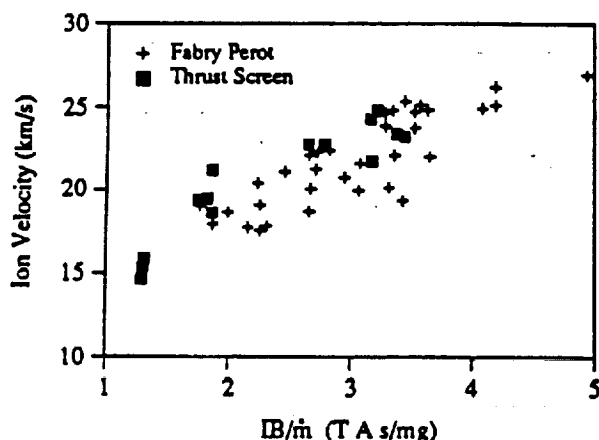


Figure 6: Comparison of velocities measured with a Fabry Perot interferometer and calculated from measured thrust for the LANL lithium engine.

measured with an energy analyzer mounted in the end of the tank were only slightly higher, an effect attributed to additional acceleration in the plume beyond the position of the other velocity measurements.

The thrust efficiency (not including magnet electrical power) was found to depend linearly on specific impulse over the measured range and increased from approximately 25% at 1500 s to over 45% at 2500 s. These values are plotted in Fig. (7).

Cathode erosion was initially encountered in tests in which the power required to vaporize the propellant was provided by discharge heating of the cathode. Coupling between the vapor feed rate and the power was found to cause fluctuations in the time that may have contributed to the cathode degradation. Subsequent experiments with the hol-

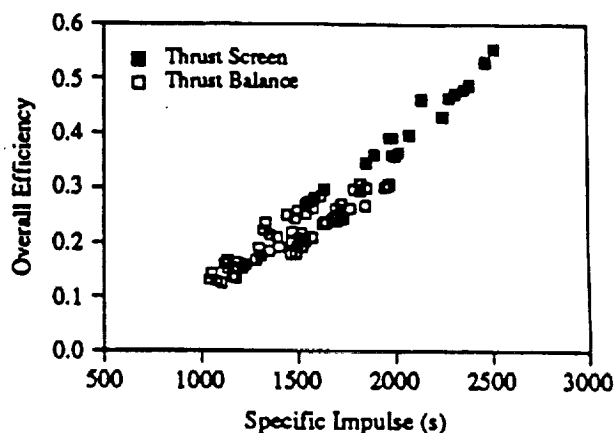


Figure 7: Performance measured in the LANL lithium accelerator.

low cathode and an externally heated vaporizer apparently eliminated these problems. The engine was capable of operating for long periods of time at powers up to 50 kWe with no damage to the electrodes.

These experiments were performed at tank pressures well below the values at which ambient gases perturb the performance measurements, as determined in the EOS experiments. However, there was evidence of currents in the plume interacting with the downstream end of the tank under some conditions. At the highest values of magnetic field strength and arc current, high voltages appeared on insulating portions of the beam stop at the end of the tank and the arc terminal voltages were suppressed.

There were no reported problems with the bellows feed system used in these experiments. The volumetric displacement rate as a function of the bellows position was calibrated using water. In operation, the bellows-piston drive speed was regulated to maintain a constant vaporizer temperature. The flow rate based on the vaporizer power and the output of a tachometer on the drive motor were found to agree within 5%.

The calorimetric measurements of the thermal efficiency were based on the power absorbed in the cooling circuit for the downstream half of the tank. The thermal efficiency was found to increase from 40–50% with no applied field to over 70% with applied fields

ranging from 0.05 to 0.20 Tesla. Calculations of the view factors for the anode indicated that only about 12% of the power radiated by the hot surfaces could be deposited in the downstream half of the tank, leading to at most a 4% overestimate of the thermal efficiency. Other possible errors, such as plume radiation lost to the upstream half of the tank, lead to underestimates of the beam power.

The thrust of this engine was subsequently measured in the larger facility on a parallel-pendulum type thrust stand which utilized flexures as pivot points. Power was supplied to the stand through coaxial mercury pots and cooling water for the electrode supports and electromagnet through banks of U-tubes. The sensitivity of the thrust stand could be calibrated to within  $\pm 0.05$  N. Thrust stand tares were measured and used to correct the force measurements. The thermal drift was determined to within  $\pm 0.05$  N by turning off the engine. These estimated uncertainties correspond roughly to the scatter in the data, so it is not evident that they represent possible systematic biases. The linear dependence of thrust on  $IB_z$  and efficiency on specific impulse was confirmed. The measured efficiency increased from about 12% at 1000 s to approximately 36% at 2000 s. The slope of this line is somewhat lower than that measured with the thrust screen, but still suggests excellent performance in that  $I_{sp}$  range. These values are plotted in Fig. (7). However, the anticipated dependence of thrust efficiency on arc input power was not found. The exhaust velocities deduced from the measured thrust and lithium mass flow rate were also measured directly with an electrostatic energy analyzer near the plume center line and 6.4 m downstream of the engine. The agreement between these two sets of data was very good.

An earlier experiment at Los Alamos involved the testing of a cesium-fed device at power levels between 4 and 12 kWe with an applied field of up to 0.1 Tesla [27]. In this engine the liquid cesium was delivered by a positive displacement bellows and piston assembly through the cathode to a ring of 12 holes arrayed on the hemispherical tip along radii  $45^\circ$  from the axis. The power required to vaporize the cesium was supplied by the discharge; there has apparently no externally heated vaporizer. This system was calibrated in the same manner as the feed system used in the lithium tests, and the authors reported that

no problems of any kind were encountered. The test chamber measured only 25 cm in diameter by 90 cm long, so plume interactions with the walls were likely.

The thrust was determined using a thrust screen. The authors calculated that very little screen deflection could be caused by currents induced in the wires and that neglect of elastic collisions would lead to overestimation of the thrust by no more than 50%. The measured thrust also correlated well with the parameter  $IB_z$ . Although the ambient pressure was maintained at about  $2 \times 10^{-5}$  Torr, there was evidence of mass entrainment, possibly from liquid cesium that collected near the electrodes. The beam power was determined by calorimetric measurements using the entire chamber cooling circuit, because both electrodes were cooled with a separate circuit. The thermal efficiency never exceeded 40%, and the largest value of the thrust efficiency observed was 20%.

This engine was operated for many months without having to replace the electrodes. Occasionally, however, insulators had to be replaced because of cracking.

### AVCO Experiments

Tests at AVCO were performed in the water-cooled applied-field engine shown in Fig. (8) with cesium propellant and with lithium in a radiation-cooled thruster with a similar geometry. The tungsten cathode had a diameter of 0.635 cm, the diameter at the entrance of the flared anode was approximately 1.0 cm and the diameter at the exit was about 6.4 cm. The mass flow rate of the propellant vapor generated from liquid in a heated reservoir was metered by an orifice downstream of the injection tube drilled in the cathode. The tests were performed in a vacuum chamber 1.2 m in diameter and 2 m long at a pressure on the order of  $10^{-4}$  Torr.

The engine thrust was determined by measuring the displacement of a thrust stand from which the thruster was suspended. The thrust efficiency for cesium, plotted as a function of specific impulse in Fig. (9), varied from about 5% at 1000 s to 14% at 3000 s. These data were obtained at power levels from 5 to 10 kWe, magnetic field strengths between 0.05 and 0.3 Tesla and flow rates of 3.5–6 mg/s. Thermal efficiencies, determined by the power deposited in the anode cooling circuit, were between 22 and 38%. The

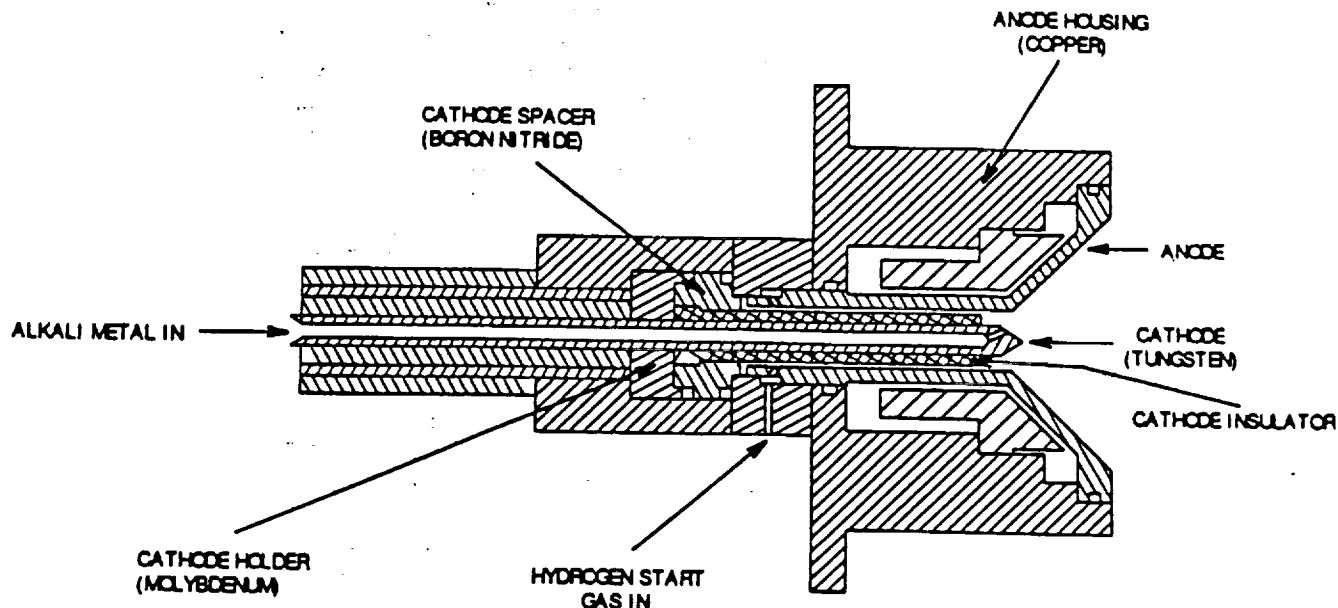


Figure 8: Water-cooled applied-field MPD thruster used with cesium at AVCO Space Systems Division.

radiation-cooled engine operating on lithium offered improved performance under similar operating conditions, with efficiencies of approximately 10% at 1000 s and 30% at 6000 s, as shown in Fig. (9). These data are somewhat lower than the values measured at EOS with a cathode-fed MPD thruster.

The design and operation of the thrust stand is not well documented in this reference, but it was apparently calibrated for magnetic tares and checked during operation for thermal drifts. The uncertainty associated with the measurement is not recorded. The calibration of the mass flow measurement (by integrated weight loss over a run) gives only average values for the flow rate and is subject to changes in the propellant temperature and arc operating conditions. Corrections for fluctuations due to temperature changes were attempted, but some uncertainty must be assigned to this measurement. No obvious interaction with the test environment was apparent. The facility pressure was below the values at which performance measurements were affected in the EOS

pressure tests. In addition, the chamber used in the AVCO studies was similar in size to that used at EOS so plume interactions with the walls were probably not any more problematic.

#### Soviet Literature

A number of Soviet references mention applied-field and self-field MPD thrusters that operate with alkali metal propellants, but few experimental details are given. Reference [28] describes an extensive series of tests with a lithium-fed engine with the basic configuration shown in Fig. (10). In this design the lithium is vaporized and injected through a cathode composed of a bundle of tungsten rods. The flow rate has a quoted uncertainty of  $\pm 5\%$ . The focus of the parametric study was to determine the effect of geometry on the onset current, at which large amplitude terminal voltage oscillations and greatly accelerated erosion occur. A number of cathode and anode geometries were tested at current levels rang-

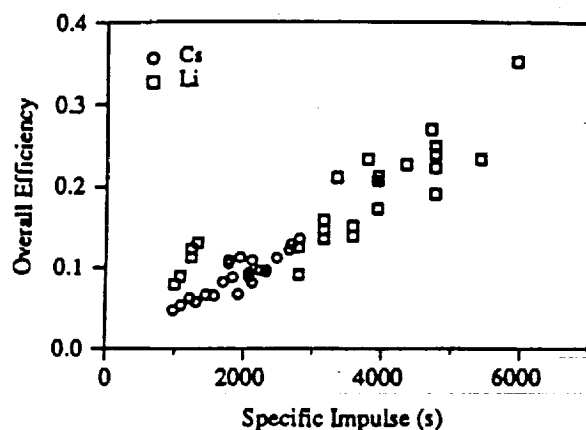


Figure 9: Performance measured with cesium and lithium in an applied-field MPD thruster at AVCO.

ing between 1000 and 2000 A and power levels on the order of 5–60 kWe. Thrust levels from 25 to 200 g were recorded for specific impulses ranging from 500–5000 s. The measured efficiencies were not reported in [28]. Unfortunately the design of the thrust stand and the uncertainty associated with the thrust measurements are detailed in a publication which has not been translated into English [29].

References [30] and [31] discuss spectroscopic and Langmuir probe diagnostics in the near-cathode region and anode failure mechanisms in the lithium self-field engines, respectively.

In a recent paper [32] Soviet researchers compared three propulsion schemes for a piloted Mars mission orbital transfer; direct nuclear thermal, advanced chemical plus electric propulsion and all nuclear-electric propulsion. Their conclusion was that the latter scheme would allow a minimum overall flight time less than one year. Four experimentally verified electric propulsion technologies were presented: three MPD thrusters utilizing bismuth, lithium and xenon and one arcjet utilizing ammonia. The experimentally verified performance of the lithium-fuelled MPD thruster was given as 6000 to 7000 s,  $I_{sp}$  at 50 to 60% efficiency and a voltage of 100 V at a power level of 10 MWe.

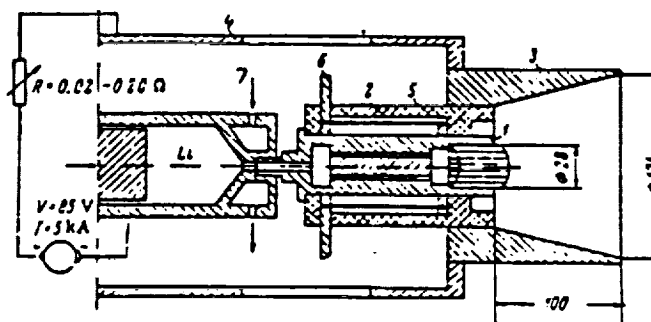


Figure 10: Self-field MPD accelerator tested with lithium in the Soviet Union. 1-tungsten cathode, 2-bushing, 3-tungsten anode, 4-feed and support, 5-insulator, 6-cathode heater, 7-coolant flow.

Reference [33] briefly discusses the state of development of electric propulsion in the USSR and its potential for space exploration as of approximately 1986. In particular they discuss a Butt-End Plasma Thruster (BEPT) operating with alkali metals as propellant. Lithium is mentioned as a prospective propellant for flights to Mars. Stated performance was a specific impulse up to 10,000 s, efficiencies of more than 50% and thrust densities of 0.1 to 1 N/cm<sup>2</sup>. The experimentally verified power range was 2 kWe to 1 MWe. The authors report that in a 1000 hour endurance test of a potassium engine operated at 2.5 kWe the cathode erosion rate was  $6 \times 10^{-6}$  g/s.

In [34] several electric thruster types are discussed, including MPD engines utilizing bismuth, lithium and potassium as their working fluid. In particular, the lithium-fuelled applied magnetic field MPD thruster is described. They also found that the thrust of this device increases with arc current and with applied magnetic field strength. This engine was operated for many hours at power levels of a few kW to 40 kW, specific impulses of 2000 to 5000 s and efficiencies of 35 to 60%. They also mention that a potassium-fuelled 3 kW MPD thruster with a specific impulse of 3000 s was tested in space on board Kosmos-728. A flight experiment involving a 1 kW MPD thruster with cesium propellant is discussed in [35].



## Experiments with Cathodes in Lithium Vapor

In a series of experiments conducted at Princeton University with a low-power, steady-state MPD thruster with a lithium-seeded argon propellant, Chamberlain determined that the cathode temperature was reduced by approximately 300 K, and the erosion rate dropped by a factor of 20 compared to pure tungsten. Similar results were predicted analytically in [36]. Data and theoretical calculations for a multiple rod cathode operating in lithium vapor demonstrate that the cathode work function varies between 3.5 eV and 4.5 eV, the value for pure tungsten [37,38].

## Physical Basis for the Advantages Offered by Alkali Metal Propellants

The high performance levels and low electrode erosion observed in some of the studies reviewed above can be justified qualitatively on the basis of physical and chemical properties of the alkali metals, some of which are displayed in Table (1). The properties for hydrogen and argon are included for comparison. The vapor pressures of the alkali metals are plotted as a function of temperature in Fig. (11). The pri-

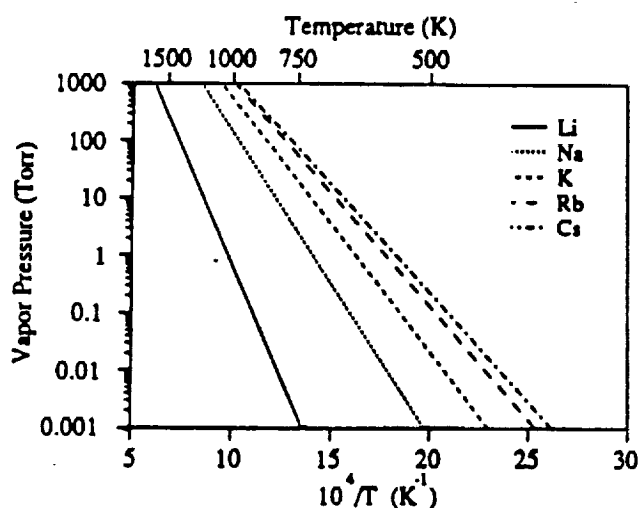


Figure 11: Vapor pressures of the alkali metals.

mary attraction of alkali metals as propellants for

plasma thrusters is based on the low ionization energies. The magnitude of the frozen flow loss associated with the unrecovered ionization energy in the exhaust depends on the energy required to ionize a unit mass of the propellant. This suggests that the lowest frozen flow losses should be achievable with the heaviest alkali metals, which have the lowest ionization energies. However, the experimental evidence indicates that lithium actually delivers performance superior to that of the heavier alkali metals. Apparently losses due to multiple ionization of the other metals offset their lower first ionization potentials. The second ionization potential for lithium is so high that comparatively little double ionization occurs. In addition, the first excited state of the lithium ion lies 61.95 eV above the ground state, so very little excitation will occur at the electron temperatures typically observed in plasma accelerators. This explanation provides some physical rationale for the high measured efficiencies.

The cathode, which is typically the life-limiting component in MPD thrusters, erodes through five mechanisms—evaporation, sputtering by high-energy particles, chemical attack by ambient gases or cathode additives, ejection of molten material, and loss of solid particles [8]. Melting, evaporation and the sensitivity to chemical attack all depend fundamentally on the cathode surface temperature. Alkali metal propellants can potentially increase cathode life by decreasing the operating temperature.

The current density  $j_e$  of electrons emitted thermionically from a surface at a temperature  $T$ , is described by the Richardson equation,

$$j_e = AT_e^2 \exp(-e\phi/kT_e), \quad (4)$$

where  $e$  is the charge of an electron,  $k$  is Boltzmann's constant,  $A$  is a constant that is theoretically equal to  $120 \text{ A/cm}^2\text{K}$ , and the work function  $\phi$  represents the potential barrier at the surface of the conductor. The work function is weakly dependent on the temperature but sometimes it is assumed to be constant and  $A$  is modified to contain the temperature dependence. For a surface to supply electrons at a certain current density, the electrons must have a sufficiently high thermal energy to escape over the potential barrier  $\phi$ . The required operating temperature therefore depends strongly on the surface work function.

The work function of a refractory metal cathode

Parameter	Li	Na	K	Rb	Cs	H <sub>2</sub>	Ar
Atomic Number	3	11	19	37	55	1	18
Atomic Weight	6.94	22.99	39.10	85.47	132.9	2.02	39.95
Melting Point (°C)	180.5	97.8	63.2	39.0	28.5	-259.1	-189.2
Boiling Point (°C)	1317	883	754	688	671	-252.9	-185.7
Density (kg/m <sup>3</sup> )	507	904	797	1390	1740	70.0	1390
Specific Heat (J/kg°C)	506	58.3	20.1	5.42	3.36	14400	519
Heat of Vaporization (kJ/kg)	21200	4310	2020	886	500	449	163
Dissociation Energy (eV)	1.117	0.740	0.558	0.503	0.460	2.26	-
1 <sup>st</sup> Ionization Potential (eV)	5.39	5.14	4.34	4.18	3.89	13.60	15.76
2 <sup>nd</sup> Ionization Potential (eV)	75.64	47.29	31.63	27.28	25.10	-	27.63

Table 1: Physical and chemical properties for the alkali metals, hydrogen and argon.

immersed in an alkali metal vapor can be substantially reduced by the adsorption of alkali metal atoms on the surface. The potential barrier at a composite surface arises from a component determined by the relative electronegativity of the substrate and adsorbate and from a component due to the dipole moment of the polarized adatom-substrate molecules. The work function variation for a metallic surface with adsorbed metal atoms as a function of surface coverage was successfully modelled by Gyftopoulos and Levine [39]. This model was used with the material physical properties given in [39] to generate the work function curves shown in Fig. (12), where the abscissa is  $\theta$ , the fraction of surface sites occupied by adsorbate atoms. Unity corresponds to a complete monolayer, at which point the work function is equal to that of the adsorbate material. The curves demonstrate a substantial reduction in the surface work function from that of pure tungsten.

The surface coverage that can actually be realized in an alkali metal-fed engine is given by an equilibrium between the desorption rate of particles from the cathode surface and the arrival rate of vapor atoms, which depend on the surface temperature and the temperature and pressure of the alkali metal vapor. In reference [40] Gyftopoulos and Levine derive theoretical correlations between atom and ion desorption rates and the coverage  $\theta$  and the substrate temperature using a statistical mechanics formalism with desorption energies calculated in [41]. The flux of vapor atoms to the surface can be expressed in terms of the pressure and temperature of the vapor phase by the normal kinetic equation, and when equated to the

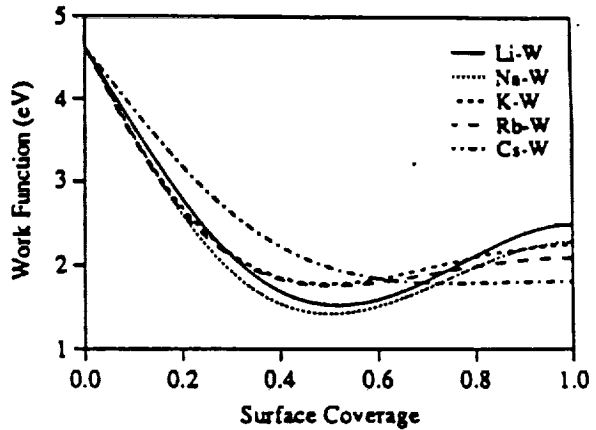


Figure 12: Work function for alkali metal-tungsten composite surfaces.

desorption rate gives the equilibrium surface coverage as a function of surface temperature.

When coupled with the work function relations given in Fig. (12) and the Richardson equation this relationship allows the determination of the emission current density as a function of surface temperature and the temperature and pressure of the alkali metal gas. Examples of these calculations<sup>1</sup> are shown in Figures (13)-(15). The emission current density for pure tungsten is displayed in all three figures as a bold line for comparison. The curves for the com-

<sup>1</sup> For these calculations the adsorbate and substrate physical property estimates given in references [39,40,41,50] were used.

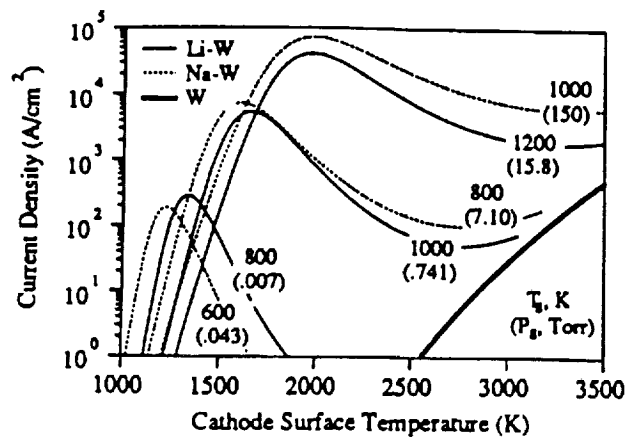


Figure 13: Electron emission curves for tungsten surfaces with adsorbed lithium and sodium atoms.

posite surfaces increase exponentially at low temperatures in accordance with the Richardson equation with the work function characteristic of a complete monolayer. At higher temperatures the current density drops as the work function increases due to a lowering of the equilibrium surface coverage. The curves ultimately asymptote to the value for pure tungsten as the surface coverage drops to zero. These examples demonstrate that substantial reductions in cathode temperature for a given current density should be achievable.

The alkali metal gas temperature and pressure for these examples were linked using the vapor pressure relationships shown in Fig. (11). This in essence assumes that the propellant pressure is determined by the temperature of the reservoir or vaporizer. In practice, the pressure and temperature of the vapor near the cathode attachment point will deviate from this relationship because of heating in the discharge. Figure (16) shows the optimum gas pressure and temperature required to achieve the maximum current density for a given surface temperature. These curves represent the loci of maxima in the curves displayed in Figures (13)-(15) and is free of an assumed relationship between vapor pressure and temperature.

Thoriated tungsten is used as the cathode material in most MPD thruster experiments. As the thorium is reduced to thorium metal a thorium surface layer

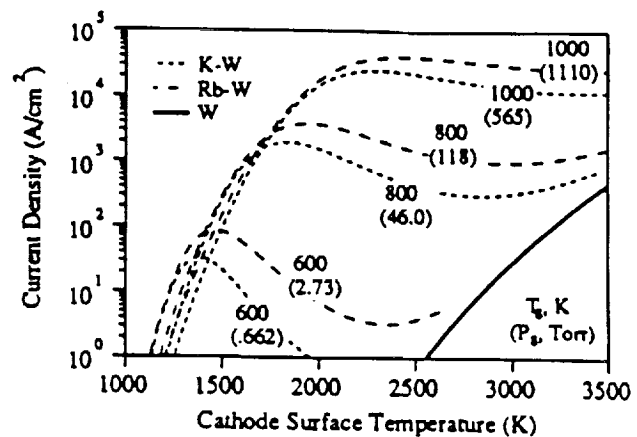


Figure 14: Electron emission curves for tungsten surfaces with adsorbed potassium and rubidium atoms.

can form at moderate temperatures. This layer acts in the same way to reduce the work function; however, the desorption rate from the surface must be balanced by diffusion of thorium from the interior of the cathode. It can be shown that at the operating temperatures required to achieve current densities of interest for MPD thrusters the desorption rate of thorium from the surface exceeds the diffusion rates in the solid. This imbalance prevents the establishment of a thorium layer on the surface. The advantage of using the low work function material as a propellant is that much higher resupply rates can be achieved in the gas phase for sufficiently high pressures and low gas temperatures.

### Testing and Systems-Level Considerations

Alkali metal fuels must be evaluated not only in the context of engine performance and lifetime, but also in terms of their impact on ground-based testing requirements and on other spacecraft systems. In this section some of the most important implications of alkali metal-fed MPD thrusters for testing and system design will be discussed.

### Test Facility Pumping Requirements

One of the largest demonstrated advantages of alkali metals as propellants is that they are eas-

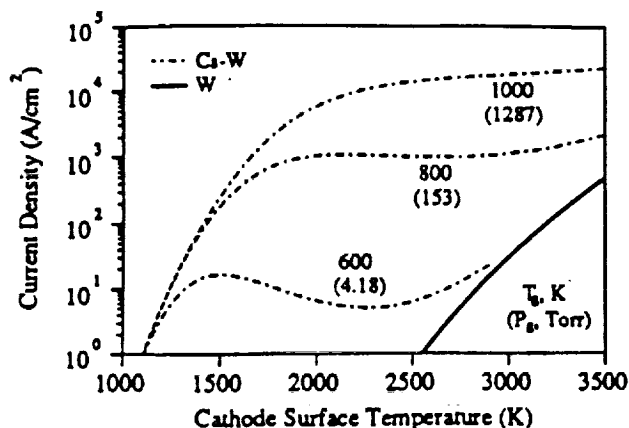


Figure 15: Electron emission curves for tungsten surfaces with adsorbed cesium atoms.

ily pumped. The condensation coefficient for alkali metal atoms and ions on metal surfaces is essentially unity [40,42] so the incident particles condense and equilibrate with the surface. The re-emission rate is then determined by the surface temperature. The vapor pressure curves in Fig. (11) demonstrate that extremely low pressures of alkali metal vapors can be maintained with water-cooled condensation targets. However, baffles may be required to suppress sputtering of deposited material exposed to the high energy exhaust, since sputtering is a nonequilibrium process that is largely independent of the surface temperature. The pumping requirements are then determined by the leak or outgassing rate of noncondensable gases. Alkali metals have the additional benefit of being efficient getters for residual gases when deposited on vacuum chamber surfaces [16,20], further reducing the required pumping speed. With these propellants, extremely low tank pressures can be achieved with very modest pumping plants.

Because the condensation coefficient of the alkali metals is near unity, the walls of the vacuum chamber can be considered perfectly absorbing. Under these conditions, meaningful plume studies can be performed in relatively small facilities. Chamber sizing then depends on avoiding interactions between the wall and the current patterns in the plume.

Alkali metal deposition on optical ports in the

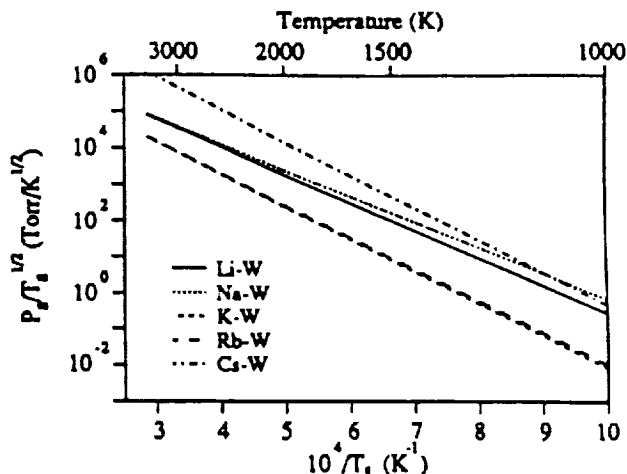


Figure 16: Gas pressure and temperature required for maximum current density.

chamber can make optical measurements difficult, and thin films on insulators may destroy their insulating value. Special care may be required to prevent condensation on these surfaces or actively remove films during operation.

### Alkali Metal Handling and Safety

The reactivity of the alkali metals is very high, increasing with electropositive nature from lithium to cesium [43,44,45]. The tendency to react with most materials mandates care in handling these propellants. The primary safety hazard is associated with the reaction between the alkali metals and water or water vapor. The alkali metals in contact with water produce heat and hydrogen gas, creating the potential for fires. The corrosion resistance of some ceramic materials to the liquid alkali metals, particularly lithium, is low, so discharge chamber insulator material choice and placement are critical for engine lifetime. Corrosion of metals is a strong function of temperature, and impurities in the alkali metal can tremendously accelerate corrosion processes. It is therefore important to use clean flow systems and pure metals. A typical problem encountered with im-

pure metals in vaporizer systems is the clogging of the porous tungsten plug with corrosion products transported from upstream. However, analysis, purification, and system cleaning techniques are well developed [43,44,46]. Alkali metal systems should not pose any new launch hazards, because the safety issues are similar to those for liquid hydrogen.

### Propellant Storeability and Management

Because the alkali metals can easily be stored as solids, low tankage fractions are expected, and the higher densities allow lower tank volumes compared to liquid hydrogen. The technology for liquid metal flow systems is well developed [45,46,47], and the space nuclear power program will produce valuable experience for space systems. The high heat capacity and heat of vaporization of lithium make it a good candidate for regenerative or active cooling of the engine. Engine thermal management may then be integrated with the power supply radiator, if pumped lithium loops are used. The large tank of solid propellant may also be useful as a heat sink for the system.

### Spacecraft Contamination

The high desorption energies which underly some of the biggest advantages of alkali metals also make them particularly dangerous potential spacecraft contaminants. Spacecraft surfaces that are particularly vulnerable to contamination by condensable materials were summarized in a review by Byers [48] and include solar arrays, thermal control surfaces, optical sensors, communications equipment, structures and scientific instruments. Condensation of propellant on spacecraft can adversely affect component function by altering the optical properties of the material (including alteration of the radiation or absorption capabilities of thermal control surfaces), changing the surface conductivity, eroding the surface or degrading the material by chemical or diffusion processes [48,49].

The proper approach to analyzing the contamination potential of a propellant is to model or measure the particle fluxes in the exhaust to calculate the arrival rates at the various spacecraft surfaces, employ a relationship for the surface kinetics of the contaminant-component interaction to predict the

surface coverage, and finally determine the impact of that interaction on the function of the components. It is presently infeasible to undertake a sophisticated assessment of the contamination hazard for alkali metal-fed MPD thrusters, however. There is very little experimental data on the mass flux in the plumes of alkali metal MPD engines, and no models which could reliably provide the required fluxes. In addition, the surface kinetics of the alkali metals on a number of materials used in spacecraft are not sufficiently well understood to model the adsorption process, although the model of Levine and Gyftopoulos [39,40,41,50] may be useful for interactions with metal surfaces. Finally, the effect of alkali metal films (with the exception perhaps of cesium [51,52]) on the optical, thermal, electrical and chemical properties of the substrates of interest is not known in the detail required to assess the damage.

A simple analysis can be used to obtain an estimate of the contamination potential, however. The condensation rate  $\dot{m}_c$  of a contaminant on a spacecraft surface which is already covered by at least one monolayer of a metallic adsorbate is given by the relationship

$$\dot{m}_c = \dot{m}_i \alpha - \dot{m}_e \quad (5)$$

where  $\dot{m}_i$  is the flux of contaminant to the surface,  $\alpha$  is the condensation coefficient of the incident flux on the bulk condensate and  $\dot{m}_e$  is the evaporation rate from the bulk deposit. The growth of the first monolayer is governed by a similar balance equation which includes terms describing the adsorption and desorption on surface sites free of the bulk condensate. Adequate treatment of this problem requires an understanding of the surface diffusion and nucleation processes and the desorption energies from the bare surface, which in general are not available. However, by assuming that the condensation coefficient  $\alpha$  is unity and that the evaporation can be described by the vapor pressure and the surface temperature, the maximum allowable flux of alkali metal vapor for which no further growth of the contaminant layer occurs can be calculated. The maximum allowable fluxes for the five alkali metals are presented in Fig. (17) as a function of the surface temperature. This plot demonstrates that the contamination potential decreases with increasing atomic mass.

The only available data on the mass flux in the plume of an alkali metal-fed MPD thruster are for

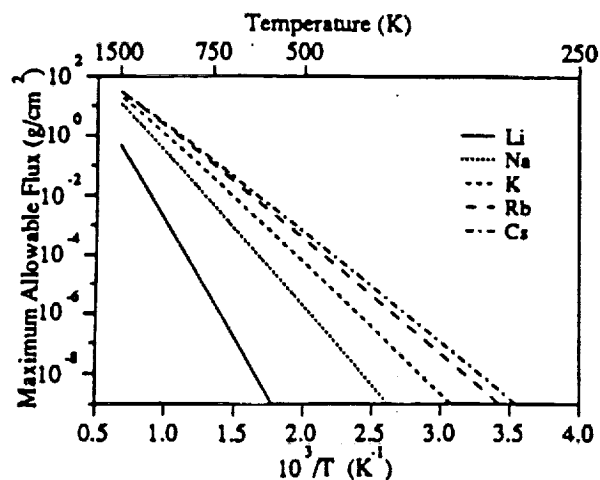


Figure 17: Maximum particle flux at which no bulk condensation occurs.

the applied-field engine developed at Los Alamos [20]. They found that at an arc current of 400 A, an applied field strength of 0.125 Tesla and a mass flow rate of 22.4 mg/s, the flux at an axial position 90 cm downstream of the anode plane was on the order of 45  $\mu\text{g}/\text{cm}^2\text{s}$  on the centerline and dropped to less than 1  $\mu\text{g}/\text{cm}^2\text{s}$  with increasing radius. Figure (17) shows that fluxes of lithium on the order of 1  $\mu\text{g}/\text{cm}^2\text{s}$  will not lead to bulk condensation if the surface temperature is above about 750 K. Similar fluxes of the heavier, more volatile alkali metals can be tolerated on much lower temperature surfaces.

There are a number of strategies for minimizing the contamination potential from condensable propellants. The large spacecraft size envisioned for SEI missions permits considerable flexibility in isolating critical spacecraft components from the engines. Power distribution requirements may preclude substantial separation between the nuclear power source and associated radiator surfaces and the thrusters, however. In this case, power conversion schemes such as the potassium-Rankine cycle which allow waste heat rejection at elevated temperatures may be favored to reduce accumulation of propellant material.

Another strategy for confining the propellant is to shield the spacecraft with a small cooled shadow

shield located near the engines. The re-emission rate of propellant atoms that have condensed on the cold shield is governed by the vapor pressure at the shield surface temperature, so the curves in Fig. (17) can be used to estimate the flux of material that escapes the cold target. In this approach high desorption energies are favored, and lithium becomes the optimum propellant choice.

Fixed shields for individual surfaces have been used successfully on a number of spacecraft, and retractable covers for sensitive instruments minimize interaction problems, but can be prohibitively expensive [53]. Careful choice of materials for exposed surfaces can minimize chemical incompatibilities with potential condensates. Biasing specific spacecraft components to repel low energy charged contaminants has also been demonstrated [48,54], and may be of use on spacecraft with alkali metal-fed engines.

Spacecraft contamination by condensable propellants has been studied in several flight tests. Two cesium ion engines were operated for a total of 92 hours on the ATS-6 spacecraft launched in 1974. Although 1/8 of the solar array area was directly exposed to the exhaust plumes, no signs of surface degradation were observed [48,49]. Evaluation of data from the SERT II spacecraft, which logged 5860 hours of mercury ion engine operation, indicated deposition only on contamination experiment solar cells located at the edge of the exhaust beam. Other spacecraft surfaces were unaffected [55]. Soviet experiments with cesium and potassium-fuelled MPD accelerators on the Kosmos series of satellites led to the conclusion that deposition rates on spacecraft surfaces are "low" [35], although film thicknesses on the order of 100 nm were apparently formed in 13 minute-long experiments.

## Conclusions

The data obtained in the United States in the 1960's and early 1970's and in the Soviet Union suggest that alkali metal propellants in the proper thruster geometry offer significant gains in performance and cathode lifetime. Lithium appears to give the best performance, evidently because of low frozen flow losses associated with second ionization. MPD thrusters operating at the measured performance levels could significantly enhance SEI mission capabilities. Although the validity of the results is difficult

to assess, the data are quite persuasive. The repeatability of measurements taken at EOS and the Lewis Research Center, the agreement between velocities measured in the plume and calculated from the performance data, the general agreement between maximum performance levels achieved in the US and the Soviet Union, and the consistency of thrust efficiencies and thermal efficiencies argue for acceptance of the conclusions. Although there are certainly errors associated with the measurements in individual experiments, there are no obvious sources of gross systematic bias that could invalidate the general conclusions. Sound physical arguments provide further support for the observed performance and improved cathode operation. The evidence seems credible enough to justify a research program aimed at repeating these results.

From the point of view of development cost, alkali metals have a tremendous advantage over gaseous propellants. One of the largest costs in a full-scale multimewatt MPD thruster development program will be the construction of a facility allowing valid testing of these devices, and the use of condensable propellants could enable an otherwise unaffordable test program. The greatest risk associated with the use of alkali metals as propellants is the potential for spacecraft contamination. One focus of an alkali metal-fed thruster program must be the experimental and theoretical determination of particle fluxes generated in the exhaust, the surface kinetics of alkali metals on materials used in spacecraft, and an evaluation of the impact of deposition on the function of those surfaces.

### Acknowledgements

This review and analysis was conducted at the Jet Propulsion Laboratory, California Institute of Technology, under contract with the National Aeronautics and Space Administration.

### References

- [1] J.H. Gilland. NEP Mission Sensitivities. Presentation at the MPD Thruster Technology Workshop, Washington DC, May 1991.
- [2] J.S. Sovey and M.A. Mantenicks. Performance and Lifetime Assessment of MPD Arc Thruster Technology. In 24<sup>th</sup> Joint Propulsion Conference, Boston, MA, 1988. AIAA 88-3211.
- [3] R.M. Myers. Applied-Field MPD Thruster Geometry Effects. In 27<sup>th</sup> Joint Propulsion Conference, Sacramento, CA, 1991. AIAA-99-2342.
- [4] M. Auweter-Kurtz et al. High Power Steady State MPD Thruster. Technical Report IRS-90-P4, Institut für Raumfahrtssysteme, Universität Stuttgart, Stuttgart, Germany, 1990.
- [5] J.E. Polk, A. J. Kelly, and R. G. Jahn. Characterization of Cold Cathode Erosion Processes. In 20<sup>th</sup> International Electric Propulsion Conference, Garmisch-Partenkirchen, W. Germany, 1988. AIAA-88-075.
- [6] D.W. Esker, J.C. Kroutil, and R.J. Checkley. Radiation Cooled MPD Arc Thruster. Technical Report MDC-H296 (NASA CR-72557), McDonnell Douglas Corporation, St. Louis MO, 1969.
- [7] M. Auweter-Kurtz, H. Kurtz, W. Merke, O. Loesener, H. Schrade, T. Wegmann, D. Willer, and J. Polk. Cathode Phenomena in Plasma Thrusters. In 21<sup>st</sup> International Electric Propulsion Conference, Orlando, FL, 1990. AIAA-90-2662.
- [8] J.E. Polk, A.J. Kelly, and R.G. Jahn. Mechanisms of Hot Cathode Erosion in MPD Thrusters. In 21<sup>st</sup> International Electric Propulsion Conference, Orlando, FL, 1990. AIAA-90-2673.
- [9] F.R. Chamberlain, A.J. Kelly, and R.G. Jahn. Electropositive Surface Layer MPD Thruster Cathodes. In 25<sup>th</sup> Joint Propulsion Conference, Monterey, CA, 1989. AIAA-89-2706.
- [10] M.E. Mantenicks, May 1991. Private communication.
- [11] R.A. Moore, G.L. Cann, and L.R. Gallagher. High Specific Impulse Thermal Arc Jet Thruster Technology, Part I: Performance of Hall Arc Jets With Lithium Propellant. Technical Report AFAPL-TR-65-48, Part I, Electro-Optical Systems, Pasadena, CA, 1965.

- [12] J.H. Gilland. Multimegawatt Electric Propulsion System Design Considerations. In *AIAA/DGLR/JSASS 21<sup>st</sup> International Electric Propulsion Conference*, Orlando, FL, 1990. AIAA 90-2552.
- [13] A.C. Ducati et al. Design and Development of a Thermo-Ionic Electric Thruster, Final Report. Technical Report FR-056-968 (NASA CR-54703), Giannini Scientific Corp., Santa Ana, CA, 1966.
- [14] J.W. Barnett. A Review of Soviet Plasma Engine Development. In *AIAA/DGLR/JSASS 21<sup>st</sup> International Electric Propulsion Conference*, Orlando, FL, 1990. AIAA 90-2600.
- [15] A.C. Ducati. Study of the Factors Affecting the Efficiency in Thermal Acceleration of Propellants. Technical Report 6QS-112-1161, Giannini Scientific Corp., Santa Ana, CA, 1963.
- [16] S.T. Nelson, G.L. Cann, and R.L. Harder. High Specific Impulse Thermal Arc Jet Thruster Technology, Part II: Performance of Hall Arc Jets With Lithium Propellant. Technical Report AFAPL-TR-65-48, Part II, Electro-Optical Systems, Pasadena, CA, 1967.
- [17] D.J. Connolly, R.J. Sovie, C.J. Michels, and J.A. Burkhart. Low Environmental Pressure MPD Arc Tests. *AIAA Journal*, 6(7):1271-1276, 1968.
- [18] G.L. Cann, R.L. Harder, R.A. Moore, and P.D. Lenn. Hall Current Accelerator, Final Report. Technical Report 5470-Final (NASA CR-54705), Electro-Optical Systems, Pasadena, CA, 1966.
- [19] P.F. Jacobs, L.R. Gallagher, and R.W. Richard. Diagnostic Measurements in an Alkali Plasma Hall Accelerator. In *AIAA 5<sup>th</sup> Aerospace Sciences Meeting*, New York, NY, 1967. AIAA 67-46.
- [20] D.B. Fradkin. *Analysis of Acceleration Mechanisms and Performance of an Applied Field MPD (Magnetoplasma dynamic) Thruster*. PhD thesis, Princeton University, Princeton, NJ, 1973.
- [21] G.L. Cann et al. High Specific Impulse Thermal Arc Jet Thruster Technology. Technical Report 5090-IR-2, Electro-Optical Systems, Pasadena, CA, 1965.
- [22] N.M. Nerheim and A.J. Kelly. A Critical Review of the Magnetoplasma dynamic (MPD) Thruster for Space Applications. Technical Report 32-1196, Jet Propulsion Laboratory, California Institute of Technology, Pasadena, CA, 1968.
- [23] D.B. Fradkin and D.J. Roehling. Experiments in the New LASL MPD Arcjet Test Facility. Technical Report LA-5199-MS, Los Alamos Scientific Laboratory, University of California, Los Alamos, NM, 1973.
- [24] D.B. Fradkin, March 1991. Private communication.
- [25] D.B. Fradkin et al. Experiments Using a 25-kw Hollow Cathode Lithium Vapor MPD Arcjet. *AIAA Journal*, 8(5):886-894, 1970.
- [26] N.A. Black and D.B. Fradkin. Macroscopic Analysis of Magnetoplasma dynamic Arc Jets. Technical Report LA-3736, Los Alamos Scientific Laboratory, University of California, Los Alamos, NM, 1967.
- [27] A.W. Blackstock, D.B. Fradkin, D.J. Roehling, and T.F. Stratton. A Cesium MHD Arc Jet. *Journal of Applied Physics*, 39(7):3201-3209, 1968.
- [28] S.D. Grishin, A.K. Litvak, S.N. Ogorodnikov, and V.N. Stepanov. Intermediate Power Steady-State Plasma Accelerator. *Soviet Physics-Technical Physics*, 22(2):280-283, 1977.
- [29] L.I. Ageev et al. *Izmeritel' Tekh.*, 2:32, 1973.
- [30] G.V. Babkin, V.G. Mikhalev, S.N. Ogorodnikov, R.V. Orlov, and A.V. Potapov. High-Current Coaxial Plasma Source. *Soviet Physics-Technical Physics*, 20(9):1175-1178, 1977.
- [31] L.I. Vainberg, G.A. Lyubimov, and G.G. Smolin. High Current Discharge Effects and Anode Damage in an End-Fire Plasma Accelerator. *Soviet Physics-Technical Physics*, 23(4):439-443, 1978.



- [32] A.S. Koroteev, V.F. Semyonov, V.N. Akimov, and M.N. Vatel. Power-Propulsion Systems for Orbital Nuclear Transfer. In 41<sup>st</sup> IAF Congress, Dresden, GDR, 1990. AIAA 65-296.
- [33] V.I. Brukhty et al. Electric Propulsion for Space Research. Moscow Physical-Technical Institute, 8, Onezhskaya, Moscow, 12438 USSR.
- [34] V.V. Zhurin, A.A. Porotnikov, and V.P. Shadov. Electric Propulsion Research and Development in the USSR. In 12<sup>th</sup> International Electric Propulsion Conference, Key Biscayne, FL, 1976. AIAA 76-1073.
- [35] V.V. Zhurin et al. Electric Propulsion in the USSR, Part III: Active Experiments in Space Using MPD Accelerators. Undated paper distributed at the Specialist Conference on Nuclear Power Engineering in Space, Obninsk, USSR, May 15-19, 1990.
- [36] V.N. Karasev et al. Mutual Relationship of Adsorption Processes on the Surface of a Cathode and the Processes Taking Place in the Parts of a Heavy Current Discharge Close to the Electrodes. *Journal of Applied Mechanics and Technical Physics*, 5:625-627, 1972.
- [37] V.M. Ogarkov, S.N. Ogorodnikov, and V.N. Stepanov. The Design of a Multirod Cathode for a High-Current Plasma Source. *Radio Engineering and Electronic Physics*, 21(12):98-103, 1976.
- [38] V.K. Medvedev. *Izv. Akad. Nauk SSSR, Ser. Fiz.*, 33(3):529, 1969.
- [39] E.P. Gyftopoulos and J.D. Levine. Work Function Variation of Metals Coated by Metallic Films. *Journal of Applied Physics*, 33(1):349-360, 1962.
- [40] J.D. Levine and E.P. Gyftopoulos. Adsorption Physics of Metals Partially Covered by Metallic Particles. II: Desorption Rates of Atoms and Ions. *Surface Science*, 1:225-241, 1964.
- [41] J.D. Levine and E.P. Gyftopoulos. Adsorption Physics of Metals Partially Covered by Metallic Particles. I: Atom and Ion Desorption Energies. *Surface Science*, 1:171-193, 1964.
- [42] H.S.W. Massey and E.H.S. Burhop. *Electronic and Ionic Impact Phenomena*. Oxford Press, 1956.
- [43] C.C. Addison. *The Chemistry of the Liquid Alkali Metals*. John Wiley and Sons, Chichester, 1984.
- [44] H.U. Borgstedt and C.K. Mathews. *Applied Chemistry of the Alkali Metals*. Plenum Press, New York, NY, 1987.
- [45] R.H. Cooper and E.E. Hoffman, editors. *Refractory Alloy Technology for Space Nuclear Power Applications*. Technical Information Center, Office of Scientific and Technical Information, US-DOE, 1984. CONF-8308130 (DE84001745).
- [46] American Chemical Society. *Handling and Uses of the Alkali Metals, Number 19 in the Advances in Chemistry Series*, 1957.
- [47] J.W. Mausteller, F. Tepper, and S.J. Rodgers. *Alkali Metal Handling and Systems Operating Techniques*. Gordon and Breach Science Publishers, New York, NY, 1967.
- [48] D.C. Byers. A Review of Electron Bombardment Thruster Systems/Spacecraft Field and Particle Interfaces. In AIAA 13<sup>th</sup> International Electric Propulsion Conference, San Diego, CA, 1978. AIAA 78-677 (NASA TM-78850).
- [49] R. Sperber. Why Don't We Use Ion Propulsion? 1984. AIAA 84-0730.
- [50] J.D. Levine and E.P. Gyftopoulos. Adsorption Physics of Metals Partially Covered by Metallic Particles. III: Equations of State and Electron Emission S-Curves. *Surface Science*, 1:349-360, 1964.
- [51] R.F. Kemp, D.F. Hall, and E.E. Luedke. Electrostatic Propulsion Beam Divergence Effects on Spacecraft Surfaces, Vol. III. Technical Report TRW-11985-6003-RU-00 (NASA CR-136933), TRW Systems Group, Redondo Beach, CA, 1973.
- [52] R.F. Kemp, J.C. Beynon, D.F. Hall, and E.E. Luedke. Effects of Cesium Ions and Cesium Vapor on Selected ATS-F Samples. In AIAA 10<sup>th</sup>

*Electric Propulsion Conference, Lake Tahoe, NV, 1973. AIAA 73-1099.*

- [53] J. Millard, April 1991. Private communication.
- [54] R. Worlock, G. Trump, J.M. Sellen, and R.F. Kemp. Measurement of Ion Thruster Exhaust Characteristics and Interactions with Simulated ATS-F Spacecraft. In *AIAA 10<sup>th</sup> Electric Propulsion Conference, Lake Tahoe, NV, 1973. AIAA 73-1101.*
- [55] N.J. Stevens. Determination of the Extent of Ion Thruster Efflux Deposition on Spacecraft Surfaces from the SERT II Flight Thermal Data. In *11<sup>th</sup> Electric Propulsion Conference, New Orleans, LA, 1975. AIAA 75-356.*